Technische Universität Berlin

Fakultät V - Verkehrs- und Maschinensysteme
Institut für Strömungsmechanik und technische Akustik (ISTA)
Fachgebiet Experimentelle Strömungsmechanik
– Hermann-Föttinger-Institut –

On the Influence of Steam in Premixed Hydrogen Flames for Future Gas Turbine Applications

vorgelegt von

Diplom-Ingenieur
Oliver Krüger
geb. in Berlin

von der Fakultät V - Verkehrs- und Maschinensysteme
der Technischen Universität Berlin
zur Erlangung des akademischen Grades

Doktor der Ingenieurwissenschaften
– Dr.-Ing. –

genehmigte Dissertation

Promotionsausschuss:

Vorsitzender:	Prof. Dr. rer. nat. Wolfgang H. Müller	(Technische Universität Berlin)
Gutachter:	Prof. Dr.-Ing. C. O. Paschereit	(Technische Universität Berlin)
Gutachter:	Prof. Dr. Laszlo Fuchs	(KTH Royal Institute of Technology)
Gutachter:	Prof. Dr. Christophe Duwig	(Volvo Car Corporation)

Tag der wissenschaftlichen Aussprache: 19. Februar 2015

Berlin 2015
D 83

> *Denn es ist eines ausgezeichneten Mannes nicht würdig, wertvolle Stunden wie ein Sklave im Keller der einfachen Berechnungen zu verbringen. Diese Aufgaben könnten ohne Besorgnis abgegeben werden, wenn wir Maschinen hätten.*

Gottfried Wilhelm Leibniz, *1685*

> *It is unworthy of excellent men to lose hours like slaves in the labour of calculation which could safely be relegated to anyone else if machines were used.*

Gottfried Wilhelm Leibniz, *1685*

Zusammenfassung

Oliver Krüger

On the Influence of Steam in Premixed Hydrogen Flames for Future Gas Turbine Applications

Aufgrund der limitierten Verfügbarkeit fossiler Rohstoffe, ist der Umschwung auf neue Energieträger, neben der Entwicklung effizienter Energiespeichertechniken und einer intelligenten Lastverteilung, eine der größten Herausforderungen des 21. Jahrhunderts. Erzeugt aus regenerativen Energiequellen ist Wasserstoff hierfür ein aussichtsreicher Kandidat. Auch wenn Wasserstoff ein herausragender Energieträger ist, ist seine Handhabung nicht trivial. Daher ist es bis heute mit konventionellen Methoden noch nicht möglich eine herkömmliche Gasturbine mit Wasserstoff zu betreiben. Insbesondere die hohen Flammengeschwindigkeiten erhöhen das Risiko eines Flammenrückschlages erheblich. Daher ist es notwendig neue Verbrennungskonzepte zu untersuchen um ein tiefgreifendes Verständnis für die Verbrennungsvorgänge von neuartigen Treibstoffen zu entwickeln.

In der vorliegenden Arbeit wird eine Methode untersucht um eine effiziente Verbrennung von Wasserstoff in Gasturbinenprozessen zu ermöglichen. Dafür wird dem Verbrennungsprozess Wasserdampf beigefügt, welcher die Verbrennungstemperatur erheblich absenkt und gleichzeitig den Wirkungsgrad erhöht. Zusätzlich wird ein Gasturbinenzyklus vorgestellt, der eine saubere und effiziente Verbrennung von Wasserstoff erlaubt und gleichzeitig als effizienter Energiespeicher dient.

Im Rahmen dieser Arbeit wird der Verbrennungsprozess von Wasserstoff unter hohen Dampfmengen analysiert. Mit Hilfe von detaillierter Chemie und laminaren Vormischflammen wird Luft und reiner Sauerstoff als Reaktionspartner untersucht. Dazu werden in einem ersten Schritt diverse Reaktionsmechanismen untersucht und mit Literaturdaten zu laminaren Brenngeschwindigkeiten und Zündverzugszeiten verglichen. Es wird außerdem gezeigt, dass Wasserdampf den Verbrennungsprozess hauptsächlich als Stoßpartner beeinflusst, indem er starken Einfluss auf die Erzeugung von Radikalen nimmt. Dadurch wird die Brenngeschwindigkeit und die Selbstzündung stark gehemmt. Außerdem wird nachgewiesen, wie Wasserdampf positiv auf die Bildung schädlicher Stickoxide einwirkt. Bei der Untersuchung von turbulenten Vormischflammen beeinflusst Wasserdampf maßgeblich das Flammenbild. So breitet sich die Wärmefreisetzungszone weiter aus, die Flammenfront verdickt sich und die Flamme nimmt an Länge zu. Die Grobstruktursimulationen (LES) können im Vergleich mit den Experimenten das Strömungsfeld und die Flammencharakteristik sehr gut reproduzieren.

Der Beitrag dieser Arbeit ist ein tief gehender Einblick in den Verbrennungsprozess von Wasserstoff unter hohen Wasserdampfeinflüssen, der die Eignung von Wasserdampf für eine emissionsreduzierte und sogar emissionsfreie Verbrennung aufzeigt. Darüber hinaus liefert diese Arbeit validierte Entwicklungsmethoden für die Konzeptionierung von zukünftigen mit Wasserstoff betriebenen Gasturbinenbrennkammern.

Schlagwörter: Wasserstoff Verbrennung, Gasturbine, Detailierte Chemie, Grobstruktursimulation

Abstract

Oliver Krüger

On the Influence of Steam in Premixed Hydrogen Flames for Future Gas Turbine Applications

Following the limited availability of fossil fuels and growing environmental concerns, energy transition is beside energy storage and grid balancing one of the major challenges of the 21st century. Among the variety of alternative and renewable fuels, hydrogen is a promising candidate if produced from water and excess electricity or biomass. However, hydrogen combustion properties differ significantly from established fossil fuels. For example, it is not possible to operate safely a traditional gas turbine on high hydrogen content fuels, due to the high risk of flashback. In particular it is challenging to retrofit conventional gas turbine applications to allow for an efficiently and clean usage of hydrogen or hydrogen-rich fuels. In fact, it calls for a new generation of combustion technologies based on deep understanding of new fuels and their combustion behavior.

The present thesis addresses the possibility to utilize hydrogen as a efficient and clean gas turbine fuel. At nearly stoichiometric conditions steam is added directly into the combustion process, which significantly reduces the flame temperature. Moreover, a possible future gas turbine cycle is discussed that allows for the efficient combustion of hydrogen, energy storage and grid balancing. The scope of the thesis is to investigate the premixed combustion of pure hydrogen diluted with varying amounts of steam for gas turbine applications. The combustion process is modeled accurately using detailed chemical description of the complex oxidation reactions. In order to assess this several reaction mechanisms were identified and compared. Their respective performances are assessed based on laminar premixed flame calculations and auto-ignition events under dry and steam diluted conditions, for which experimentally determined measurements are available. A detailed study enabled to identify the effect of steam focusing on the third-body reactions with a significant increase of some key radial concentrations. In addition, high steam concentration results in a modification of the nitrogen oxides formation pathways, resulting in significantly lower emission concentrations. For the assessment of turbulent flames it is shown that the heat release spreads, the flame front thickens and the flame extends slightly further downstream with the addition of steam. In comparison with the OH^* chemiluminescence images the simulated flame shape and positions are well in line with the experiments. In conclusion it is shown that the LES together with the assembled detailed reaction mechanism is able to predict the flow field and oxidation process of steam diluted hydrogen flames.

Within the scope of this thesis, new insight into the combustion process of highly steam diluted hydrogen flames is given, showing that steam dilution is a promising alternative for low- or zero-emission combustion. An additional outcome of this study is a accurate and validated set of tools and methods for a further design process of a hydrogen powered gas turbine cycle.

Key words: Hydrogen combustion, Gas turbines, Detailed chemistry modeling, Large Eddy Simulation

Contents

Acronyms

Notation	Description
CFD	Computational Fluid Dynamics
CPU	Central Processing Unit
DNS	Direct Numerical Simulation
EBU	Eddy Break-Up Model
EDC	Eddy Dissipation Concept
EPOD	Extended Proper Orthogonal Decomposition
FDF	Filtered Density Function
FFW	Fractal Flame Wrinkling
FLOX	Flameless Oxidation
HGT	Humid Gas Turbine
ILES	Implicit Large Eddy Simulation
IRZ	Inner Recirculation Zone
JHC	Jet in Hot Coflow
LDV	Laser Doppler Velocimetry
LEM	Linear-Eddy Model
LES	Large Eddy Simulation
LIF	Laser-Induced Fluorescence
MILD	Moderate or Intense Low-oxygen Dilution
MILES	Monotonically Integrated LES
ODT	One-Dimensional Turbulence
ORZ	Outer Recirculation Zone
PaSR	Partially Stirred Reactor
PDF	Probability Density Function
PIV	Particle Image Velocimetry
PLIF	Planar Laser-Induced Fluorescence

Notation	Description
POD	Proper Orthogonal Decomposition
PVC	Precessing Vortex Core
RANS	Reynolds-averaged Navier-Stokes
RCM	Rapid Compression Machine
TFM	Thickened Flame Model
TVD	Total Variation Diminishing Scheme

List of Symbols

Symbol	Description	Unit
Dimensionless Quantities		
Co	Courant number	–
Da	Damköhler number	–
Ka	Karlovitz number	–
Ma	Mach number	–
Pr	Prandtl number	–
Re	Reynolds number	–
St	Strouhal number	–
Greek Letters		
α	Thermal diffusivity	$\mathrm{m^2/s}$
χ	Steam concentration	–
χ	Exponent	–
Δ	Filter width	m
$\hat{\lambda}$	Eigenvalue	varies
Λ	Radial pressure eigenvalue	$\mathrm{m/s}$
λ	Thermal conductivity	$\mathrm{W/m\,K}$
λ_f	Taylor length scale	m
μ	Dynamic viscosity	$\mathrm{kg/m\,s}$
μ_t	Eddy viscosity	$\mathrm{kg/m\,s}$
ν	Kinematic viscosity	$\mathrm{m^2/s}$
ν	Spectral wavelength	m
ν''_{kj}	Stoichiometric coefficient for species k in reaction j, reverse direction	–
ν'_{kj}	Stoichiometric coefficient for species k in reaction j, forward direction	–
ν_t	Turbulent kinematic viscosity	$\mathrm{m^2/s}$
Φ	Variable for eigenvalue problem	–
ϕ	Equivalence ratio	–
$\Phi(\vec{x})$	Spatial eigenfunction	varies

$\Psi(\vec{x})$	Extended spatial eigenfunction	varies
ϱ	Density	kg/m^3
σ	Variance of concentration	$\mathrm{mol}^2/\mathrm{m}^6$
τ_{ij}	Subgrid scale stress tensor	$\mathrm{m}^2/\mathrm{s}^2$
τ_0	Turbulent integral time scale	s
τ_c	Chemical time scale	s
Ξ	Flame wrinkling	–
ξ	Steam fraction	–
$\dot{\omega}$	Reaction rate	$\mathrm{mol}/\mathrm{m}^3\,\mathrm{s}$
Ω	Steam-air ratio	–

Latin Letters

A	Diagonal matrix	–
A	Model constant	–
A	Pre-exponential constant	varies
$a_i(t)$	Time coefficient	varies
A_l	Area of the laminar flame front	m^2
A_t	Area of the turbulent flame front	m^2
B	Model constant	–
C_1	Model constant	–
C_3	Model constant	–
c_p, c_v	Specific heat capacity	$\mathrm{J}/\mathrm{kg\,K}$
C_s	Smagorinsky constant	–
D	Diffusion coefficient	m^2/s
D_h	Hydraulic diameter	m
E	Efficiency function	–
E_A	Activation energy	J/mol
e_i	Solution coefficient	varies
F	Flame thickening factor	–
F	Function	–
F_i	Volume force	m/s^2
h	Planck constant	$\mathrm{m}^2\mathrm{kg}/\mathrm{s}$
h	Specific enthalpy	J/kg
h_t	Total enthalpy	J/kg
J	Diffusion flux	$\mathrm{kg}/\mathrm{m}^2\mathrm{s}$
J	Jacobian matrix	–
k	Index of species	–
k	Turbulent kinetic energy	$\mathrm{m}^2/\mathrm{s}^2$
$k_{f,j}$	Rate constant for reaction j, forward direction	varies
$k_{r,j}$	Rate constant for reaction j, reverse direction	varies
l_0	Integral length scale	m
M	Molar mass	kg/mol
m	Model constant	–

m	Reaction multiplier	–
n	Model constant	–
n	Temperature exponent	–
p	Pressure	Pa
Q	Vector of field variables	varies
q	Reaction rate	$^{\mathrm{mol}}/_{\mathrm{m^3\,s}}$
R	Universal gas constant	$^{\mathrm{J}}/_{\mathrm{mol\,K}}$
S	Sensitivity matrix	varies
S_l	Laminar burning velocity	$^{\mathrm{m}}/_{\mathrm{s}}$
S_{ij}	Strain rate tensor	$^{1}/_{\mathrm{s}}$
S_{th}	Swirl number	–
S_{eff}	Effective swirl number	–
$\hat{S}$	Normalized sensitivity matrix	–
S_t	Turbulent burning velocity	$^{\mathrm{m}}/_{\mathrm{s}}$
T	Temperature	K
t	Time	s
T_b	Temperature of the burnt gases	K
T_u	Temperature of the unburnt gases	K
e	Specific internal energy	$^{\mathrm{J}}/_{\mathrm{kg}}$
u'	Velocity fluctuation	$^{\mathrm{m}}/_{\mathrm{s}}$
u_0	Bulk velocity	$^{\mathrm{m}}/_{\mathrm{s}}$
u_Δ	Subgrid velocity fluctuation	$^{\mathrm{m}}/_{\mathrm{s}}$
u_i	Velocity component	$^{\mathrm{m}}/_{\mathrm{s}}$
$U_{s,t}$	Degree of unmixedness	–
u_{in}	Inlet velocity	$^{\mathrm{m}}/_{\mathrm{s}}$
X	Mole fraction	–
Y	Mass fraction	–
Δz	Displacement length	mm
x,y,z	Spatial coordinate	m

Symbols

δ_{ij}	Kronecker delta	–
ϵ_{ijk}	Levi-Civita symbol	–
$\mathrm{HP}(\cdot)$	High-pass filter	–
$\widetilde{[\cdot]}$	Molar concentration	$^{\mathrm{mol}}/_{\mathrm{m^3}}$
$\widetilde{(\cdot)}$	Density weighted filter	–
$\overline{\lvert\cdot\rvert}$	Magnitude	–
$\overline{(\cdot)}$	Spatial filter	–
$\langle\cdot\rangle$	Time averaging operator	–

1

Introduction

> *Begin at the beginning," the King said, gravely, "and go on till you come to an end; then stop.*
>
> Lewis Carroll, *Alice in Wonderland*, 1899

1.1 Motivation

Beginning with the first oil crisis in 1973 the depletability regarding the global energy resources became self-evident. The crisis was a direct consequence of the US oil production peak in the late 1970s. Peak oil is the point at which the global production of conventional oil reaches the maximum and thus, subsequent flow rates decrease. Even though the theory of Hubbert (1971) predicted precisely the US production peak in 1971, his forecast of a global oil production peak in 1995 was proven to be inaccurate. Numerous predictions of when the oil will peak have been published since then (Chapman, 2014). However, the latest peak is suggested for the 2040s. Although the oil production and proven resources are not directly linked with the remaining reserves of other natural energy resources, it is apparent that their availability is limited too. Thus, Hubbert's peak theory has also been applied to other natural resources. According to Maggio et al. (2012) the world natural gas resources are likely to peak between 2024 and 2046 and the world coal between 2042 and 2062. The study by Gabriel et al. (2013) stresses the fact that also the available natural uranium is considered to be consumed by 2050. Hence, all main energy carrier are assumed to peak within the next half century. Furthermore, the impact of mankind on its habitat needs to be minimized to secure an environmentally sustainable future. By that means the pollution of the environment is of the same paramount importance as the assurance of a future energy supply.

Although much effort has been spent in reducing energy consumption, increasing process efficiencies, and investigating and developing renewable energy resources, we are far from being independent from fossil reserves. Renewable energies are a promising alternative to conventional fuels, due to the fact that they replenish on a human timescale and are supposed to have an overall minor impact on the environment. However, they are also bound by limitations. This fact is exemplified in Figure 1.1, where the electrical power demand and the wind and solar

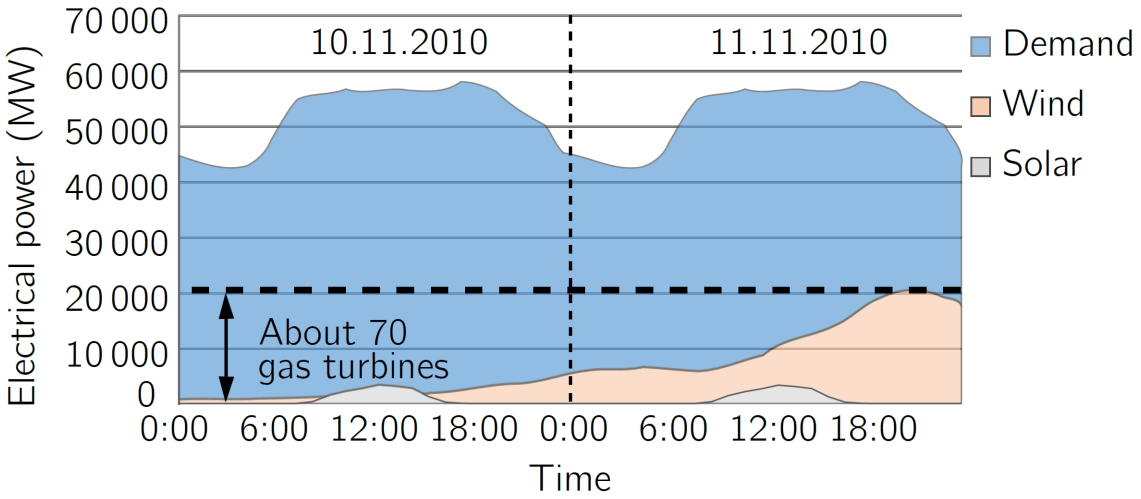

Figure 1.1: Hourly electrical power demand for two arbitrary days. Source: European Energy Exchange AG

electricity generation are depicted for two days in Germany. As shown in the presented case wind power can replace up to 70 conventional heavy-duty gas turbines, but not on a regular basis. Moreover, renewable energies rarely provide immediate response to the power demand as these sources do not deliver a reliable constant supply adjustable to consumption needs. This stresses the fact that the growth of decentralized power production leads to greater network load stability problems and requires energy storage. Several energy storage techniques have been proposed (Hadjipaschalis et al., 2009; Ibrahim et al., 2008) but are either of questionable environmental soundness (lead batteries), limited to geographical conditions (pumped-storage hydroelectricity) or still in the research and development phase (flywheel, super-capacitors). Nevertheless, the present thesis proposes a different avenue to store energy: producing hydrogen from renewable resources in times of overproduction and using it as gas turbine fuel in times of underproduction. This way it is possible to store and re-store energy at zero-emissions.

Produced from renewable energy sources, hydrogen offers the possibility to overcome severe constraints on greenhouse gas emissions, since hydrogen combustion produces no harmful products such as CO_2, CO, SO_x and etc. Due to a lack of fuel bound NO_x, only thermal NO_x emissions can arise from the combustion process based on intake air. Operating a gas turbine with hydrogen is, however, a challenging task. Compared to conventional gas turbine fuels, hydrogen features a much higher burning velocity, and thus, a high risk of flashbacks. This thesis addresses the possibility to burn hydrogen in heavy-duty gas turbine applications by adding steam directly into the combustion process as presented in Figure 1.2. Compared to combined cycles such a Humid Gas Turbine (HGT) offers the attractive possibility of increasing the plant efficiency without the need of an additional steam turbine, and hence, reduce the capital expenditures. In addition to efficiency gains, the humid cycles have a reduced turn on time, a smaller footprint, and the injection of steam into the combustion process reduces NO_x emissions. It also increases the specific heat capacity and thus lowers the peak temperature and the oxygen concentration. Supplementary to the thermodynamic influence of the steam on

the combustion process, it alters the NO_x formation pathways. Even at constant adiabatic flame temperatures, it was observed that NO_x is reduced with increasing humidity (Bhargava et al., 2000; Göke et al., 2013). In addition, steam injection allows operation with a variety of fuels, including hydrogen and hydrogen-rich fuels. Therefore, ultra-wet gas turbine operation is an attractive solution for future industrial application. The wet gas turbine cycle was already proposed by John Barber in the first gas turbine patent specification from 1791 where water is added to the process to lower the flame temperature and further cooling purposes:

> "It consists of metallic vessel called a retort, so contrived that ... coal, wood, oil, or any other combustible matter may be put therein, and the smoke or vapour therein collected may be brought out by a small pipe, and conveyed in a regular stream into another metallic vessel called an exploder ... The fluid stream is also considerably augmented both in quantity and velocity by water injected into the exploder ..., which water is also intended to prevent the inward pipes and the mouth of the exploder for melting by the velocity and intenseness of the issuing flame." (Barber, 1791, P. 2)

It took more than a century until Elling constructed one of the first gas turbines with a positive net power output in 1903. This turbine also employed steam as cooling agent for the compressor and combustion gases. Numerous humidified cycles were investigated and reviewed by Jonsson et al. (2005). According to Jonsson's findings, the cogeneration of power and district heating seems to be the most promising application for humidified gas turbines because estimations showed that the specific investment costs and costs of electricity and heat are supposed to be significantly lower than for combined cycles. For the usage of hydrogen as gas turbine fuel, several avenues have been suggested. One way to accommodate for peak demands was suggested by Sternfeld et al. (1982), who investigated the possibility to extend a conventional base load power plant (coal) by an additional steam generator based on the combustion of hydrogen and air or hydrogen and pure oxygen. They reported that the suggested cycle is most efficient for the combination of pure hydrogen-oxygen and a net load above 50 MW.

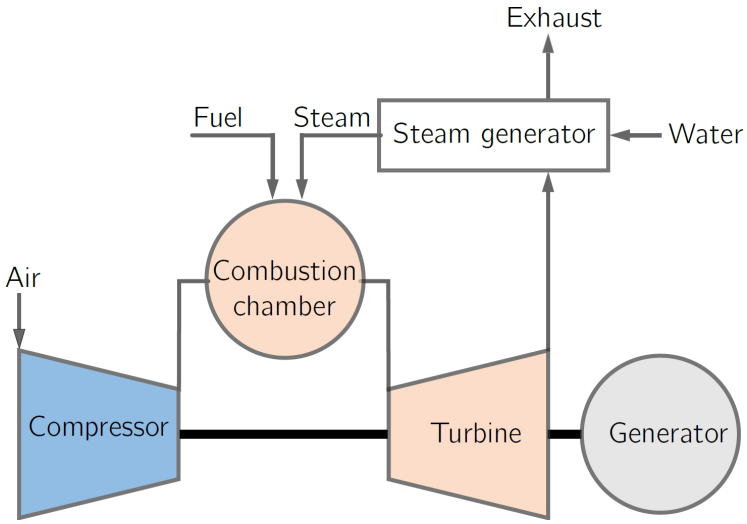

Figure 1.2: Schematic of Humid Gas Turbine cycle.

Sternfeld further investigated the usage of pure hydrogen and oxygen as a spinning reserve unit for an industrial steam network and steam turbine power plant (Sternfeld et al., 1989). For demonstration and simplification they used a conventional rocket engine as steam generator. The results indicate that a pure hydrogen and oxygen spinning reserve unit can be integrated into existing steam networks and power plants. Malyshenko et al. (2004) focused on the steam generator itself. In their study a high-pressure H_2-O_2 steam generator was evaluated. It was shown that for power units featuring more than 10 MW, steam turbine hydrogen units are preferable over fuel cell units. Moreover, the assessment of a self-contained H_2-O_2 steam turbine power unit cycle lead to an efficiency of 64.9% at 200 atm. Juste (2006) examined the solution to inject hydrogen as additional fuel in a gas turbine combustor, showing that adding small quantities of hydrogen contributes to a reduction in CO_2 caused by a substitution effect. Directly using hydrogen as gas turbine fuel was assessed by Bannister et al. (1999). Employing a Rankine cycle they could calculate a net plant efficiency of 71.4%. This findings are supported by the review paper of Yang (2006), who scrutinized several cycles and concluded that a hydrogen-fueled power plant with an efficiency above 70% can be accomplished.

Whereas the aforementioned studies did not contemplate the generation of hydrogen for the combustion process, the paper by Kato et al. (1997) goes a step further and proposes an alternative energy scheme. The main idea is a small sized decentralized hydrogen gas turbine with 10 kW for each house to generate electricity and heat. The dump electricity from renewable energies is used for electrolysis to store and produce hydrogen and oxygen. The presented hydrogen-oxygen gas turbine cycle is part of the EU funded project *BlueStep*, which will start in March 2015. The main idea is to employ renewable energies to generate hydrogen and oxygen in the off-peak hours via electrolysis as it is illustrated in Figure 1.3. For the electrolysis pressurized liquid water is used, hence the gaseous products are already in a pressurized state before they are stored. Because it is more efficient to pressurize liquid water than to compress the gaseous products (Cicconardi et al., 2004; Janssen et al., 2001; Turner, 2004), there is no need for a gas compressor. From the storage the hydrogen and oxygen are fed to the combustion chamber, ignited and the hot flow is expanded in the turbine, which is itself driving the generator. In turn, the generator supplies electricity back to the power supply. This concept allows to produce hydrogen and oxygen through pressurized electrolysis in off-peak hours through excessive renewable energies and stores them for peak-hours. Then, the pressurized products are processed in a gas turbine generating electricity (and heat) which is fed back into the main grid. Unfortunately, there is currently no study concerning the efficiency of the cycle available. However, Gambini et al. (2005) reported an efficiency of 62.6% for an updated version of the cycle presented in Figure 1.2. Even though this cycle is very attractive, the possibility to retrofit existing gas turbines with the ability to utilize hydrogen is also considered (Stathopoulos et al., 2014). Since the availability of hydrogen and hydrogen-enriched syngases is increasing, a short-term perspective is to retro-fit existing gas turbine concepts to work as humid gas turbine cycle according to the scheme in Figure 1.2. This allows for the usage of already established concepts with lower investment costs than is the case for developing a new design from scratch. Therefore, this thesis investigates the influence of steam on hydrogen flames with pure oxygen as well as with air as oxidizer. Even though specifications regarding gas turbine conditions are rare in the literature, in particular for turbine inlet temperatures, an adiabatic flame temperature of 1573 K is assumed to reasonable.

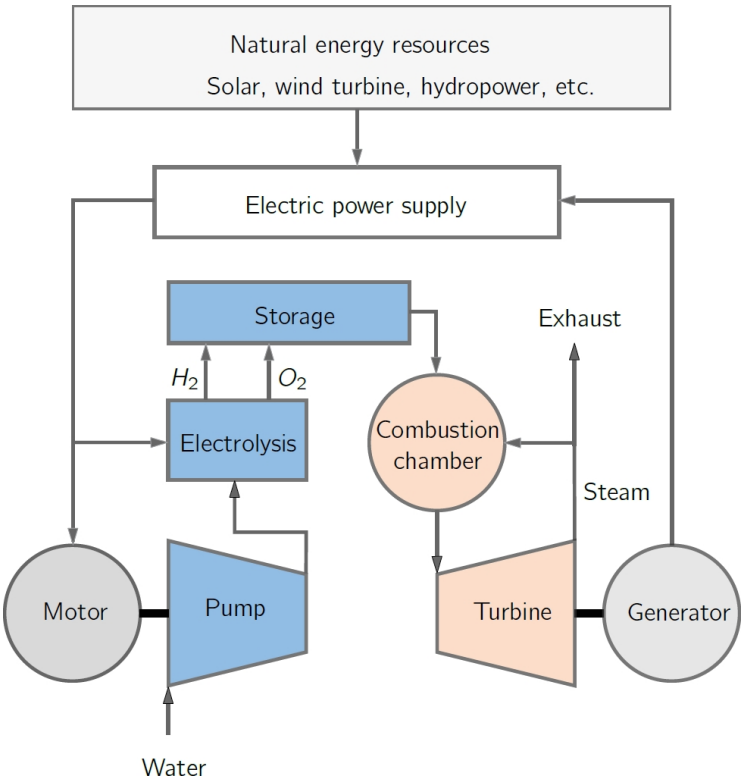

Figure 1.3: Renewable energy driven hydrogen-oxygen gas turbine cycle derived from Kato et al. (1997).

The concept of directly injecting high steam contents into the combustion process to increase efficiency and reduce harmful emissions is developed in several projects at the *Chair of Fluid Dynamics* at the *Technische Universität Berlin*. In 2009, the research was awarded with the prestigious "Advanced Investigators Grant" of the European Research Council funding the project *GREENEST* for five years. The main objective of this project is to investigate the fundamentals of the combustion process at steam diluted conditions, and to develop a combustor prototype for application in a practical gas turbine. The present thesis originated from this project. Successors of this project are the *CleanGT* and the *BlueStep* project. The aim of the *CleanGT* project is to implement an ultra-wet gas turbine cycle into a domestic gas turbine whereas the aim of the project *BlueStep* is to develop and implement an oxyfuel (H_2-O_2) gas turbine cycle into a domestic gas turbine.

1.2 Purpose and Objectives

This study is dedicated to the investigation of the premixed combustion process of pure hydrogen diluted with varying amounts of steam for gas turbine applications. Both molecular oxygen and air are considered as oxidizer and the effect of steam on the combustion process is addressed by using detailed chemistry. One aim of this study is to identify an adequate detailed reaction scheme. Employing one-dimensional laminar premixed flame computations, several candidates are identified and compared. Their respective performances are assessed at several steam levels

for which experimentally determined flame speeds are available. Further, the influence of steam on the combustion process is assessed and the underlying mechanism identified. In addition subsets for OH^* chemiluminescence and $\mathrm{NO_x}$ conversion are also evaluated. Thus, a reaction scheme is created for the investigation of turbulent combustion processes. A further objective is to identify a suitable turbulence and combustion closure to perform three-dimensional reacting simulations and to determine the impact of turbulence on the combustion process. The results are compared to experimental data. Thus, a complete and validated process chain for a future hydrogen combustor design is developed.

1.3 Outline of the Dissertation

The thesis is divided into two main parts. The first part is dedicated to laminar flames. The part begins with a short introduction and the presentation of the numerical methodology. Subsequently, a suitable reaction mechanism is identified by comparing several candidates with experimental data. Afterward, the influence of steam on the combustion process is investigated. In a further step, several reaction subsets for OH^* chemiluminescence are interrogated and the effect of steam on the OH^* conversion is assessed. In the last chapter of the first part, a similar approach is used to evaluate the production of nitrogen oxides under the influence of steam. The first part is concluded by a concise summary. In the second part, the resulting reaction scheme is used for Large Eddy Simulations of a turbulent flame in a generic swirl burner fed with hydrogen and humidified air. Therefore, the second part begins with a brief introduction into turbulent combustion and the numerical schemes are explained in detail. Afterward, the investigated geometry, and the experimental and numerical techniques are presented. In a first step, an isothermal LES is conducted to assess the sensitivity of the spatial grid resolution and turbulence closure. Based on the findings, the influence of the grid resolution as well as the chosen combustion closure is evaluated for a reacting flow. Velocity profiles, flame shape and positions are compared to OH^* chemiluminescence recordings and PIV measurements. The second part is also concluded by an intermediate summary. Finally, in the last chapter of the thesis the overall results are summarized and conclusions are drawn.

> *It is noteworthy that some chapters are rounded up by intermediate conclusions to give the reader a better overview of the findings. The conclusions are indicated by a gray line at the left margin, as is the case for this paragraph.*

PART I

Laminar Flames

2

Laminar Flames

> *Play the man, Master Ridley; we shall this day light such a candle, by God's grace, in England, as I trust shall never be put out.*
>
> Hugh Latimer, *October 1555*

2.1 Physical Chemistry Background

The investigation of laminar flames is a basic problem in combustion and is of paramount interest because it allows for detailed comparisons between theory, experiments, and numerical modeling. These flames offer the advantage of well-defined flame conditions suitable for fundamental investigations of the combustion process, and thus allow for examination of isolated effects (e.g., the impact of steam on the combustion process). When detailed chemistry is considered, there is no analytical solution to the problem and numerical solutions are required. However, some configurations may be simplified leading to lower dimensional models (zero- or one-dimensional) that reduce the computational burden significantly.

The laminar burning velocity is perhaps one of the most fundamental parameters in flame theory (Law, 2006). It is a key parameter in characterizing a combustible mixture because it practically indicates the rate with which the combustible mixture is consumed by a propagating laminar flame. The laminar burning velocity (S_l) is defined as the local velocity at which the flame front propagates normal to itself into the unburned gas. It depends primarily on the pressure, temperature, and the composition. The propagation mechanism of a premixed flame is based on the diffusive transport of heat and radicals into the unburnt gas and is directed orthogonal to the flame front, as long as the flame is only weakly stretched or unstretched. This is due to the fact that in the tangential direction the necessary temperature and species concentration gradients are negligible.

Figure 2.1 illustrates a typical premixed flat flame. Mallard et al. (1883) separated the temperature distribution into two regions. In the inert preheat zone the unburned gas is heated up to the ignition temperature. Subsequent to this region is the reaction zone located where the main combustion process takes place and the heat release occurs. This zone is marked by the rapid increase in temperature and concentration of the main radicals H, O, OH. These radicals

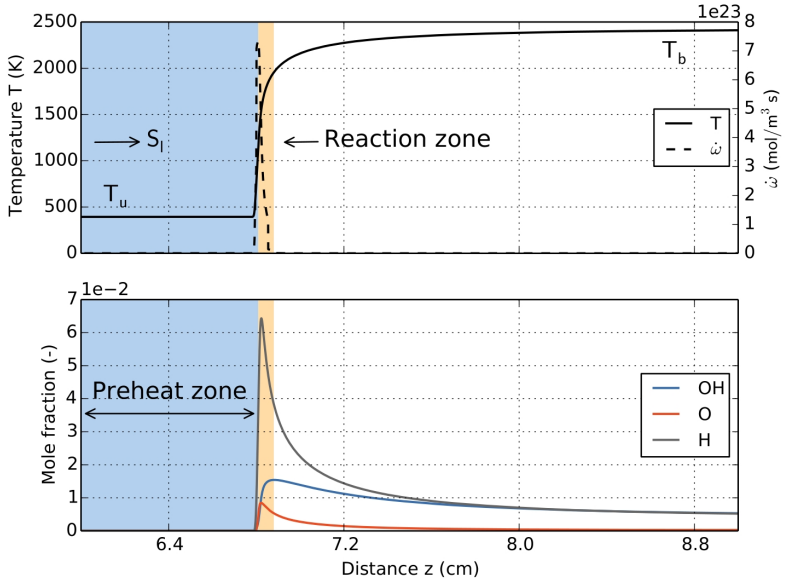

Figure 2.1: Schematic of a one-dimensional premixed hydrogen-air flat flame at atmospheric pressure. Initial temperature is 500 K at stoichiometric conditions.

recombine after the active oxidation process is completed yielding temperature increase until they reach their equilibrium. Due to the assumption of an adiabatic system, the temperature of the burnt gases (T_b) remains constant to the end of the domain. A steady-state solution exists if the inlet velocity equals the laminar burning velocity. This means the laminar burning velocity is an *eigenvalue* and thus, the problem to solve is an *eigenvalue* problem. This fact is used to compute one-dimensional flames, as presented in the next section. To determine the laminar burning velocity, several techniques are available. Beside the extensive efforts toward the determination of the laminar burning velocity over the years, accurate data have first become available since Wu et al. (1985) first identified the importance of flame stretch and proposed a methodology to systematically correct measurements for this effect. Due to various limitations (see Tse et al., 2000), stretch-free data is only available for pressures up to a few atmospheres. The most prominent measuring techniques to determine the laminar burning velocity are Bunsen burner configurations (nozzle (Koroll et al., 1988) or slot burners (Göckeler et al., 2014)), counterflow flame burners (Das et al., 2011), and explosion bombs (Kuznetsov et al., 2011; Tse et al., 2000).

Beside the laminar burning velocity, the ignition delay time is one of the most important parameters characterizing a combustible process and is therefore of importance for combustion modeling and analysis. *Ignition* is defined as the time-dependent process of starting with reactants and evolving towards a steadily burning flame (Warnatz et al., 2001). Hence, the ignition delay time is the time span between a combustible condition is achieved and the combustion takes place. In internal combustion engines, based on self-ignition, it is the time span between the injection of the fuel and the appearance of the flame. The ignition time delay depends on the composition of the fuel-oxidizer-mixture, the pressure and the temperature.

Internal combustion engines, for example Diesel engines or homogeneous charge compression ignition engines (HCCI), are based on the self-ignition principle and thus, the ignition time delay is a key parameter for describing the combustion process within these engines (Finesso et al., 2014; Gauthier et al., 2004). With combustion phases lasting only milliseconds, these engines are rather dynamical; so one could think that the ignition delay plays a subordinate role when considering gas turbines due to the constant combustion process. However, gas turbines as for example the GT24/26 from Alstom (Hiddemann et al., 2011) feature a second combustion stage where flame stability is based on self-ignition of the fuel emphasizing the importance of the self-ignition event. Furthermore, from an operational point of view, variations in the fuel composition and thus in the self-ignition delay time can result in pre-ignition in lean premixed gas turbines, which may lead to physically damage the engine (Lee et al., 2014). Thus, it is crucial to know the auto-ignition time delay of the used fuel at the full range of operating conditions. In addition, it serves as a key validation parameter of chemical kinetics mechanisms.

Figure 2.2 illustrates the constant-volume self-ignition event of a hydrogen-air mixture at atmospheric pressure, a preheat temperature of 1000 K and stoichiometric conditions. Beside the main radical pool, it depicts the temperature history as well as the according gradient. Apparently, the temperature increases rapidly after about 230 µs. After $\approx$ 280 µs the active oxidation process is completed, but the temperature continues to rise due to the heat release caused by the radical recombination (Kee et al., 2003). In the main oxidation period the principal radicals H, O, OH peak and subsequently recombine until they reach their equilibrium values. Due to the short timescales, it is challenging to determine the ignition time delay experimentally. However, in the past years several methods were established. The most prominent techniques are the *shock tube* (Gutman, 1969), the *rapid compression machine* (Das

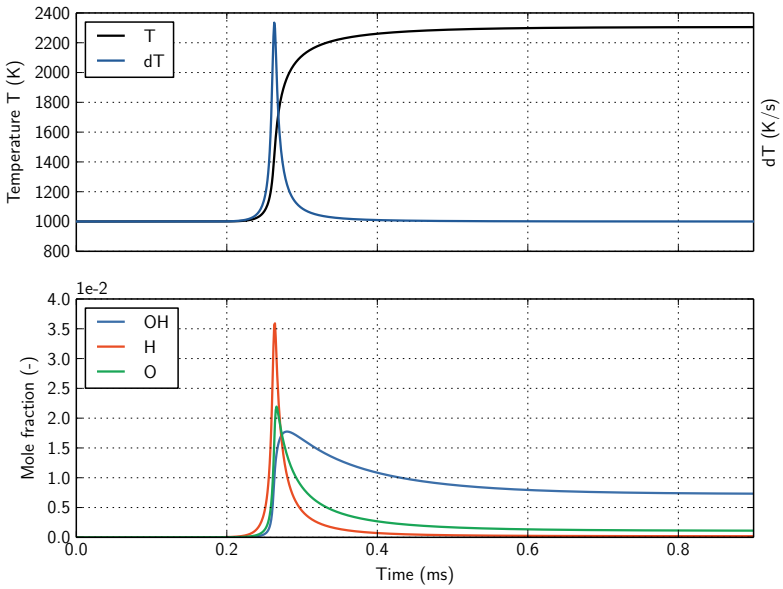

Figure 2.2: Schematic of a hydrogen-air self-ignition problem at atmospheric pressure. Initial temperature is 1000 K at stoichiometric conditions.

et al., 2012), the *continuous flow reactor* (Beerer et al., 2008; Reinke et al., 2005), and the *explosion bomb* (Srivastava et al., 2011). Most of these techniques usually use the peak of a radical concentration (OH^*, CH^*), the temperature or pressure peak as an indicator for the ignition delay time (Lee et al., 2014).

2.2 Literature Overview

There is extensive literature concerning hydrogen-oxygen and hydrogen-air flames. An early study concerning the measurement of laminar burning velocities was presented by Scholte et al. (1959). In the subsequent years further reports were published about the laminar flame speed of hydrogen (Dixon-Lewis et al., 1964; Edmondson et al., 1971; Senior, 1961). All of these investigations employed the Bunsen-like burners and schlieren technique. Edmondson reported in his study discrepancies to the measurements of Scholte and attributed them to the small burner Scholte used. This indicates that either or even both configurations were prone to flame stretch, which was not revealed before 1985 (Wu et al., 1985). Further experiments were conducted by Takahashi et al. (1983) and Iijima et al. (1986). Both are included in the comprehensive review on laminar flame speeds which was given by Ó Conaire et al. (2004). The outcome of their investigation was that the flame speed measurements of Dowdy (1991) and Tse et al. (2000) can be considered to be the most representative and accurate of the entire available data set. In addition to the determination of burning velocities Oran et al. (1982) performed a numerical simulation of shock tube experiments in hydrogen-oxygen-argon mixtures and it was observed that the ignition starts at a distance away from the reflecting wall much earlier than the calculated time. This effect was attributed to the sensitivity of the chemical induction time to fluctuations in the computations. The according experiments were conducted by Cohen et al. (1967). However, a vast body of literature exists concerning hydrogen safety in nuclear power plants. Under severe accident conditions in nuclear power plants, hydrogen can be generated from reactions with zirconium and hot steam as well as with nuclear core meltdown materials with concrete. As demonstrated in the *Three-Mile-Island* accident in 1979 this can result in an explosive combustion of premixed hydrogen and air, and thus can threaten the containment integrity. In order to assess the thermal and pressure loads, it is important to predict the burning velocity, explaining the increase of available literature after 1979 (Alkishali et al., 1983; Marshall, 1986; Pilch, 1996; Sherman, 1984). Due to the low flammability limits of hydrogen, safety surveys concerning hydrogen as ground transportation fuel (Knowlton, 1984) and even for pipeline applications were conducted (Wilkening et al., 2007).

Even though a large body of literature exists concerning hydrogen combustion, only relatively few studies were conducted on steam diluted hydrogen flames. Early studies by David et al. (1942) revealed that steam diluted flame temperatures are lower than for dry flames. Heimel (1957) investigated hydrogen-air mixtures and also substituted nitrogen with water vapor. He measured laminar burning velocities with a schlieren system and observed that a mole-for-mole substitution of nitrogen for steam caused no change in burning velocity even though the substitution increased the flame temperature. In contrast to the findings of Heimel, the survey by Kuehl (1962) reported that replacing N_2 with steam in low-pressure hydrogen/air flames leads to an increase of the laminar burning velocity. He claimed that the substitution with steam accelerates the combustion process by increasing the radiative heat transport from the hot

products to the fresh gases. Levy (1963) and Dixon-Lewis et al. (1964) offered an interpretation based on chemical kinetics for this effect. Liu et al. (1983) measured the burning velocity with a laminar nozzle burner up to steam fractions of 15% and derived a correlation for the burning velocity. In the study by Koroll et al. (1988), the burning velocity was examined in a similar experiment with molar steam fractions up to 50%. They concluded that steam does not act as an inert diluent. In 1993 Koroll presented an updated version where correlations for laminar and turbulent burning velocities of hydrogen and air mixtures where presented (Koroll et al., 1993). More recent work on hydrogen diluted flames was done by Sohn et al. (1999), with focus on nuclear power plant safety, correlations for hydrogen-air-steam flames were numerically obtained based on the experimental work of Koroll. Kwon et al. (2001) reported on experimentally obtained laminar flame speeds for $\mathrm{N_2}$-He-Ar as diluents in freely propagating spherical flames whereas Kuznetsov presented two methods to obtain burning velocities, namely an optical high-speed shadow video technique and pressure method. Flame speeds were determined for several preheat temperatures at different pressure levels (up to 70 bar) and steam concentrations (up to 80%) for pure hydrogen-air-steam mixtures. Using a spherical bomb, such as Kuznetsov, Lamoureux et al. (2002) determined the laminar flame velocity for $\mathrm{H_2}$-air-steam mixtures for steam levels up to 30%. The water vapor dilution effects of hydrogen was also experimentally investigated by Le Cong et al. (2008) in a jet-stirred reactor over a temperature range $800 - 1500$K and a steam content of up to 10%. An accompanying kinetic modeling revealed that the main effect of water addition may stem from the third body efficiencies of $\mathrm{H_2O}$. Moreover, it was shown that the addition of steam yields lower flame speeds, lower flame temperatures and reduced $\mathrm{NO_x}$ emissions. Santner et al. (2011) investigated experimentally and numerically the effect of steam dilution of up to 15% on the burning rates of $\mathrm{H_2}$ and $\mathrm{H_2}$-CO mixtures for up to 10 atm. Burning rates were measured in a pressurized spherical combustion chamber. The results showed a monotonic decrease in mass burning rate with steam addition at elevated pressures. The numerical analysis revealed the influence of water addition on the radical pool through $\mathrm{H_2O + O \rightleftharpoons 2OH}$. Das et al. (2011) conducted combustion experiments of moist hydrogen-air and syngas-air mixtures using a counterflow twin-flame configuration under ambient pressure. A new correlation for the laminar burning velocity as a function of pressure, temperature and the hydrogen-air-steam composition was recently reported by Szabó et al. (2012).

Wang et al. (2003) conducted shock-tube experiments to assess the auto-ignition time delay in moist hydrogen air mixtures for several temperatures ($900 - 1350$ K), pressures ($3 - 17$ bar) and steam concentrations (up to 40%). The auto-ignition process of hydrogen-oxidizer mixtures using a Rapid Compression Machine (RCM) was studied by Das et al. (2012). It was shown that at high pressures (70 bar) the presence of water vapor ($30 - 40\%$) promotes the auto-ignition process. However, at initial pressures of 10 bar and moderate dilution with water (10%) the reactivity of the mixture is impeded, and thereby increasing the ignition time delay. Very recently Donohoe et al. (2014) investigated the influence of steam dilution (up to 30%) on the self-ignition process for hydrogen, carbon monoxide, and natural gas blends at elevated pressure ($10 - 30$ bar). Donohoe reported that for all other mixtures, except for carbon monoxide the addition of steam did not show any significant chemical effect. Furthermore, it was observed that only for the mixtures with pure carbon monoxide steam has a significant effect by forming OH radicals, which decrease the ignition time delays.

In the first part of the thesis laminar flames are investigated. Beside a brief introduction to the topic of laminar flames, the numerical methodology is discussed in detail in the first chapter. In order to identify an adequate oxidation mechanism, several candidates are identified and compared in the second chapter. The respective performances are assessed based on laminar premixed flame calculations under dry and wet conditions, for which experimentally determined flame speeds and self-ignition times are available. In a third step, further insight is gained by observing the effect of steam on the combustion process, in particular on one-dimensional flames and ignition time delays. The influence of steam on the flame is scrutinized in detail by assessing the sensitivity of the reaction rates under the influence of steam. The findings are supported by investigating the dependence of the species concentration and the extension of the preheat zone. In order to compare the experimentally obtained data of the second part with the Large Eddy Simulations also an OH^* chemiluminescence subset is needed. Therefore, different OH^* subsets are compared with experimental data from the literature and one subset is chosen for the Large Eddy Simulations. To shed some light on the influence of steam on the emission production arising from the combustion process, the reaction pathways of nitrogen oxide emissions are briefly discussed in the fifth chapter. The first part of the thesis is rounded out by a summary and conclusions are drawn.

3

Numerical Methodology

Figure 3.1 presents two types of one-dimensional laminar flames used within this study. The first configuration represents a laminar premixed flat flame, which consists of a porous disk burner. Oxidizer and fuel are premixed and emerge from the disk into the flame. This flame manifests as a disc floating few millimeters above the burner outlet. Curvature effects at the border of the flame can be neglected if the burner diameter is chosen large enough. Flat flames can be considered as one-dimensional due to the fact that there is no heat or pressure loss in radial direction. The second flame configuration is a non-premixed counter flame and is only used for validation of reaction schemes in Chapter 7. This flame would require to be solved in a three-dimensional formulation; however, the problem can be reduced spatially to one dimension if axis symmetry is taken into account. This approach assumes that the axial velocity, the species mass fraction distribution and the temperature field are only a function of the axial coordinate. While with these configurations it is possible to determine characteristic properties as the laminar burning velocity or the thermal flame thickness, a zero-dimensional approach is employed in order to compute ignition time delays.

In order to analyze the influence of steam on the combustion process, the first part of this study is based on a large set of lower dimensional chemical computations obtained using the open-source chemical kinetics software CANTERA (ver. 2.0.2) (Goodwin, 1994). The software includes important effects for hydrogen combustion such as thermal diffusion and multicomponent diffusion. A reactive flow system may be described by balance equations of momentum, mass, species and energy. Thus, the flow is characterized by its properties such as pressure, density, temperature, velocity, and concentration at each point in space and time.

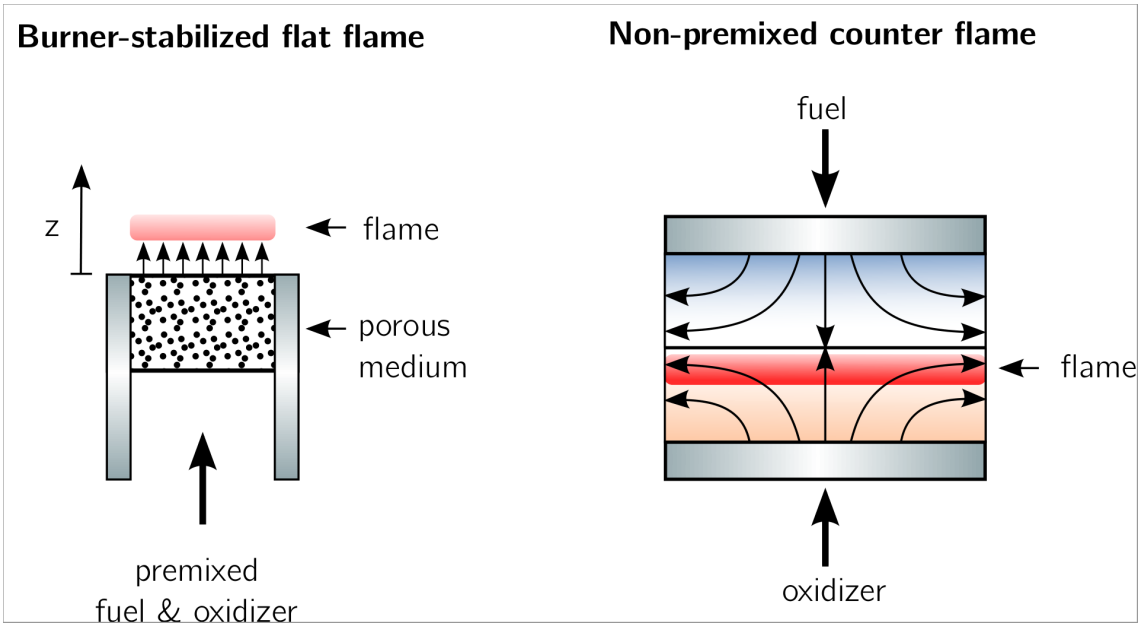

Figure 3.1: Different burner types used for one-dimensional analysis. The left schematic shows a laminar burner-stabilized premixed flame. The schematic on the right shows a non-premixed counter flame.

3.1 One-Dimensional Analysis

3.1.1 Premixed Flames

For one-dimensional premixed flames the governing equations for energy, mass and momentum reduce to a system of ordinary differential equations in the axial coordinate. By assuming that:

- the ideal gas law is valid.
- the pressure is constant.
- no external forces are present.
- thermal radiation of gases is negligible.
- non-sooting flames.
- the system is in local equilibrium.
- the Dufour effect can be neglected.

The conservation equations can be expressed as:

Continuity

$$\frac{\partial \varrho}{\partial t} + \frac{\partial}{\partial z}(\varrho u) = 0\,. \tag{3.1}$$

Here, ϱ denotes the density, u the axial velocity, and z the spatial coordinate. The independent variable t represents the time. Thus, the mass flux will remain constant through the domain. For the conservation of species k of the mixture follows:

Species

$$\frac{\partial\left(\varrho Y_k\right)}{\partial t}+\frac{\partial\left(\varrho\, u\, Y_k\right)}{\partial z}+\frac{\partial J_k}{\partial z}=M_k\dot{\omega}_k\,, \tag{3.2}$$

where Y_k stands for the mass fraction of species k. M_K and $\dot{\omega}_k$ are the molar mass and the reaction rate of species k. The diffusion flux $J_k=-\varrho D_k{}^{\partial Y_k}/_{\partial z}$ is a function of the species gradient and the diffusivity D_k. For speed of computation, the diffusion coefficient D_k can be calculated as a function of the mixture average. Consequently, thermal diffusion effects (i.e., Soret diffusion (Eastman, 1928)) are ignored. Diffusion is an essential element in the structure of laminar flames. Due to the fact that the diffusion brings the reactants to the reaction zone and transports the combustion products and chemical heat away from it, it controls the total enthalpy entering the reaction zone and thus directly the flame temperature. As presented by Yang et al. (2010) the H_2 and H Soret diffusion has a strong impact on diffusion hydrogen flames, but only a subordinate influence on premixed hydrogen flames. In contrast to that Grcar et al. (2009) findings underscore the importance of incorporating diffusion effects for lean hydrogen premixed flames. They reported a difference of the flame propagation speed of about 18% between a case with and without Soret effect. Nonetheless, hydrogen has a high diffusivity and since the Soret diffusion has an effect on the hydrogen molecule concentration in the reaction zone the effect is incorporated in the simulations to avoid misinterpretation of the burning velocity. In addition, the Soret effect also affects the strain rate downstream of the reaction zone. Therefore, the diffusion coefficient D_k is calculated against each species in the composition (multicomponent). The energy conservation accounts for heat transfer by convection, conduction within the mixture, diffusion of individual species, and heat generation due to chemical reaction and is derived from the enthalpy equation. It reads as follows:

Energy

$$\varrho\frac{\mathrm{D}h}{\mathrm{D}t}=\varrho\left(\frac{\partial h}{\partial t}+u\frac{\partial h}{\partial z}\right)=\varrho c_p\left(\frac{\partial T}{\partial t}+u\frac{\partial T}{\partial z}\right)+\sum_k\left(-\frac{\partial}{\partial z}J_{q,k}+\dot{m}_k\right)h_k\,, \tag{3.3}$$

where T is the temperature, $c_{p,k}$ the specific heat capacity at constant pressure and h_k the enthalpy of species k. The heat flux J_q can be further expressed with the diffusion flux J_k and the thermal conductivity λ for each species by:

$$J_q=-\lambda\frac{\partial T}{\partial z}+\sum_k J_k h_k. \tag{3.4}$$

With Equation 3.3 and Equation 3.4 the temperature equation can be derived as it is used in CANTERA:

$$\varrho c_p \frac{\partial T}{\partial t} = \frac{\partial}{\partial z}\left(\lambda \frac{\partial T}{\partial z}\right) - \frac{\partial T}{\partial z}\left(\varrho c_p u + \sum_k J_k c_{p,k}\right) - \sum_k \dot{\omega}_k h_k M_k \,. \tag{3.5}$$

As the pressure remains constant the ideal gas equation of state is of importance to calculate the density ϱ:

$$\varrho = \frac{p_0}{RT} \sum_k Y_k \cdot M_k \,. \tag{3.6}$$

Here, p_0 is the reference pressure and R the universal gas constant. The reaction rates within the species and energy equation are solved using a chemical reaction mechanism.

3.1.2 Non-premixed Flames

The nature of non-premixed flames would require to solve the three-dimensional conservation equations. By assuming that the diffusion in the radial direction (orthogonal to the streamlines) can be neglected, the system can be reduced to a one-dimensional axisymmetric assumption. Assuming furthermore that:

- the axial velocity $u = u(z)$ is only a function of the axial coordinate,
- the radial velocity v is linear in the radial direction r,
- the low Mach number Ma assumption ($\mathrm{Ma} \ll 1$) is valid and therefore the pressure is nearly constant,
- all species mass fractions and temperature are independent of the radial direction,

leads to the following axisymmetric formulation where the only independent variables are the spatial coordinate z and the time t:

Continuity

$$\frac{\partial \varrho}{\partial t} + \frac{\partial}{\partial z}\left(\varrho u\right) + 2\varrho V = 0 \,. \tag{3.7}$$

Here, V is the radial velocity gradient $V = \frac{\partial v}{\partial r}$.

Momentum

$$\varrho \frac{\partial V}{\partial t} = \frac{\partial}{\partial z}\left(\mu \frac{\partial V}{\partial z}\right) - \Lambda - \varrho u \frac{\partial V}{\partial z} - \varrho V^2 \,. \tag{3.8}$$

In this formulation μ denotes the dynamic viscosity and $\Lambda = \frac{1}{\varrho}\frac{\partial p}{\partial r}$ the radial-pressure gradient. The gradient is assumed to be constant throughout the entire field and thus an *eigenvalue* of the system.

Species

$$\frac{\partial\left(\varrho Y_k\right)}{\partial t}+\frac{\partial\left(\varrho\, u\, Y_k\right)}{\partial z}+\frac{\partial J_k}{\partial z}=M_k\dot{\omega}_k\,. \tag{3.9}$$

Energy

$$\varrho c_p\frac{\partial T}{\partial t}=\frac{\partial}{\partial z}\left(\lambda\frac{\partial T}{\partial z}\right)-\frac{\partial T}{\partial z}\left(\varrho c_p u+\sum_k J_k c_{p,k}\right)-\sum_k\dot{\omega}_k h_k M_k\,. \tag{3.10}$$

The system of equations becomes complete with an ideal gas equation of state:

$$p=\varrho RT\sum_k\frac{Y_k}{M_k}\,. \tag{3.11}$$

The equations are similar to the premixed flame except that the mass flux ϱ is not constant due to the mass flux in radial direction.

For all reaction configurations the species reaction rate $\dot{\omega}_k$ is computed from a reaction scheme by summarizing the product of the single reaction rates q_j and the stoichiometric coefficient matrix ν_{ki} over all reactions:

$$\dot{\omega}_k=\sum_j\nu_{ki}q_j\,. \tag{3.12}$$

The reaction rates q_j are calculated from the product of the forward and reverse reaction rate coefficients k_f and k_r and the respective stoichiometrically weighted concentrations:

$$q_j=k_{f,j}\prod_k\left[X_k\right]^{\nu'_{kj}}-k_{r,j}\prod_k\left[X_k\right]^{\nu''_{kj}}\,. \tag{3.13}$$

Thus, forward and reverse reaction coefficients are multiplied by the species concentrations $[X_k]$ raised to their respective stoichiometric coefficients. The reaction rate q is also often denoted as rate of progress as is the case in CANTERA (Goodwin, 2004). The reaction rate coefficients are calculated by the modified Arrhenius formulation (Kee et al., 2003):

$$k=AT^n\mathrm{e}^{\frac{-E_A}{RT}}\,. \tag{3.14}$$

Here, A is the pre-exponential factor, E_a the activation energy, n an unit less temperature exponent, and R is the universal gas constant. The necessary constants (A, n, E_a) for each elementary reaction are empirically determined and cataloged as a database, usually denoted as reaction scheme or mechanism. Reaction mechanisms are accompanied by according thermodynamic and transport properties per species.

Every one-dimensional problem in CANTERA is partitioned into a stack of discrete domains. By applying finite differences to either of the flame formulations, a system of nonlinear algebraic equations is formed from the flow. In order to solve the problem, a hybrid Newton/time-stepping algorithm is used. The solver is fully implicit and in addition to ensure numerical stability, upwind schemes are used for the convective terms. The diffusive terms are treated using central differences. In a first step, a steady-state solution is attempted via a classical Newtonian method that linearizes the discretized function F about an initial solution estimate Φ^0:

$$F^0_{\mathsf{lin},n} = F_i(\Phi^0) + \sum_j \left.\frac{\partial F_i}{\partial \Phi_j}\right|_{\Phi=\Phi^0} \left(\Phi_j - \Phi^0_j\right) \,. \tag{3.15}$$

Solving this linear system gives:

$$\Phi_n = \Phi_{n-1} - J_{ij} F(\Phi_{n-1}), \tag{3.16}$$

where J_{ij} is the Jacobian matrix $\partial F_i / \partial \Phi_j$. If the Newton algorithm fails to find the steady-state solution, transient terms are added to the conservation equations to solve the problem with a larger domain of convergence:

$$F(\Phi) = A\frac{\partial \Phi}{\partial t} F(\Phi^{n+1}) - A\frac{\Phi^{n+1} - \Phi^n}{\Delta t} = 0 \,. \tag{3.17}$$

The diagonal matrix A is set to 1 on the diagonal for equations with a transient term, and to 0 on the diagonal for constraint equations. It is noteworthy that if A is equal to the identity matrix in Equation 3.17 and for a sufficiently small time step, the function will approach a linear problem. On the other hand, if A contains zeros on the main diagonal, the convergence of the transient Newton problem cannot be guaranteed, regardless of the time step size. In case that convergence cannot be achieved, a better starting estimation is the only solution. Due to the fact that the spatial discretization is the largest source of errors, each domain is refined/coarsened to ensure sufficiently resolved gradients and a suitable initial solution. As refinement criterion serve the ratio, slope, and curve within the solution set and are user-specified. The ratio defines the maximum spacing between two grid points whereas the slope and curve restrict the maximum allowable gradients and curvature within the solution. CANTERA calculates an initial solution as a constant temperature increase to the equilibrium predictions on the first 20% of the user-specified initial grid. The remaining domain is set as a flat temperature profile. The initial solution is automatically refined by adding grid points until user-specified values for ratio, slope, and curve are attained. As reported by Goodwin (2004), the by far most computational cost is caused by computing the Jacobian. Due to the fact that the exact Jacobian is not required, the solver tries to re-use the previously computed Jacobian. The Jacobian is recomputed if the Newton algorithm fails and the Jacobian is outdated, or a user-specified maximum number of times it may be used is exceeded. Consequently, the final solution grid will be non-uniform with a dense point distribution within the reaction zone.

Convergence tolerances of interest are the relative and absolute steady-state and time-stepping error tolerances, as well as the maximum number of iterations until the Jacobian is recomputed for the Newtonian and unsteady solutions.

For the presented simulations the convergence tolerances are set to 10^{-14} and 10^{-15} for relative and absolute tolerances for steady-state and transient time-stepping error. The maximum age of the Jacobian was varied to support convergence from 10 to 20. The time stepping was decreased to a time step of 10^{-7}s. As refining criterion the ratio was set to 2.0, and slope and curve to 0.005.

3.1.3 Boundary Conditions

For one-dimensional flames the boundary conditions can be divided into two categories: freely propagating adiabatic premixed flame and burner-stabilized non-premixed flame. For the adiabatic premixed flame the CANTERA needs the specification of the unburnt inlet composition $Y_{k,u}$, temperature T_u and pressure p:

$$Y_k(z = -\infty) = Y_{k,u} \tag{3.18}$$
$$T(z = -\infty) = T_u\,, \tag{3.19}$$

whereas a zero gradient condition is assumed for the concentration and temperature gradients at the outlet:

$$\frac{\partial Y_k}{\partial z}\,(z = \text{outlet}) = 0 \tag{3.20}$$
$$\frac{\partial T}{\partial z}\,(z = \text{outlet}) = 0\,. \tag{3.21}$$

Additionally, a trivial temperature T_{fix} has to be user-specified at which the flame is stabilized. It was found that the fixed temperature is playing a major role in finding a stable solution. However, it turned out that setting the temperature 300 K higher than the inlet temperature is a good starting point.

For the burner-stabilized flame the inlet and outlet conditions remain the same as for the premixed flame; however, an additional user-defined mass flow is mandatory, which makes the need for setting the fixed temperature obsolete.

$$\dot{m}(z = 0) = \dot{m}_u \tag{3.22}$$

CANTERA allows for inlet diffusion, such that the user-specified inlet composition $Y_{k,u}$ is met in an upstream position beyond the current domain ($z = -\infty$):

$$\dot{m}_{\text{inlet}} Y_{k,\text{inlet}} = \dot{m} Y_k - \varrho D \frac{\partial Y_k}{\partial z} \tag{3.23}$$

The adiabatic case is certainly not much affected due to the fact that the gradients are close to zero within the preheat zone. However, the diffusion effect may be quite pronounced for burner-stabilized flames. Nevertheless, flashback cannot occur in any case since the inlet temperature remains user-specified.

If not stated otherwise all one-dimensional flames are computed employing a freely propagating flame configuration.

3.2 Ignition Delay Analysis

Ignition models were used to compare the ignition time delays obtained experimentally by Wang et al. (2003). Wang and coworkers conducted experiments with hydrogen and different levels of steam dilution for different pressures and compared these with theoretical predictions based on detailed chemical kinetics. Their computational methods for the calculation of ignition time delays were based on a constant-volume model. The model assumes that the reactions proceed in an adiabatic, homogeneous fluid parcel. They also considered a constant-pressure model, assuming a homogeneous mixture in a fluid parcel of fixed pressure. The constant-volume model predicts an ignition process with a fast energy release, thus the short time scale of the spontaneous heat release does not allow for expansion of the gas. On the contrary, the constant-pressure model represents an ignition process with a slow energy release. Wang et al. (2003) compared both models and found the difference to be not significant. However, to assure comparability with the data obtained by Wang et al. (2003) the constant-volume model was used. The governing mass and energy equations for a zero-dimensional reactor reads as follows:

Species

$$\frac{\mathrm{d}Y_k}{\mathrm{d}t} = \frac{\dot{\omega}_k M_k}{\varrho} \,. \tag{3.24}$$

Energy

$$\frac{\mathrm{d}T}{\mathrm{d}t} = -\frac{1}{\varrho c_v} \sum_k e_k \dot{\omega}_k M_k \,. \tag{3.25}$$

Here Y_k stands for the mass fraction, $\dot{\omega}_k$ for the molar production rate, M_k for the molar mass, and e_k for the specific internal energy of species k. In addition, T denotes the temperature, t the time, ϱ the density, and c_v the mean specific heat capacity at constant volume.

4

Detailed Chemistry Modeling

The oxidation of hydrogen is an elementary reaction and a fundamental part in the combustion of all hydrocarbon and hydrogen-enriched fuels. Thus, an accurate description of hydrogen conversion is essential for predicting combustion processes. This explains the existence of a vast body of literature with numerous reaction schemes including detailed H_2-O_2 subsets can be found. A comprehensive overview was given by Ströhle et al. (2007). They assessed the performances of several mechanisms for different criteria such as ignition delay, burning velocity and pressure dependence with experimental data. They concluded that the mechanism of Li et al. (2004a) is the most suitable. This mechanism is based on previous publications by the group of F. L. Dryer at Princeton University. Recently Burke et al. (2012) updated the mechanism of Li. The primary motivation of the updated model was to incorporate recent improvements in rate constants as well as enhanced predictions by kinetic models in diluted, high-pressure flames. An even more comprehensive study was recently published by Olm et al. (2014). Olm accumulated a tremendous amount of experimental data from the literature, including self-ignition measurements in shock tubes and rapid compression machines, concentration profiles, laminar burning velocity measurements, and more. He then assessed the performance of 19 of the most important reaction schemes. According to the report, the reaction scheme of Kéromnès et al. (2013) is the best suited mechanism for predicting burning velocities and ignition times. However, other mechanisms like Ó Conaire et al. (2004) or Li et al. (2004b) showed a similarly good performance. It is also stated that the ignition time delay and burning velocities measured with the cone methods were poorly reproduced by all employed schemes.

Although these comprehensive reviews showed clearly which reaction schemes are generally suitable for hydrogen combustion, they do not account for steam dilution in particular. Therefore, several schemes are chosen and re-evaluated by comparison with experimental data. Olm et al. (2014) proposed Kéromnès' mechanism (Kéromnès et al., 2013), which is therefore included in the following investigation. The mechanism consists of 15 species and 36 reactions and includes an OH^* chemiluminescence subset. The mechanism is an extension of the previous model by Ó Conaire et al. (2004) which is also included in the present investigation. Ó Conaire's mechanism consists of 10 species and 21 reactions. Due to the outcome of Ströhle's work (Ströhle et al., 2007), Burke's mechanism is also employed in this study. The model consists of

13 species and 27 reactions and was validated using the data by Li et al. (2004b).

Three more mechanisms as representatives of C_1/C_2 species oxidation are considered. Both mechanisms are based on a detailed H_2-O_2 subset. The first of them was published by Le Cong et al. (2008) and contains 128 species and 924 reversible reactions overall the H_2 oxidation subset is represented by 12 species and 22 reactions. The second mechanism was developed by the *Creck* Modeling Group (Frassoldati et al., 2007). The H_2/O_2 subset including NOx formation pathways can be used separately and consists of 32 species and 174 reactions. Nikolaou et al. (2013) derived a skeletal mechanism from the GRI 3.0 scheme and adjusted it for gas turbine conditions. The skeletal scheme is suited for multicomponent fuels based on CO, H_2, CH_4 and CO_2 and consists of 18 species and 49 reactions. In addition, the GRI-Mech 3.0 Smith et al., 2000 (26 reversible reactions for H_2/O_2 kinetics) is also included because it is used as a reference by many researchers. If not stated otherwise a freely propagating flame configuration is used for the one-dimensional analysis.

4.1 One-Dimensional Flames

4.1.1 H_2-Air-Steam Mixtures

Of particular concern is the comparison of calculated flame speeds with corresponding measurements. The laminar burning velocity (S_l) is defined as the local velocity at which the flame front propagates normal to itself into the unburned gas. It is a key parameter in characterizing a combustible mixture and depends primarily on the pressure, temperature and the composition. Many hydrogen-air studies have been performed within the last 60 years to determine the laminar burning velocity over various ranges of equivalence ratios as mentioned in section 2.2. Iijima et al. (1986), Takahashi et al. (1983), and Koroll et al. (1993) performed their experiments over a wide range of equivalence ratios ($\Phi \leq 5.5$). However, these data were not corrected for flame stretch. The earliest experiments that accounted for the effect of flame stretch were reported in 1985 by Wu et al. (1985). Since then, the effect was corrected in most publications (Dowdy, 1991; Tse et al., 2000), except for Koroll et al. (1993). Figure 4.1 depicts the measurements of Takahashi, Iijima, Koroll, Dowdy, and Tse for ambient conditions. Apparently, the results

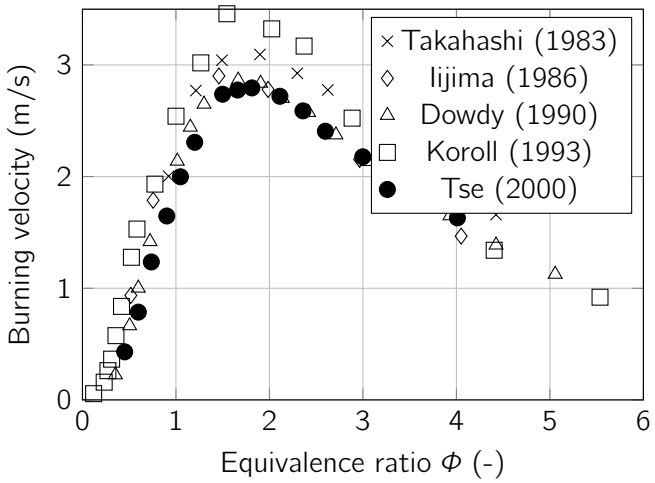

Figure 4.1: Atmospheric H_2-air laminar burning velocities as the function of the equivalence ratio for $T_u =$ 298 K and atmospheric pressure. The data of Dowdy (1991) and Tse (2000) was corrected for flame stretch.

of Iijima and Dowdy are in line with the findings of Tse, which can be seen as a reference according to Ó Conaire et al. (2004). Although Iijima's data tends to be faster in the lean regime, the measurements of Takahashi are considerably faster and are only surpassed by Koroll's experiments. Koroll used the so-called double-kernel technique to overcome some of the limitations of nozzle-burners and spherical bomb methods. Hereby, the mixture is ignited simultaneously at two points and the progress of the flame front is tracked with a schlieren system. Koroll et al. (1993) stated that flame stretch effect increases the burning velocity for lean mixtures and has only a small impact for rich mixtures. However, that does not explain the strong overprediction of his data for near-stoichiometric conditions ($1 \leq \Phi \leq 2.5$). Nevertheless, the figure demonstrates the high reactivity of hydrogen flames under atmospheric conditions, because a stoichiometric conditions a pure methane flame would result in a an about ten times slower flame velocity (Krüger et al., 2013).

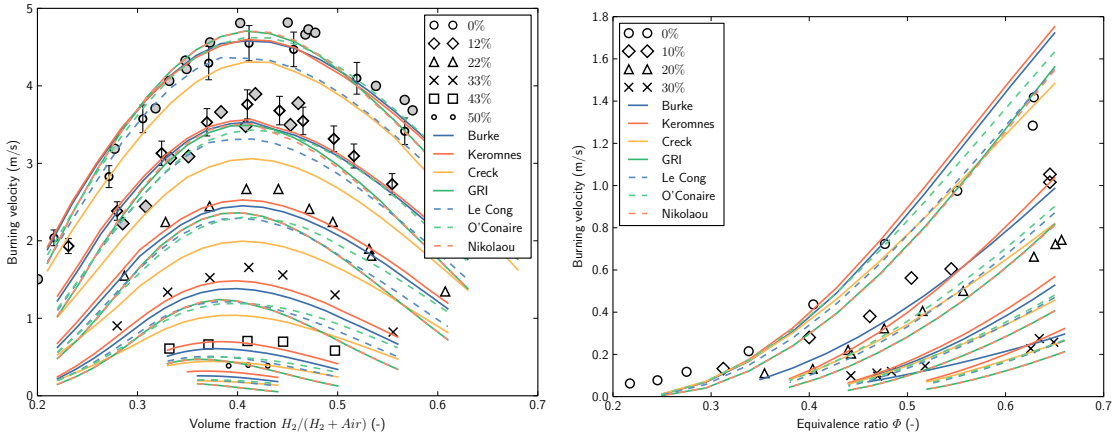

(a) Liu (1983) (filled symbols) & Koroll (1988) (transparent symbols); $T_u = 373\,\mathrm{K}$

(b) Lamoureux (2002); $T_u = 353\,\mathrm{K}$

Figure 4.2: Laminar burning velocity of hydrogen-air-steam flames for different steam levels and reaction mechanisms at atmospheric pressure. Comparison between experimental data (symbols) and model predictions (lines).

As presented in section 2.2 only a few studies on the dilution of hydrogen flames with high amounts of steam were examined. Liu et al. (1983) measured the burning velocity with a laminar nozzle burner up to steam fractions of 15% and derived a correlation for the burning velocity. Koroll et al. (1988) investigated H_2-air-steam compositions up to molar fractions of 50% steam at ambient conditions. Burning velocities were measured with a nozzle burner applying the schlieren cone angle method and particle tracking with Laser Doppler Velocimetry (LDV). The experiments with H_2-air-steam compositions were conducted at an inlet temperature of 373 K and a burner diameter of 5 mm. According to Koroll et al. (1988) the crucial effect of flame curvature was evaluated with different nozzle diameters and they reported that a further increase in the nozzle diameter had a negligible effect on burning velocity. The overall accuracy of the measurements was not given, but Edmondson et al. (1971) estimated a relative error of less than $\pm 5\%$ for a similar configuration. Lamoureux et al. (2002) conducted laminar burning velocity measurements for H_2-air-steam mixtures for steam levels up to 30% utilizing

the spherical bomb method. At ambient pressure two inlet temperatures (298 K and 353 K) and different diluents (steam, helium, and carbon dioxide) were used. These measurements (Koroll and Lamoureux) were used for identifying a suitable reaction because they offer the highest dilution concentration range and are the most referred to. As previously stated, most of the surveys concerning laminar burning velocities of diluted hydrogen flames were conducted over a wide range of equivalence ratios, in order to investigates hydrogen flames for fundamental research and model validation. Even though none of theses studies was in particular conducted close to gas turbine conditions, especially not at elevated pressures (except for Kuznetsov et al. (2011)) at least most of the reaction mechanisms were validated for this kind of conditions (Burke et al., 2011b). The computations of a laminar burning velocity are performed using a one-dimensional freely propagating flame approach according to section 3.1.

Figure 4.2(a) presents the results of the burning velocity computations for $\mathrm{H_2}$-air-steam compositions at 373 K and compares them with the sets of Koroll and Liu. For steam levels of 0% and 12%, error bars according to Edmondson et al., 1971 were added. The two experimental sets agree well, both predicting a maximum of the burning velocity around a volume fraction of ≈ 0.4 throughout all steam levels. The Kéromnès and Burke mechanism predicts similar results that are generally in good agreement with the measurements. With higher steam content both mechanisms are close to the experimental data, but Burke tends to slightly underestimate the flame velocity. Ó Conaire's mechanism shows a close agreement to Burke, however predicts slightly slower velocities. The GRI mechanism lies well in line for the dry case. With increasing steam, the mechanism predicts a significantly lower flame velocity, in particular for hydrogen fractions higher than 0.3. The Nikolaou mechanism is almost identical to the GRI, which is due to the fact that they share almost the same hydrogen subset. However, a common tendency for the $\mathrm{C_1/C_2}$ mechanisms (Le Cong, Creck, Nikolaou, GRI) can be observed. With increasing steam contents the mechanisms tend to underestimate the burning velocities. Out of the $\mathrm{C_1/C_2}$ family the Le Cong mechanism is the closest to the measurements.

Lamoureux et al. (2002) conducted their measurements in the lean regime and thus, the significant lower hydrogen content results in considerably lower burning velocities. This also manifested in numerical instabilities and long computational times, in particular with increasing steam content. Therefore the computations could not be carried out over the full range of equivalence ratios. Evidently, at dry conditions Burke and Kéromnès are close to each other. However, both overpredict the velocities for the higher equivalence ratios. For the dry case Creck and Le Cong agree well with the experiments whereas the GRI and Nikolaou tend to under predict the velocities in the leaner regions. Apparently, all mechanisms tend to predict too low velocities with increasing steam content. Even though Kéromnès is close to Burke, Burke is the only mechanism that is close to the experiments for the highest steam content (30%). It is also noteworthy that all schemes, except for Burke and Kéromnès, differ significantly from the experimental data although the trends are reproduced. However, the very lean regime seems to be challenging for all employed reaction schemes.

Defining and calculating the flame thickness is an obvious requirement for numerical combustion processes because it controls the required mesh resolution. For most combustion modeling approaches, the flame structure must be resolved by enough points to resolve gradients sufficiently. Different definitions are available, based either on scaling laws or on one-dimensional flame calculations. According to Poinsot et al. (2005), the thermal thickness δ_L^0 is the best

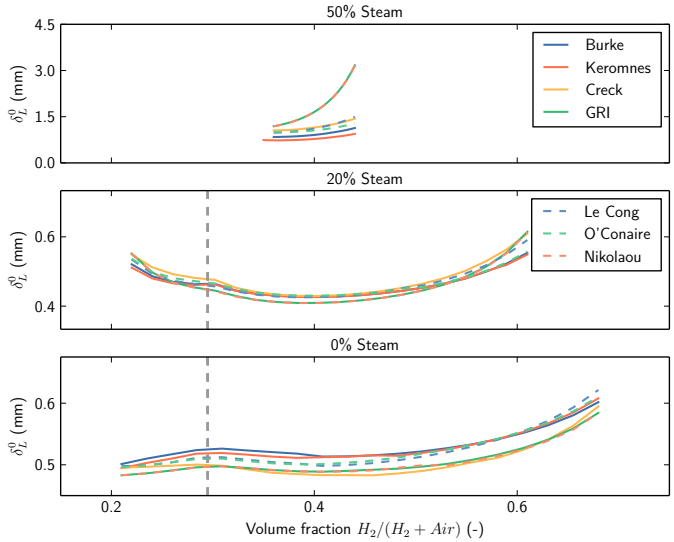

Figure 4.3: Thermal thickness δ_L^0 of a hydrogen-air-steam flame at 1 atm and $T_u = 373\,\mathrm{K}$ for different steam contents and reaction mechanisms.

suitable definition. It requires a temperature distribution and is defined by the temperature difference of the inlet temperature T_u and the temperature of the burnt gases T_b, divided by the maximum of the temperature gradient:

$$\delta_L^0 = \frac{T_b - T_u}{\max\left(\left|\frac{\partial T}{\partial x}\right|\right)}. \tag{4.1}$$

For the different reaction models, the thermal thickness is assessed for different steam levels as a function of the hydrogen content, as presented in Figure 4.3. As expected, the thermal thickness for a hydrogen flame is very thin. In the absence of steam the flame thickness increases with the hydrogen input. The mechanisms show a common tendency, but differ slightly from each other. The predictions of the Creck mechanism deviate from Burke and Kéromnès by about 17%. With the increase of steam, the flame thickness grows, especially in the lean ($[H_2]/[H_2 + air] \lesssim 0.3$) and very rich ($[H_2]/[H_2 + air] > 0.5$) regime. At a steam content of 20%, the $\mathrm{C_1/C_2}$ mechanisms are now much closer to the predictions of the Burke mechanism. With a further increase of the steam content to 50%, the $\mathrm{C_1/C_2}$ mechanisms predict significantly larger thermal thickness. In particular, the GRI and Nikolaou mechanism shows a high deviation to the pure hydrogen mechanisms (Burke and Kéromnès).

A local maximum around the volume fraction of $[H_2]/[H_2 + air] \approx 0.3$ is observed and predicted by almost all reaction schemes. This effect has not been reported in the literature yet and without accompanying experimental data, it is difficult to distinguish between a chemical effect or numerical artifact due to high temperature gradients. However, this effect can probably be associated with reaching stoichiometric conditions, which is the case for $[H_2]/[H_2 + air] = 0.29$. Furthermore, all calculations show a global minimum at $[H_2]/[H_2 + air] \approx 0.4$. Here, the burning velocity reaches its maximum and hence, explains the minimum of the thermal thickness.

4.1.2 H_2-O_2-Steam Mixtures

Effects of elevated temperatures and pressures on pure hydrogen-oxygen-steam flames were examined by Kuznetsov et al. (2011). Stoichiometric hydrogen-oxygen mixtures were diluted with steam up to 85% (mol.) and evaluated in a spherical explosion chamber. High-speed shadow technique as well as a pressure method were used to determine the laminar burning velocity. Koroll also conducted experiments on H_2-O_2-steam flames and reduced the diameter of his nozzle burner down to 3 mm in order to avoid critical Reynolds numbers. A comparison of the experimental work of Kuznetsov and Koroll's data at practically the same initial temperature is depicted in Figure 4.4. The laminar burning velocity is plotted as a function of the molar steam dilution. It is seen that the effect of water addition on laminar burning velocity for this case exhibits a decreasing trend throughout the range of dilution. The lower temperature experimental sets of Koroll ($T_u = 373\,\mathrm{K}$) and Kuznetsov ($T_u = 383\,\mathrm{K}$) agree well, giving confidence in the measurement methods of Koroll. As can be seen in the according reviews to Koroll's publication, some doubts in the used flame stretch compensation emerged. The second set of Kuznetsov with the slightly higher initial temperature ($T_u = 393\,\mathrm{K}$) shows gradually higher velocities with a faint scatter. Kuznetsov determined the flame velocity accuracy to be $\pm 5\%$. However, the marginally higher velocity is probably caused by the increased preheat temperature. All of the seven kinetic mechanisms give a good agreement with the experimental data. Near the dry region the schemes of Burke, Kéromnès, and Creck show the smallest difference to the experimental data.

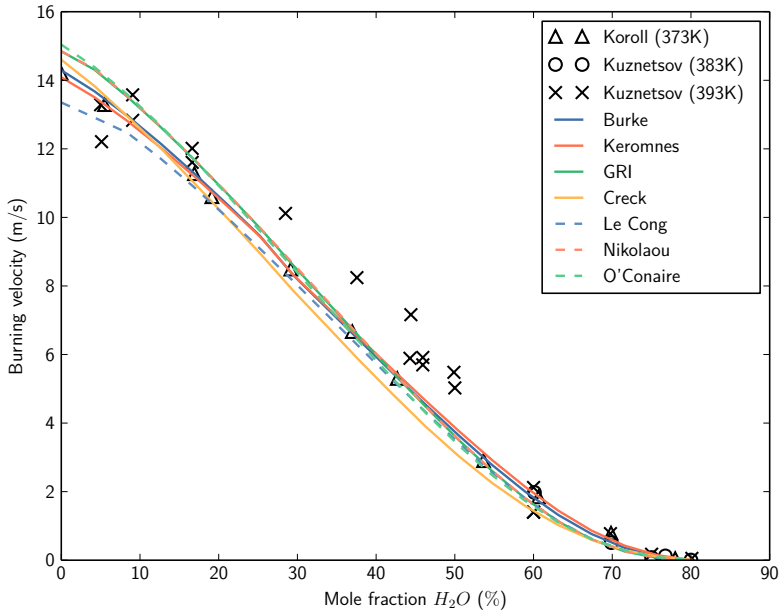

Figure 4.4: Laminar burning velocity of hydrogen-oxygen flames (2:1) as a function of the mole fraction of H_2O at 1 atm and $T_u \approx 383\,\mathrm{K}$ for different reaction mechanisms. Comparison between experimental data (symbols) and model predictions (lines). Experimental data is according to Koroll et al. (1988) and Kuznetsov et al. (2011).

4.2 Auto-Ignition Events

Wang et al. (2003) measured the ignition time delays for various hydrogen-air-steam compositions ($15\%H_2$ and $0 - 40\%H_2O$) over a temperature range of 955 K to 1352 K at a pressure of 0.5 MPa. Figure 4.5 compares these data with the computations. It can be seen that both temperature and steam have a strong impact on the onset of the ignition event. Wang et al. (2003) stated that the delay time increases exponentially with the decrease in initial temperature. On the other hand, for the same temperature the delay time increases with the steam concentration, in particular for mixtures with small amounts of steam.

In the absence of steam the computations tend to underpredict the reactivity for temperatures below 1000 K. Low-temperature ignition time delays may be subject to large underestimations. These effects are currently reconsidered by the community as reported by Le Cong et al. (2009). With increasing steam concentration the differences between experiment and computations significantly decrease. At $\chi = 40\%$ all mechanisms are well in line with the measured ignition time delays. Experiments closer to gas turbine conditions were recently presented by Donohoe et al. (2014). By using a Rapid Compression Machine (RCM), the influence of steam dilution on the auto-ignition process of hydrogen, carbon monoxide, methane, and natural gas under elevated pressures (10 & 30 bar) in the temperature range $895 - 1140$ K were examined.

Figure 4.6 details the effect of steam addition on the self-ignition times for hydrogen mixtures at 10 and 30 bar and stoichiometric conditions. The experiments show a significant impact of water addition on the ignition time delays. The differences between the cases with and without water addition is caused by thermal effects. The increase of the steam concentration reduces the thermal diffusivity, and thus decreases the heat loss in the RCM. Donohoe et al. (2014) stated that the ignition time delay is also a function of the whole temperature and pressure history. As observed in the experiments, steam dilution leads to a lower decrease

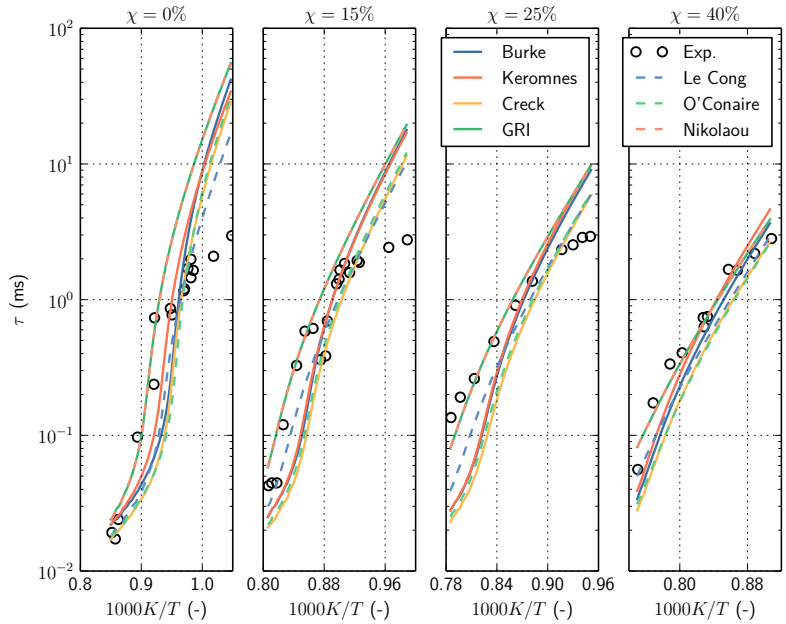

Figure 4.5: Ignition time delay of hydrogen-air-steam mixtures as a function of the initial temperature and the steam concentration. X is the steam concentration and the composition is given by: $(100 - X) \cdot (15\%H_2 + 85\%\text{Air}) \cdot X\%\text{Steam}$. Experimental data according to Wang et al. (2003).

in pressure and temperature and thus, to shorter ignition time delays. They concluded that therefore the addition of water has no significant chemical effect on the ignition time delay. Figure 4.6 depicts also the comparison with the kinetic models. Over all conditions it is evident that all schemes predict an exponential slope with similar gradient. In the higher temperature region Burke, GRI and Nikolaou are close to the experiments. As expected, the rise of the pressure level accelerates the auto-ignition process, whereas the addition of steam seems to have a subordinate effect. In the absence of steam, significant differences to the experiments in the low-temperature regime are present. Donohoe et al. (2014) also compared the experiments with numerical simulations. There, heat losses were modeled as virtual expansion, leading to lower temperatures and pressures, which in turn increase the ignition time. Without a closer description of the heat losses and the according correction function, the results cannot be reproduced. Therefore, the results of Donohoe are not further regarded in the following.

As it was demonstrated, most of the mechanisms showed a similar performance in reproducing ignition time delays. The shock tube measurements were well predicted, on the other side the rapid compression showed some discrepancies in the lower temperature regime. Nevertheless, the mechanisms showed an overall good performance and a clear candidate did not stick out. However, Burke showed for higher concentrations of steam slightly better results and is thus further recommended.

> *In this chapter several reaction mechanisms are compared in order to identify an adequate oxidation mechanism. Their respective performances are assessed based on laminar premixed flame calculations under dry and wet conditions, for which experimentally determined flame speeds and ignition delay times are available. Olm et al. (2014) evaluated the most important hydrogen mechanism for a vast range of measurements presented in the literature. As result the reaction scheme of Kéromnès was proposed to be the most accurate mechanism over the*

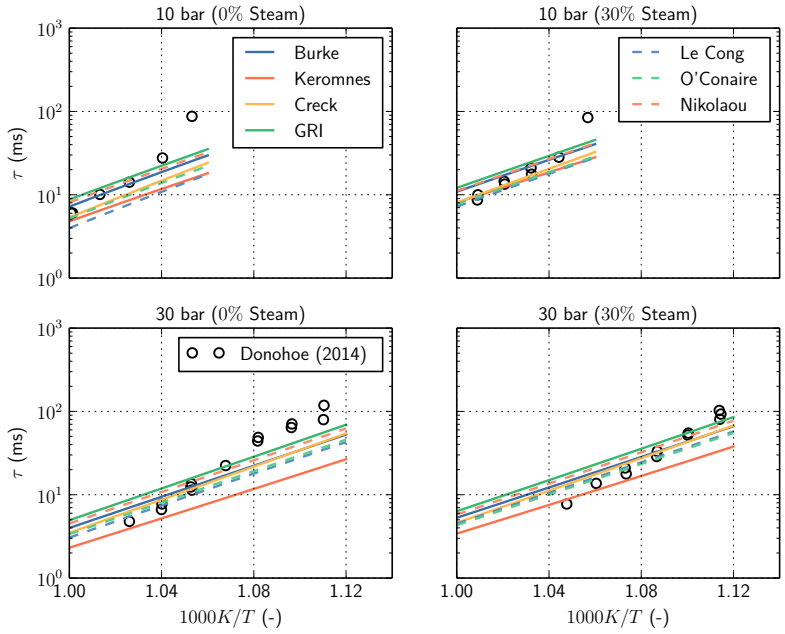

Figure 4.6: Ignition time delay of hydrogen-air-steam mixtures as a function of the initial temperature and the steam concentration. The experiments were conducted at stoichiometric conditions. Left column: 100% H_2, 0% H_2O, right column: 70% H_2, 30% H_2O. Experimental data according to Donohoe et al. (2014).

wide range of conditions. As said, Olm et al. (2014) considered a wide range of experimental conditions but did not focus on steam diluted gas turbine conditions in particular, therefore a new benchmark was conducted. Beside the scheme of Kéromnès also the mechanism of Burke was included in the performance test since it showed a good agreement in previous investigations (Krüger et al., 2013). Five further models were included in the tests. In comparison with the experimental data from Koroll et al. (1993) and Liu et al. (1983) for hydrogen-air-steam flames the reaction mechanisms of Kéromnès and Burke achieved the best agreement, especially at high steam concentrations. Both showed an almost identical behavior. Compared to the data of Lamoureux et al. (2002) all mechanisms showed some weaknesses in the very lean regime. In the absence of steam most schemes overpredicted the burning velocities. With increasing steam content the differences got more significant. At the highest steam dilution only Burke's mechanism was able to reproduce the experiments. Even though Kéromnès showed a similar good performance. Since the flame thickness is of high importance for most combustion modeling approaches (e.g., Large Eddy Simulation (LES)) the thermal thickness was assessed for the different reaction models and steam levels. Although all mechanisms show a similar trend the differences between the models increase with increasing steam content. The GRI mechanism shows for instance a two times thicker flame thickness compared to Burke. Burke and Kéromnès predict the thinnest flames. Hence the flame thickness is for example of importance for mesh generation of reacting flows these results have a direct impact on the resulting mesh size and thus on the computational costs. It is noteworthy that all models predict a local maximum for the flame thickness near stoichiometric conditions. However, without according experiments it is not possible to exclude numerical artifacts as reasons for this effect.

For pure hydrogen-oxygen-air flames the differences between the models become almost marginal. Although Kéromnès and Burke reproduce the experiments slightly better. In addition to the laminar burning velocity investigations, also the auto-ignition process was examined. Compared to the data of Wang et al. (2003) it was found that the schemes are well in line with the experiments, except for the low-temperature regime for no and low steam dilution where all models seem to fail. These effects are currently under reconsideration by the community as reported by Le Cong et al. (2009). In a final step the candidates were also compared against the recently reported auto-ignition time delays by Donohoe et al. (2014). In the higher temperature regime all candidates are in line with the measurements; however, the low temperature regime shows significant differences. Donohoe et al. (2014) compensated these effects with artificial extension of the domain in his numerical studies. Nonetheless, the correlation function was not reported and a comparison of the low temperature regime is not possible.

Therefore, it is concluded that the recently published mechanism of Burke and Kéromnès are the most suited schemes for predicting combustion processes with dilution of high steam contents at gas turbine conditions. Thus, both schemes are used for the further investigations.

5

Influence of Steam on the Combustion Process

5.1 One-Dimensional Flames

Aside from the temperature effect of steam on the flame, as reported by David et al. (1942), Kuehl (1962) was one of the first who observed that steam dilution directly affects the burning velocity. He concluded that the change in burning velocity is directly linked to the amount of radiant energy transfer. Levy (1963) did not disagreed with Kuehl's interpretation, however, stated that the radiant energy transfer is subordinate to the an increase in OH radical concentration due to following reactions:

$$\mathrm{H_2O} + \mathrm{HO_2} \rightleftharpoons \mathrm{OH} + \mathrm{H_2O_2} \tag{5.1}$$

or

$$\mathrm{H_2O} + \mathrm{H} + \mathrm{O_2} \rightleftharpoons \mathrm{OH} + \mathrm{H_2O_2} \tag{5.2}$$

While Liu et al. (1983) reported that steam dilution results also in a bell-shaped form when the burning velocity is plotted as a function of the hydrogen content, no further explanation was given. This is probably the reason why the laminar burning velocity is often plotted as a function of the hydrogen content. It was Koroll et al. (1988) who made a first comprehensive attempt to explain the effect of steam on the combustion process of hydrogen flames. He stated that steam is usually considered to act as a simple diluent and is supposed to lower the burning velocity by acting as a heat sink. This is due to the higher specific heat capacity of steam, which results in a reduc2tion of the flame temperature. Koroll considered a general expression where the laminar burning velocity is represented by a transport term and a reaction rate term:

$$S_L = \underbrace{\left(\frac{\lambda}{\rho c_p}\right)^{1/2}}_{\text{transport term}} \cdot \overbrace{\dot{\omega}^{1/2}}^{\text{reaction term}} \quad , \tag{5.3}$$

where λ is the thermal conductivity and c_p the specific heat capacity. He further stated that replacing one inert diluent with another one would alter the transport term if the diluents differ in material properties. Figure 5.1 depicts thermophysical data for various gaseous species as a function of the temperature at ambient pressure. Helium and argon have identical specific heat capacities, which is supposed to result in the same adiabatic flame temperature. However, due to their different thermal diffusivities, they differ in their effects on the burning velocity. On the other hand argon and nitrogen have similar thermal diffusivities, therefore, their difference in burning velocity results from different heat capacities. Koroll deduced that all three species are known to act as ideal inert diluents, as is presented in the following.

In order to examine this statement and to illustrate the effect of different diluents on the burning velocity, Figure 5.2 presents measurements of the burning velocity as a function of the dilution content. The experiments of the $\mathrm{H_2}$-$\mathrm{O_2}$-$\mathrm{H_2O}$ mixtures were conducted by Koroll et al. (1988) at ambient pressure and an inlet temperature of 373 K. In addition, the results of Kuznetsov et al. (2011) at inlet temperature of 383 K and of 393 K are also depicted. The calculations are conducted numerically by employing the reaction schemes of Burke et al. (2012) and Kéromnès et al. (2013). As diluents argon, molecular nitrogen, helium, carbon dioxide, carbon monoxide, steam, and virtual steam are used. Virtual steam ($\mathrm{vH_2O}$) denotes an inert

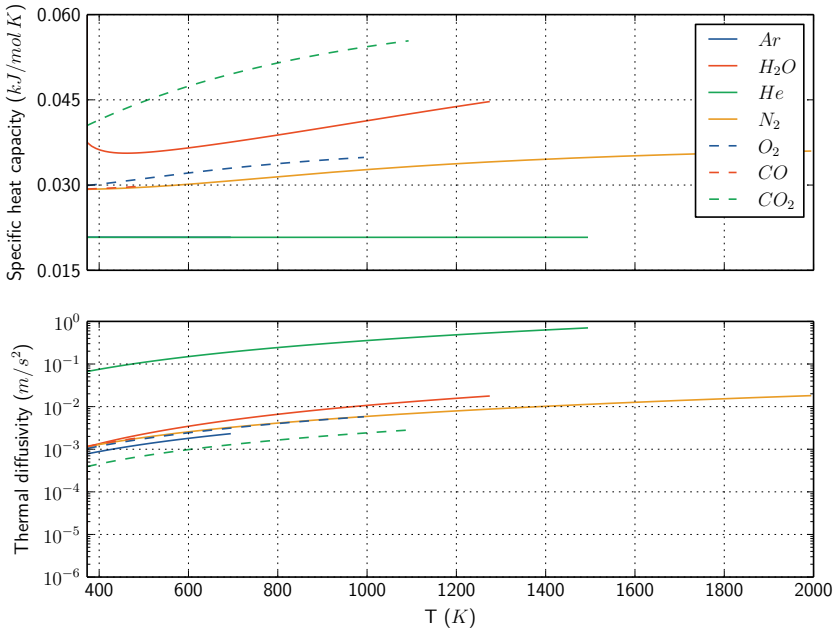

Figure 5.1: Specific heat capacity and thermal diffusivity as a function of the temperature at ambient pressure for various species. Source: Burgess (2014)

species with the same thermophysical properties as steam. It accounts as third body in collision reactions, but without a distinguished efficiency level. For CANTERA the default efficiency level is one.

Evidently, the experimental sets of Koroll and Kuznetsov are in good agreement, even though Kuznetsov's set shows slightly higher velocities, probably caused by the slightly higher inlet temperature. A common tendency that the burning velocity decreases with increasing fraction of the diluent can be observed for all cases. As was predicted by Koroll, argon and helium are not in line, neither are nitrogen and argon. To support his theory also carbon monoxide is used, because it has the same specific heat capacity and thermal diffusivity as nitrogen. According to Koroll's theorem, this must result in the same laminar burning velocity, as is the case for the computations with Burke's mechanism. Due to a lack of experimental data, the question cannot be finally concluded which mechanism predicts carbon monoxide correctly. Steam features a similar thermal diffusivity as nitrogen, however, the heat capacities are different. Comparing steam and virtual steam proves the existence of a chemical effect, because otherwise these lines must collapse. In contrary to what is expected, steam dilution reduces the burning velocity for steam fractions $\lesssim 40\%$ significantly stronger as is the case for virtual steam. Beyond this point, steam dilution decreases the velocity more as is the case for $\mathrm{vH_2O}$.

Koroll identified three reactions on which steam is supposed to have the highest impact (Koroll et al., 1988):

$$\mathrm{OH + H_2 \rightleftharpoons H_2O + H} \tag{R4}$$
$$\mathrm{OH + OH \rightleftharpoons H_2O + O} \tag{R5}$$
$$\mathrm{H + O_2 + M \rightleftharpoons HO_2 + M} \tag{R15}$$

Please note that the reactions are labeled in the notation of Burke's mechanism as listed in Table 5.1. The complete scheme may be found in the Appendix A (p. 165).

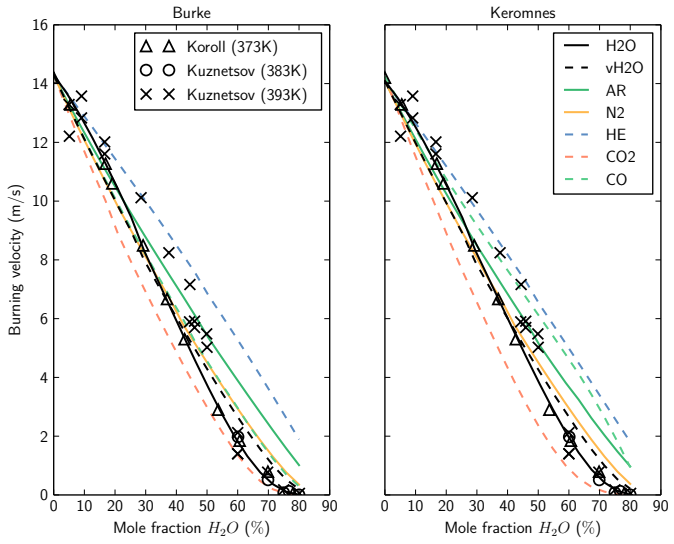

Figure 5.2: Burning velocities of $2:1$ H_2-O_2 mixtures at $373 - 393\,\mathrm{K}$ and ambient pressure with the diluents Ar, He, N_2, CO, CO_2 and H_2O. Experimental data (symbols) according to Koroll et al. (1988) and Kuznetsov et al. (2011). Lines indicate model predictions employing the mechanism of Burke et al. (2012) and Kéromnès et al. (2013). Virtual steam ($\mathrm{vH_2O}$) denotes an inert species with the same thermophysical properties as steam. Please note that for the specific heat capacity, argon is in line with helium.

Table 5.1: Elementary reactions according to Burke's mechanism (Burke et al., 2012). The complete scheme including the coefficients can be found in the Appendix A (p. 165).

#	Equation	#	Equation
$R1$	$H + O_2 \rightleftharpoons O + OH$	$R15$	$H + O_2(+M) \rightleftharpoons HO_2(+M)$
$R2$	$O + H_2 \rightleftharpoons H + OH$	$R16$	$HO_2 + H \rightleftharpoons H_2 + O_2$
$R3$	$O + H_2 \rightleftharpoons H + OH$	$R17$	$HO_2 + H \rightleftharpoons OH + OH$
$R4$	$H_2 + OH \rightleftharpoons H_2O + H$	$R18$	$HO_2 + O \rightleftharpoons O_2 + OH$
$R5$	$OH + OH \rightleftharpoons O + H_2O$	$R19$	$HO_2 + OH \rightleftharpoons H_2O + O_2$
$R6$	$H_2(+M) \rightleftharpoons H + H(+M)$	$R20$	$HO_2 + HO_2 \rightleftharpoons H_2O_2 + O_2$
$R7$	$H_2 + AR \rightleftharpoons H + H + AR$	$R21$	$HO_2 + HO_2 \rightleftharpoons H_2O_2 + O_2$
$R8$	$H_2 + HE \rightleftharpoons H + H + HE$	$R22$	$H_2O_2(+M) \rightleftharpoons OH + OH(+M)$
$R9$	$O + O(+M) \rightleftharpoons O_2(+M)$	$R23$	$H_2O_2 + H \rightleftharpoons H_2O + OH$
$R10$	$O + O + AR \rightleftharpoons O_2 + AR$	$R24$	$H_2O_2 + H \rightleftharpoons HO_2 + H_2$
$R11$	$O + O + HE \rightleftharpoons O_2 + HE$	$R25$	$H_2O_2 + O \rightleftharpoons OH + HO_2$
$R12$	$O + H(+M) \rightleftharpoons OH(+M)$	$R26$	$H_2O_2 + OH \rightleftharpoons HO_2 + H_2O$
$R13$	$H_2O(+M) \rightleftharpoons H + OH(+M)$	$R27$	$H_2O_2 + OH \rightleftharpoons HO_2 + H_2O$
$R14$	$H_2O + H_2O \rightleftharpoons H + OH + H_2O$		

Koroll stated that by adding steam, the reverse rates would increase in the reactions R4 and R5 probably leading to an increase in OH concentration. However, he concluded that due to their high activation energy, even a decrease of the reverse rates is more likely as presented in the following.

Figure 5.3 presents the molar fraction of OH as a function of the inverse temperature computed with a one-dimensional hydrogen flame configuration and Burke's mechanism. Results are depicted for three constant adiabatic flame temperatures close to gas turbine conditions ($T_b = 1573, 1673, 1773\,\mathrm{K}$). A common tendency can be observed. With increasing diluent content, the OH concentration decreases. Moreover, it is apparent that for the inert steam ($\mathrm{vH_2O}$) the decrease of the radical concentration is slightly higher as is the case for the real steam. It is also noteworthy that the OH concentration peaks at the same (high) temperature for both cases and for all initial temperatures. This indicates that rather a dissociation reaction is impaired by the dilution than R4 or R5, because virtual steam can only interact through third-body reactions. Possible candidates are $\mathrm{R13}$ and $\mathrm{R14}$ ($H_2O(+M) \rightleftharpoons H + OH(+M)$), since both equations describe in principle the same reaction just with different coefficients for inert diluents and water.

In addition to molar fractions, Figure 5.3 depicts the preheat zones for the dry and wet cases. According to Poinsot et al., 2005, the preheat zone is defined as the region preceding the heat release peak and can be expressed by a temperature range. The lower limit is the inlet temperature T_u and the upper limit is denoted as the preheat temperature T_{pre}. For a fixed outlet temperature of 1773 K and an inlet temperature of $T_u = 500\,\mathrm{K}$, this results in a preheat temperature of $T_{pre} < 681\,\mathrm{K}$ for the dry case ($\Omega = 0\%$), in $T_{pre} < 740\,\mathrm{K}$ for the moderately wet case ($\Omega = 20\%$) and in $T_{pre} < 759\,\mathrm{K}$ for the ultra-wet case ($\Omega = 50\%$). The preheat zones are calculated with an one-dimensional approach and Burke's mechanism. Upon adding steam, the preheat zone extends to higher temperatures, and evidently the inert steam has a less pronounced impact on the preheat zone.

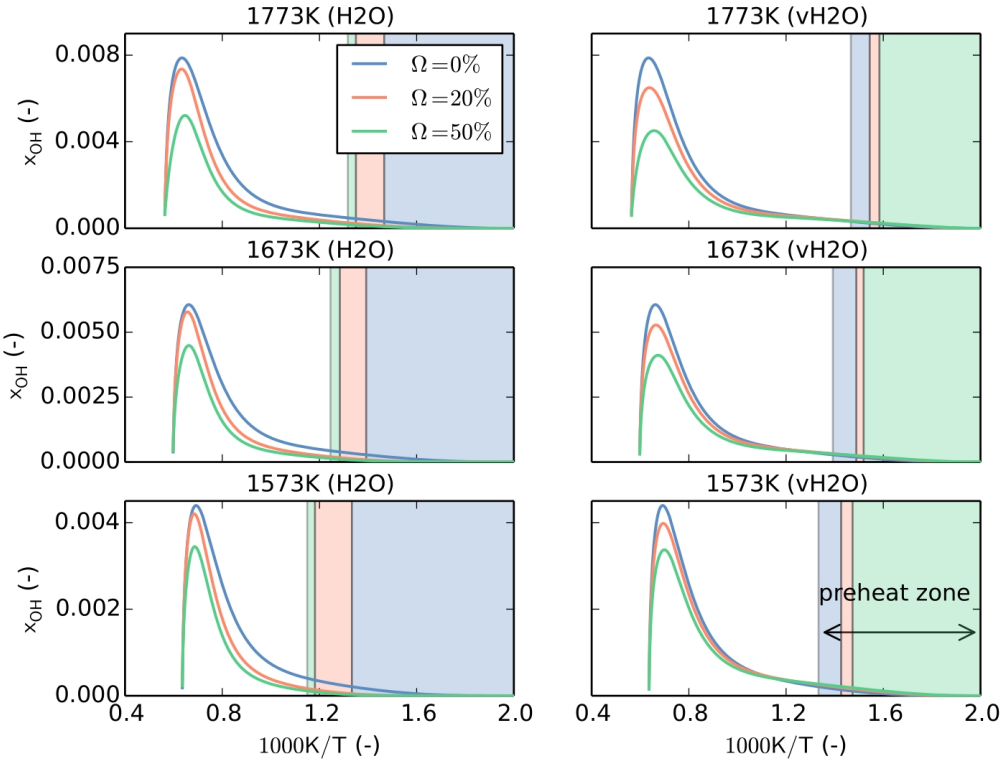

Figure 5.3: Molar fraction of OH as a function of the inverse temperature for three different steam contents $\Omega = 0{,}20{,}50\%$ ($T_u = 500\,\mathrm{K}$). The temperature of the burned gases was kept constant ($T_b = 1573, 1673, 1773\,\mathrm{K}$). Preheating zones for all steam contents cases are also provided as colored zones. Computations are conducted with Burke's mechanism (Burke et al., 2012).

Figure 5.4(a) shows the impact of steam (and virtual steam) on the preheat zone temperature at constant adiabatic flame temperatures. Evidently, with increasing steam content the heat release peak is shifted towards higher temperatures. In turn the preheat temperature is decreased with rising adiabatic flame temperatures. In contrast to the behavior with steam, the inert diluent moves the heat release peak towards lower temperatures. This effect is further supported by the increased adiabatic flame temperatures. Replacing the inert species with steam at constant dilution levels leads to the results depicted in Figure 5.4(b). As expected, the preheat temperature decreases with the rising content of the inert diluent $\xi = 0$. With ascending ξ this behavior is reversed. It is noteworthy that all dilution levels seem to meet in a single point, indicating that the chemical effect of steam becomes the dominant dilution effect beyond a steam fraction of $\xi \approx 30\%$.

As is well noted in literature (e.g., Li et al. (2004b)) the hydrogen mechanism is sensitive to key chain branching and the important chain termination reaction (R15). Reaction (R15) is highly exothermic and initiates the low-activation reactions of HO_2 and H_2O_2 with other participants of the radical pool such as H, OH and O. Koroll suggested that steam has a high impact on this reaction due to its high third-body efficiency coefficient. To investigate this,

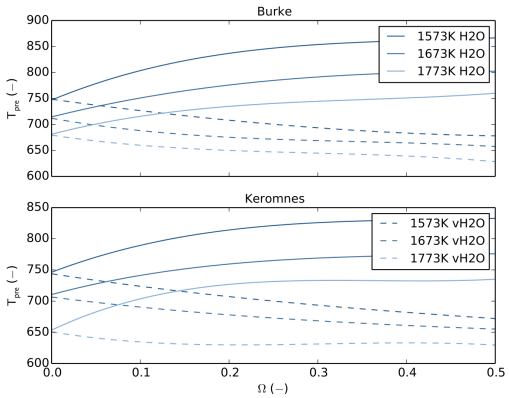

(a) Preheat temperature as a function of the steam content.

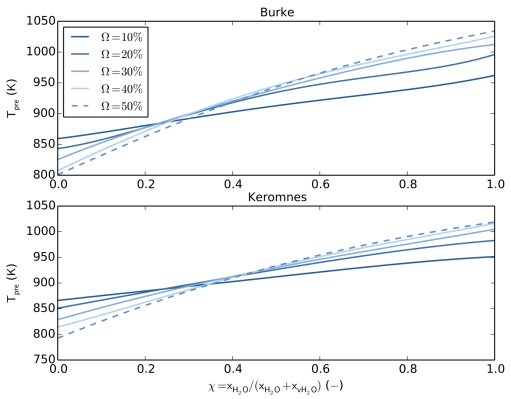

(b) Preheat temperature as a function of the steam content within the $\mathrm{vH_2O}$-$\mathrm{H_2O}$ mixture.

Figure 5.4: Impact of steam dilution on the preheat temperature ($T_u = 500\,\mathrm{K}$). Top: influence of the steam to air ratio Ω. Bottom: dilution with variable $\mathrm{vH_2O}$-$\mathrm{H_2O}$ composition. Steam fraction ξ is defined as: $\xi = {x_{H_2O}}/{(x_{H_2O} + x_{vH_2O})}$

the molar fraction of $\mathrm{HO_2}$ is shown in Figure 5.5(a) as a function of the inverse temperature. Due to steam addition, the concentration peaks are shifted towards higher temperatures with the extension of the preheat zone. On the other hand, the inert diluent ($\mathrm{vH_2O}$) reduces the concentration of $\mathrm{HO_2}$ with increasing diluent concentration and shifts the peak towards lower temperatures. A similar behavior can be observed for $\mathrm{H_2O_2}$ as depicted in Figure 5.5(b). $\mathrm{HO_2}$ can be considered as a precursor for combustion and is mainly found in the low temperature regimes. For propagating flames $\mathrm{HO_2}$ marks the end of the inert preheating zone and auto-ignition occurs in pools of $\mathrm{HO_2}$. By adding steam to the combustion process, the preheat zone shifts toward higher temperatures, and thus, increases the concentration of $\mathrm{HO_2}$ (and $\mathrm{H_2O_2}$), while the concentrations of O and H Figures 5.5(c) and 5.5(d) are simultaneously decreased. O and H species are mainly found in the inner reaction layer. Moreover, H is the main radical in the inner reaction layer, explaining why the decreases of the H concentration by the steam has a globally inhibiting effect on the combustion process.

The consumption and formation pathways are presented in Figures 5.6 to 5.8 for $\mathrm{H_2}$-$\mathrm{O_2}$-diluent flames at a constant adiabatic flame temperature $T_{ad} = 1573\,\mathrm{K}$, an initial temperature $T_u = 500\,\mathrm{K}$, and at ambient pressure for different levels of dilution. Steam and virtual steam ($\mathrm{vH_2O}$) serve as diluents. In the undiluted case, the OH radical evidently exhibits the highest production rates and is mainly produced from reactions involving O, probably via the chain reactions R1-R3. In combination with $\mathrm{HO_2}$, H, and $\mathrm{H_2O_2}$, OH is then further converted into water. At moderate dilution levels (20%) of inert steam, the pathways stay mostly unaffected. The main effect is an uniform increase of the reaction and production rates. In contrast to the addition of the inert diluent, steam leads to positive production rates of OH, and thus, it is rather produced than consumed. The same is found for $\mathrm{H_2O_2}$ and O. However, this effect was not observed for the concentration profiles of OH in Figure 5.3. With a further increasing of the diluent content (50%), this effect is reversed and it seems that for the case with steam a

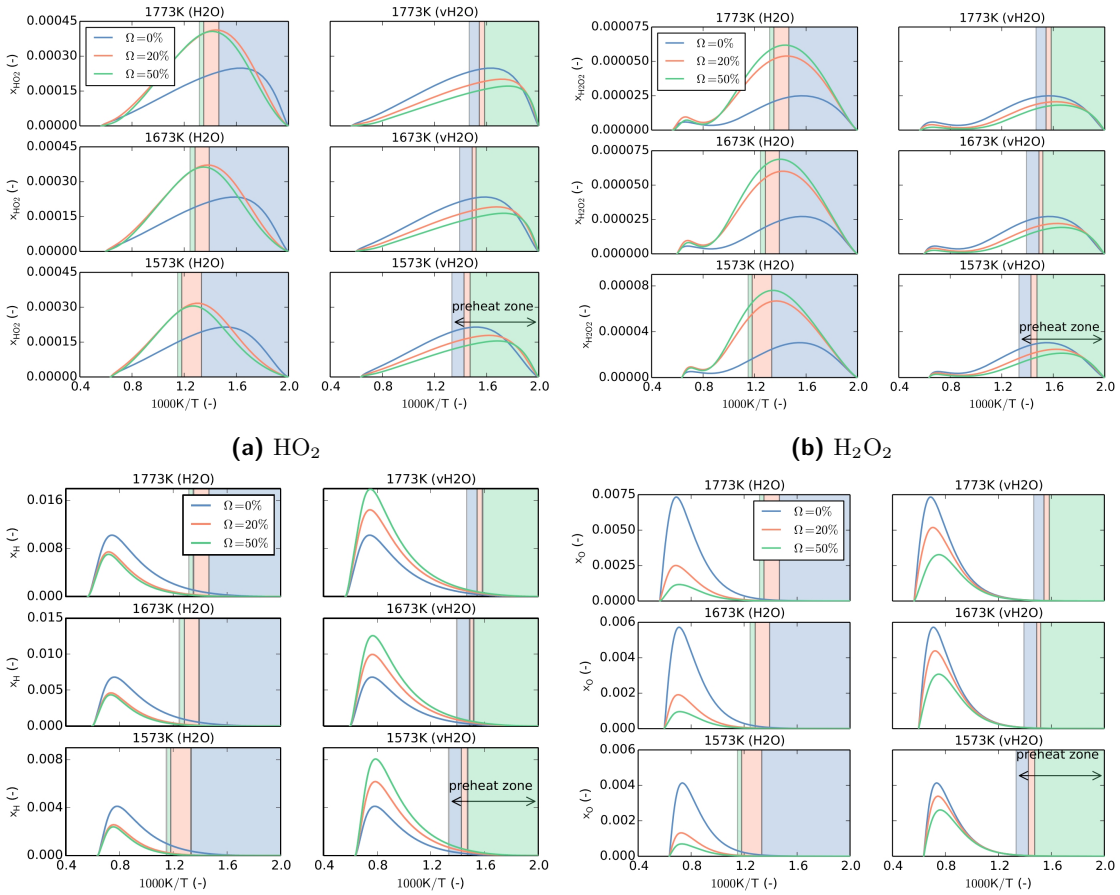

(a) HO_2 **(b)** H_2O_2

(c) H **(d)** O

Figure 5.5: Molar fraction of HO_2, H_2O_2, H, and O as a function of the inverse temperature for three different steam contents $\Omega = 0{,}20{,}50\%$ ($T_u = 500\,\mathrm{K}$). The temperature of the burned gases was kept constant ($T_b = 1573\,,1673\,,1773\,\mathrm{K}$). Preheating zones for all steam contents cases are also provided. Computations are conducted with Burke's mechanism (Burke et al., 2012).

state comparable to the non-diluted or ideal diluted case is recovered, only at different rates. In order to further investigate the contribution of the pathways, another technique must be applied. Nevertheless, the consumption pathways clearly show the interaction between the two main reactive species OH and HO_2, which are mainly altered by the addition of diluents.

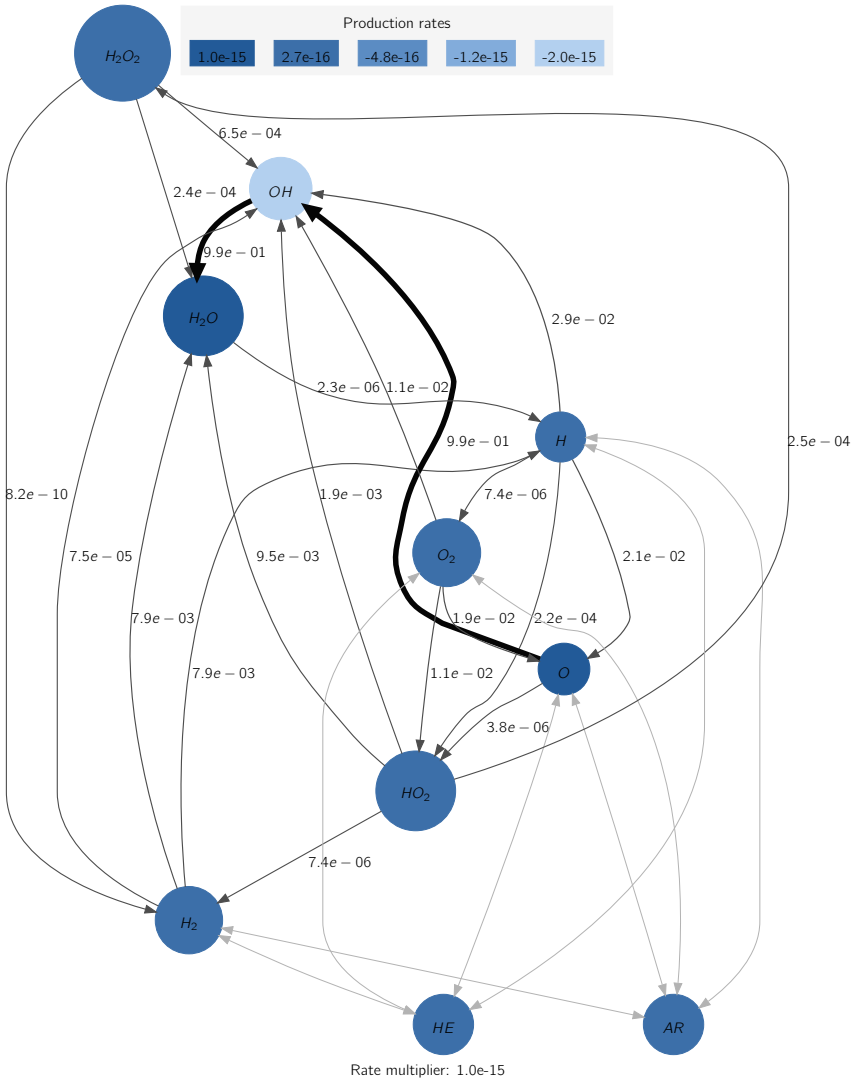

Figure 5.6: Integrated species consumption path using the mechanism of Burke et al. (2012) for a H_2-O_2 at ambient pressure, $T_{ad} = 1573\,\mathrm{K}$, and $T_u = 500\,\mathrm{K}$. The color of the species represents the production rates and the line thickness of the arrows the net rate of progress.

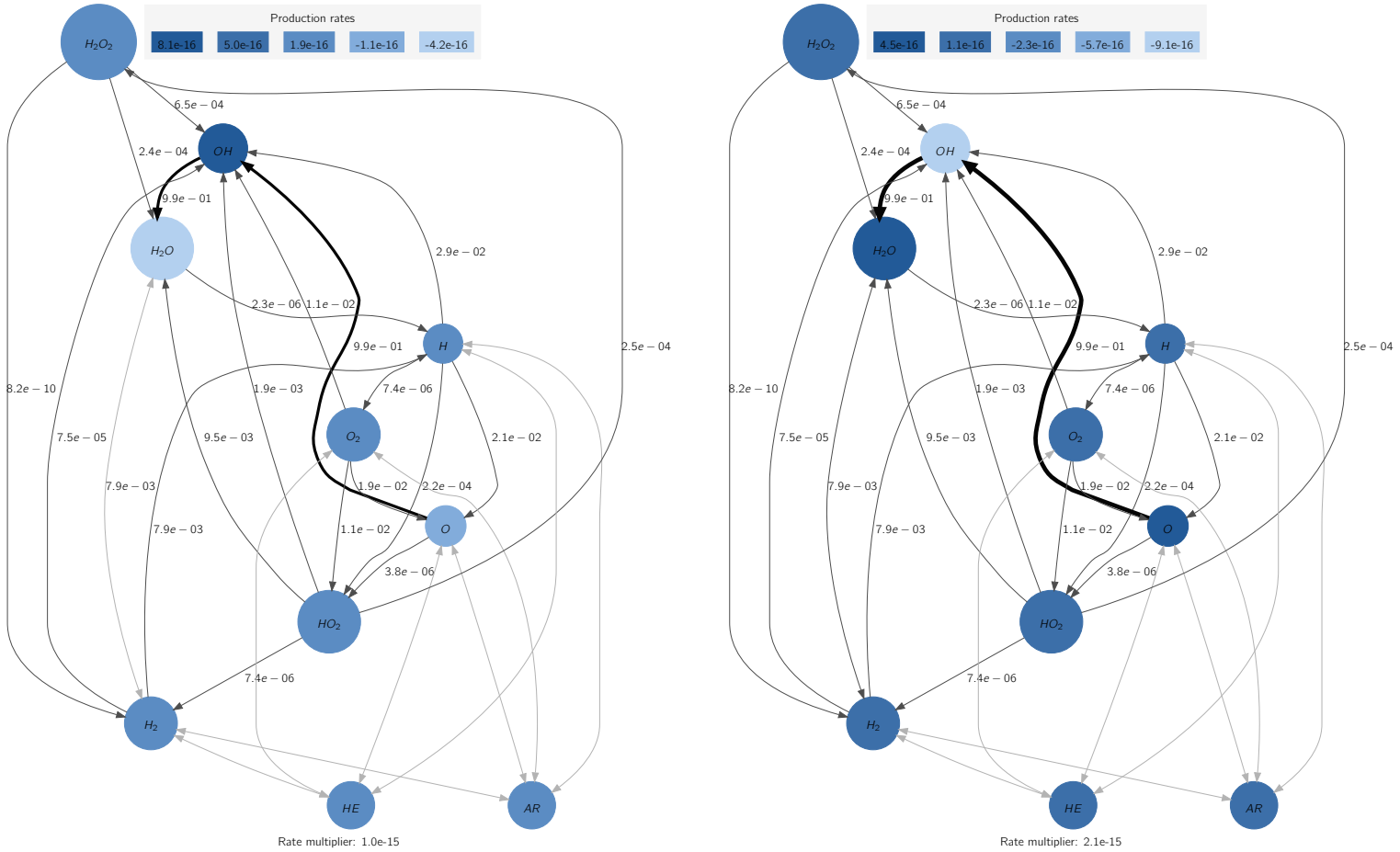

(a) Steam (H_2O) **(b)** Virtual steam (vH_2O)

Figure 5.7: Integrated species consumption path using the mechanism of Burke et al. (2012) for a H_2-O_2-diluent at ambient pressure, $T_{ad} = 1573\,\mathrm{K}$, $T_u = 500\,\mathrm{K}$, and 20% dilution. The color of the species represents the production rates and the line thickness of the arrows the net rate of progress.

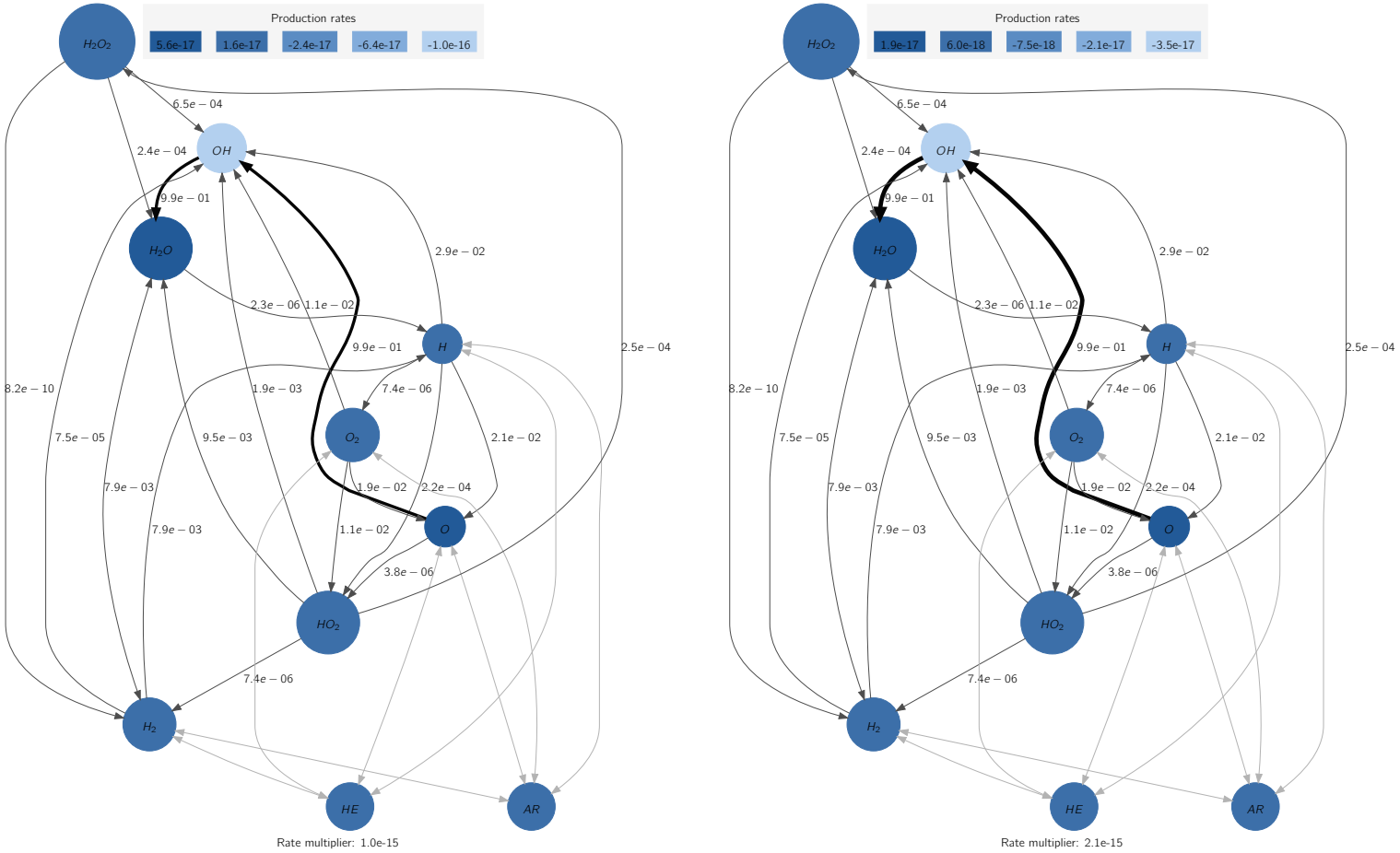

(a) Steam (H_2O) **(b)** Virtual steam (vH_2O)

Figure 5.8: Integrated species consumption path using the mechanism of Burke et al. (2012) for a H_2-O_2-diluent at ambient pressure, $T_{ad} = 1573\,\mathrm{K}$, $T_u = 500\,\mathrm{K}$, and 50% dilution. The color of the species represents the production rates and the line thickness of the arrows the net rate of progress.

The contribution of a single parameter (e.g., steam) on the combustion process can be determined through sensitivity analysis. Therefore the response of the system to a perturbation of an individual parameter is evaluated. The application of sensitivity analysis in combustion is usually either related to reduce detailed reaction schemes by identifying reactions that play a subordinate role or to assess the uncertainty of distinct parameters. However, it can also be used for the analysis of the combustion process itself, on the condition that the employed reaction scheme is detailed and accurate enough for this purpose. For this purpose it is common to use a *brute force* method (Frenklach, 1984; Turányi, 1997). Thus, the sensitivity coefficient S_{ij} of the parameter Φ_i to the parameter k_i is given by:

$$S_{ij} = \frac{\partial \Phi_i}{\partial k_j}. \tag{5.4}$$

Since it is more convenient to deal with normalized and logarithmic measures of sensitivities the entries of the normalized sensitivity matrix $\hat{S}$ reads as:

$$\hat{S}_{ij} = \frac{k_j}{\Phi_i}\frac{\partial \Phi_i}{\partial k_j} = \frac{\partial \ln \Phi_i}{\partial \ln k_j} \approx \frac{\Delta \ln \Phi_i}{\Delta \ln k_j}. \tag{5.5}$$

Here, the normalized sensitivity coefficients represent the fractional change of ϕ_i caused by a fractional change of the parameter k_j. In combustion the temperature is the dominant variable and any perturbation affects the concentration of species mainly through changes in the induced temperature (Turányi, 1997). Nevertheless, the sensitivity of model features, such as laminar burning velocity and auto-ignition time can also be investigated as is the case in the present thesis. Therefore, sensitivity is assessed by sequentially multiplying each reaction rate k with a constant factor m, which is usually denoted as reaction multiplier. In the literature it is common to use $m = 2$ as a reaction multiplier, but also very small values of $m = 0.05$ are selected to ensure a response within the linear regime. Hence, both values are used for the investigations.

The sensitivity analysis regarding the laminar burning velocity is employed using the reaction mechanism of Burke. The results of the sensitive analysis regarding the laminar burning velocity of a $2:1$ $\mathrm{H_2}$-$\mathrm{O_2}$ flame is presented in Figure 5.9. The computations are conducted at ambient pressure and at $T_u = 393\,\mathrm{K}$ with varying degree of dilution. Steam ($\mathrm{H_2O}$) as well as virtual steam ($\mathrm{vH_2O}$) serve as diluents. The most sensitive reactions are depicted in color, whereas the remaining reactions are plotted in gray and reactions only containing noble gases (He, Ar) are omitted for clarity.

It is seen that for virtual steam the sensitivities remain almost constant up to a mole fraction of $\approx 20\%$. Beyond this point the sensitivity of $\mathrm{R15}$ decreases significantly whereas $\mathrm{R1}$, $\mathrm{R4}$, and $\mathrm{R17}$ simultaneously increase. $\mathrm{R1}$, $\mathrm{R4}$, and $\mathrm{R17}$ are chain branching reactions whereas $\mathrm{R15}$ is a chain terminating reaction, acting as a counter part. The same behavior just stronger pronounced is observed for the dilution with steam. It has been widely suggested in the literature (Le Cong et al., 2009; Santner et al., 2011; Singh et al., 2012) that steam addition mostly affects $\mathrm{R15}$ ($H + O_2(+M) \rightleftharpoons HO_2(+M)$) through the high third-body efficiency of water.

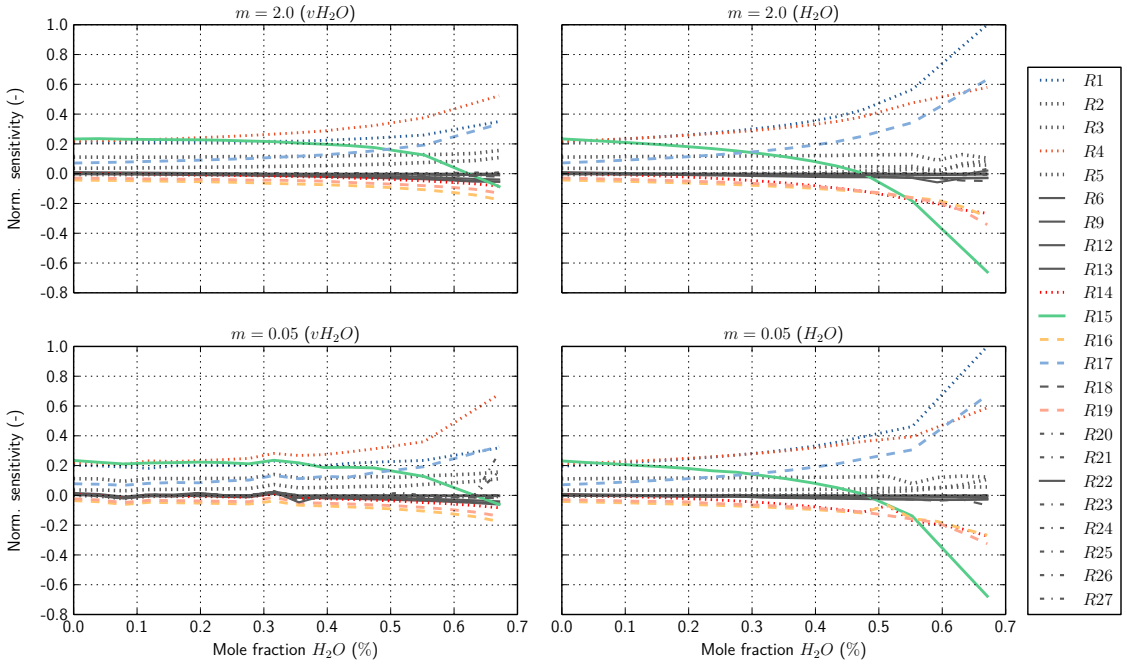

Figure 5.9: Sensitivity analysis of the laminar burning velocity of $2:1$ H_2-O_2 flames at $T_u = 393\,\mathrm{K}$ and ambient pressure with varying degree of dilution and different reaction multipliers m. Steam (H_2O) and virtual steam (vH_2O) serve as diluents. The most contributing reactions are depicted in color, the remaining are colored in gray. Reactions only containing noble gases (He, Ar) are omitted.

By adding steam to the system the left hand side of R15 is promoted, leading to a higher concentration of HO_2 and a lower concentration of H, as was previously seen in Figure 5.5, and thus, to an inhibiting effect on the laminar burning velocity. In contrast to that the chain branching reactions R1, R4, and R17 have a promoting effect on the laminar burning velocity and are highly temperature dependent. In Figure 4.4 a promoting and inhibiting effect of steam on the laminar burning velocity was apparent, which is also represented by the sensitivities. Furthermore, it was also observed in Figure 5.5 that the HO_2 concentration decreases for the addition of virtual steam, which is probably caused by the significantly lower third-body efficiency. Due to the fact that the temperatures were kept constant for the tests a consumption of HO_2 through other reactions is unlikely. The same argumentation can be applied for reaction R22 explaining the increase of H_2O_2 concentration when steam is added. The anomaly observed in the reaction pathways at moderate steam levels (20%) is probably triggered by the dissociation reaction R14, which converts water molecules at high temperatures directly into H and OH. Even though this is also supported by the pathway diagram (Figure 5.7(a)). There, only a change in the species production and not in the reaction pathways itself was observed. For higher levels of dilution, this effect becomes less dominant.

In order to investigate the role of the third-body efficiencies for diluted hydrogen flames, a numerical experiment is conducted. Therefore, laminar burning velocities are computed with the baseline reaction schemes and with reaction schemes where the third-body efficiencies

for water are set to zero. Figure 5.10 presents the results for diluted stoichiometric H_2-O_2 and H_2-air flames at ambient pressure and an initial temperature of $T_u = 300\,\mathrm{K}$. Obviously, the laminar burning velocities are very high for the H_2-O_2 case. With the addition of inert steam, the burning velocity almost decreases linearly. Under the influence of steam, the burning velocity forms a S-type slope. If the effect of steam on the laminar burning velocity is only caused by the third-body efficiency of water and no further chemical effect is present, the results of the reaction scheme with the modified third-body efficiency of water and the results of the inert species must collapse. This is the case for both flame configurations, and thus, it is stated that the high third-body efficiency of water is the dominant chemical effect.

Due to the fact that gas turbines are operated at elevated pressures, it is important to investigate the pressure effects on the laminar flame velocity of hydrogen-oxygen-steam mixtures. Kuznetsov et al. (2011) conducted experiments with stoichiometric hydrogen flames in a spherical explosion chamber up to 72 bar. The experiments serve as validation for the computations with Burke's and Kéromnès' reaction mechanisms. The results with steam and virtual steam are presented in Figure 5.11. Obviously, both mechanisms are well in line with the experiments even at elevated pressures. It is also seen that with increasing pressure as well as with increasing steam content, the laminar burning velocity is reduced. Also the virtual steam shows a significant difference to the experimental data. Virtual steam has only a small contribution on the chemical equilibrium, and hence, only a limited constraining effect on the burning velocity. The opposite is the case for steam, which has a distinguished constraining effect on the equilibrium which yields in a reduced burning velocity.

To conclude the investigation of the influence of steam on one-dimensional flames, the flame cooling effect is presented in Figure 5.12. Evidently, the adiabatic flame temperature is significantly reduced with increasing steam content. For instance, the addition of 50% steam leads to a reduction of more than 700 K for a constant equivalence ratio. However, gas turbines are operated at constant turbine inlet temperatures, and by utilizing steam it is possible to

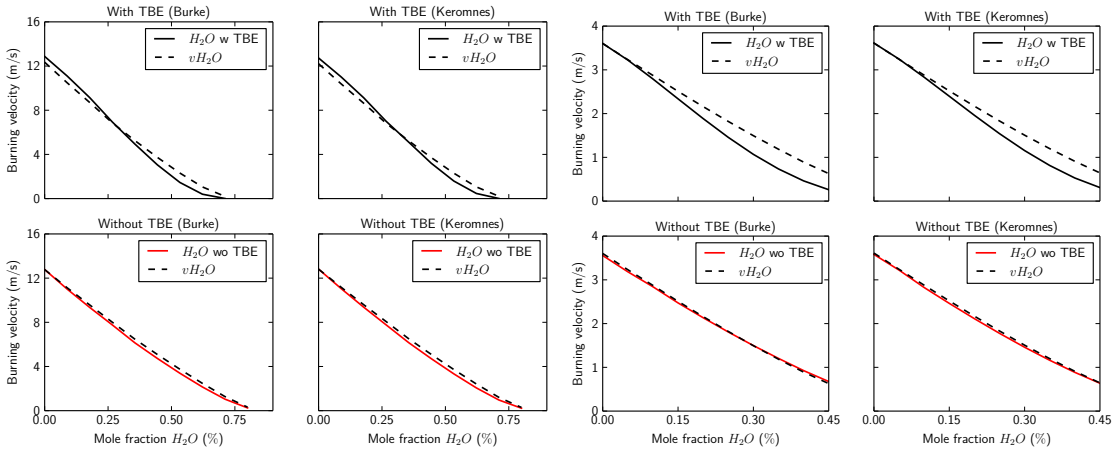

(a) $2:1$ H_2-O_2-diluent flame ($T_u = 300\,\mathrm{K}$) **(b)** H_2-air-diluent flame ($T_u = 300\,\mathrm{K}$ and $\phi = 1$)

Figure 5.10: Influence of third-body efficiency. Reaction schemes with (top row) and without (bottom row) third-body efficiencies for water.

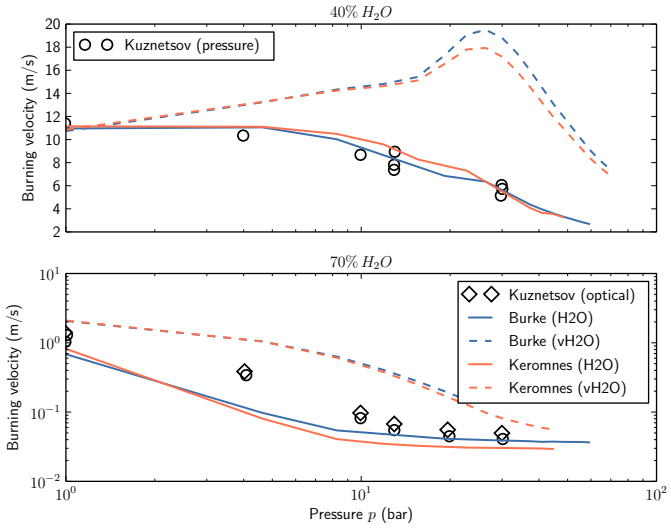

Figure 5.11: Laminar burning velocities of 40% (top) and 75% (bottom) steam diluted stoichiometric H_2-O_2 flames as a function of the pressure ($T_u = 573\,\mathrm{K}$). Experimental data according to Kuznetsov et al. (2011). Lines indicate model predictions employing the mechanism of Burke et al. (2012) and Kéromnès et al. (2013).

lower the adiabatic flame temperature of hydrogen flames to a technical applicable range.

Göke (2012) investigated steam diluted flames employing low order modeling. However, the focus of his work laid on the formation of emission, and thus, did not investigate the influence of steam on the laminar burning velocity or self-ignition. Nevertheless, he also reported a decrease of the concentrations of OH, H, and O if steam is added to the combustion process. He also attributed the decrease of the H concentration to the third body reaction R15. This findings are in line with the finding of the present study.

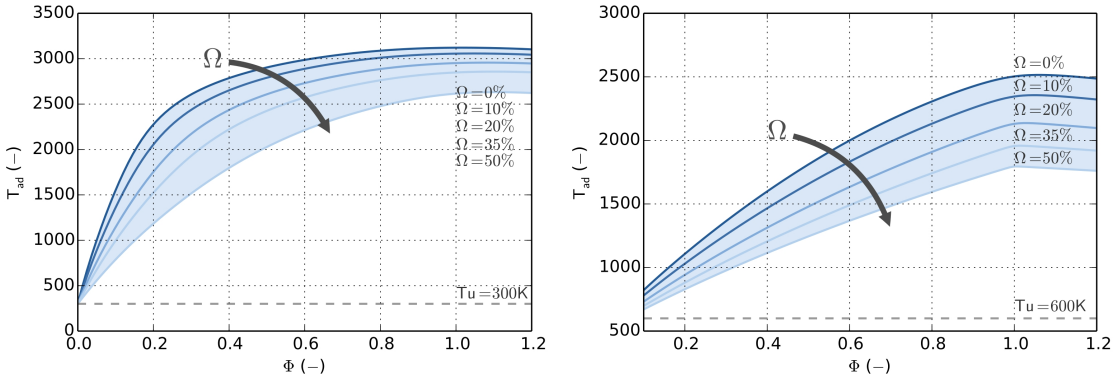

(a) Hydrogen-oxygen-steam ($T_u = 300\,\mathrm{K}$) **(b)** Hydrogen-air-steam ($T_u = 600\,\mathrm{K}$)

Figure 5.12: Adiabatic flame temperature of a hydrogen flames at ambient pressure as a function of the equivalence ratio and steam content. Computations are conducted employing the mechanism of Burke et al. (2012).

5.2 Auto-Ignition Events

Wang et al. (2003) measured the ignition time delays for various hydrogen-air-steam compositions ($15\%\mathrm{H_2}$ and $0-40\%\mathrm{H_2O}$) over a temperature range of 955 K to 1352 K at a pressure of 5 bar. The experiments showed a significant prolongating effect of water addition on the ignition time delays. Figure 5.13 presents the ignition time delays as a function of the initial temperature at a constant dilution level of $\chi = 25\%$ and varying pressures (4,10,16bar). According to Wang et al. (2003), the dilution level χ defines the composition as: $(100-\chi)\cdot(15\%\mathrm{H_2}+85\%\mathrm{air})\cdot\chi\%$ diluent.

It is seen that there is no pressure influence apparent for the experimental data within the given pressure interval. Evidently, both reaction schemes have problems reproducing the experimental data for the lowest pressure level (4 bar). However, the predictions of both reaction mechanisms are well in line with the measurements for the higher pressure levels. On the contrary, the results for the inert diluent ($\mathrm{vH_2O}$) show a strong pressure dependence. Thus, with increasing pressure, the ignition time rises significantly. This effect is well in line with the above findings, where a significant difference between the inert diluent and steam was determined for the laminar burning velocity at elevated pressures. It was found that steam has an impeding effect on the kinetics caused by the high third-body efficiencies of water, caused by the shift of the preheat zone and the impact on the radical pool (especially on $\mathrm{HO_2}$ and H).

As previously stated, steam shifts the heat release peak towards higher temperatures. This effect can also be observed for auto-ignition events, where the dilution of steam prolongates the ignition time delay, as is shown in Figure 5.14. There, the ignition time delay is plotted as a function of the dilution ratio Ω and the initial temperature. For clarity the logarithm of delay times is depicted. In the case of dilution with inert steam, it is seen that the ignition time delay decreases with the rising initial temperature. Moreover, it is apparent that the ignition time delay mainly depends on the initial temperature rather than on the level of dilution. This

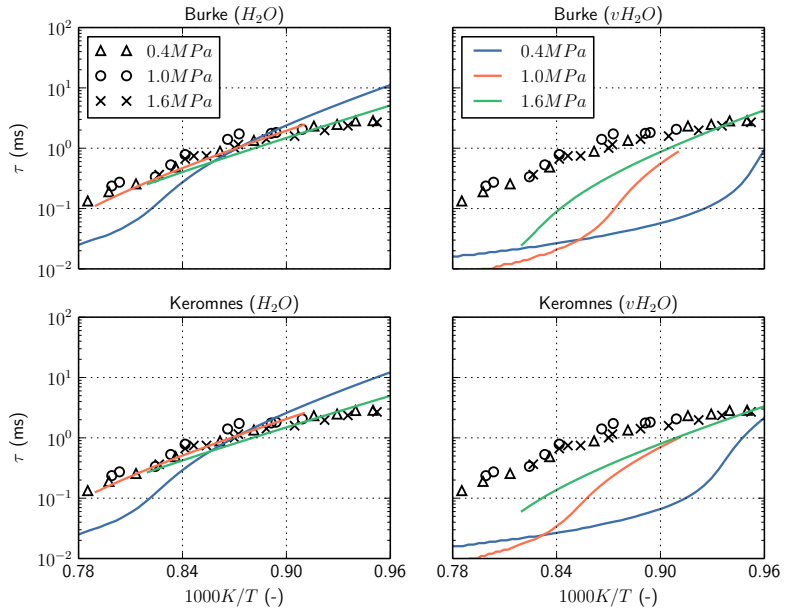

Figure 5.13: Ignition time delay of hydrogen-air-steam mixtures as a function of the initial temperature and pressure at a dilution level of $\chi = 25\%$. χ is the steam concentration and the composition is given by: $(100 - \chi) \cdot (15\%\mathrm{H_2} + 85\%\mathrm{Air}) \cdot \chi\%$ Steam. Experimental data according to Wang et al. (2003). Left column: computations with steam, right column: computations with inert steam ($\mathrm{vH_2O}$).

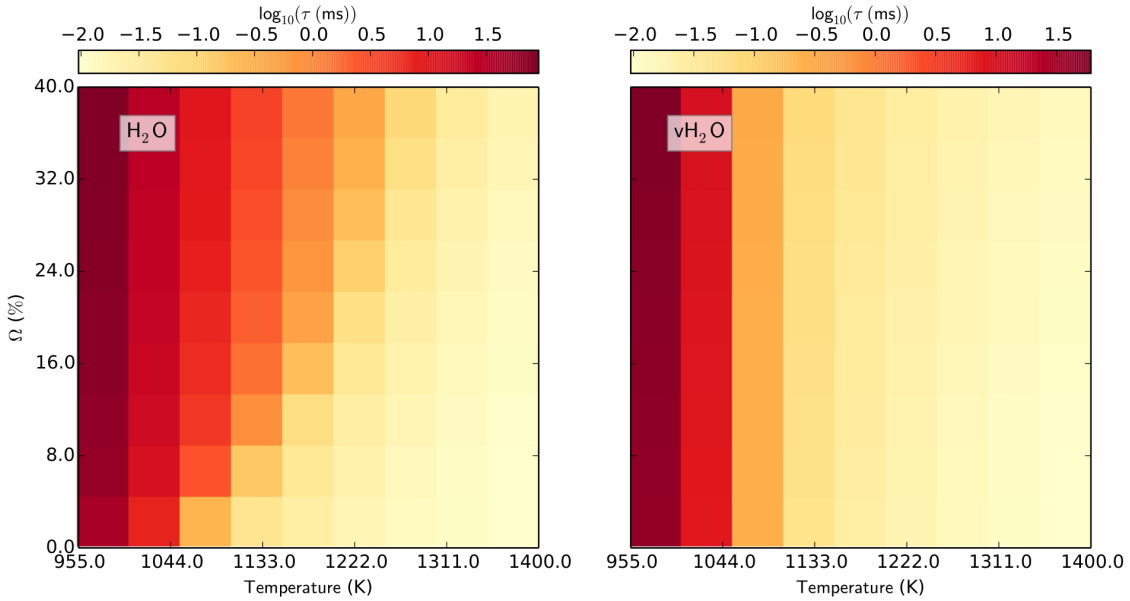

Figure 5.14: Ignition time delay of a hydrogen-oxygen as a function of the dilution level Ω and the initial temperature. Computations are conducted employing the mechanism of Burke et al. (2012). Left: computations with steam, right: computations with inert steam (vH_2O).

manifests in a insignificant color change in the Ω direction. On the other hand, in the case of dilution with steam, also a significant dilution level dependency is observed in addition to the temperature dependency. This emphasizes the effect of steam on the temperature regimes in combustion processes.

A sensitivity analysis of ignition time delays of hydrogen-oxygen flames as a function of the initial temperature and the dilution level is depicted in Figure 5.15. The sensitivity coefficients are calculated for different reaction multipliers ($m = 0.05\,,2$) and steam as well as inert steam as diluents. In the linear response regime ($m = 0.05$), the largest sensitivities for virtual steam are found for dissociation reactions ($\mathrm{R6\text{-}R14}$), reactions including the formation or consumption of HO_2 ($\mathrm{R15\text{-}R19}$), and the third-body reactions ($\mathrm{R6}$, $\mathrm{R12}$, $\mathrm{R13}$, $\mathrm{R15}$). Moreover, it is evident that these sensitivities show a strong temperature dependence and only insignificantly depend on the dilution level, which agrees with the previous findings. For the presence of steam, the sensitivities of the linear regime are shifted towards higher temperatures. Compared to the inert diluent (vH_2O), also reaction $\mathrm{R19}$ ($HO_2 + OH \rightleftharpoons H_2O + O_2$) exhibits a significant change of the sensitivities, implying that steam directly affects this reaction. Moreover, this reaction does not involve a third collision partner and is therefore a direct chemical effect on the combustion process. In the non-linear regime ($m = 2.0$), the large sensitivities are only found for $\mathrm{R15}$, emphasizing the importance of this third-body and chain termination reaction. Due to the high third-body efficiency of water, the temperature dependency of this reaction is shifted towards higher temperature regimes, and thus, impairs the auto-ignition process through chain termination.

Concluding, it can be stated that for the sensitivity analysis concerning the laminar burning

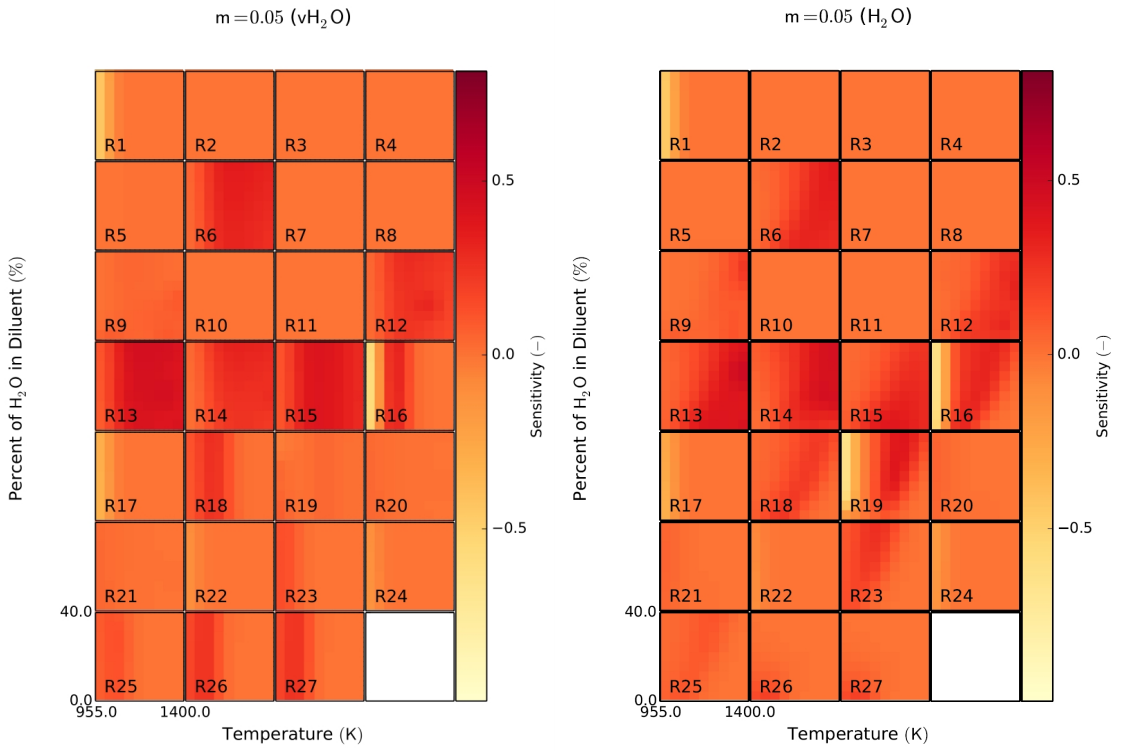

(a) $\mathrm{vH_2O}$ **(b)** $\mathrm{H_2O}$

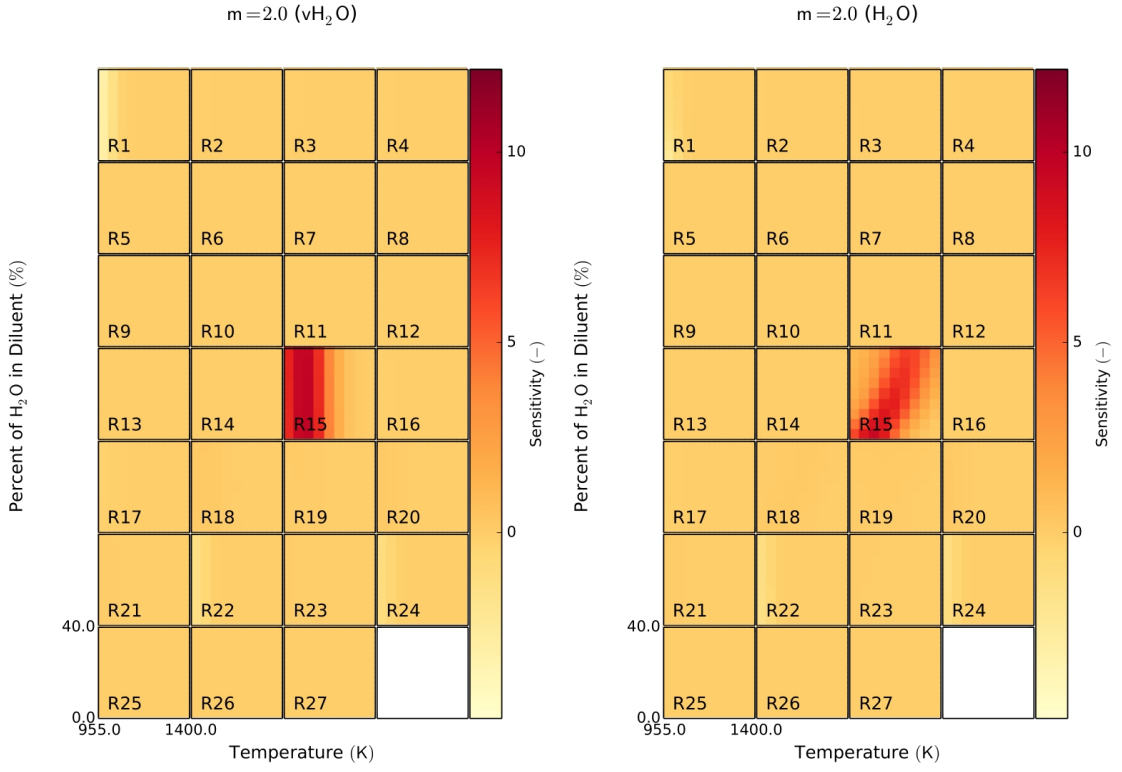

(c) $\mathrm{vH_2O}$ **(d)** $\mathrm{H_2O}$

Figure 5.15: Sensitivity analysis of ignition time delays of hydrogen-oxygen flames. The sensitivity coefficients are depicted for each reaction as a function of the steam content and the initial temperature. The computations are conducted employing the mechanism of Burke et al. (2012).

velocity, almost no differences in the response of the system between the two reaction multipliers could be determined. On the other hand, for evaluating the sensitivities of auto-ignition processes, the usage of both reaction multipliers allowed for the investigation of local and global effects.

In this chapter the influence of steam addition on the laminar burning velocity and on auto-ignition events is investigated. By introducing an inert species with the same thermophysical properties as steam, but without any chemical effect except as a collision partner, it was shown that steam has a significant chemcial effect that is different from ideal diluents. Employing one-dimensional flames it was revealed that steam shifts the preheat zone towards higher temperatures. The preheat zone is defined as the region preceding the heat release peak and can be expressed by a temperature range. Applying a sensitivty analysis in combination with species concentration profiles, it was shown that the addition of steam mostly affects the reaction $\mathrm{R15}$ *(* $H + O_2(+M) \rightleftharpoons HO_2(+M)$ *), which has an inhibiting effect on the combustion process, leading to a shift of the preheat zone, and thus, has a strong impact on the radical pool. Steam promotes the formation of* $\mathrm{HO_2}$ *and simultaneously decreases the concentration of* H *radicals, impairing the laminar burning velocity. By setting all third-body efficiencies of steam to zero an ideal diluent behavior was achieved emphasizing that the high third-body efficiency of water is the dominant chemical effect. In addition, the effect of steam dilution on self-ignition events was evaluated. In contrast to the computations of auto-ignition processes of hydrogen-oxygen flames employing an ideal diluent showed that the ignition event primarily depends on the initial temperature rather than on the level of dilution. The contrary was observed when using steam. As previously mentioned steam shifts the heat release peak towards higher temperatures, and thus, prolongates the ignition time delay. This stems from the effect of steam on the radical pool.*

Furthermore, the cooling effect of steam on the adiabatic flame temperature was presented. It was shown, that the addition of steam significantly lowers the adiabatic flame temperature. Additionally, steam reduces the laminar burning velocity and thus, allows for the safe operation of gas turbines with hydrogen. These effects also allow for the retrofit of current gas turbine designs for the combustion of pure hydrogen and hydrogen-rich fuels.

6

Chemiluminescence

Gazing at flames has probably been enthralling for humans since the first flames were discovered. Driven by scientific curiosity people try to explain the combustion phenomena ever since. Precursor scientific attempts lead to concepts such as phlogiston theory. This theory was presented by Becher (1669) and attempts to explain combustion processes with the release of a fire-like element from the combustible bodies, a first attempt to explain what is today known as oxidation. However, long time later this gave birth to the modern field of flame spectroscopy. Hydrogen flames with air are practically non-luminous for the human eye. However, impurities such as sulfur, even in very small quantities, cause the flame to shimmer in a blue-violet tone; for premixed flames this may manifest in a bluish flame color close to the invisible spectrum. The only radiation from a pure hydrogen flame is in the OH band (Gaydon, 1974). Orange flickers can be related to a contamination with sodium or calcium. In contrast to hydrogen-air flames, premixed hydrogen oxygen flames do give a strong visible emission with a bluish white core and an orange to red mantle, as reported by Gaydon (1974). In addition, a yellow-greenish flame tip may be observed when a hydrogen-oxygen flame comes in contact with surrounding air and is due to the reaction of nitric oxides reacting with free oxygen atoms.

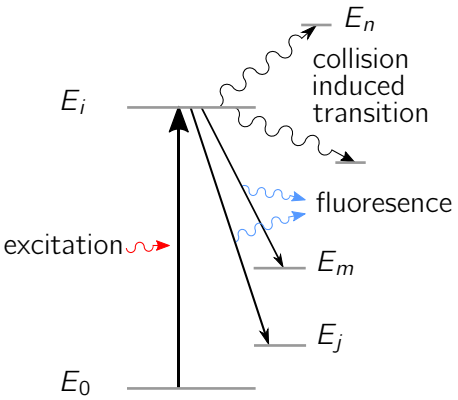

Fig. 6.1: Radiative and collision induced decay channels of an exited species.

Besides the fascinating visual effects, the light emitted from flames (*chemiluminescence*) allows for deeper understanding of combustion fundamentals. Chemiluminescence occurs due to chemical excitation and is found in the visible and ultra-violet band of flame spectra. Pioneering work on flame spectroscopy has been done by Gaydon (1974) reporting that the four major electronically excited molecules emitters in hydrocarbon flames are OH^*, CH^*, C_2^* and CO_2^*. For higher carbons, such as diesel, broader emission bands were identified and could be attributed to excited species of CO_2^*, CHO^* or $\mathrm{CH}_2\mathrm{O}^*$ as reported by Mancaruso et al. (2011).

In the reaction zone, the electronically excited species are formed from the energetic intermediate ground species. These species are highly reactive and only of a short lifetime. By releasing their energy they fall either back to the ground state or lower excited state. This emits radiation in form of light ($h\nu$) and is denoted as chemiluminescence when luminescence is caused by chemical excitation. This process is illustrated in Figure 6.1. The emitted signal rather depends on the composition than on the temperature (De Leo et al., 2007). Additionally, the excited molecules are susceptible to collisional quenching. This quenching effect is caused by collision with another molecule and results in a return of the excited molecule to a lower state and the excess energy is transferred into translational energy of the surrounding molecules. Of course an exited species can also chemically interact with another molecule.

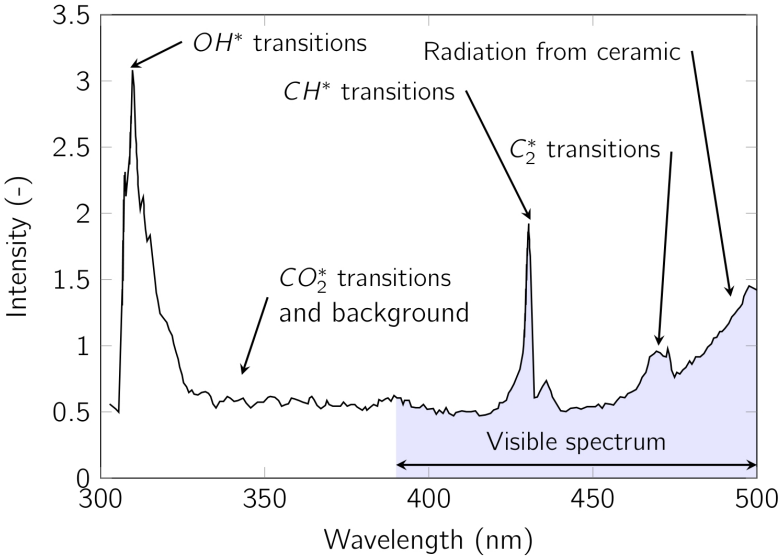

Figure 6.2: Spectral wavelength of a hydrocarbon-air flat-flame burner. Source: Haber et al., 2003

A typical spectrum of a simple flat burner hydrocarbon flame is depicted in Figure 6.2. The OH^* radical transition results in a strong spectrum peak with a maximum at 309 nm. Except for OH^*, the most combustion products do not give strong emission peaks in the ultraviolet spectrum. In the visible spectrum other unstable species such as CH^* and C_2^* emit light in the visible spectrum. Due to the fact that the present work focuses on hydrogen flames, only the OH^* emissions are further considered. The ground state of OH^* is an inverted doublet state $(\mathrm{X}^2\Pi)$, while the higher state is the normal doublet Σ state $\mathrm{OH}^*(\mathrm{A}^2\Sigma^+)$. Even though two further excited states exist ($\mathrm{OH}^*(\mathrm{B}^2\Sigma^+) \rightarrow 420 - 600\mathrm{nm}$ & $\mathrm{OH}^*(\mathrm{C}^2\Sigma^+) \rightarrow 225 - 260\mathrm{nm}$), these bands cannot be identified with combustion processes. Thus, in the present work only $\mathrm{OH}^*(\mathrm{A}^2\Sigma^+ \rightarrow \mathrm{X}^2\Pi)$ is considered for OH^* chemiluminescence.

In combustion devices the usage of non-intrusive optical emissions from flames is of importance for operating industrial applications to avoid pollutions, increase the efficiency and control instabilities inside the device. Due to the harsh environments in practical combustion applications, non-intrusive optical techniques have been considered for online measurements. However, pressure and temperature resistant optical accesses are costly, may affect the efficiency (i.e.,

heat loss), need further active illumination (e.g., scattering, fluorescence), and can impair structural integrity of the device, which made them unattractive. Chemiluminescence on the other hand is a passive technique and only simple optical sensors are necessary. It was shown by various studies (Hardalupas et al., 2004; Panoutsos et al., 2009) that the excited species such as OH^* and CH^* occur within the reaction zone and are correlated with the heat release zone, as well as the equivalence ratio. Thus, chemiluminescence is a potential marker to identify the heat release zone. However, Haber et al. (2003) investigated OH^* and CH^* in a Bunsen burner configuration. It was found that OH^* serves adequately as heat release marker, whereas CH^* fails as marker in methane flames. Among the vast body of literature, Nori et al. (2009) found the ratio of OH^* and CH^* to correlate with the local equivalence ratio in lean methane flames, but the correlation failed beyond certain conditions. Nonetheless, the ratio of OH^* and CH^* has been demonstrated to be the best option to monitor stoichiometry in methane flames, but is not suited to monitor syngas flames or flames with high hydrogen content, where the ratio OH^* and CO_2^* is seen as a promising alternative as revealed by García-Armingol et al. (2014). Nevertheless, for pure hydrogen flames OH^* is still seen as the best suited heat release marker as reported by Smith et al. (2005) and is widely used for detecting auto-ignition events (Schönborn et al., 2014).

6.1 Identification of a Suitable Chemiluminescence Subset

For the subsequent part of this thesis, a reaction mechanism is needed that describes the formation OH^* chemiluminescence in order to compare the LES simulations with according OH^* recordings from the experiments. In order to describe the chemiluminescent process, the knowledge of elementary reactions concerning the consumption and formation of excited species and the according reaction rates. The kinetics of an excited species X^* can be described by three different elementary reactions. First, there is the formation reaction:

$$\mathrm{A} + \mathrm{B} \Rightarrow \mathrm{C} + \mathrm{X}^* \tag{6.1}$$

with the subsequent consumption through radiative decay:

$$\mathrm{X}^* \Rightarrow \mathrm{X} + h\nu\,, \tag{6.2}$$

and the collisional quenching reaction:

$$\mathrm{X}^*(+M) \Rightarrow \mathrm{X}(+M) + \dot{Q}\uparrow, \tag{6.3}$$

where species M acts as an inert and $\dot{Q}\uparrow$ denotes the conversion into translation energy, and thus into heat.

Throughout the literature the proposed kinetic schemes are very similar. Table 6.1 presents the most common elementary reactions as they are found in most subsets. However, most publications detail the reactions $\mathrm{R2}$-$\mathrm{R14}$ to be reversible, which disagrees with the definition. Furthermore, most of the subsets are based on the findings of Tamura et al. (1998) who revealed most of the collisional quenching reactions ($\mathrm{R5}$ to $\mathrm{R14}$ in Table 6.1) for low pressure hydrocarbon flames. To identify and validate a chemiluminescence subset, several candidates are chosen and their respective performance is compared with experimental data from the literature. Out of several mechanisms five candidates are selected. The first one was reported by Smith et al. (2002) and developed for low pressure methane-air-flames. The rate constants for OH^* and CH^*were determined using recorded chemiluminescence images and calibrated against Rayleigh scattering. In 2005 Smith updated the rate constants and recommended new constants for $\mathrm{R1}$ and $\mathrm{R2}$ (Smith et al., 2005). These recommendations were included in the subset. The second scheme was proposed by Hall et al. (2006a). This scheme was derived from high temperature shock tube measurements at atmospheric pressure for various fuel blends (e.g., hydrogen-oxygen-argon). 2009 Nori presented a subset for the CH^* chemiluminescence for combustion diagnostic purposes, which were experimentally validated with premixed methane-air and Jet-A-air flames. This model incorporates of course an OH^* chemiluminescence subset. Panoutsos et al. (2009) evaluated equivalence ratio measurements of premixed and non-premixed methane-air flames. The last used scheme was developed by Kathrotia et al. (2010) especially for hydrogen combustion systems. This mechanism is also included in the standard version of Kéromnès hydrogen mechanism (Kéromnès et al., 2013). For hydrogen configurations OH^* production is considered to be mainly formed by the reaction of atomic H and O and a third-body collision partner, as suggested by Gaydon (1974):

Tab. 6.1: Elementary OH^* chemiluminescence reactions. h is the Planck constant and ν is the wavelength of chemiluminescent emission.

#	Equation		
$R1$	$H + O\,(+M)$	$\rightleftharpoons$	$OH^*\,(+M)$
$R2$	$OH + OH + H$	$\rightarrow$	$OH^* + H_2O$
$R3$	OH^*	$\rightarrow$	$OH + h\nu$
$R5$	$OH^* + AR$	$\rightarrow$	$OH + AR$
$R6$	$OH^* + CO$	$\rightarrow$	$OH + CO$
$R7$	$OH^* + CO_2$	$\rightarrow$	$OH + CO_2$
$R8$	$OH^* + CH_4$	$\rightarrow$	$OH + CH_4$
$R9$	$OH^* + H$	$\rightarrow$	$OH + H$
$R10$	$OH^* + H_2$	$\rightarrow$	$OH + H_2$
$R11$	$OH^* + H_2O$	$\rightarrow$	$OH + H_2O$
$R12$	$OH^* + O$	$\rightarrow$	$OH + O$
$R13$	$OH^* + O_2$	$\rightarrow$	$OH + O_2$
$R14$	$OH^* + OH$	$\rightarrow$	$OH + OH$

$$\mathrm{H + O\,(+M)} \;\rightarrow\; \mathrm{OH^*\,(+M)} \tag{6.4}$$

This reaction is reported to be not only important for hydrogen flames, but also for methane flames (García-Armingol et al., 2014). The coefficients for this particular reaction is listed for the different subsets in Table 6.2. The reaction rates are calculated from the coefficients in Table 6.2 employing an Arrhenius expression and plotted as a function of the inverse temperature in Figure 6.3. The rates differ by almost two orders of magnitude. Another important difference between the models is the assigned activation energy E_a, which directly impacts the temperature dependence. For the subsets of Panoutsos and Smith a zero activation energy results in a constant rate for over temperature ranges, proofing a temperature independent behavior. On

the other hand, a monotonic decrease of the rate towards lower temperatures can be seen for the subsets with a non-zero activation energy. However, the activation energies are not very high, implying a weak temperature dependence.

Table 6.2: Reaction kinetics coefficients of reaction R1 ($\mathrm{H + O\,(+M)} \rightarrow \mathrm{OH^*\,(+M)}$) for different subsets. $k = AT^n \exp\left(-E_a/RT\right)$

Subset	A ($\mathrm{cm^3}$,mol,s)	n $(-)$	E_a (kJ/mol)
Hall	$3.10 \cdot 10^{14}$	0.0	23
Kathrotia	$1.50 \cdot 10^{13}$	0.0	25
Nori	$6.00 \cdot 10^{14}$	0.0	29
Panoutsos	$3.63 \cdot 10^{13}$	0.0	0.0
Smith	$5.45 \cdot 10^{12}$	0.0	0.0

The computations are conducted with a zero-dimensional reactor as presented in section 3.2. In order to assess the respective performance of the $\mathrm{OH^*}$ schemes, the baseline reaction mechanisms Burke, Kéromnès, and the GRI mechanism are used and extended by the $\mathrm{OH^*}$ subsets. Petersen et al. (2003) performed several shock tube experiments concerning $\mathrm{OH^*}$ formation in $\mathrm{H_2}$-$\mathrm{O_2}$ mixtures with high levels of Ar dilution to re-evaluate the formation rates of $\mathrm{OH^*}$. Figure 6.4(a) depicts the normalized $\mathrm{OH^*}$ intensity from chemiluminescence recordings at constant pressure and optical settings as a function of the temperature. For comparison the computed peak normalized $\mathrm{OH^*}$ concentrations are superimposed on the measurements. For all baseline mechanisms and all mixtures it is apparent that the subsets of Smith and Panoutsos show the closest agreement to the experiments over the whole temperature range.

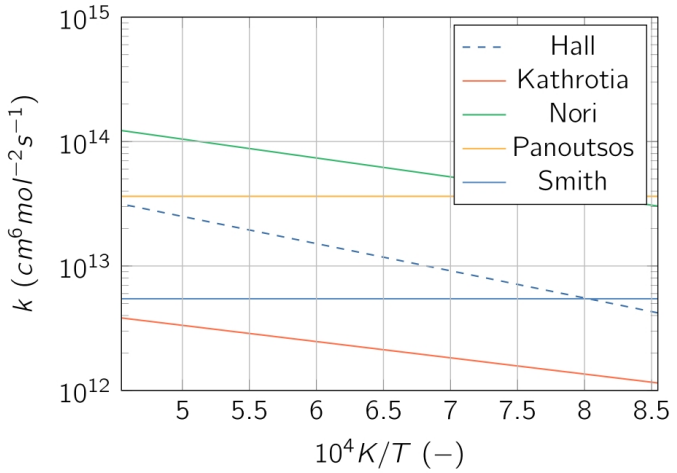

Figure 6.3: Reaction rates as a function of the inverse temperature for different $\mathrm{OH^*}$ subsets. Reaction rates are calculated with the Arrhenius expression ($k = AT^n \exp\left(-E_a/RT\right)$) for reaction R1: $\mathrm{H + O\,(+M)} \rightarrow \mathrm{OH^*\,(+M)}$

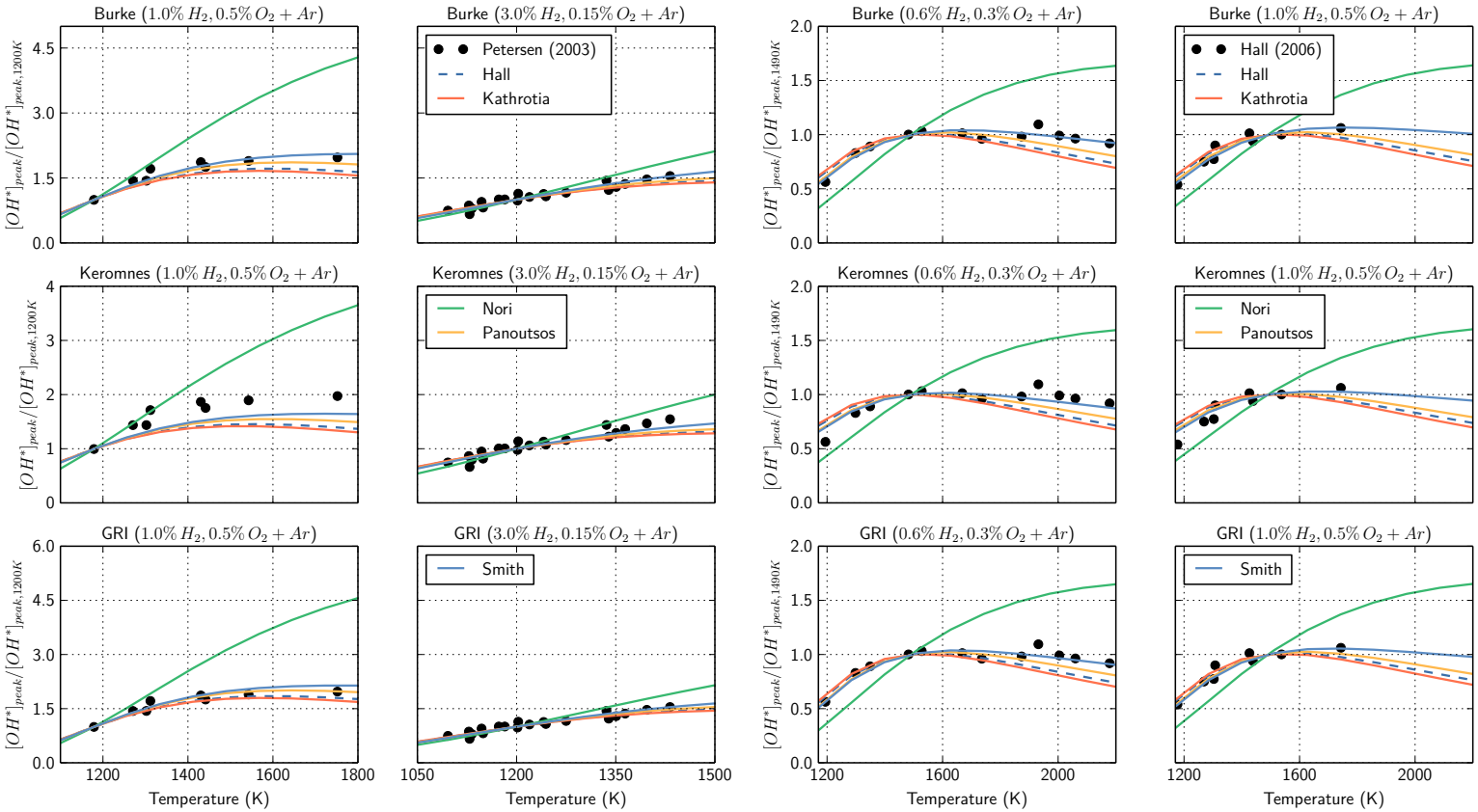

(a) Petersen (2003), $p = 1.15$ atm

(b) Hall (2006), $p = 0.96$ atm

Figure 6.4: Maximum OH^* concentration as a function of temperature at constant pressure for different experimental sets and computations. Experimental data according to Petersen et al. (2003) (left) and Hall et al. (2006b) (right).

It is also evident that Nori is not suited for these conditions, as it was not created for predicting auto-ignition processes and on the other hand it was made for higher carbons (Jet A) at lower temperatures (450 K) and higher pressures (up to 15 atm). Nori et al. (2009) stated that chemiluminescence is strongly pressure depended and also non-linear. However, the differences between the models become less significant with increasing hydrogen content. Unexpectedly, the results with the baseline mechanism of Kéromnès differ the most to the experiments, which however becomes less pronounced with increasing hydrogen content. Hall et al. (2006b) also conducted shock tube experiments with several mixtures. Among others H_2-O_2 mixtures with high Ar dilution ($> 98\%$) were used. A comparison between these measurements and the computations is shown in Figure 6.4(b). A similar trend is observed as for the set of Petersen. Again, the subset by Smith reproduces the measurements best, directly followed by Panoutsos, Hall, and Kathrotia. Nori's subset predicts the highest differences. Overall, the differences to the measurements are higher compared to the computations of the Petersen configuration (Figure 6.4(a)). This is due to the higher oxygen content which yields higher temperatures, and thus a stronger impact of the temperature dependence.

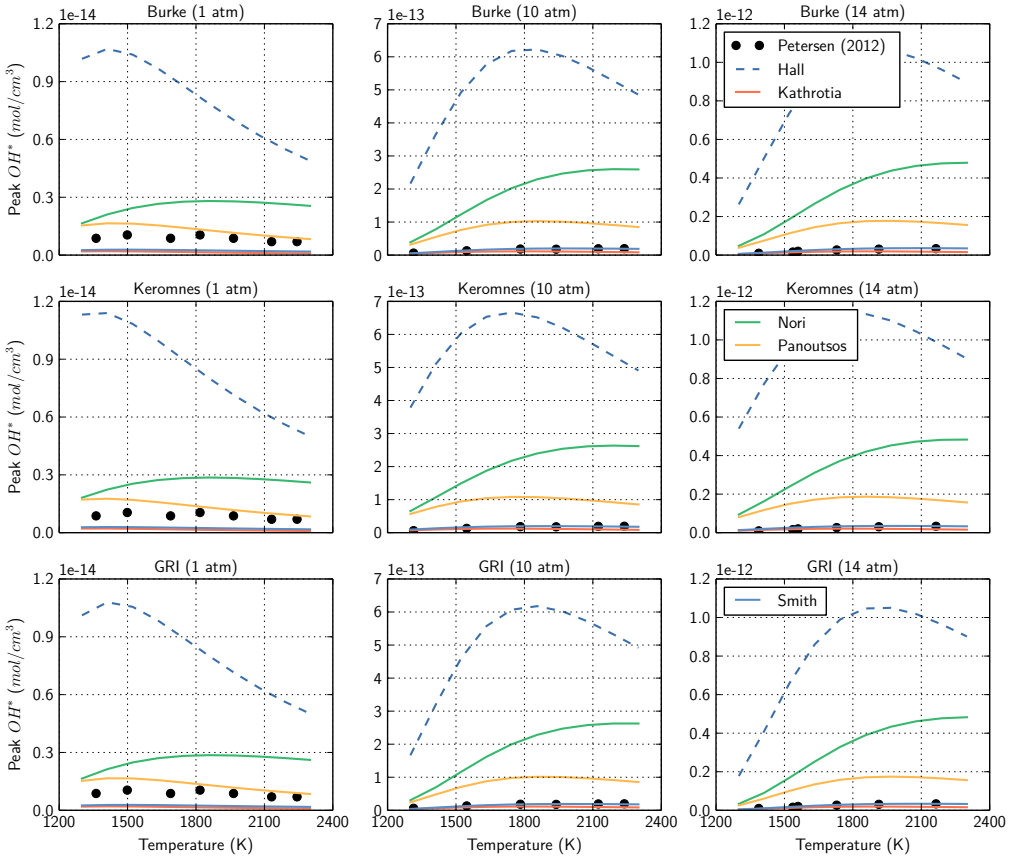

Figure 6.5: Comparison of OH* mechanism and data at three different pressures ($1\%H_2, 0.5\%O_2, 98.5\%Ar$). Experimental data according to Petersen et al. (2012).

Petersen et al. (2012) also performed shock tube experiments in highly diluted mixtures

of H_2-O_2-Ar/N_2 but at a wide range of pressures (up to 15 atm) to evaluate their kinetic model. They reported that at elevated pressures their currently used reaction rate of OH^* significantly over predicts the amount of formed OH^*. However, an explanation was not given. The results of the computations at elevated pressure are depicted in Figure 6.5. As can be seen, Panoutsos' mechanism is close to the experiments at atmospheric conditions. With increasing pressure the subsets clearly overpredict the formation of OH^*, whereas the subsets of Kathrotia and Smith are well in line with the experiments. The growth of the OH^* concentration with increasing pressure is reproduced by all subsets. However, the subsets of Hall, Nori and Panoutsos overpredict the measurements significantly. This behavior cannot be attributed to the temperature dependence, since representatives of subsets with and without non-zero activation energy overestimate the OH^* concentration. The reason lies in the third-body efficiencies of reaction $R1$. With increasing pressure also the probability increases that molecules collide. Except for the Smith and Kathrotia subset, no subset exhibits distinguished third-body efficiencies for reaction $R1$, especially not for H_2O. As shown in Chapter 5 H_2O is of great importance in hydrogen combustion due to its high third-body efficiency. In this case with increasing pressure the H_2O production impairs reaction $R1$ through collisional effects.

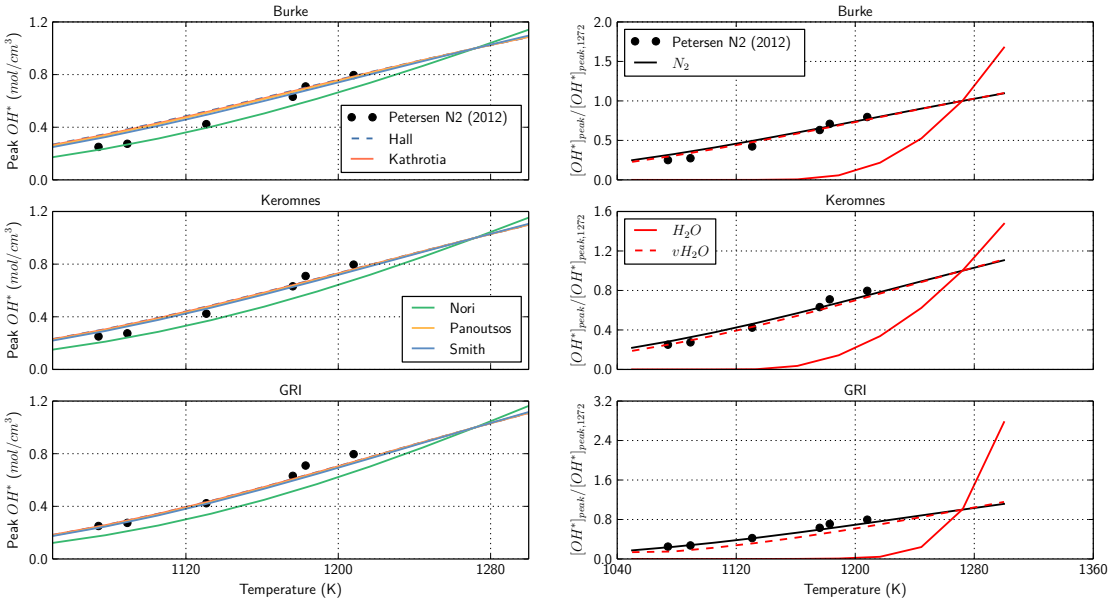

(a) Comparison of subsets. $(2\%H_2, 1.0\%O_2, 97.0\%N2)$

(b) Replacement of nitrogen through other diluents (X = $N2, vH_2O, vH_2O$) of steam. $(2\%H_2, 1.0\%O_2, 97.0\%X)$

Figure 6.6: Comparison of OH^* concentration with N_2 dilution. For the computations N_2 was also replaced with water (H_2O) and virtual water (vH_2O). Experimental data according to Petersen et al. (2012).

To the author's knowledge, there is currently no data on quantitative OH^* concentration measurements with steam dilution available in the literature. This would allow to determine the influence of steam on the OH^* formation, and thus the applicability as combustion diagnostic device in Humid Gas Turbine (HGT)s. Nonetheless, Petersen et al. (2012) also conducted

experiments with nitrogen dilution ($2\%\mathrm{H}_2, 1.0\%\mathrm{O}_2, 97.0\%\mathrm{N2}$) at 1.3 atm. As mentioned in Chapter 5, nitrogen and water feature a similar thermal diffusivity, and thus a similar ability to conduct thermal energy relative to its ability to store it. In order to investigate the influence of water on the combustion process, the nitrogen was replaced by virtual water ($\mathrm{vH_2O}$) and steam ($\mathrm{H_2O}$). First of all, the subsets are compared regarding their performance in reproducing nitrogen diluted conditions, as shown in Figure 6.6(a). Obviously, all subsets agree well with the measurements, except for Nori. Therefore, the subset of Smith is used to further assess the influence of steam. Replacing nitrogen with virtual water, a completely inert species, results in collapsing lines as detailed in Figure 6.6(b). This stems from the almost equal thermal diffusivities. By the replacement of nitrogen through water a significant lower $\mathrm{OH^*}$ concentration can be detected up to a temperature of $\approx$ 1180 K, which is caused by the initially higher amount of $\mathrm{H_2O}$ impairing $\mathrm{R1}$ through third-body effects. For temperatures above $\approx$ 1180 K the $\mathrm{OH^*}$ formation increases exponentially clearly showing that the forward pathway of $\mathrm{R1}$ becomes more dominant. Nonetheless, without accompanying measurements this result cannot be validated. Even though the thermal diffusivity is similar between both diluents, the ratio of thermal diffusivity to mass diffusivity (*Lewis* number) is known to be not unity for hydrogen flames. Thus, a replacement of one diluent through another always bears the risk of neglecting the effect of flame stretch. However, this effect is supposed to be low for very lean hydrogen flames according to Bouvet et al. (2013).

With respect to the findings of this section, it is suggested to use the $\mathrm{OH^*}$ chemiluminescence subset of Smith et al. (2002) with the updated coefficients from 2005 (Smith et al., 2005), because this scheme showed the overall best performance. Thus, this reaction subset in combination with Burke's hydrogen mechanism is used for the further investigations.

6.2 Chemiluminescence as a Heat Release Marker

Since it was discovered that the radiation intensity increases linearly with the fuel flow rate in laminar and low-turbulent flames (Clark, 1958), it was assumed that the emissions of chemiluminescence serve as a marker for the heat release rate. However, the potential link between the heat release and chemiluminescence emissions fails in highly turbulent flames or in conditions with extreme local strain where chemiluminescence can approach zero emissions without flame extinction (Najm et al., 1998).

To the author's knowledge, there is currently no literature available concerning the evaluation of chemiluminescence in highly steam diluted configurations. Hence, a numerical experiment is performed to assess the differences between the locations of the heat release and excited species ($\mathrm{OH^*}$) peak by employing a premixed laminar hydrogen-air flame under the influence of several steam dilution levels. Therefore, a freely propagating flame configuration, as presented in section 3.1.2, is used in combination with Burke's reaction scheme and the $\mathrm{OH^*}$ subset of Smith.

Two different configurations are performed. For the first configuration the steam content ($\Omega = 0.0 \cdots 0.5$) is varied, whereas the adiabatic flame temperature is kept constant $T_{ad} =$ 1573 K. For the second experiment the equivalence ratio is varied at an initial temperature of $T_u = 300$ K for constant steam levels. Both configurations are conducted for three pressure levels ($p = 1, 10, 20$ atm). The results for both studies are presented in Figure 6.7. The left figure illustrates the displacement length Δz as a function of the steam content Ω for different

pressure levels. The displacement length is defined as the spatial difference between the location of the heat release peak and the peak in OH^* concentration. In the absence of steam the displacement is minimal. With increasing pressure the displacement decreases, whereas the steam concentration has an adverse effect on the displacement effect. The maximum displacement is reached at the maximum of the steam concentration; however, the deviation is with 0.27 mm rather small. The right figure (Figure 6.7(b)) presents the displacement length Δz as a function of the equivalence ratio. Evidently, the displacement length reaches a maximum for lean conditions near the extinction limit. With rising equivalence ratio and thus with higher adiabatic temperatures the displacement length decreases and converges to significantly lower values. Increasing the steam content displaces the slope towards higher equivalence ratios and values, indicating a shift of the preheat zone caused by steam. The pressure has an adverse effect on the displacement length and is in line with the previous findings. Obviously, the temperature effects have a significant higher effect on the displacement length, which can be in the range of millimeters for very lean mixtures. Nevertheless, for operating conditions in technical applications the spatial differences in OH^* from the peak heat release location are relatively small compared to the resolution of the measurement devices implying the potential of sensing local equivalence ratios and heat release by employing OH^* emissions.

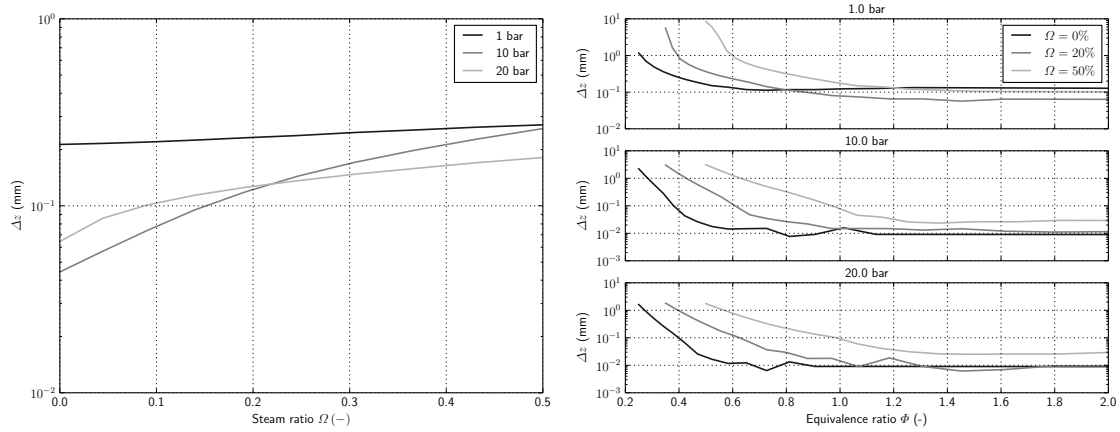

(a) Displacement length Δz as a function of the steam content Ω.

(b) Displacement length Δz as a function of the equivalence ratio Φ.

Figure 6.7: Spatial difference (Δz) between heat release and excited species (OH^*) for varying conditions. Left: constant adiabatic temperature $T_{ad} = 1573\,\mathrm{K}$, Right: constant steam level.

Chemiluminescence of excited species are widely used as indicator for heat release and as measure for the local equivalence ratio. For the subsequent part of this thesis a reaction mechanism is needed that allows for prediction of OH^* *chemiluminescence in order to compare the LES simulations with according* OH^* *recordings from the experiments. Therefore, five promising candidates (Hall, Kathrotia, Nori, Panoutsos, Smith) were identified and concatenated with detailed hydrogen reaction mechanisms (Burke, Kéromnès, GRI). While analyzing the* OH^* *subsets it became apparent that these sets mainly differ in the reaction coefficients for the* OH^* *formation reaction* ($\mathrm{R1: H + O\,(+M) \rightleftharpoons OH^*\,(+M)}$), *whereas the collision quenching reactions are throughout implemented as proposed by*

Tamura et al. (1998). All subsets were tested against in the literature available shock tube measurements of highly diluted hydrogen-air flames.
It was observed that for the highly argon diluted cases the subset of Nori predicts the highest differences. Even though the subset of Smith in combination with Burke's detailed reaction scheme shows the closest agreement to the experimental data, the other schemes also predict reasonable results. In addition, the schemes were also tested against the recently published measurements of Petersen et al. (2012). Petersen performed shock tube experiments in highly diluted mixtures of $\mathrm{H_2}$-$\mathrm{O_2}$-$\mathrm{Ar}/\mathrm{N_2}$ *but at a wide range of pressures (up to 15 atm). It was found that at ambient pressure Panoutsos' mechanism is closest to the experiments. With increasing pressure the subsets clearly overpredict the formation of* OH^**, except for the subsets of Kathrotia and Smith, both agreed well with the experiments. This overprediction stems from third-body collisions with* $\mathrm{H_2O}$ *which impairs the production of* OH^* *and shifts the equilibrium of reaction* $\mathrm{R1}$ *towards the reverse reaction side. Except for Kathrotia and Smith, no subset features distinguished third-body efficiencies for reaction* $\mathrm{R1}$*, hence explaining the overprediction.*
To assess the influence of steam on the formation of OH^**, experimental data concerning steam dilution would be necessary. However, Petersen et al. (2012) also conducted experiments with nitrogen dilution. Since nitrogen and steam share a similar thermal diffusivity, nitrogen was replaced by steam and virtual (inert) steam. All subsets were more or less able to satisfactorily reproduce the experimental results when employing nitrogen. Thus, the mechanism of Smith was used while nitrogen was surrogated. It was found that the results of the nitrogen and inert steam computations collapse, whereas the replacement with steam leads to significant different behavior. The presence of steam impairs the production of* OH^* *through third-body effects over a wide range of temperature. For temperatures above* $\approx 1180\,\mathrm{K}$ *the vitiation becomes less pronounced and the equilibrium of reaction* $\mathrm{R1}$ *is shifted towards the production of* OH^* *leading to substantially higher* OH^* *concentrations as is the case for nitrogen.*
In conclusion, the benchmark of the different OH^* *chemiluminescence subsets revealed that the combination of Burke's (Burke et al., 2012) detailed reaction scheme in combination with Smith's* OH^* *subset (Smith et al., 2002; Smith et al., 2005) was the best suited combination for predicting highly diluted hydrogen flames. Therefore, the assembled reaction mechanism as listed in Appendix A (p. 165) is used for the LES in the second part.*
In addition, the potential of OH^* *for sensing the heat release was evaluated. Therefore, numerical experiments were conducted. It was found that at gas turbine conditions the addition of steam results in a growth of the spatial difference between the heat release and* OH^* *concentration peak, whereas the pressure has an opposing effect. At very lean conditions the displacement significantly increases. However, these conditions are close to flame extinction and not present in technical applications. In technical applications the differences in* OH^* *from the peak heat release location are in the range of a tenth of a millimeter and thus small compared to the resolution of the measurement devices. Hence, it is stated that* OH^* *emissions bear a high potential for online sensing local equivalence ratios and heat release.*

7

Nitrogen Oxide Emissions

Nitrogen oxides ($\mathrm{NO_x}$) is a generic term for a group of highly reactive gases, containing nitrogen and oxygen in various amounts, such as nitrogen monoxide NO, nitrogen dioxide $\mathrm{NO_2}$ and nitrous oxide $\mathrm{N_2O}$. These molecules are formed during combustion processes and their lifespan ranges up to several days. Although there exist various different compounds of nitrogen and oxygen, mainly NO and $\mathrm{NO_2}$ are formed as combustion products in gas turbine processes. As an important cellular signaling molecule NO is naturally found in all mammals and is non-toxic by itself, it rapidly oxidizes in air to nitrogen dioxide. Nitrogen dioxide on the other hand dissolves in water forming nitric acid. In a moist atmosphere this results in acid rain, which is known to damage entire ecosystems. Additionally, $\mathrm{NO_2}$ reacts in air with oxygen to produce ozone and is believed to aggravate asthmatic conditions. Moreover, in the higher atmosphere it contributes to the ozone depletion. Therefore, predicting and controlling the formation of nitrogen oxides is crucial for the air quality in the lower, but also in the higher atmosphere.

The main purpose of this chapter is to identify a reaction subset which is capable of predicting $\mathrm{NO_x}$ formation in diluted hydrogen flames. A detailed analysis of the $\mathrm{NO_x}$ formation pathways with high amounts of steam dilution and their implications on the combustion process is beyond the scope of this thesis and therefore only briefly discussed. The impact of steam on the production of $\mathrm{NO_x}$ has been discussed in detail by Göke (2012), however for turbulent flames.

Skottene et al. (2007) conducted counter-flow flame measurements with highly nitrogen diluted flames to benchmark four reaction schemes. The flames were laminar with a Reynolds number of $\mathrm{Re} \approx 400$ at ambient pressure. As reaction mechanisms the kinetic mechanism of Glarborg et al. (1994) and the University of San Diego UCSD (2014) were used, both in a standalone version and also with the $\mathrm{H_2}$-$\mathrm{O_2}$ subsets replaced with hydrogen model of Li et al. (2004b). The best results were achieved with the San Diego mechanism. Based on the findings of Skottene, three subsets are selected in order to identify a suitable reaction scheme for highly diluted hydrogen flames. All three subsets are concatenated with the updated version of Li's mechanism, namely Burke's (Burke et al., 2012) detailed reaction scheme. Due to the poor performance in the previous benchmarks only the nitrogen part of the *Creck* mechanism (Frassoldati et al., 2007) is used. The subset consists of 134 reactions and 18 species. As a second candidate the scheme of Glarborg et al. (1994) is employed containing 96 reactions and 13 species. The third candidate is the San Diego (ver. 2004-12-09) nitrogen subset UCSD

(2014), which incorporates 52 reactions and 15 species. Additionally, the comprehensive GRI 3.0 (Smith et al., 2000) reaction mechanism serves as a reference (325 reactions, 53 species).

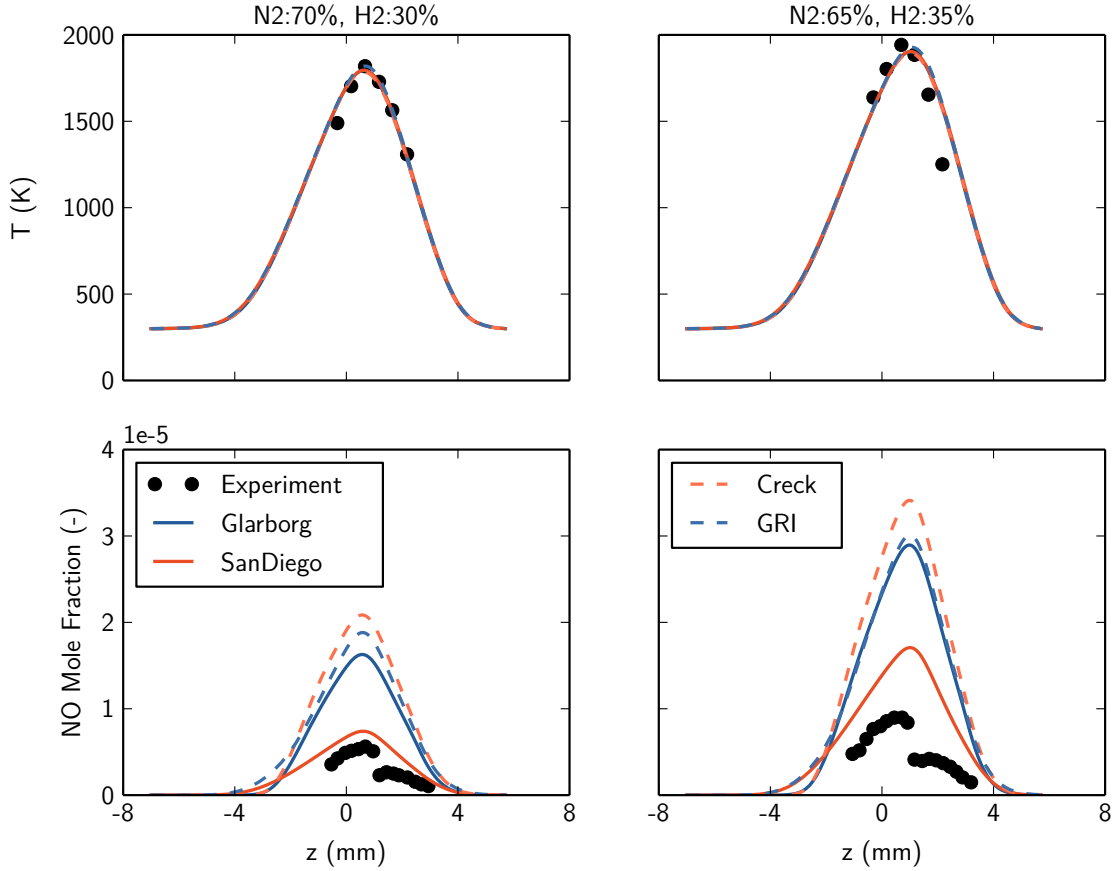

Figure 7.1: Validation of computed laminar hydrogen counter flames with high nitrogen dilution. Numerical results (lines) from four different chemical mechanisms compared with experimental data (symbols). Top row: temperature distribution, bottom row: NO concentration. Left column: fuel composition of $70\%N_2 - 30\%H_2$ and $\Phi = 0.9$; right column: fuel composition of $65\%N_2 - 35\%H_2$ and $\Phi = 1.0$. Experimental data according to Skottene et al. (2007).

For the computations a non-premixed counter-flame configuration, as presented in section 3.1.2, is used and the grid was adaptively refined until convergence was achieved. The numerical results are compared with experimental data in Figure 7.1 where the temperature and the mole fraction of NO are given as a function of the distance of the flame center. Two mixtures with a fuel composition of $70\%N_2 - 30\%H_2$, and $65\%N_2 - 35\%H_2$ in combination with air at 300 K are used. This results in a equivalence ratio of $\Phi = 0.9$ for the case with 70% N_2 and 30% H_2, and respectively in $\Phi = 1.0$ for the other case. In both cases the temperature profiles are well reproduced by all mechanisms. This was not unexpected since the Creck, Glarborg, and San Diego share the same hydrogen subset. For the higher diluted case (70% N_2) only the San Diego scheme is close to the experimental values for the NO mole fraction. The other mechanisms overpredict the mole fractions significantly. With rising hydrogen content

the deviation from the predictions to the experiments grow further, possibly an effect of the increased flame temperature. Skottene et al. (2007) also observed an overprediction of the mole concentrations and assumed higher total values of NO due to the removal of NO by chemical reactions on the probe walls during sampling. However, NO measurements are far from trivial and thus, it is assumed that the San Diego mechanism is in line with the experimental observations.

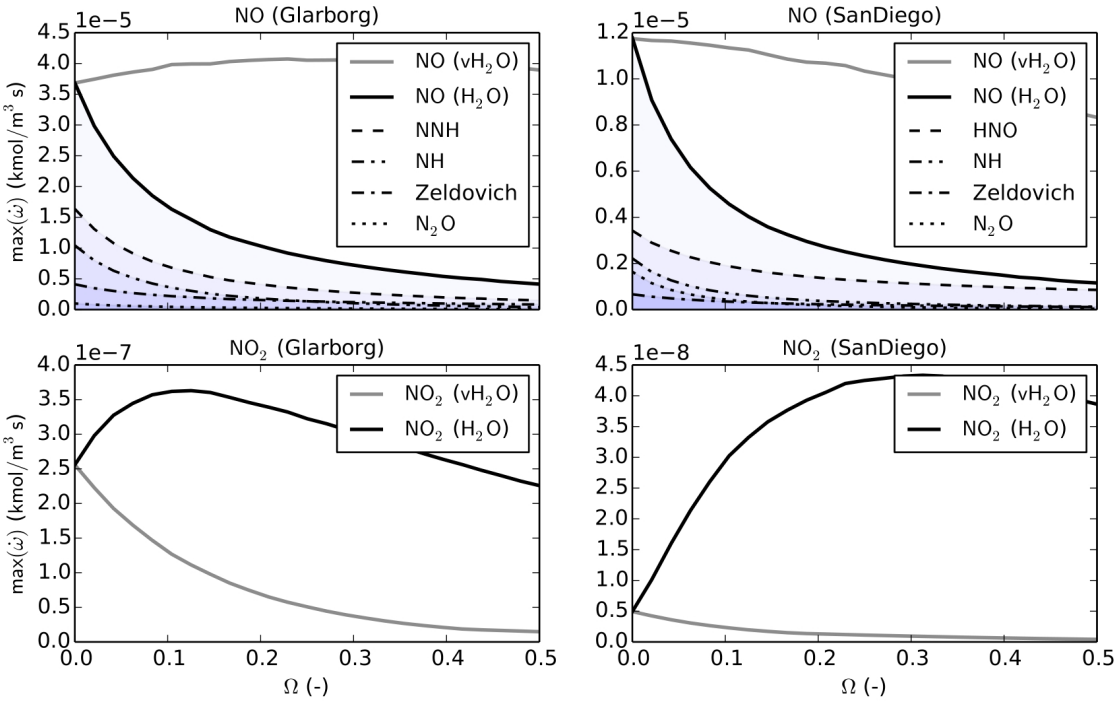

Figure 7.2: Mechanisms of $\mathrm{NO_x}$ formation in a hydrogen-air-steam flame as a function of the steam content Ω at a constant adiabatic flame temperature $T_u = 1573\,\mathrm{K}$. Please note the different rate scalings.

Even though a detailed analysis is not the intention of this chapter, a numerical experiment is conducted to evaluate the influence of steam on the $\mathrm{NO_x}$ formation process. Therefore, a one-dimensional free flame configuration is used. While the steam content is varied between a state without steam and a state with high steam dilution ($\Omega = 0.0 \cdots 0.5$), the adiabatic flame temperature is kept constant $T_u = 1573\,\mathrm{K} \pm 1\,\mathrm{K}$. Figure 7.2 presents the maximum NO and $\mathrm{NO_2}$ production rates as a function of the steam content Ω for the two reaction schemes. The solid black line represents the overall production rate of NO. The production rate is further distinguished in formation mechanisms:

1. Zeldovich:
   The thermal NO formation was first proposed by Zeldovich (1946) and is usually the dominating pathway at high temperatures and long residence times. It consists of the reactions:

$$\mathrm{O} + \mathrm{N_2} \rightleftharpoons \mathrm{NO} + \mathrm{N} \tag{7.1}$$
$$\mathrm{N} + \mathrm{O_2} \rightleftharpoons \mathrm{NO} + \mathrm{O} \tag{7.2}$$
$$\mathrm{N} + \mathrm{OH} \rightleftharpoons \mathrm{NO} + \mathrm{H} \tag{7.3}$$

The first step is rate limiting and has a high activation energy. Thus, the thermal mechanism requires high temperatures to be efficient.

2. NH and $\mathrm{N_2O}$:
Another pathway to NO proceeds through nitrous oxide $\mathrm{N_2O}$ and is initiated by:

$$\mathrm{O} + \mathrm{N_2} + \mathrm{M} \rightleftharpoons \mathrm{N_2O} + \mathrm{M} \tag{7.4}$$
$$\mathrm{N_2O} + \mathrm{O} \rightleftharpoons \mathrm{NO} + \mathrm{NO} \tag{7.5}$$

which is followed by

$$\mathrm{N_2O} + \mathrm{H} \rightleftharpoons \mathrm{NH} + \mathrm{NO}. \tag{7.6}$$

At gas turbine conditions these mechanism compete with thermal NO formation and become the major source of NO.

3. NNH:
The NNH pathway is similar to the nitrous oxide mechanism:

$$\mathrm{H} + \mathrm{N_2} \rightleftharpoons \mathrm{NNH} \tag{7.7}$$
$$\mathrm{NNH} + \mathrm{O} \rightleftharpoons \mathrm{NH} + \mathrm{NO} \tag{7.8}$$
$$\mathrm{NNH} + \mathrm{O} \rightleftharpoons \mathrm{N_2O} + \mathrm{H} \tag{7.9}$$

The NNH radical is only of short lifespan and quickly equilibrated at high temperatures. Although most of NNH is of low stability, it may contribute significantly on the formation of NO.

Obviously, steam affects all NO formation mechanisms similarly, resulting in an exponential decrease of the formation rates. At the present conditions the NNH pathway has a significant influence on the formation of NO and is thus in line with the findings of Konnov et al. (2001). Konnov investigated hydrogen-air flames in a well-stirred reactor and reported that the NNH mechanism is of high importance over the complete temperature range ($1500 - 2200\,\mathrm{K}$). For both subsets the NO formation rates show the same trend; however, Glarborg predicts almost three times higher values. Due to the fact that the Glarborg mechanism also overpredicts the measurements of Skottene et al. (2007), it is assumed that results predicted by the San Diego set are closer to reality. However, without according experiments a concluding answer cannot be given. In Figure 7.2 also simulations with virtual steam $\mathrm{vH_2O}$ are depicted as solid gray

line. Whereas steam has a significant impairing influence on the NO formation, the overall production is less distinct. For the case of Glarborg the NO formation slightly increases from $\Omega \approx 0.25$ and decreases beyond this point again, whereas the predictions of the San Diego scheme the formation rate decreases monotonically. Figure 7.2 also illustrates the formation rates of $\mathrm{NO_2}$. The formation rates are two to three orders of magnitude lower as for NO and a contrary trend is observed. Whereas virtual steam ($\mathrm{vH_2O}$) has a decreasing influence on the formation rates steam ($\mathrm{H_2O}$) increases the production, reaches a maximum (Glarborg: $\Omega \approx 0.1$, San Diego: $\Omega \approx 0.3$), and decreases again.

Virtual steam can only interact as a third-body collision partner, whereas steam is involved in many reactions. To shed some light on the formation of NO, Figure 7.3 visualizes the formation pathways of NO for both subsets, as well as for dilution with steam ($\mathrm{H_2O}$) and virtual steam ($\mathrm{vH_2O}$). For all conditions the lower branch clearly shows the conversion of $\mathrm{N_2}$ via N to NO due to the Zeldovich mechanism. Another branch is present for both subsets and all conditions: the $\mathrm{N_2O}$ mechanism. In the presence of steam another branch becomes apparent, involving NH. Although the NH pathways is in the literature usually counted as part of the $\mathrm{N_2O}$ mechanism, steam seems to have a significant influence, that is not present for the inert steam. Thus, it can be stated that steam has a major impact on the formation pathways of NO. However, to explain in detail this effect further investigations with according laminar experiments are necessary. Nevertheless, it is shown that steam has a significantly decreasing effect on the formation of nitrogen oxides and thus, is a promising method to reduce these harmful emissions.

As mentioned before Göke (2012) investigated steam diluted flames with focus on the formation of emissions. He used a reactor network model in conjunction with the GRI 3.0 mechanism, to reproduce and forecast the experimental results of a turbulent swirl-stabilized flame. For a hydrogen flame configuration he observed that the $\mathrm{NO_x}$ formation is dominated by the NNH pathway for a dry hydrogen flame, due to a high H concentration. He also reported that with increasing steam content, all pathways are restrained, while the relative pathway contributions remain similar. This statement is in line with the here presented findings.

> *Nitrogen oxides are harmful to health and environment. Thus, the control and prediction of nitrogen oxides is crucial for protecting the air quality and health. Hence, the main purpose of this chapter was to identify a reaction subset which is capable of predicting* $\mathrm{NO_x}$ *formation in diluted hydrogen flames. Skottene et al. (2007) conducted counter-flow flame measurements which served as a reference. Four reaction schemes were benchmarked and the nitrogen oxide subset from the University of California in San Diego (UCSD, 2014) in combination with the detailed hydrogen mechanism of Burke (Burke et al., 2012) agreed best with the experimental data. Therefore, this assembly is recommended for simulating highly steam diluted flames with* $\mathrm{NO_x}$ *formation. However, the* $\mathrm{NO_x}$ *subset could only be validated for high degrees of nitrogen dilution. The complete combined reaction scheme as it is used for the LES, including Burke's reaction scheme, the* $\mathrm{OH^*}$ *chemiluminescence mechanism of Smith (Smith et al., 2002; Smith et al., 2005) and the San Diego* $\mathrm{NO_x}$ *subset is listed in Appendix A (p. 165).*
>
> *In addition, a numerical experiment was conducted to get an impression of the influence of steam on the formation of nitrogen monoxide, nitrogen dioxide, and nitrous oxide. It*

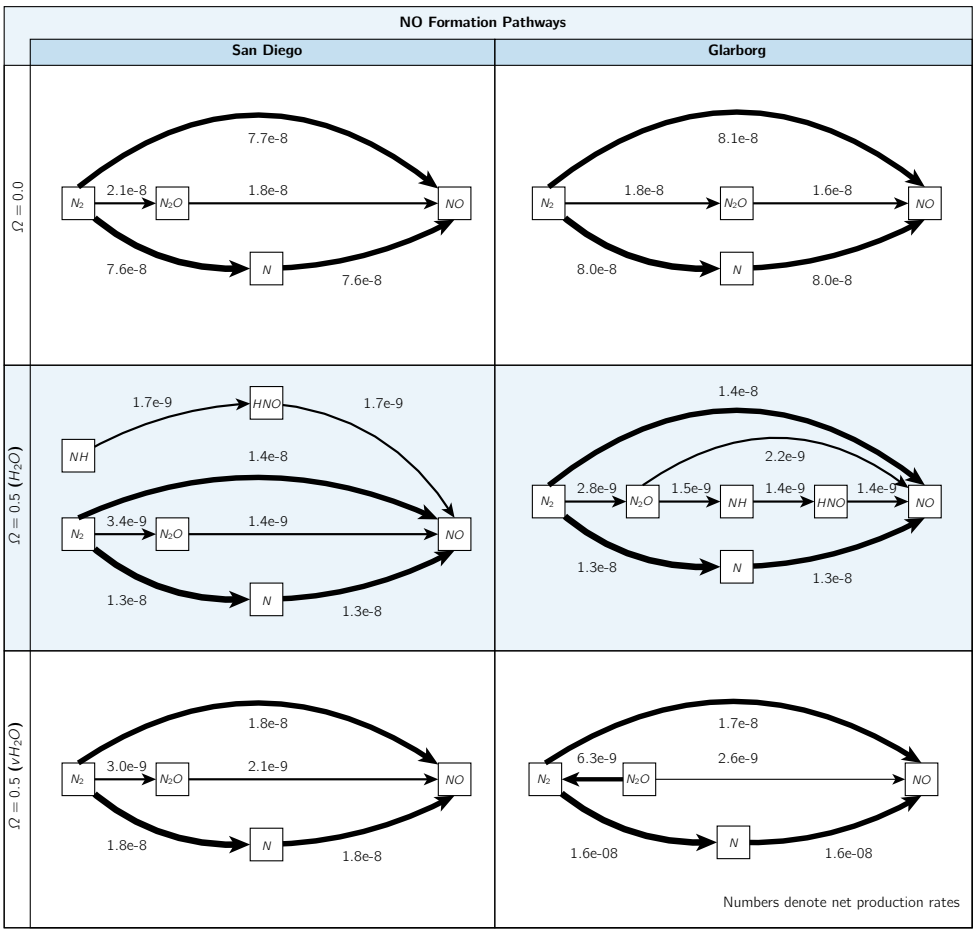

Figure 7.3: Visualization of the NO formation pathways.

was shown that steam has a significantly affects the formation of harmful emissions. Thus, steam reduces the production rates by more than a factor of 6. It was also found that steam alters the nitrous oxides pathway, especially NH *seems to play an important role. Overall, it is shown that steam has a significantly decreasing effect on the formation of nitrogen oxides and thus is a promising method to reduce harmful emissions*

8

Summary of the Laminar Flame Assessment

The first part of this thesis is dedicated to laminar flames and aims at two main aspects. The first purpose is identify an adequate reaction mechanism for steam diluted hydrogen oxidation at gas turbine conditions, for the Large Eddy Simulation (LES) of the subsequent part. The second purpose is to investigate the influence of steam on the combustion process and the implied consequences.

In order to identify an adequate oxidation mechanism several reaction mechanisms were benchmarked. Their respective performances were assessed based on laminar premixed flame calculations under dry and diluted conditions, for which experimentally determined flame speeds and ignition delay times are available. Olm et al. (2014) benchmarked the most important hydrogen mechanism that have been published within the last decade for a wide body of measurements available in the literature. The outcome was that the reaction scheme of Kéromnès was found to be the most accurate mechanism. Although Olm et al. (2014) considered a wide range of experimental conditions, he did not did not focus on steam diluted gas turbine conditions in particular, therefore the assessment was re-evaluated. Seven reaction mechanisms were included in the tests. In comparison with the experimental data for hydrogen-air-steam flames the reaction mechanisms of Kéromnès and Burke showed the best agreement, especially at high steam concentrations. Due to the fact that the flame thickness is of importance for most combustion modeling approaches (e.g., Large Eddy Simulation (LES)), it was assessed for the different reaction models and steam levels. Although all mechanisms showed a similar trend the differences between the models increased with increasing steam content. Nevertheless, the reaction schemes of Burke and Kéromnès predict the reasonable flame thicknesses, it is recommended to perform measurements for further validation. It is also noteworthy that all models predict a local maximum for the flame thickness near stoichiometric conditions. However, without according experiments it is not possible to exclude numerical artifacts as reasons for this effect. In a final step the candidates were also compared to auto-ignition time delay measurements. It was found that the schemes are well in line with the experiments, except for the low-temperature regime for no and low steam dilution, where all models failed. According to the findings of the benchmarks, it is concluded that the mechanism of Burke and Kéromnès are the most suited schemes, for predicting combustion processes with dilution of high steam contents at gas turbine conditions. Thus, both schemes were used for the further

investigations.

The second purpose of this part was to investigate the influence of steam addition on the combustion process, in particular, on the effect on the laminar burning velocity and auto-ignition event. By assessing laminar premixed flames and simultaneously introducing an inert species with the same thermophysical properties as steam, it was shown that steam has a significant chemical effect that differs from ideal diluents. The one-dimensional hydrogen flame computations revealed that steam shift the preheat zone towards higher temperatures. Applying a sensitivity analysis in combination with an analysis of species concentration profiles, it was seen that the addition of steam mostly affects the third-body reaction ($H + O_2(+M) \rightleftharpoons HO_2(+M)$) leading to a shift of the preheat zone, and thus, has a strong impact on the radical pool. Steam promotes the formation of $\mathrm{HO_2}$ and simultaneously decreases the concentration of H radicals, impairing the laminar burning velocity. In addition it was proven that the high third-body efficiency of water is the dominant chemical effect, by setting all third-body efficiencies of steam to zero, and thus, achieving an ideal diluent behavior. The impact of steam on the preheat zone was also observed for self-ignition events. Computations of the auto-ignition processes of hydrogen-oxygen flames diluted with an inert species revealed that the ignition event primarily depends on the initial temperature rather than on the level of dilution. In contrast to that dilution with steam showed a shift of the ignition event towards higher temperatures, and thus, prolongates the ignition time delay. This effect can also be related to the impact of steam on the radical pool, and hence impairing the self-ignition process. In addition to the chemical effects impairing the reactivity, steam has also a cooling effect on the adiabatic flame temperature, due to the higher specific heat capacity. Thus, the flame temperature can be significantly reduced to achieve technical applicable gas turbine conditions.

In the combustion test rig $\mathrm{OH^*}$ chemiluminescence images are recorded in order to assess the flame shape and location. For the subsequent part of this thesis a reaction subset is needed that allowed for prediction of $\mathrm{OH^*}$ chemiluminescence, in order to compare the LES simulations with according $\mathrm{OH^*}$ recordings from the experiments. Therefore five promising candidates (Hall, Kathrotia, Nori, Panoutsos, Smith) were selected and compared to in the literature available shock tube measurements of highly diluted hydrogen-air flames. In conclusion the benchmark of the different $\mathrm{OH^*}$ chemiluminescence subsets revealed that the combination of Burke's (Burke et al., 2012) detailed hydrogen reaction scheme in combination with Smith's $\mathrm{OH^*}$ subset (Smith et al., 2002; Smith et al., 2005) is the best suited scheme for predicting highly diluted hydrogen flames.

Even though there is currently no experimental data available for validation purposes, the influence of steam on the formation of $\mathrm{OH^*}$ was also assessed. However, Petersen et al. (2012) also conducted experiments with nitrogen dilution. Since nitrogen and steam share a similar thermal diffusivity, nitrogen was replaced by steam and virtual (inert) steam. All subsets were more or less able to satisfactorily reproduce the experimental results when employing nitrogen. Thus, the mechanism of Smith was used while nitrogen was surrogated. It was found that the results of the nitrogen and inert steam computations collapse, whereas the replacement with steam leads to significant different behavior. The presence of steam impairs the production of $\mathrm{OH^*}$ through third-body effects over a wide range of temperature. For temperatures above $\approx 1180\,\mathrm{K}$ the vitiation becomes less pronounced and the equilibrium of reaction $\mathrm{H + O\,(+M)} \rightleftharpoons \mathrm{OH^*\,(+M)}$ is shifted towards the production of $\mathrm{OH^*}$ leading to

substantially higher OH^* concentrations as is the case for nitrogen.

Due to the fact that nitrogen oxides are harmful to health and environment the control and prediction of nitrogen oxides is of high importance. Therefore, four NO_x subsets were benchmarked and the subset from the University of California in San Diego (UCSD, 2014) showed the best agreement to the experimental data of Skottene et al. (2007). To get an impression of the influence of steam on th emission formation a numerical experiment was conducted. It was observed that steam significantly affects the formation of harmful emissions. It was also found that steam alters the nitrous oxides pathway, especially NH seems to play an important role. Overall it is shown that the addition steam is a promising method to reduce harmful emissions

The complete combined reaction scheme as it is used for the LES, including Burke's detailed hydrogen reaction scheme (Burke et al., 2012), the OH^* chemiluminescence mechanism of Smith (Smith et al., 2002; Smith et al., 2005) and the San Diego NO_x subset is listed in Appendix A (p. 165).

PART II

Turbulent Flames

9

Turbulent Flames

> *I am an old man now, and when I die and go to Heaven there are two matters on which I hope for enlightenment. One is quantum electrodynamics and the other is turbulent motion of fluids. And about the former I am rather more optimistic.*
>
> Sir Horace Lamb, *Address to the British Association for the Advancement of Science*, 1932

In laminar flames the velocity and the scalar fields such as pressure, temperature, and species concentration are deterministic. When turbulence is introduced to a combustion process, the flame front may be affected by stochastic fluctuations and the analysis of the premixed flames needs to be extended beyond the laminar flow regime. Whereas laminar combustion is almost entirely limited to candles, lighters and some domestic furnaces, turbulent combustion is encountered in most technical combustion systems such as internal combustion engines, industrial burners, furnaces and of course gas turbines. The interaction of turbulence with the flame is complex due to the strong coupling between both non-linear systems across all scales. This makes modeling of these kind of devices challenging. When considering thin flame fronts the main effect of the turbulent field is a wrinkling of the flame front due to eddies. Because of the flame wrinkling, the flame front is increased leading to an increase of the combustion rate.

A first explanation of turbulent flames was given by Damköhler (1940), who developed a theoretical relationship between the laminar and turbulent flame speed propagation. Damköhler (1940) considered a wrinkled flame front with a laminar burning velocity S_l as shown in Figure 9.1. Correlating the mass flux through the total instantaneous laminar wrinkled flame front area A_l with the mean turbulent flame front area A_t gives:

$$\dot{m} = \varrho S_t A_t = \varrho S_l A_l \,. \tag{9.1}$$

Reshaping this equation leads to:

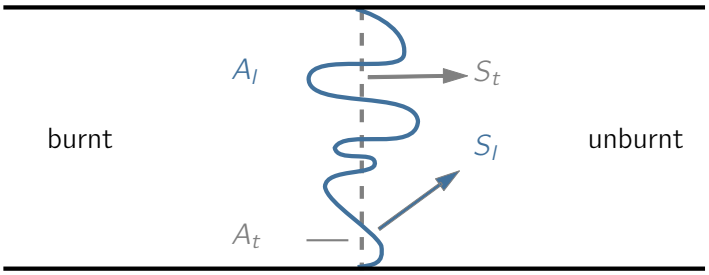

Figure 9.1: Schematic of turbulent flame front propagation (Damköhler, 1940).

$$\frac{S_t}{S_l} = \frac{A_l}{A_t}\,. \tag{9.2}$$

Thus, the propagation speed depends on the area ratio between the laminar and turbulent flame front. Hence, the turbulent flame speed is always higher as the laminar burning velocity due to the increase of the flame front area. However, when the turbulence level is increased the eddies eventually quench the flame locally due to high shear stresses. In addition, the flame also affects the flow field caused by the quick change of temperature, species concentration, density, and viscosity in the flame front. These strong interaction between both non-linear phenomena are rather complex. To support the further discussion on turbulent premixed combustion two non-dimensional numbers are introduced, the *Damköhler* number Da and the *Karlovitz* number Ka. Both relate the chemical and turbulent timescales, although at different scales of the spectrum. The *Damköhler* number relates the turbulent integral time scale τ_0 with the chemical time scale τ_c. It is common to express the *Damköhler* number by expressing τ_0 with the integral length l_0 over the velocity fluctuation u' and the chemical timescale with the ratio of the laminar flame thickness δ_L^0 and the laminar burning velocity S_l (Poinsot et al., 2005):

$$\mathrm{Da} = \frac{\tau_0}{\tau_c} \approx \frac{D_h/u'}{\delta_L^0/S_l}. \tag{9.3}$$

Similarly, the *Karlovitz* number compares the chemical τ_c with the *Kolmogorov* timescale τ_μ:

$$\mathrm{Ka} = \frac{\tau_c}{\tau_\mu} \approx \left(\frac{u'}{S_L}\right)^{\frac{3}{2}} \left(\frac{D_h}{\delta_L^0}\right)^{-\frac{1}{2}}\,, \tag{9.4}$$

With these characteristic numbers it is possible to define different flame regimes that support the understanding of the possible interaction between the premixed flame front and the turbulent eddies. These regimes are usually discussed in terms of velocity and length scale ratios as depicted in Figure 9.2. The diagram is also known as the *Borghi* diagram and presents five different regimes (Poinsot et al., 2005):

- **Laminar flames**

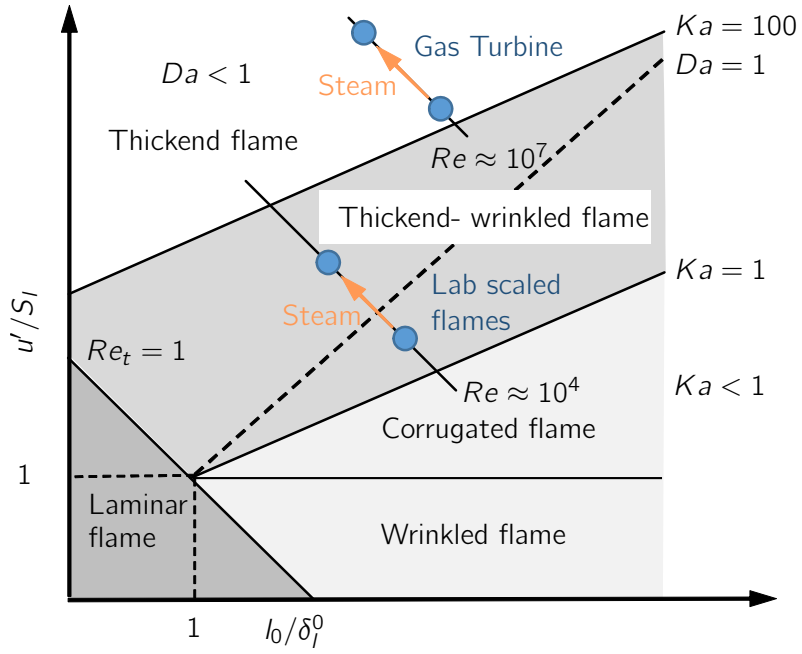

Figure 9.2: Flame regime diagram for turbulent premixed flames. According to Poinsot et al. (2005).

In the bottom left corner the flow is laminar, and the flame structure as discussed in the first part of this thesis is valid.

- **Wrinkled flames**
  As the Reynolds number increases, the flow becomes turbulent. If the turbulence intensity is still less than the laminar burning velocity, the eddies cannot enter the reaction layer and the flame front is only wrinkled.
- **Corrugated flames**
  If the turbulence intensity is higher than the laminar burning velocity ($u' > S_l$) the smallest scales in the flow are larger than the laminar flame thickness and do not interfere with the local structure of the flame. Still, the front may be locally altered and curvature effects may appear. However, the wrinkled and the corrugated flame regime are of minor relevance for industrial applications.
- **Thickened-wrinkled flames**
  In this regime the eddies are smaller and can interact with the preheat zone, but not with the inner reaction layer that is responsible for the most important reactions. Thus, the reaction layer is thickened and the propagation speed is increased.
- **Thickened flame**
  With further increase of the turbulence intensity the eddies can enter the inner reaction layer. As they enter, they perturb the chemical reactions by increasing the heat and loss of radicals. This may lead to local extinction through quenching, hence this regime is also denoted as the *Broken Reaction Zone*.

- **Well stirred reactor**
  In addition to the classical flame regime scheme with five regimes sometimes the *well stirred reactor* regime is quoted as a separate regime (Poinsot et al., 2005). For small *Damköhler* numbers ($\mathrm{Da} < 1$) the mixing time of the large turbulent scales is smaller than the chemical time. Hence, the mixing is fast and the reaction rate is limited by chemistry.

Although this classification is very useful for the discussion of the turbulence-kinetic interaction, it is noteworthy that most technical flames are far more complex and may fall in more than one regime. Thus, one can assume that a technical flame can be seen rather as an area or point distribution than to be a single point in the *Borghi* diagram. However, for simplicity reasons the average flame regime of a stationary gas turbine and the turbulent H_2 flames, as they are investigated in this thesis, are also presented in Figure 9.2. Due to the high mass flow rates, real gas turbines feature very high Reynolds numbers ($\mathrm{Re} = 10^6 - 10^7$). The *Kolmogorov* scales are very small and interfere with inner reaction layer and hence, they operate in the *thickened flame regime*. As will be shown later (see section 12.3) the investigated H_2 flames work at lower Reynolds numbers in the *thickened flame* regime and the flame front is prone to the perturbations of the smallest eddies. Additionally, Figure 9.2 depicts the influence of steam on the combustion regime. By injecting steam to the process the flames are shift towards higher *Karlovitz* numbers along constant Reynolds numbers assuming an overall constant mass flow. This is due to the fact that by the addition of steam, both the thermal thickness as well as the laminar burning velocities are decrease whereas the perturbation level remain almost constant.

9.1 Flame Stabilization

The main focus in developing modern stationary gas turbine combustors is to reduce harmful nitrogen oxides NO_x emissions and to guarantee flame stabilization. A milestone in the reduction of NO_x was the introduction of lean premixed combustion. However, due to the high mass flows this kind of flames need to be stabilized to prevent the flame from being blown out. A flame is anchored where its propagation velocity matches the flow speed of the fresh gases. One way to achieve this, is to place a *bluff body* in the flow to create a wake causing a reverse flow with lowered velocities in the shear layer. The main disadvantage is that the flame is close to the body with consequences on the materials and the induced pressure-loss. The preferred way to stabilize a premixed or partially premixed flame is to employ a swirl induced *vortex breakdown*. When the static pressure on the centerline of the vortex decreases to the point that the regular spiraling motion becomes unstable and develops a stagnation point on or near the axis (Leibovich, 1984).
Usually, this low-pressure region appears around the axis region close to the sudden expansion between the burner and the combustion chamber. If the pressure gradient is strong enough, the swirl creates an adverse axial pressure gradient which is sufficiently large to result in reverse flow along the axis, and thus setting up of an Inner Recirculation Zone (IRZ). This recirculation zone stabilizes the flame due to the constant support of thermal energy and burnt gases as well as the lower velocities in the shear layer between the recirculation zone and the outer swirling flow.

In case of a confined flow also an Outer Recirculation Zone (ORZ) is established, as presented in Figure 9.3. This effect is generally termed as vortex breakdown and studied in detail in numerous experimental and numerical studies, but the mechanisms are only partly understood. The reason lies in the multi-scale and chaotic nature of turbulence and complex flow field associated with vortex breakdown. Comprehensive reviews on the topic of vortex breakdown are given by Lucca-Negro et al. (2001) and Syred (2006), who summarized several patterns, of which two, the bubble- and the spiral-type breakdown are typical for turbulent flows with high Reynolds numbers. Billant et al. (1998) and Escudier et al. (1985) characterized the vortex breakdown process taking place in a swirling water jet experimentally and also determined the criticality of the flow concerning the confinement. Despite all these efforts no final explanation for the formation of a vortex breakdown is currently available. The large structures resulting from vortex breakdown and swirling shear layers directly affect the flame stabilization, leading to heat release fluctuations and combustion instabilities (Huang et al., 2009; Pope, 2013). This unsteady behavior is the main difficulty in assessing the problem. These structures cause large deterministic fluctuations in the flow field, as presented in several other studies (Anacelto et al., 2003; Cala et al., 2006; Canepa et al., 2006; Midgley et al., 2005; Paschereit et al., 1999).

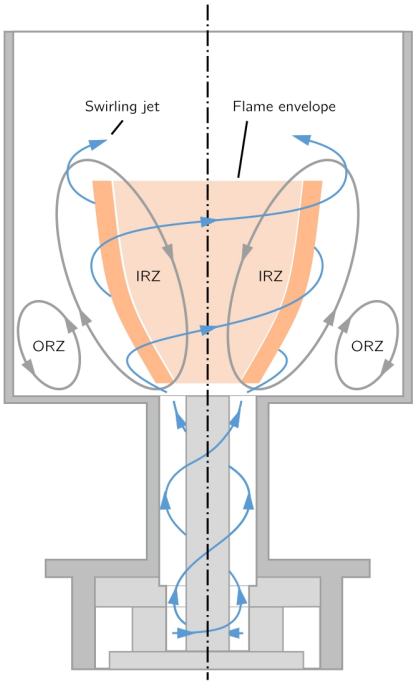

Fig. 9.3: Schematic of a swirl-stabilized combustor flow configuration.

9.2 Literature Overview

Swirl burners are not new in combustion, however the comprehensive work of Leuckel (1967), Lilley (1977), and Syred et al. (1974) end of the 1970's pointed for the first time out why swirling flows have such an important influence on the flame stability. Beér and Chigier conducted their experimental and theoretical studies in the 1960's on oil burners at the IFRF[1] . Due to the oil crisis in the 1970's, natural gas gained more interest regarding the swirl combustion and was further explored by Syred et al. (1974), and Gupta et al. (1977), mainly focusing on industrial furnaces and boilers. In the 1980's the research was broadened by Gouldin et al. (1985) and Rhode et al. (1983) towards confined swirling flows due to the fact that emissions, efficiency, and stability are key issues for gas turbine combustors. With the demonstration of the first laser diagnostic for flow measurements (e.g., Laser Doppler Velocimetry (LDV)) in the 1960's by Yeh et al. (1964) the interest in this technique opened up for the accurate measurement of burner flow fields. Much progress in laser techniques has been made since then, leading not only to Particle Image Velocimetry (PIV) but also to advanced laser diagnostic techniques for

1 International Flame Research Foundation, `http://www.ifrf.net/`

turbulent combustion (Eckbreth, 1996; Janicka et al., 2013; Moeck et al., 2013; Tropea et al., 2007). Since swirl-stabilized burners are widely used in aeronautical and industrial applications, experimental investigations are accompanied by numerical studies. In the beginning the focus laid on studying isothermal swirling flows, mainly with Reynolds-averaged Navier-Stokes (RANS) models (e.g., k-ϵ turbulence model) due to restricted computational resources in the end of the 1980's (Koutmos et al., 1990; Riahi, 1990; Sloan et al., 1986). Because of the complexity of combustor flows, the route that was usually followed was to concentrate on validation studies and model fitting. However, the strong curvature of the streamlines in swirling flows affects the turbulent shear stresses and the velocity field significantly (Riahi, 1990). With the increase of computational power more demanding or higher order models were applied (Cambon et al., 1992; Shih et al., 1997). Since then different avenues have been followed up. On the one hand there was the further development and model fitting of the RANS models, mainly for industrial applications (Fudihara et al., 2003; Lu et al., 2003) and on the other hand the focus on accurately predicting swirling flows by applying Large Eddy Simulation (LES) (Duwig et al., 2007a; Pierce et al., 1998; Ranga Dinesh et al., 2009) or Direct Numerical Simulation (DNS) (Freitag et al., 2006; Gui et al., 2010; Hu et al., 2001) to gain further insight in the underlying flow field dynamics. Although RANS methods represent the most efficient methodology for the calculation of turbulent flows, the use of standard RANS models for swirling flow simulations has, to date, turned out to be inappropriate. In contrast, LES has proven to be an accurate and computationally feasible approach for turbulent swirl flow simulations (García-Villalba et al., 2006; Wang et al., 2005; Zemtsop et al., 2009); and it is assumed that with further increase of computational power LES will play a more important role for future computations.

Reacting turbulent flows are often calculated with averaged or filtered equations. Unfortunately, these equations lead to unclosed terms, which are usually modeled with the resolved variables. Beside the turbulence, also the mean (filtered) reaction rate has to be modeled when it comes to simulating combustion. This reaction rate is challenging to assess due to its highly nonlinear nature. Various combustion models have been proposed and are briefly discussed in more detail in section 12.3 (96). Also, several recent reviews are available in the literature (Bilger et al., 2005; Bray, 1996; Pitsch, 2006; Pope, 2013; Veynante, 2002).

As for the simulation of swirling flows also three main avenues are followed up for simulating reacting turbulent flows: RANS, LES, and DNS. In the gas turbine industry, RANS is still the main working horse, mainly due to the relatively low computational costs. RANS models benefit from extensive research and have been successfully calibrated on simple fundamental configurations. However, fast turnaround times are accompanied by limitations and a lack of precision when complex flows in modern gas turbines are considered (Gicquel et al., 2012). For example, James et al. (2006) reported that the standard k-ϵ model predicts incorrect turbulence levels when both the liner and annuli of a gas turbine combustor are regarded. In addition, for RANS modeling was realized that the direct closure of the mean reaction rate in the averaged species transport balance can hardly be accomplished, leading to the development of conserved scalar methods. However, these methods are insufficient for predicting combustion instabilities. Modeling approaches which overcome these restrictions are found at the other extreme; DNS suppresses any notion of modeling but demands for high computational costs and is thus mainly used to validate turbulence and combustion models (Doom et al., 2007; Jiang et al., 2001; McMurtry et al., 1986; Montgomery et al., 1993). LES is also computationally

intensive, however, to a far lesser degree than DNS. A disadvantage in performing LES for wall-bound flows is the near-wall treatment. If the focus lays on resolving the boundary layer accurately, either the near wall regions features are sufficiently resolved in terms of mesh elements or a sophisticated wall function has to be used. Combustion usually takes place away from the combustor walls in gas turbine combustor. Thus, a sophisticated wall treatment is not required (James et al., 2006). With the increase of computational power and the availability of distributed computing platforms, LES is considered to be the next generation practical design tool for gas turbine combustors (Huang et al., 2009). For scientific applications LES proved its capabilities as a clear scientific alternative to RANS for the combustion community. Recent developments now focus on transient phenomena with added complexities, for example combustion instabilities (Ranga Dinesh et al., 2010; Schmitt et al., 2007), flame stabilization (Duwig, 2011; Duwig et al., 2007a), supersonic combustion (Berglund et al., 2007), and so forth.

Although lean-premixed combustion is for some time state-of-the-art in stationary gas turbines, it is still in the focus of the combustion community. This is due to the fact that especially LES and DNS methods allow for a deeper insight in the fundamental processes, and thus for a further improvement of this low NO_x combustion technique. For instance, Huang et al. (2003) investigated a laboratory sized lean-premixed swirl combustor by employing LES and a level-set flamelet library. With a compressible solver they found that the energy release in the methane flame zone triggers acoustic waves in the chamber and that a coherent structure was present. Freitag et al. (2007) focused further on the identification of coherent structures in a strongly swirled lean premixed flame with LES. They used an industrial like radial burner and observed that the coherent structure diminished under reacting conditions. Sengissen et al. (2007) conducted further numerical (LES) and experimental studies of a cold and reacting flow in a swirled partially premixed burner with and without fuel modulation. Their results showed that LES and acoustic analysis predict the flame dynamics in this complex configuration with accuracy when heat losses are taken into account. Using a simplified cylindrical model combustor, Duwig et al. (2012) investigated the stabilization dynamics of swirling partially premixed flames. The problem is addressed using LES and Planar Laser-Induced Fluorescence (PLIF). The flame was linked to a helical instability and the interaction between the structure and the air-fuel mixing lead to a torus type flame shape. Also the comprehensive review paper by Gicquel et al. (2012) is recommended, which renders the potential of LES for real applications, but also points out that validation of these approaches in the context of industrial burners is more difficult to assess due to the limited set of available measurements. The mentioned studies are just an excerpt of the broad available literature without any claim to comprehensiveness. However, relatively few studies have examined the role of steam diluted combustion.

Bianco et al. (2001) performed a RANS (RNG k-ϵ) simulation of a lean premixed combustor, fed with homogeneous mixture formed by methane and moist air, in order to predict velocity field, temperatures and emissions. The water-air mass ratio was varied from 0% to 5% and the chemical reactions were described using a reduced five-step mechanism including the oxidation process and the NO_x formation. It was found that at the same equivalence ratio the NO_x and CO emissions are reduced when steam is added to the combustion process. As a feasibility case for flaring applications in the petrochemical industry, Castiñeira et al. (2006) investigated

a Sandia Flame configuration (A, S, D)[1] with different steam-air ratios. The investigation was intended to improve understanding thermochemistry effects of steam and air addition on the combustion process of industrial flares for the development of a control model. As fuels methane and a H_2-CO mixture were used, with according reduced reaction schemes (Drake et al., 1989; Kazakov et al., 1994). The mass fraction of steam was increased up to a value of ≈ 0.6. For their analysis they used Fluent with the realizable k-ϵ model and the Eddy Dissipation Concept (EDC) as combustion closure. They observed that inefficient combustion occurs at certain heating values, which were in line with the experimental observations and in addition that the injection of steam also leads to beneficial chemical interactions with carbon particles. Further reduction of NO_x emissions were described by Lei et al. (2007). For an experimental validation a 40 MW gas turbine fired with syngas was used. The simulation of combustor according to the experimental parameters was carried out using the realizable k-ϵ turbulence model and the P-1 radiation model. Unfortunately, the study does not contain information about the combustion closure or reaction scheme. However, the steam-air ratio was increased up 17% and the results show a decrease of the NO_x levels. Compared to the experimental results, the simulation consequently under predicts the NO_x emissions, suggesting various possibilities for the offset (i.e., reaction scheme, combustion closure, etc.). Guo et al., 2008 also investigated a Sandia/Sydney Flame configuration under the influence of steam and validated the results against experimentally obtained velocity and temperature fields, which were measured using PIV and high temperature thermocouples. Although, the simulations showed discrepancies to the experiments, which are supposed to be caused by the confined simulation area, it was found that the existence of the methane flame alters the location of the minimum velocity, whereas additional steam contributes to a momentum loss of air co-flow, leading to a lower penetration limit.

Whereas the aforementioned studies are mainly based on methane or natural gas oxidation with or without steam dilution, the studies of turbulent hydrogen flames in the literature are rather scarce. Of course this is attributed to the fact that hydrogen is not used in terms of industrial scale power generation. However, few CFD analyses are available and shall be mentioned in the following. Due to the fact that hydrogen oxidation is assumed to be a fundamental subset in most combustion processes, the percentage of turbulent DNS simulations is higher as for higher hydrocarbons. For instance, Doom et al. (2009) investigated the self-ignition process of a hydrogen vortex ring with hot air employing DNS ($\mathrm{Re} = 1000$) and detailed chemistry. Hydrogen was diluted with N_2 at ambient temperatures and injected into hot air. It was found that the coupling between the flow and chemistry is far from trivial. The Lewis number does not only affect directly the ignition time as well as the subsequent evolution of the flame, it also affects the location of the initial ignition regions. Hence, the influence of higher oxidizer temperature on the burnout time is significantly different when Lewis numbers close to one are considered. A more complex case with a swirling jet undergoing vortex breakdown was investigated by Wang et al. (2011). For the stoichiometric hydrogen-air flame featuring a Reynolds number of $\mathrm{Re} = 3000$ vortex and turbulence characteristics were examined also using

1 International Workshop on Measurement and Computation of Turbulent Nonpremixed Flames `http://www.sandia.gov/TNF`

DNS and detailed chemistry. A cone type vortex breakdown was observed and two instabilities, a Kelvin-Helmholtz and centrifugal instability, are responsible for the transition from the laminar to the turbulent flow regime. Moreover, it was found that most of the flame elements lie in the laminar flame regime and the thin reaction zones regime. Carlsson et al. (2014) conducted three-dimensional direct numerical simulation with detailed chemical kinetics of hydrogen air flames at high Karlovitz numbers. Using the mechanism of Li et al. (2004b), it was found that the high intensity turbulence along with differential diffusion resulted in a much more rapid transport of H radicals to the unburned mixtures rather than that in laminar flamelets.

On the LES side the evaluation of a air-hydrogen reacting flow inside a diffusion flame combustor of a single shaft gas turbine by Gobbato et al. (2011) is noteworthy. The paper focuses on medium size heavy duty gas turbine combustors fueled with pure hydrogen. A coarse grid and reduced reaction scheme were used to predict the temperature field inside the combustor, more precisely on the liner wall temperatures and the turbine inlet temperature profile because these parameters potentially affect the reliability of subsequent turbine components. For validation purposes data of full-scale experimental tests were employed. Albeit the spatial resolution and simplified reaction mechanism, a close match was found between CFD profiles and experimental data at the combustor discharge. Further studies on hydrogen combustion have mainly been conducted for flameless combustion concepts, namely Moderate or Intense Low-oxygen Dilution (MILD) or Flameless Oxidation (FLOX). An overview over the MILD combustion is given by Cavaliere et al. (2004), however, the main idea is to preheat the combustible mixture to a higher value then the self-ignition temperature. This leads to a non-luminous oxidation process with lower temperature increase. Due to the lower temperature increase the application of the MILD concept seems promising for hydrogen combustion. For example, Christo et al. (2005) investigated a non-premixed methane-hydrogen flame issuing from a Jet in Hot Coflow (JHC). Using a RANS model, it turned out that both scalar based models, namely the β-PDF and flamelet models, are inadequate for modeling JHC flames. However, the EDC was found to perform reasonably well. The EDC model was also employed by Frassoldati et al. (2010). There, methane-hydrogen jet flames were studied with regards to various turbulence models. As oxidation scheme the *Creck* Modeling Group mechanism (Frassoldati et al., 2007) was used. The study focuses on the description of pollutant formation in steady turbulent flows to verify its applicability to the MILD combustion regime. The overall agreement with experimental measurements was found to be satisfactory, however, discrepancies between measured and predicted NO profiles were apparent and are attributed to an overestimation of the temperature field. Even so, no clear explanation for the temperature overshoot is given.

Despite much progress in the application of the MILD combustion concept various parameters such as stabilization, auto-ignition, start-up, and the structure of reaction zone remain unclear and need further evaluation. Therefore, hydrogen combustion with steam dilution is assumed by the author of this study to be a more promising way for future gas turbine application.

The second part of the thesis investigates turbulent hydrogen-air-steam flames in a generic model gas turbine burner and has a dual purpose. The first purpose is to demonstrate by comparison with accompanying measurements that the simulation technique can reliably predict reactive swirling flows. Therefore, in a first step isothermal LES simulations are conducted to gain confidence in the numerical schemes and modeling techniques. A sensitivity study is

performed to determine the influence of grid sizes and turbulence modeling. The isothermal flow field is discussed in detail and validated against experimental data. Then, the reacting flow field is assessed numerically and also validated against experimentally obtained data. Again, the sensitivity is determined regarding the mesh resolution and combustion closure. The second purpose is to gain a deeper understanding of the turbulent combustion process of steam diluted hydrogen flames. Therefore, the amount of steam is varied between a state without steam, a moderately diluted level of steam and a highly diluted case.
The second part of this thesis is structured in the following way. First, a brief introduction on turbulent flames. Followed by a presentation of the investigated burner. For the validation of the simulations experimentally obtained data is used. The measurement techniques and operational conditions are discussed in the tenth and eleventh chapter of this part. The governing equations on which the LES simulations are based, are presented in the twelfth chapter. The governing equations are preceeded by the introduction of the turbulence and combustion closures. Then, the computational setup and the meshing strategy are reported. This chapter is followed by presenting the detailed results of the isothermal and reactive flow simulations. Finally, the second part is concluded by a concise summary of the findings.

10

Investigated Configuration

Figure 10.1 presents the computational domain. It consists of an unscaled radial swirl generator with an attached cylindrical combustion chamber. The domain is adopted from the experimental setup. Due to limited computational resources, the length of the combustion chamber is truncated. However, the length of the combustion chamber is chosen in such a way as to minimize the influence of the outlet boundary on the flow in the region of interest. In order to minimize the impact of the prescribed inflow conditions on the results, the complete swirl generator is taken into account. This is an ideal approach because turbulence readily develops at the sharp edges of the obstacles in the swirl generator. For normalization a characteristic length and velocity, the hydraulic diameter D_h and the mean bulk velocity u_0 at the burner

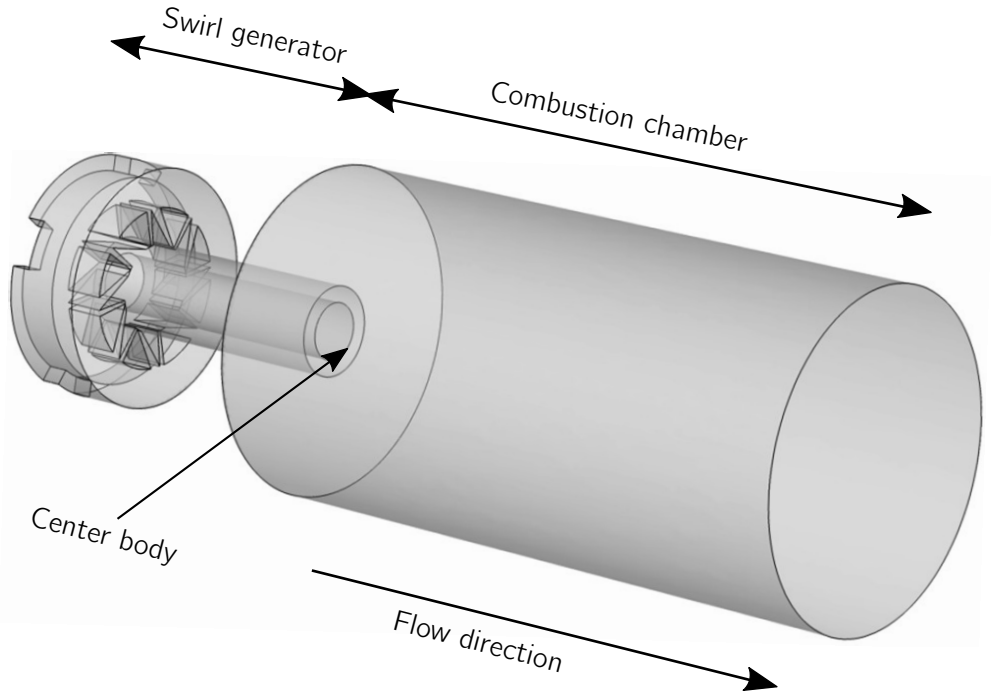

Figure 10.1: Schematic drawing of the computational domain.

exit can be defined, respectively. In addition, a characteristic timescale $\tau = \frac{D_h}{u_0}$ and volume flow $\dot{V}_0 = (u_0 \cdot A)$ can be derived for normalization. The dimensions for the isothermal and reacting simulations are not completely equal due to the fact that a smaller center body was used in the combustion test rig to prevent flashbacks. The dimensions of the configurations are given in Table 10.1.

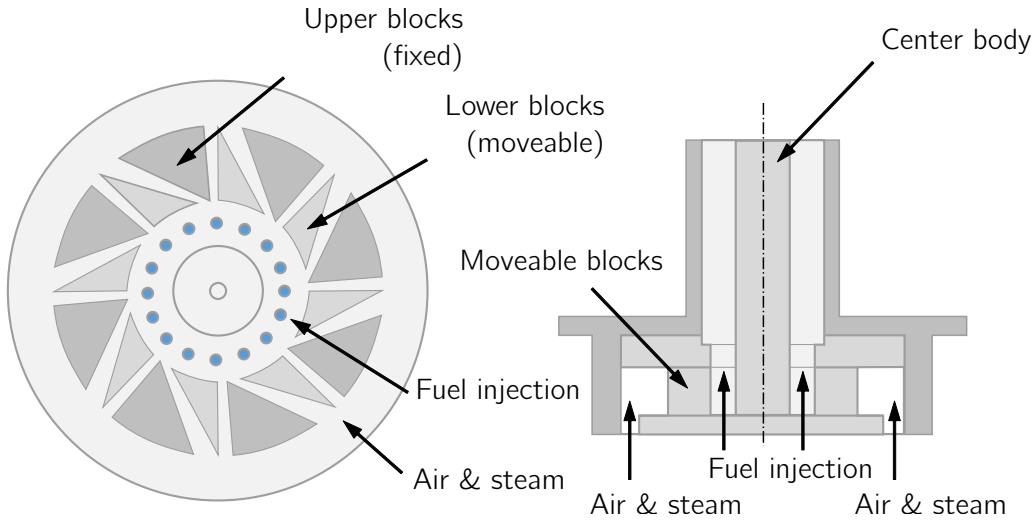

Figure 10.2: Schematic of the swirl generator.

The swirl burner used in this investigation is a MOVEABLE BLOCK BURNER is based on a design by Beér et al. (1972). The burner consists of eight movable and eight fixed alternately placed blocks as shown in Figure 10.2. Due to simultaneous rotation of the movable blocks about the symmetry axis, the oblique passages are opened while the non-oblique parts are narrowed and vice versa. This yields modulation of the swirl intensity between 0 and 2 (Fudihara et al., 2003). For the reacting case the main gas flow consists of an adjustable amount of air and steam and is premixed before entering the swirl generator. In order to increase the mixing quality, the fuel injection strategy was changed, by placing 16 fuel injection hole in the burner plate, instead of using the original 4 fuel injection holes in the center body. Thus, the fuel, in this case hydrogen, is injected at the bottom plate of the swirl generator through the 16 holes. In previous investigations the spatial and temporal degree of unmixedness of the air-fuel mixture was addressed (Göke et al., 2011). The degree of unmixedness is defined as:

$$U_{s,t} = \frac{\sigma_{s,t}^2}{\overline{[X]}(1 - \overline{[X]})}\,, \tag{10.1}$$

where $\sigma_{s,t}$ is the temporal (subscript t) or spatial (subscript s) variance of concentration fluctuations and $\overline{[X]}$ is the mean molar fuel concentration. It was found that the spatial and temporal degree of unmixedness was of the order of 10^{-4}. Thus, it is assumed that the air-steam-fuel composition is technically premixed. This is taken into account for the simulations by directly applying the air-steam-fuel composition to the inlet, without considering the mixing process. For the isothermal case water is used as fluid and directly fed to the inlet

of the radial swirl generator.

Table 10.1: Dimensions of the computational domain.

	Isothermal Case	Reacting Case
Hydraulic diameter D_h	27.5 mm	20.0 mm
Length combustion chamber	$14.5D_h$	$20.0D_h$
Diameter combustion chamber	$7.3D_h$	$10.0D_h$

11

Experimental Techniques

11.1 Experimental Database

Isothermal Experiments

The isothermal flow experiments were conducted by Katharina Göckeler, Steffen Terhaar, and Christoph Strangfeld in a vertically oriented water tunnel facility. The model is made of acrylic glass to allow access for the application of laser diagnostics. In order to record the plain velocity field the non-intrusive technique Particle Image Velocimetry (PIV) was applied. Distinct refraction indices of glass and water are taken into account. The PIV measurements are performed using a Nd:YAG pulse laser (18 mJ per pulse) and a PCO Sensicams (Resolution: 1024x1024 pixel). By tilting the laser sheet to the diagonal of the test section it was ensured that the camera looked almost straight through the glass window. In addition to the PIV recordings also a non-intrusive Laser Doppler Velocimetry (LDV) system is applied to measure the axial velocities at various axial positions. A three-dimensional traverse system ensures the proper positioning within the measurement volume. The complete experimental set-up and equipment is presented in detail by Göckeler et al. (2010).

Reacting Experiments

The reacting flow measurements are also conducted by Steffen Terhaar and are performed in a gas-fired test rig under atmospheric conditions. The burner was fired with hydrogen, and the air was preheated and mixed with overheated steam before entering the burner. The combustion chamber consists of a cylindrical silica glass to provide optical access, and thus, allows for the application of PIV. For the PIV measurements, aluminum oxide particles of a nominal diameter of 1 µm are seeded into the flow upstream of the swirl generator using a fluidized bed seeding generator. Additionally, the flame shape and position is assessed by recording its OH^* chemiluminescence using an ICCD camera. In order to recover the radial intensity distribution the images were decomposed applying an inverse Abel transformation according to Jaffe et al. (1991). The combustor inlet temperature was measured in the mixing tube upstream of the burner outlet. Further information on the experimental setup is reported by Terhaar et al. (2011).

11.2 Operating Conditions

Isothermal Experiments

For the simulations the same geometry is used as for the experiments. The latter is carried out in a model combustion chamber with a diameter of 0.2 m resulting in an area expansion ratio of 17.5. The experiments are conducted for a swirl intensity of $S_{th} = 0.7$. This swirl number corresponds to a high-swirling flow where the flow undergoes vortex breakdown. The operating conditions were atmospheric pressure, water as fluid, inlet velocity of 0.6 m/s, and an inlet temperature of 293 K. The operating conditions are chosen to result in a Reynolds number of $\mathrm{Re} \approx 33.000$ similar to the gas-fired tests and are summarized in Table 11.1.

Table 11.1: Operating conditions for the isothermal cases.

Condition		Case 1 (low swirl)	Case 2 (moderate swirl)	Case 3 (high swirl)
Fluid		Water	Water	Water
Swirl number	S_{th}	0.5	0.6	0.7
Inlet velocity	u_{in}	0.6 m/s	0.6 m/s	0.6 m/s
Bulk velocity	u_0	1.3 m/s	1.3 m/s	1.3 m/s
Kinematic viscosity	ν	$1.004 \cdot 10^{-6}$m²/s	$1.004 \cdot 10^{-6}$m²/s	$1.004 \cdot 10^{-6}$m²/s
Pressure	p	101.325 Pa	101.325 Pa	101.325 Pa
Reynolds number	Re	$33{,}000$	$33{,}000$	$33{,}000$

Reacting Experiments

Three cases at different levels of steam are investigated to assess the influence of steam on the combustion process. In the first case the experiment is conducted in the absence of steam at ambient temperature and pressure, and will be denoted in the following as "dry". The two remaining cases are carried out at moderate and high steam contents and are referred to as "moderate-wet" and "ultra-wet" in the following. The steam content $\Omega = \dot{m}_{steam}/\dot{m}_{air}$ is defined as the ratio of the mass flow rate of steam $\dot{m}_{steam}$ to the mass flow rate of air $\dot{m}_{air}$. One objective of this survey is to show that adding steam directly into the combustion process allows for hydrogen combustion at realistic gas turbine conditions, with regards to the turbine inlet temperature ($\approx$ 1643 K).

During the experiments, the total mass flow rate of air plus steam was kept constant. The swirl number was adjusted to $S_{th} = 0.7$ to assure vortex breakdown in the combustion chamber. The operation conditions are summarized in Table 11.2.

Table 11.2: Operating conditions for the reacting cases.

Condition		Case 1 (Dry)	Case 2 (Moderate-Wet)	Case 3 (Ultra-Wet)
Inlet velocity	u_{in}	14.94 m/s	26.55 m/s	38.89 m/s
Bulk velocity	u_0	34.71 m/s	61.65 m/s	88.37 m/s
Pressure	p	101.325 Pa	101.325 Pa	101.325 Pa
Reynolds number	Re	39,000	31,000	26,000
Steam content	Ω	0%	20%	50%
Equivalence ratio	Φ	0.5	0.6	0.75
Inlet temperature	T_u	293 K	463 K	633 K
Adiabatic flame temperature	T_{ad}	1643 K	1623 K	1643 K

12

Numerical Methodology and Computational Setup

12.1 Conservation Equations

Isothermal Flow

The fundamental equations describing the motion of an isothermal and incompressible fluid are those of conservation of mass and momentum. Therefore, the incompressible NAVIER-STOKES equations are used within the LES framework to simulate the turbulent flow field. In LES, a *low-pass* filter is applied to the dependent variables so that the filtered equations only describe the larger turbulent fluctuations (Ferziger et al., 2001). The "low-pass" filtered (denoted by the superscript $-$) equations read as follows:

Continuity $(i = 1,2,3)$

$$\frac{\partial\left(\bar{u}_i\right)}{\partial x_i} = 0\,. \tag{12.1}$$

Momentum $(i = 1,2,3)$

$$\frac{\partial \bar{u}_i}{\partial t} + \frac{\partial \bar{u}_i \bar{u}_j}{\partial x_j} = -\frac{1}{\varrho}\frac{\partial \bar{p}}{\partial x_i} + \frac{\partial}{\partial x_i}\left[2\nu \bar{S}_{ij} + \tau_{ij}\right], \tag{12.2}$$

where u_i represents the velocity component,ϱ the density ,p the pressure,τ_{ij} the subgrid-scale stress tensor,S_{ij} the tensor of the strain rate, and ν the kinematic viscosity. The filtering is a linear function which is assumed to be commutative with temporal and spatial derivatives. However, the filtering is not commutative for the non-linear terms. Therefore, these terms cannot be expressed as filtered expressions and are gathered on the right-hand side. These terms are collectively called the subgrid-scale (SGS) term.

Reacting Flow

In order to describe the motion of a reactive flow also the species and energy balances have to be regarded in addition to eqs. (12.1) and (12.2). Again, a "low-pass" filter is applied to the dependent variables, and thus removes the dependence on the small eddy scales, so that the equations only describe the larger turbulent fluctuations (Poinsot et al., 2005; Weller et al., 1998). This results in unclosed terms, usually referred as the subgrid scale (SGS). To avoid

the modeling of sub-filter scales of the mass conservation equation Favre (1983) proposed a density-weighted filtering operation, called Favre filtering for any variable ϕ:

$$\tilde{\phi} = \frac{\overline{\varrho\phi}}{\overline{\varrho}} \,. \tag{12.3}$$

Applying the filtering to the balance equations leads to the Favre averaged filtered equations, which reads as follows (Poinsot et al., 2005):

Continuity $(i = 1,2,3)$

$$\frac{\partial\overline{\varrho}}{\partial t} + \frac{\partial\overline{\varrho}\tilde{u}_j}{\partial x_j} = 0. \tag{12.4}$$

Momentum $(i = 1,2,3)$

$$\frac{\partial\overline{\varrho}\tilde{u}_i}{\partial t} + \frac{\partial(\overline{\varrho}\tilde{u}_j\tilde{u}_i)}{\partial x_j} = -\frac{\partial}{\partial x_j}\left[\overline{\varrho}\left(\widetilde{u_i u_j} - \tilde{u}_i\tilde{u}_j\right)\right] - \frac{\partial\overline{p}}{\partial x_i} + \frac{\partial\overline{\tau}_{ij}}{\partial x_j} + \overline{F_i} \,. \tag{12.5}$$

Here, the superscripts $-$ and $\sim$ denote filtered and Favre filtered quantities, rather than ensemble means. In addition, u_i is the velocity component, ϱ the density, p the pressure, μ the dynamic viscosity, F_i a volume force and τ_{ij} is an unclosed term, usually denoted as the subgrid scale stress tensor.
The mass conservation equation for chemical species k is described as follows:

Species $(i = 1,2,3)$

$$\frac{\partial\overline{\varrho}\tilde{Y}_k}{\partial t} + \frac{\partial}{\partial x_i}\left(\overline{\varrho}\tilde{u}_i\tilde{Y}_k\right) = \frac{\partial}{\partial x_i}\left[\overline{J_i^k Y_k} - \overline{\varrho}\left(\widetilde{u_i Y_k} - \tilde{u}_i\tilde{Y}_k\right)\right] + \overline{\dot{\omega}_k}, \tag{12.6}$$

where Y_k is the mass fraction of the species k, $\dot{\omega}_k$ is the reaction rate and J_i^k is the i-component of the laminar diffusive flux of species k. For the conservation of energy, the enthalpy balance equation is employed, where a low Mach assumption is regarded:

Energy $(i = 1,2,3)$

$$\frac{\partial\overline{\varrho}\tilde{h}_t}{\partial t} + \frac{\partial\overline{\varrho}\tilde{u}_i\tilde{h}_t}{\partial x_i} = \frac{\partial}{\partial x_i}\left(\frac{(\mu_t + \mu)}{\mathrm{Pr}}\frac{\partial\tilde{h}_t}{\partial x_i}\right) \,. \tag{12.7}$$

Here, $h_t = h + {}^{u_i u_j}/_2$ is the total enthalpy and can be described by the specific enthalpy h. μ denotes the dynamic viscosity of the fluid, μ_t the eddy viscosity and $\mathrm{Pr} = {}^{\nu}/_{\alpha} = 0.7$ the

Prandtl number. A low Mach approximation results in an additional simplified equation of state, where the density is a function of the temperature and the composition only. Again, as was previously stated, the filtering is assumed to be linear. However, the assumption is invalid for the non-linear terms, and thus, cannot be described by filtered variables. These terms are gathered on the right-hand side and since they are unclosed must be modeled. These terms are usually referred to as subgrid scale (SGS) terms.

12.2 Turbulence Modeling

Isothermal Flow

In order to close the residual stress of eq. (12.2) and to analyze the sensitivity of the models on the flow field predictions two different subgrid-scale models are employed. The first is the classical Smagorinsky closure Smagorinsky, 1963. This approach models the unresolved stress tensor $\tau_{ij} = \overline{u_i u_j} - \bar{u}_i \bar{u}_j$ by using the BOUSSINESQ hypothesis, in which the effect of the unresolved turbulence on the large-scale flow manifests as an increase in the viscosity:

$$\tau_{ij} = \frac{2}{3} k \delta_{ij} - 2\nu_t \left(\overline{S}_{ij} - \frac{1}{3} \overline{S}_{kk} \delta_{ij} \right) . \tag{12.8}$$

Here $k = \overline{u_i u_i}$ is the turbulent kinetic energy and ν_t the turbulent kinematic viscosity. Whereas the shear strain tensor can be written as:

$$\overline{S_{ij}} = \frac{1}{2} \left(\frac{\partial \overline{u}_i}{\partial x_j} + \frac{\partial \overline{u}_j}{\partial x_i} \right) . \tag{12.9}$$

By applying a dimensional analysis the form of the subgrid-scale eddy viscosity can be derived:

$$\nu_t = {C_s}^2 \Delta^2 \sqrt{\overline{S}_{ij} \overline{S}_{ij}} \, , \tag{12.10}$$

where C_s is a model parameter and Δ is the filter length scale. According to Smagorinsky, 1963 the Smagorinsky constant C_s is set to $C_s = 0.1683$.

The second subgrid-scale model is based on a spatial high-pass filter to prevent large scales from contributing to the eddy viscosity. Thus, the model is less sensitive to low-frequency modes. The filter is based on the formulations of Sagaut et al. (2000) and describes the subgrid-scale eddy viscosity as

$$\nu_t = C_3 \, \Delta^2 \sqrt{\frac{1}{2} \left(\frac{\partial \mathrm{HP}^{(n)}(\bar{u}_i)}{\partial x_j} + \frac{\partial \mathrm{HP}^{(n)}(\bar{u}_j)}{\partial x_i} \right)} . \tag{12.11}$$

The filter $\mathrm{HP}^{(n)}(\bar{u})$ is explained in detail by Sagaut et al. (2000). The constant C_3 can be expressed by:

$$C_3 = C_1 \sqrt{\frac{B + 3.0 - m}{A(3.0 - m)}}, \tag{12.12}$$

with $C_1 = 0.01$ and $m = \frac{5}{3}$. It was shown by Sagaut et al. (2000) that for an LES of a spatially growing boundary layer, it yields $A = 40^n$, $B = 3.05 \cdot n$, and $n = 3$.

Reacting Flow

For the reactive flow also the classical Smagorinsky approach (Smagorinsky, 1963) as for the isothermal flow was used. Thus, the formulation for the turbulent viscosity ν_t is equal to eq. (12.10). The filter length scale is the cubic root of the local grid cell volume. The Smagorinsky constant C_s was set to $C_s = 0.1683$.

12.3 Combustion Modeling

Addressing turbulent combustion spans a broad range of disciplines. At the heart of the challenge is the broad range of length and time scales spanned by the combustion processes and the degree of coupling between these processes across all scales (Echekki et al., 2011). Bilger et al. (2005) stated in his comprehensive publication about turbulent combustion that remarkable advances have been made in turbulent non-premixed combustion, which can be closely associated with a series of international workshop on these topics. However, he further stated that there is no generally accepted set of experiments for the study of turbulent premixed flames. The much stronger coupling between chemistry and turbulence makes clear why accurate modeling of turbulent premixed combustion is still challenging. In turbulent flames a wide range of coupled problems have to be considered (Veynante, 2002):

- The flow field properties must be well known. In particular, all transfer phenomena occurring in turbulent flames (i.e., heat transfer, molecular diffusion, convection, turbulent transport) must be carefully described.
- A sufficient detailed kinetic reaction scheme is necessary to precisely describe the formation of combustion products and educts, ignition, heat release, and the extinction within reaction zones.
- For multiphase problems the spatial distribution of gaseous reactants depends on the breakdown, vaporization, turbulent mixing, and the droplet combustion of the liquid sheets.
- Radiative heat transfer is produced in the flame, and is in particular important when the formation of soot occurs.

Turbulent combustion modeling is therefore a very broad subject. In order to model such strongly coupled systems different modeling avenues have been followed up. In many respects these strategies have been successful for a large class of problems, and thus, enable the use of Computational Fluid Dynamics (CFD) for the design of combustion devices. These strategies have been subject of a large body of literature. A comprehensive overview on the topic is given in the reviews by Bilger et al. (2005), Bray (1996), Pitsch (2006), Pope (2013), and Veynante (2002).

Due to computational costs, the traditional strategy is based on Reynolds-averaged Navier-Stokes (RANS) and associated equations for scalar transport. Although Large Eddy Simulation (LES) is more expensive in terms of computationally costs it offers the advantages over the RANS framework that it resolves the large-scale motion directly, which contain the most

turbulent kinetic energy. Additionally, LES predicts the scalar mixing process and dissipation rates with considerably improved accuracy compared to RANS, which is of significant importance for reaction modeling (Pitsch, 2002). Thus, the usage of LES increasingly becomes a viable modeling framework for practical combustion flows incorporating unsteady flow effects. For LES the main issue lies in closing the residual terms in the filtered species equations (eq. (12.6)) containing the filtered reaction rates $\overline{\dot{\omega}}$. These are non-linear functions of species concentration and temperature. Different avenues have been used for modeling the filtered reaction rates, starting by extending Reynolds-Averaged Navier-Stokes (RANS) combustion models to LES applications. Recently modern methods have been proposed that were specifically designed for the LES framework (Poinsot et al., 2005).
Baudoin et al. (2009) classified the different combustion models into four categories, whereby this list does not claim to be exhaustive:

1. Models based on turbulent mixing descriptions.
2. Models based on flame front topology.
3. Models based on one-point statistical probability density functions or geometrical flame surface analysis.
4. Models based on finite chemistry.

Turbulence mixing models are usually a direct extension of RANS models, based on the assumption that the turbulent mixing rather controls the combustion process than the chemical reaction rates. Examples of such models include the Eddy Break-Up Model (EBU) (Spalding, 1971) and the Eddy Dissipation Concept (EDC) (Giacomazzi et al., 2004). The flame front topology approach is developed for flames that fall in the flamelet region or thin reaction regimes. It is based on the assumption that the reaction layer is smaller than the Kolmogorov length scale. Meaning for premixed combustion that the flame front is wrinkled but that eddies do not affect the flame front significantly. Hence, the local flame structure is similar to a one-dimensional flame, which allows to decouple the chemistry and the flow and solve them separately. The main issue for these models lies in tracking the propagating flame front, for which a progress variable is introduced. Representatives of this modeling approach can be found in numerous publications (Duwig et al., 2005; Duwig et al., 2007b; Fureby, 2007; Peters, 1984; Pitsch et al., 2003). Probability Density Function (PDF) and PDF-like models use a statistical approach to close the residual terms. The probability density function of all variables (that are solved via the PDF) have to be expressed either experimental, by Direct Numerical Simulation (DNS) or estimated by using transported or presumed probability functions. According to Pope (2013) the Linear-Eddy Model (LEM) (Kerstein, 1988; Sankaran et al., 2000; Sen et al., 2010) and the One-Dimensional Turbulence (ODT) (Echekki et al., 2011) are parts of these categories. The LEM locally reduces the flame front to a one-dimensional problem in the direction of the temperature gradient. To resolve the flame front along the normal turbulence effects are included using stochastic rearrangements. The model allows for any type of flame, including extinction/re-ignition, but at very high computational costs. Also the transported Filtered Density Function (FDF) models as part of the PDF group (Duwig et al., 2008b; Raman et al., 2007) should be mentioned. In the finite rate chemistry models, different methods are used to estimate the filtered reaction rates. The main assumption is that the oxidation process is

time-dependent, and thus, not infinitely fast. So, turbulence can affect the flame front. As part of the finite rate chemistry group the Implicit Large Eddy Simulation (ILES) and the Thickened Flame Model (TFM) are explained in detail in the next section (sections 12.3.1 and 12.3.2). Another representative of this group is the Partially Stirred Reactor (PaSR) model. In this model the flow is divided into a fine structures and surroundings. In the fine structures most of the dissipation, and therefore, reactions take place Fureby, 2007. All of the finite chemistry models have in common that they require at least a two-step reaction mechanism and a priori not restricted to a single reaction regime. Bilger et al. (2005) identified recent trends in turbulent combustion modeling. These trends are motivated by the need to represent important finite rate and non-equilibrium chemistry effects. While most of the presented combustion models have counter-parts in the RANS framework, the ILES, TFM, and the LEM are solely valid for LES applications.

The investigated flame in the present paper is characterized by a relatively high *Karlovitz* number as a large amount of steam is added to the reactants, which spreads the heat release peak. The calculations of the *Karlovitz* number Ka and *Damköhler* number Da for the different steam levels is listed in Table 12.1. The velocity fluctuation u' was calculated from incompressible LES. The thermal thickness δ_L^0 and the laminar flame velocity S_L were calculated with the one-dimensional approach mentioned in chapter 2.

Table 12.1: *Karlovitz* and *Damköhler* numbers for the three considered cases.

Condition		Case 1 (Dry)	Case 2 (Moderate-Wet)	Case 3 (Ultra-Wet)
Steam content	Ω	0%	20%	50%
Equivalence ratio	Φ	0.5	0.6	0.75
Inlet temperature	T_u	293 K	463 K	633 K
Flame temperature	T_b	1643 K	1623 K	1643 K
Laminar burning velocity	S_l	0.5 m/s	0.81 m/s	1.37 m/s
Thermal thickness	δ_L^0	$4.4 \cdot 10^{-4}$mm	$4.8 \cdot 10^{-4}$mm	$5.4 \cdot 10^{-4}$mm
Flame thickening factor	F	2.1	2.5	2.3
Karlovitz number	Ka	8	9	8
Damköhler number	Da	3	3	3

With such high *Karlovitz* and *Damköhler* numbers, the flame front is prone to turbulent fluctuations, however the inner oxidation layer is not affected by the small scales. Thus, the flame lies in the *thickened-wrinkled flame* regime (see Figure 9.2) and is definitely subject to strong finite rate chemistry effects. It is noteworthy that the presented *Karlovitz* and *Damköhler* numbers are global estimates, while turbulence is intermittent and locally. Thus, one would have a variation of Ka with space and time and as reported by Duwig et al. (2013) this can result in variations up to two orders of magnitude. Suitable candidates for resolving high *Karlovitz* and *Damköhler* numbers are ILES, TFM, LEM, EDC, PaSR and FDF. The FDF and LEM are of high computational costs when used with LES, while presumed FDF, TFM and ILES keep the Central Processing Unit (CPU) costs at reasonable levels. Further suitable

candidates are the EDC and PaSR, both demand for an intermediate CPU costs and thus, are of particular interest when dealing with complex burner geometries. However, the present study focus on using ILES and TFM, which have the attractive feature of handling complex chemistry and are assumed to be an appealing compromise between accuracy and computational burden. In addition, it was shown in a comprehensive sensitivity analysis by Dodoulas et al. (2013) that the FDF does not necessarily performs better than the ILES.

12.3.1 Implicit Large Eddy Simulation

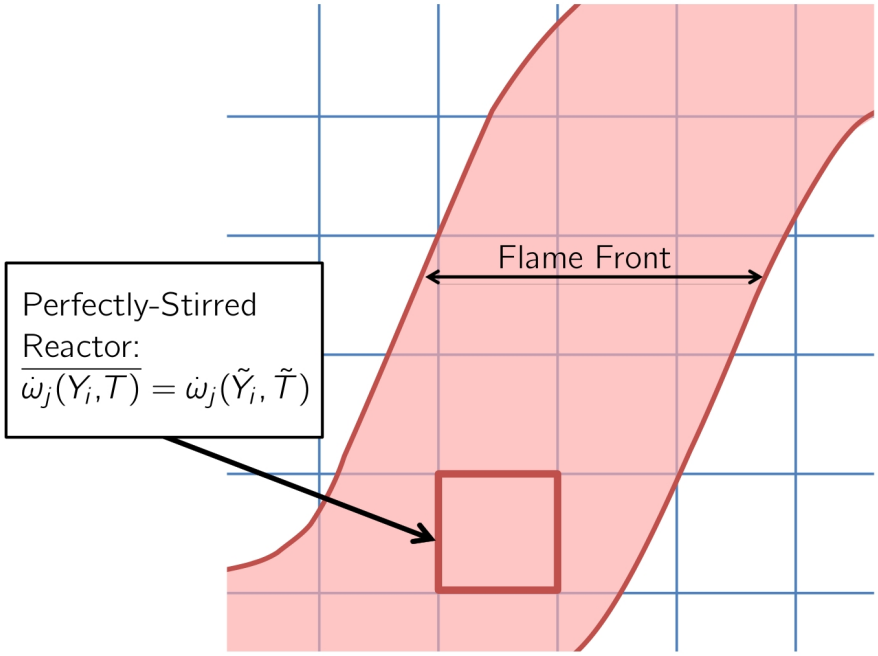

Figure 12.1: Illustration of the ILES model. The residual terms of the filtered reaction rates are simply computed through an Arrhenius expression. Thus, the basic assumption is that each cell is a perfectly stirred reactor.

The simplest possibility to close Equation 12.6 is to directly compute the reaction rate for each species through an Arrhenius expression. This model is usually referred to Implicit LES (ILES) or sometimes Monotonically Integrated LES (MILES). According to Duwig et al. (2011), Duwig et al. (2008b), Fureby (2007), and Fureby (1999) the filtered reaction terms for species k is given by:

$$\overline{\dot{\omega}_k(Y_i,T)} = \dot{\omega}_k\left(\tilde{Y}_i,\tilde{T}\right) \ . \tag{12.13}$$

The basic assumption behind ILES is that each computational cell is a perfectly-stirred reactor, and hence, that the subgrid mixing is faster than chemical reactions. An illustration of the ILES model is given in Figure 12.1. As reported by Duwig et al. (2011) the assumption is reasonable if the *Karlovitz* number is relatively high and the mesh resolution sufficient. In other words, a very intense subgrid mixing is required to ensure that the filter box, or LES grid cell, is

homogeneous. It was shown in previous studies (Krüger et al., 2011b; Krüger et al., 2013) that the ILES model is sufficient for similar configurations with high steam dilution, however, in these studies methane was used as fuel. Due to the lower laminar burning velocity of methane a similar configuration leads to a higher *Karlovitz* number. The flame thickening factor F used in the TFM is another measure for the validity of the ILES. The factor F is usually computed in order to be able to resolve the flame front on $3-5$ grid points:

$$F \sim 3\Delta/\delta_L^0\,. \tag{12.14}$$

Here, $\Delta = 4 \cdot 10^{-4}$mm (see Table 12.1) represents a characteristic element size in the shear layer. Usually F is less sensitive than the local *Damköhler* number Da, as it does not account for the subgrid stirring, though the ILES domain of validity corresponds to F close to or below 3. The calculations of F for the three cases as listed in Table 12.1 indicates that the present flame falls well into the domain of validity of ILES and the reaction brush is indeed resolved on the LES grid.
Equation 12.13 would fail in the RANS framework, but is valid for laminar flow simulation and direct numerical simulation (DNS). The validity of Equation 12.13 with LES depends on the relative grid resolution and also on the subgrid physics. Although using a typical LES-grid, far from DNS, Equation 12.13 was shown to approximate the reaction rate reasonably well, as reported in Duwig et al. (2008b), Fureby (2007), Goldin (2005), and Grinstein et al. (1994). These studies suggest that ILES is an eligible approach for combustion simulation and that it may perform equally well compared to other closures.

12.3.2 Thickened Flame Model

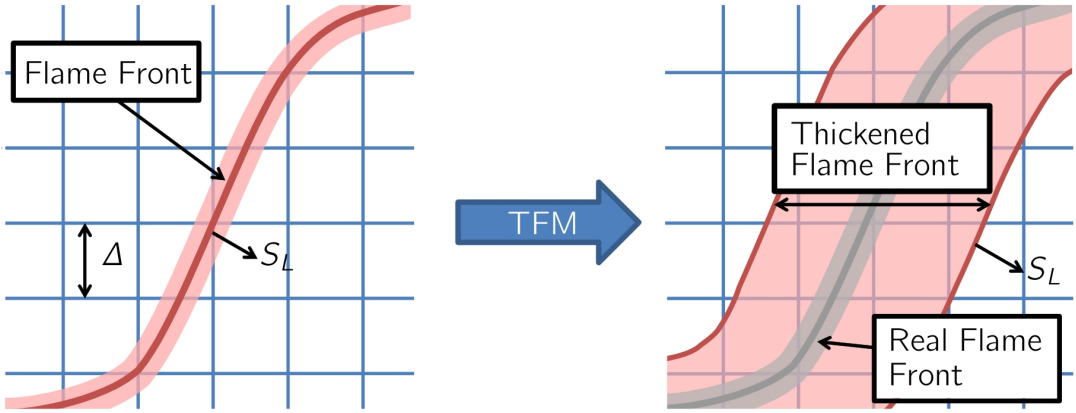

Figure 12.2: Illustration of the TFM model. It artificially thickens the flame front, in order to resolve the flame front on the LES grid.

The main idea behind the *Thickened Flame Model* (TFM) the artificially thickening of the flame front, in order to resolve the flame front on a grid which would otherwise be to coarse. An illustration of the model is presented in Figure 12.2. The model was originally proposed by

Butler et al. (1977) and is a well-established closure (Butler et al., 1977; Colin et al., 2000; Legier et al., 2000; Poinsot et al., 2005; Selle et al., 2004). Based on the laminar theory the flame speed S_l and thickness δ_l^0 can be expressed as (Poinsot et al., 2005):

$$S_l \propto \sqrt{\alpha A}\,, \qquad \delta_l^0 \propto \frac{\alpha}{S_l} = \sqrt{\frac{\alpha}{A}}\,, \tag{12.15}$$

where α is the thermal diffusivity and A the pre-exponential factor. By multiplying the thermal diffusivity, and simultaneously dividing A with the same factor F, the flame speed keeps constant, while the flame thickness is artificially increased. However, this also decreases the *Damköhler* number Da by the factor of F. To correct this Colin et al. (2000) introduced the efficiency function E, which accounts for the subgrid wrinkling to adjust the unresolved features. In the TFM approach the filtered reaction rate is handled by the usage of the Arrhenius expression Equation 3.14. The filtered reaction rate reads:

$$\overline{\dot{\omega}_k\left(Y_j, T\right)} = \frac{E}{F}\dot{\omega}_k\left(\tilde{Y}_j, \tilde{T}\right)\,. \tag{12.16}$$

Here F is the thickening factor and E the efficiency function. The unresolved scalar transport D_{TFM} is modeled similarly, by an effective diffusion related to the molecular diffusion coefficient D_i:

$$D_{TFM} = EFD_k\,, \tag{12.17}$$

If Equation 12.16, Equation 12.17, and the filtered species balance Equation 12.6 are combined it results in the species balance for the *Thickened Flame Model*:

$$\frac{\partial \overline{\varrho}\tilde{Y}_k}{\partial t} + \frac{\partial}{\partial x_i}\left(\overline{\varrho}\tilde{u}_i\tilde{Y}_k\right) = \frac{\partial}{\partial x_i}\left[\overline{\varrho}\; EFD_k\frac{\partial \tilde{Y}_k}{\partial x_i}\right] + \frac{E}{F}\;\dot{\omega}_k\left(\tilde{Y}_j, \tilde{T}\right). \tag{12.18}$$

The efficiency function $E \propto \Xi$ is modeled with concern to the flame wrinkling Ξ. The flame wrinkling is computed according to the Fractal Flame Wrinkling (FFW) approach by Fureby (2005). The flame thickening is only needed where the flame is present, and therefore E is restricted to a minimal value of 1:

$$E \propto \Xi \propto \max\left(1, \left[\frac{u_\Delta}{S_l}\right]^\chi\right), \tag{12.19}$$

with the exponent χ being 0.3 and the subgrid velocity fluctuation u_Δ, which reads as:

$$u_\Delta = 2\left|\frac{\partial^2}{\partial x_i^2}\left(\epsilon_{ijk}\frac{\partial u_k}{\partial x_j}\right)\right|\Delta^3\,. \tag{12.20}$$

As stated previously subsection 12.3.1 the thickening factor F is usually computed on $3-5$ grid points (Duwig et al., 2011). The flame thickening is only necessary where the flame is present to ensure that $F = E = 1$, which is formally identical to the ILES closure. Additionally, the

thickening factor F is an indicator of the ILES closure, which complements the local *Damköhler* and *Karlovitz* number. As a consequence F may be computed in advance to a simulation and hence serve as an indicator for the validity of ILES. Whereas, F does not hold information related to turbulence intensity, F may be considered as a necessary but not adequate indicator of the potential validity of ILES. A more sophisticated version of the *Thickened Flame Model* has been reported by Legier et al. (2000), where the flame thickening factor F is computed dynamically.

12.4 Computational Setup

Isothermal Flow

The LES simulations are performed employing the open source framework OpenFOAM (version 1.7.x). In order to gain confidence in the numerical tools one goal of the isothermal investigation is to perform a sensitivity analysis to address the influence of the spatial mesh resolution and the subgrid-scale model. For the sensitivity analysis the same swirl intensity as in the gas fired test ($S_{th} = 0.7$) is used to ensure vortex breakdown and comparability. In order to determine the grid sensitivity, two different meshes are employed using the standard Smagorinsky subgrid-scale model. Both meshes are converted from unstructured tetrahedral grids with a prismatic boundary refinement along the walls into polyhedral meshes in order to reduce the cell/face ratio. The boundary layer refinement is not affected by the conversion and was created with 10 prism layers placed with logarithmically increasing distance normal to the wall (Georgiadis et al., 2009). This resulted in a first layer thickness of 0.1 mm. For the presented meshes the conversion reduces the number of cells by a factor of about 2.7 and an according bandwith reduction of about 49, while the number of faces remains almost constant. The baseline mesh consists of around 1.7 million grid points with about 90 cells per hydraulic diameter with a characteristic cell size in the shear layer of 0.3 mm. Thus, the smallest resolved scales are assumed to be in the inertial range of the turbulent spectrum and the grid is suitable for performing LES. The second mesh (*Fine*) exhibits about 140 cells per hydraulic diameter with a cell size of 0.2 mm in the shear layer and it features more than 6.9 million grid points. Both meshes are locally refined where high velocity gradients are expected as was observed in previous investigations (Krüger et al., 2011a). To give an idea of the resulting grids the baseline mesh is depicted in Figure 12.3. The figure shows the outline mesh as well as a cut through the domain. The cut through the domain illustrates the boundary layer refinement and the shear layer refinement downstream of the burner outlet where high gradients are expected. For the conversion the OpenFOAM tool *polyDualMesh* is used with and a feature angle of $79°$. In order to determine the influence of the subgrid-scale model the *filtered Smagorinsky* model (Sagaut et al., 2000) is also employed on the baseline mesh. The conditions for the sensitivity study are listed in Table 12.2. For all cases, the pressure velocity coupling is performed using the PISO algorithm as described by Issa (1986), ensuring that continuity is satisfied. Linear reconstruction is used to compute fluxes at the faces, securing second order accuracy for spatial derivates. Time derivates are treated using a second order upwind scheme and time integration is done implicitly in a sequential manner. Dirichlet boundary conditions are enforced at the inlet for all variables, except pressure, which uses a zero gradient condition (Neumann). Similarly, the outflow is treated using a zero gradient for all variables except for pressure, which uses a

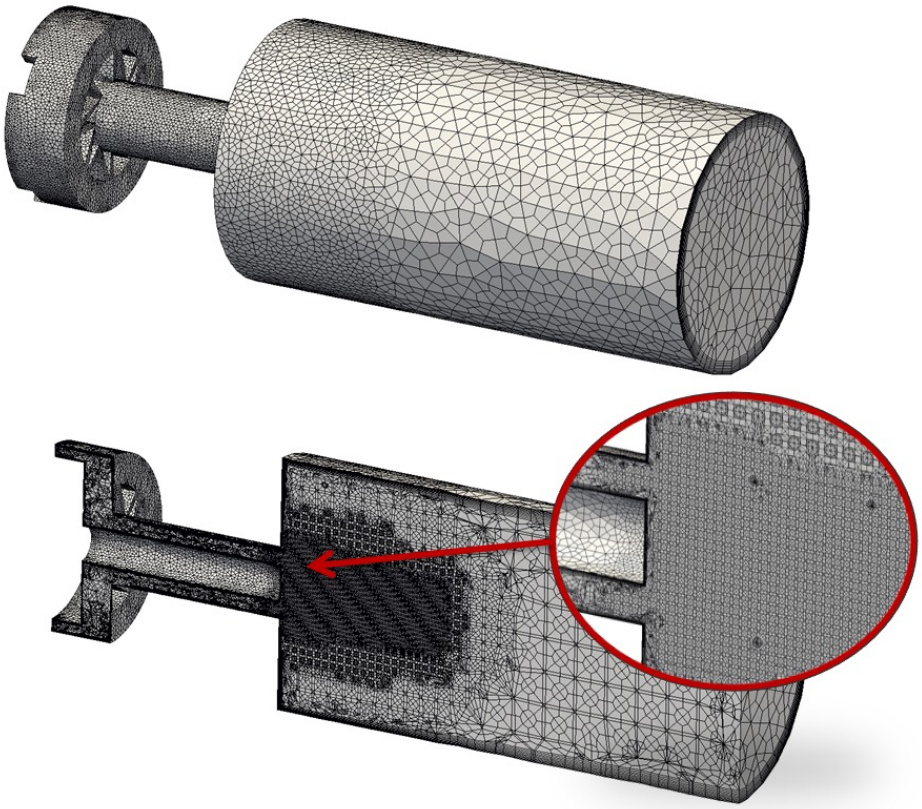

Figure 12.3: Presentation of the baseline mesh for the isothermal case.

Neumann condition. Non slip walls (zero velocity) are used with a zero gradient for the other variables. The LES simulations are computed with a constant average time step of 10^{-5}s in order to keep the maximum Courant number below $\mathrm{Co} = {}^{u \cdot \Delta t}/_{\Delta x} = 0.2$ and avoid numerical instabilities. This resulted in a characteristic Courant number in the shear layer of $\mathrm{Co} = 0.08$ for the baseline mesh. For the finer mesh the time step had to be slightly reduced. After a statistically steady state is reached averaging of the flow field was enabled. The results are time-averaged over 2 seconds, after a symmetrically averaged velocity field is reached.

Reacting Flow

As listed in Table 12.3 six computations are conducted with Reynolds numbers between $Re \approx 39{,}000$ and $Re \approx 67{,}000$. Even though a grid sensitivity is carried out for the isothermal case, the requirements regarding the mesh resolution is higher to resolve the flame front sufficiently. Therefore, the grid dependence is assessed another time with two different grids. Both meshes used within this thesis consist of unstructured polyhedral cells, and were converted from an unstructured tetrahedral mesh with a prismatic boundary refinement along the walls. This time ANSYS Fluent (Ver. 12) is tested for the conversion, to see if a better mesh quality can be achieved. Again, the boundary layer refinement is not affected by the conversion. The

Table 12.2: Presentation of the isothermal cases.

Condition		Case 1	Case 2	Case 3
Name		Smagorinsky	Smagorinsky 6M	filtered Smagorinsky
Fluid		Water	Water	Water
Swirl number	S_{th}	0.7	0.7	0.7
Inlet velocity	u_{in}	$0.6\,\mathrm{m/s}$	$0.6\,\mathrm{m/s}$	$0.6\,\mathrm{m/s}$
Bulk velocity	u_0	$1.3\,\mathrm{m/s}$	$1.3\,\mathrm{m/s}$	$1.3\,\mathrm{m/s}$
Kinematic viscosity	ν	$1.004 \cdot 10^{-6}\,\mathrm{m^2/s}$	$1.004 \cdot 10^{-6}\,\mathrm{m^2/s}$	$1.004 \cdot 10^{-6}\,\mathrm{m^2/s}$
Pressure	p	101.325 Pa	101.325 Pa	101.325 Pa
Reynolds number	Re	$33{,}000$	$33{,}000$	$33{,}000$
Subgrid-scale model		Smagorinsky	Smagorinsky	filtered Smagorinsky
Mesh		Baseline	Fine	Baseline
Grid points		$1.7 \cdot 10^6$	$6.9 \cdot 10^6$	$1.7 \cdot 10^6$
Grid faces		$4.8 \cdot 10^6$	$19.5 \cdot 10^6$	$4.8 \cdot 10^6$
Grid elements		$1.6 \cdot 10^6$	$6.5 \cdot 10^6$	$1.6 \cdot 10^6$

meshes are refined towards the inner shear layer of the inner recirculation zone, ensuring that the smaller cells are located where scalar and velocity gradients are expected to be large. For the *finer* mesh the grid resolution is almost doubled in the flame zone. The resulting *baseline* grid contains 1.1 million cells (3.9 million nodes) compared to 2.1 million (11.3 million nodes) on the *finer* mesh. The baseline mesh is presented in Figure 12.4. Apparently, the elements are distributed in a smoother way compared to the isothermal case (Figure 12.3), which is also reflected in the mesh quality due to the fact that Fluent smooths the mesh after the conversion. For the *baseline* mesh this resulted in a Taylor turbulent length scale of λ_f:

$$\overline{\left(\frac{\partial u_{ax}}{\partial x}\right)^2} = \frac{2u'^2}{\lambda_f^2} \approx 0.08 D_h\,. \tag{12.21}$$

Thus, the smallest resolved scales are in the inertial range of the turbulent spectrum and the grid is suitable for performing LES. The second grid was refined in the area of the inner shear layer. Both meshes are used to perform a grid sensitivity study with ILES as combustion closure at dry conditions according to Table 12.3. As mentioned before, due to limited computational resources the length of the combustion chamber was shortened. Terhaar et al. (2012) reported that for an effective swirl number $S_{eff} \leq 0.3$ the flow can be considered to be supercritical, and thus, the outlet has only a small influence on the upstream flow field. The effective swirl number S_{eff} can be expressed by the temperature ratio obtained using calculated flame T_b and inlet temperature T_u:

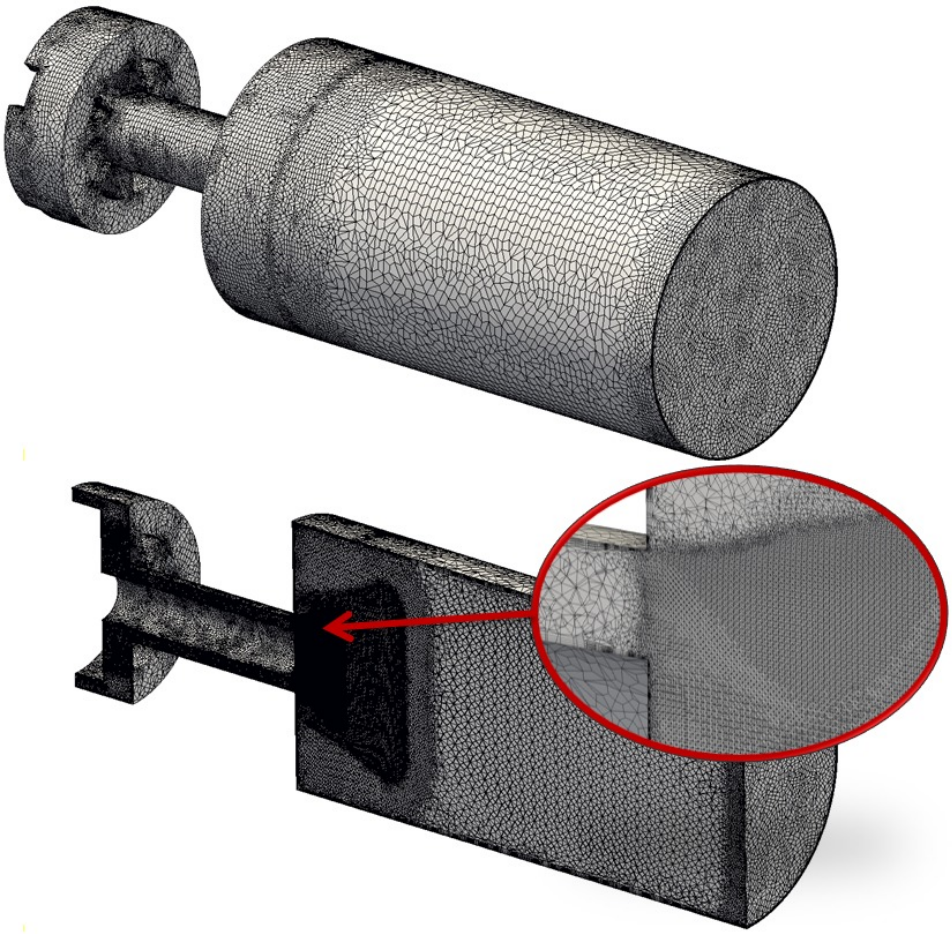

Figure 12.4: Presentation of the baseline mesh for the reacting case.

$$S_{eff} = S_{th}{}^{T_u}/_{T_b} = , \tag{12.22}$$

With a theoretical swirl number of $S_{th} = 0.7$ and the temperatures listed in Table 12.2 a maximum effective swirl number of $S_{eff} = 0.26$ can be determined for the ultra-wet case ($\Omega = 0.5$), and thus, the flow can be considered supercritical. In addition to the grid study the performance of the ILES is compared to the TFM combustion closure for different values of F. Furthermore, the influence of steam is assessed with several steam levels.

In addition to the operating conditions as listed in Table 12.3, a wall temperature ($T = 900\,\mathrm{K}$) was set for the walls of the combustion chamber, since it was observed in previous investigations (Krüger et al., 2011b; Krüger et al., 2011c) that heat losses through the walls have a major impact on the flame prediction. The wall temperature was derived from experiments.

The simulations are also carried out using the open source framework OpenFOAM (version 1.6.x). As for the isothermal case the reacting simulations are performed applying the PISO

algorithm (Issa, 1986) to ensure that continuity is satisfied. For all spatial derivatives, except for the convective terms in the enthalpy and the mass fraction equations, second order differencing is used. The convective terms are treated using a second order accurate Total Variation Diminishing Scheme (TVD) for avoiding non-physical over-shoots (Jasak, 1996; Sweby et al., 1984). Time derivatives are treated by applying a second order upwind scheme and time integration is done implicitly in a sequential manner. Dirichlet boundary conditions are enforced at the inlet for all variables except for the pressure, which uses a zero-gradient condition (Neumann). Similarly, the out flow is treated using zero-gradient for all variables. Non-slip walls (zero velocity) are used with zero gradient for the other variables except for the temperature, for which a constant wall temperature was set. The LES computations are run with an adjustable time step to ensure a maximum Courant-Friedrichs-Lewy number below $\mathrm{Co} < 0.2$. This results in an averaged time step of $\Delta t = 10^{-7}$s. The results are time-averaged over 0.05 s physical seconds after reaching a statistically steady state and show a symmetrically averaged velocity field.

Table 12.3: Presentation of the reacting cases.

Condition		ILES ($\Omega = 0.0$)	ILES (Fine)	TFM ($F = 1.5$)	TFM ($F = 2.1$)	ILES ($\Omega = 0.2$)	ILES ($\Omega = 0.5$)
Combustion closure		ILES	ILES	TFM	TFM	ILES	ILES
Steam content	Ω	0.1	0.1	0.1	0.1	20%	50%
Equivalence ratio	Φ	0.5	0.5	0.5	0.5	0.6	0.75
Inlet velocity	u_{in}	14.94 m/s	14.94 m/s	14.94 m/s	14.94 m/s	26.55 m/s	38.89 m/s
Bulk velocity	u_0	34.71 m/s	34.71 m/s	34.71 m/s	34.71 m/s	61.65 m/s	88.37 m/s
Pressure	p	101.325 Pa	101.325 Pa	101.325 Pa	101.325 Pa	101.325 Pa	101.325 Pa
Reynolds number	Re	$39{,}000$	$39{,}000$	$39{,}000$	$39{,}000$	$31{,}000$	$26{,}000$
Inlet temperature	T_u	293 K	293 K	293 K	293 K	463 K	633 K
Flame temperature	T_b	1643 K	1643 K	1643 K	1643 K	1623 K	1643 K
Wall temperature	T	900 K	900 K	900 K	900 K	900 K	900 K
Mesh		Baseline	Fine	Baseline	Baseline	Baseline	Baseline
Grid points		$3.9 \cdot 10^6$	$11.3 \cdot 10^6$	$3.9 \cdot 10^6$	$3.9 \cdot 10^6$	$3.9 \cdot 10^6$	$3.9 \cdot 10^6$
Grid faces		$5.6 \cdot 10^6$	$13.7 \cdot 10^6$	$5.6 \cdot 10^6$	$5.6 \cdot 10^6$	$5.6 \cdot 10^6$	$5.6 \cdot 10^6$
Grid elements		$1.1 \cdot 10^6$	$2.1 \cdot 10^6$	$1.1 \cdot 10^6$	$1.1 \cdot 10^6$	$1.1 \cdot 10^6$	$1.1 \cdot 10^6$

13

Results and Discussion

13.1 Isothermal Flow

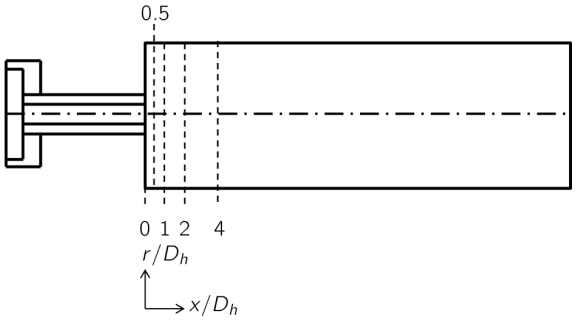

Figure 13.1: Schematic of the profile positions for the discussion.

The following section presents the results of the isothermal LES simulations. For the discussion, velocity plots are shown at several axial positions. These locations are depicted in Figure 13.1. The quantitative results presented below are normalized using the mean bulk velocity $u_0 = 1.3\,\mathrm{m/s}$ at the burner exit and all coordinates are normalized by the hydraulic diameter $D_h = 27.5\,\mathrm{mm}$.

13.1.1 Sensitivity Analysis

LES is only capable of resolving turbulent scales that are larger than the grid spacing. Therefore, the level of uncertainty in a numerical simulation is dependent upon grid quality, it is essential to verify grid convergence. A lack of grid convergence in a numerical solution may result in large discretization errors in the spatial and temporal domain. Usually, grid convergence is satisfied when the numerical solution becomes nearly insensitive to further refining the spatial resolution. Due to computational costs limitations, we consider reasonable but significant cell size variations when applying LES. Hence, the present study uses two grid resolutions as presented earlier. In addition, a second subgrid-scale model, denoted as *filtered Smagorinsky* was used. This model is intended to prevent large scales from contributing to the eddy viscosity.

The sensitivity analysis was conducted for the high swirling case in order to avoid the vicinity of the bifurcation as it was observed in past experiments. Figure 13.2 provides a comparison of the measured and simulated streamwise flow at several axial locations. It is evident that an inner recirculation zone establishes near the burner exit, due to vortex breakdown. This

leads to high velocity gradients in the shear layer between the inner recirculation zone and the surrounding swirling flow. The gradient decreases further downstream. Furthermore, an outer recirculation zone establishes at the corner of the combustion chamber walls and the burner plenum. This outer recirculation zone has the shape of a ring vortex and is fed by the surrounding swirling flow. As can be seen in Figure 13.2, the negative axial velocities within the inner recirculation zone are slightly overestimated up to an axial position of $x/D_h = 1.0$ for the cases with the coarse mesh, indicating that the unresolved scales have an impact on the recirculation near the centerline.

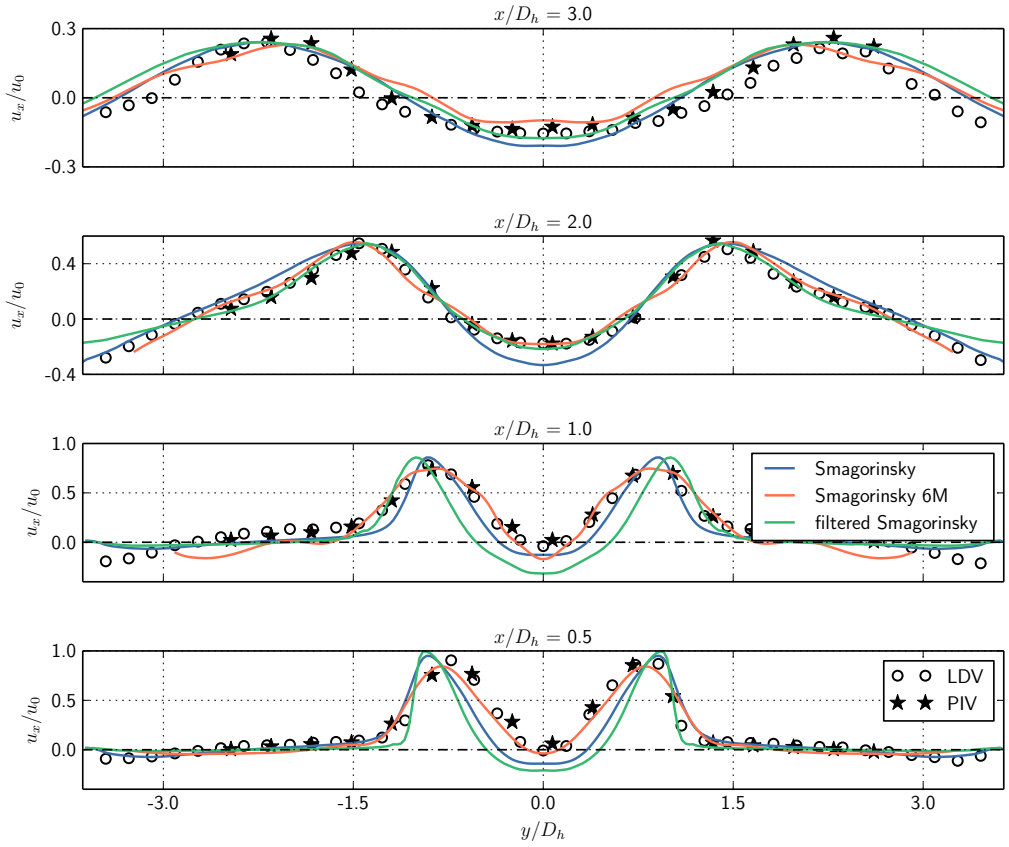

Figure 13.2: Axial velocity profiles at different axial positions for different subgrid models.

Beside some small differences, the surrounding swirling flow is well captured and the simulations are in line with the experimental data. Figure 13.3 presents the axial velocity fluctuations. The simulations are in close agreement with the measurements and only differ in the shear-layer and in the inner recirculation zone, where one would expect the highest uncertainties. Near the burner exit all three models underestimate the fluctuation level in the inner recirculation zone. Further downstream this behavior changes and the fluctuation level in the reverse flow is slightly overestimated. The *Smagorinsky* and the *Smagorinsky 6M* case are close to the measurements. However, the differences between the three simulations are rather small and all three cases predict the central recirculation zone both in terms of magnitude and size. Consequently, the

baseline grid (denoted as *Smagorinsky*) is assumed to be sufficiently fine to predict the swirling flow accurately.

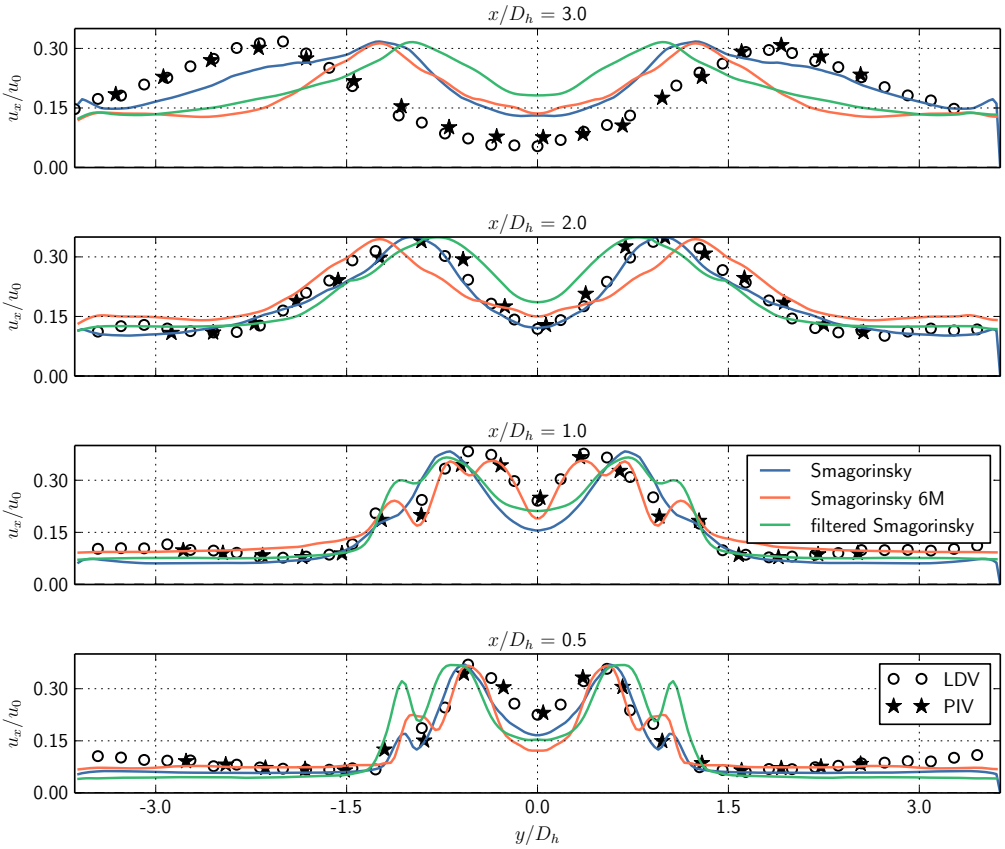

Figure 13.3: Turbulence profiles at different axial positions for different subgrid models.

In order to compare more than just averaged quantities, the highly unsteady behavior is also addressed. Therefore, the turbulent kinetic energy spectrum is computed for three points, as illustrated in Figure 13.4(a). The first point, denoted as point A, is located in the shear layer, point B in the region where the vortex breakdown occurs and point C is set downstream inside the inner recirculation zone. The energy spectrum describes the energy cascade (i.e., the energy transfer between large scales and small scales). The spectrum for the three points is plotted in Figure 13.4(b). The frequency spectrum is normalized by the hydraulic diameter and the bulk velocity, which results in the Strouhal number $\mathrm{St} = f \cdot D_h / u_0$. A comparison with the Kolmogorov-$5/3$ power law reveals that the simulation is able to predict the characteristics within the inertial subrange reasonably well. Additionally, a dominant frequency ($\mathrm{St} \approx 0.19$) is evident at all three locations, which implies the existence of a coherent structure. Using a similar configuration, García-Villalba et al. (2006) observed that a Precessing Vortex Core (PVC) can be related to a dominant frequency. However, they used a radial swirl generator with a higher swirl intensity ($S_{th} = 0.9$) resulting in a dominant frequency of $\mathrm{St} = 0.32$.

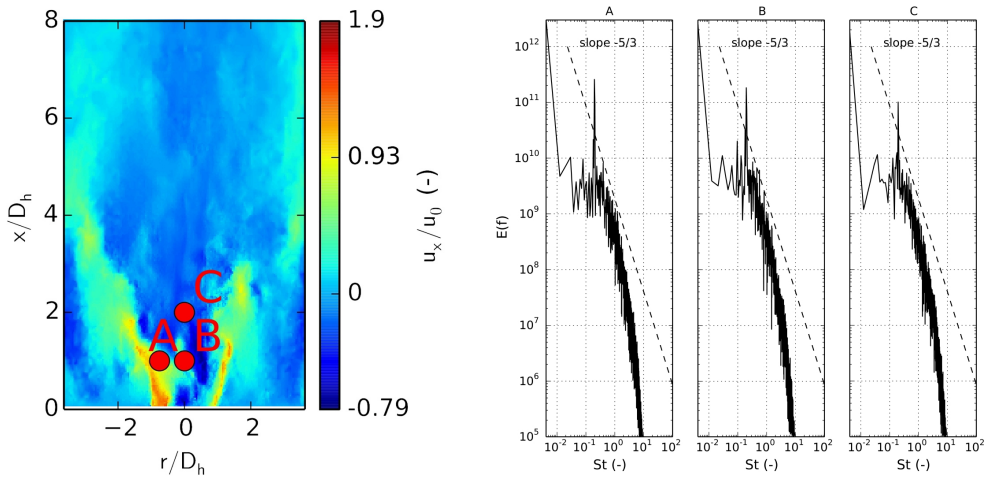

(a) Instantaneous velocity field. **(b)** Turbulent kinetic energy spectrum.

Figure 13.4: Instantaneous snapshot of the axial velocity component (left) and turbulent kinetic energy spectrum (right).

13.1.2 Flow Field Dynamics

Considering only averaged quantities to assess coherent structures is not sufficient, but the flow velocities can be decomposed into average, coherent, and stochastic turbulent fluctuations. Turbulent fluctuations can be isolated from the strong coherent structures by applying a Proper Orthogonal Decomposition (POD). The POD allows for extracting information from spatially and temporally resolved turbulent flow fields, and thus, is a key parameter for characterizing the mechanisms controlling the specific problem. Pioneer work was done by Lumley (1967), who started from the idea that flow structures containing the most kinetic energy are of the highest interest by projecting a turbulent flow field on a vector base that maximizes the turbulent kinetic energy. This allows for an accurate description of the turbulent flow by using only a few modes (Duwig et al., 2010; Lumley, 1967; Smith et al., 2005). The POD decomposition reads as follows:

$$Q^N(\vec{x},t) = a_0\Phi_0(\vec{x}) + \sum_{i=1}^{N} a_i(t)\Phi_i(\vec{x}). \tag{13.1}$$

Here the zero-th eigenfunction Φ_0 corresponds to the mean field and Φ_i are the base of the spatial eigenfunctions. The approximation of Q^N of the dataset Q converges to Q for N approaching infinity. The subsequent modes ($i > 0$) contain the fluctuation of the mean field, and by means of the time coefficients $a_i(t)$, one may reconstruct the given dynamics. Consequently, for a given vector Q containing the field variables, one seeks for a base of spatial eigenfunctions Φ. The base vectors have to satisfy the eigenvalue problem:

$$\langle Q(\vec{x},t) \cdot Q^T(\vec{x},t)\rangle\Phi(\vec{x}) = \hat{\lambda}\Phi(\vec{x}), \tag{13.2}$$

where the transposed vector is denoted by the superscript T and the time averaging by $\langle\cdot\rangle$. The vectors Φ are the eigenvectors of the temporal autocorrelation tensor. The eigenvalue $\hat{\lambda}_i$

stores the turbulent kinetic energy content of mode i. Directly solving Equation 13.2 would lead to a quadratic matrix of the dimension of the number of data points. *Sirovich's* method of snapshots (Sirovich, 1987) is used instead to reduce the computational cost. This method reduces the cost to an equivalent eigenvalue problem of the dimensions of the number of snap shots. Doing so reduces the computational cost significantly, due to the fact that in most cases the spatial resolution is much higher than the temporal resolution. In *Sirlovich's* method the modes are expressed as a linear combination of the samples:

$$\Phi_i(\vec{x}) = \frac{1}{\hat{\lambda}_i N} \sum_t e_i(t) Q(\vec{x},t), \tag{13.3}$$

where the coefficients e_i are solutions of the eigenvalue problem. The time coefficients are computed by projecting the snapshots on the modes:

$$a_i(t) = \Phi_i(\vec{x}) \cdot Q(\vec{x},t)\,. \tag{13.4}$$

Detailed information on implementing the POD method and applying it to turbulent flows may be found in various other studies (Duwig et al., 2007b; Duwig et al., 2008a; Kostas et al., 2005; Oberleithner et al., 2011; Perret et al., 2008).

The POD was processed for the PIV and LES in a longitudinal planar cross section. In

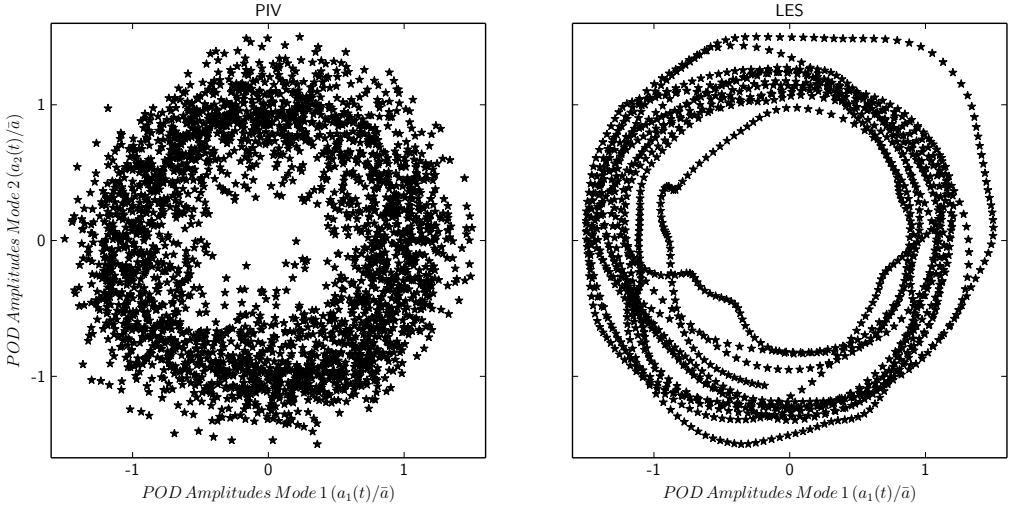

Figure 13.5: Time coefficients for the PIV (left) and the according LES (right) for a swirl number of $S_{th} = 0.7$.

Figure 13.5 the time coefficients of the first two modes for the experiments and LES are plotted. For both cases the coefficients form a circle, indicating the coupling of both modes with a phase shift of $\pi/2$. Figure 13.6 shows the time coefficients represented in Fourier space. Both modes exhibit a clear peak at the PVC frequency $St \approx 0.19$. The phase angle between both modes is $\pi/2$, indicating that both modes are orthogonal in space and time. The similarity becomes more evident as the *Power Density Spectrum* PDS of the mode coefficients $a_i(t)$, shown in Fig. Figure 13.6, yields the same Strouhal number as observed in the turbulent kinetic

energy spectrum (Figure 13.4(b)). The axial and radial velocity modes are provided for the

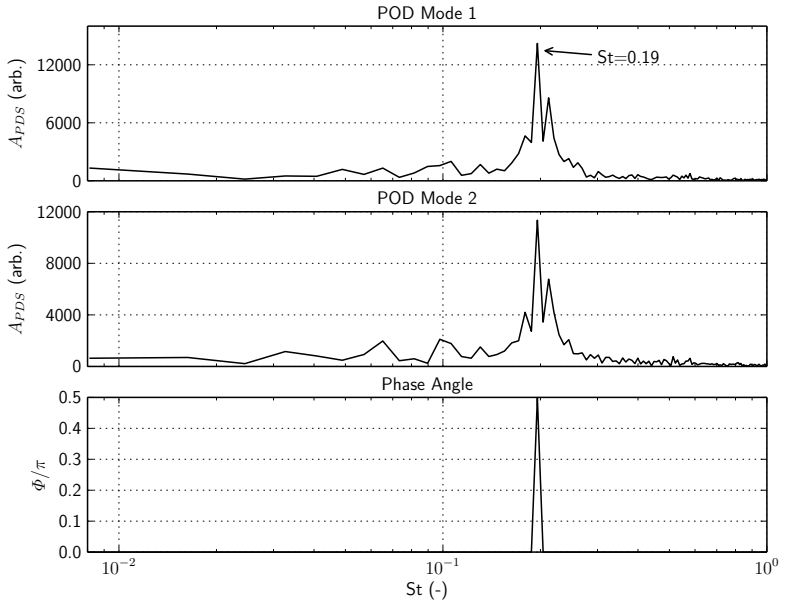

Figure 13.6: Fourier analysis of the POD time coefficients for the LES.

PIV and the LES in Figure 13.7. Obviously, an asymmetric pattern is evident for the axial PIV modes. The blue and the red structures alternate in pairs which is caused by vortices. It can be deduced that the plot shows a cut through a helical structure. This helix is accompanied by a second co-winding helix. The radial modes higher or equal to one appear to be symmetric, but due to the change of signs when transforming from a Cartesian to a cylindrical co-ordinate system, it is asymmetric too. Furthermore, for all modes the highest energy content is kept in the vortices near the burner exit, indicating a structure rotating around the center body. The LES shows similar results to the PIV. However, a faster energy decay for the vortices in axial direction is predicted. The faster energy decay may be explained by the underestimation of the turbulence levels downstream of the burner. This is supported by Figure 13.8, which shows the energy content of the first 20 modes for the PIV and for the LES. It is apparent that by far the most energy is captured in the first two POD modes. This indicates that the coherent structure that was linked to the PVC contains a large share of the total turbulent energy. As reported in several studies Dubief et al. (2000), García-Villalba et al. (2006), and Jehong et al. (1995) coherent structures are associated with the local minimum of the pressure field fluctuation. This "pressure criterion" allows for visualizing the helical structure. Figure 13.9 illustrates the helical instability through an isosurface of the minimum pressure distribution for an arbitrary time step. By subtracting the current pressure field from the mean field, a second structure appears, which is just the virtual counterpart of the structure. In addition, the coherent structure was reconstructed from the POD, by projecting an instantaneous three-dimensional velocity field onto the eigenvectors of the original POD. This technique is usually denoted as Extended Proper Orthogonal Decomposition (EPOD). In general, the EPOD associates a second set of physical quantity $\widehat{Q}(\vec{x},t)$ (scalar or vector) with the original set $Q(\vec{x},t)$ the POD was derived

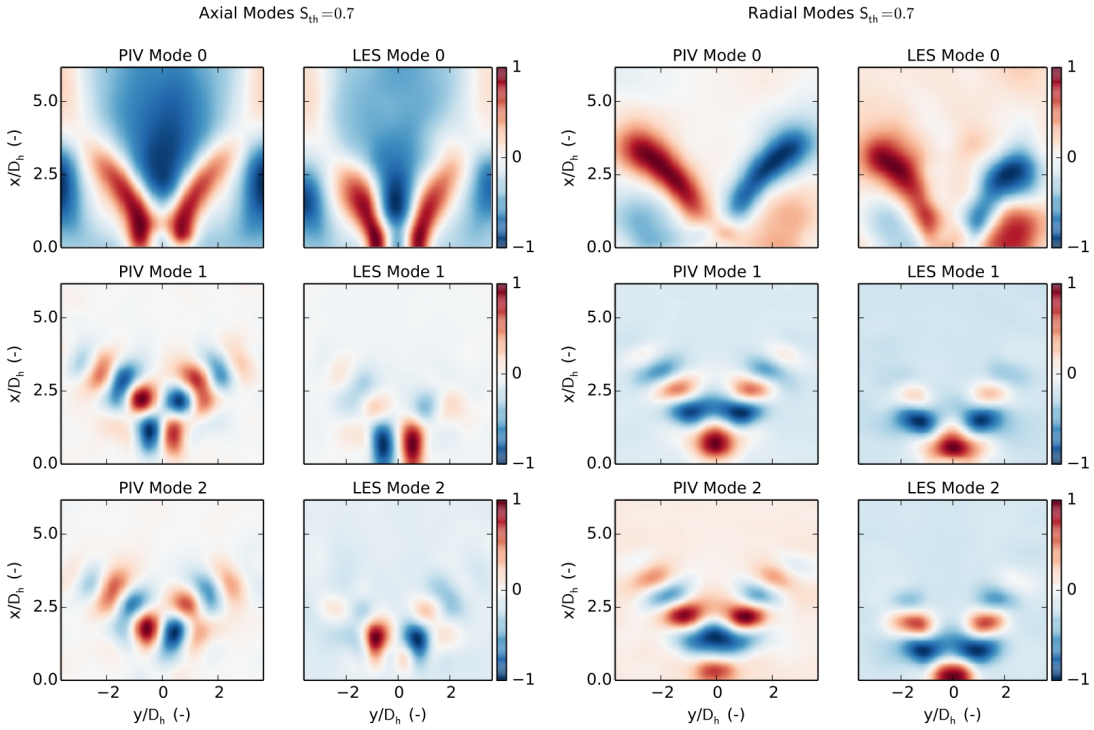

(a) axial **(b)** radial

Figure 13.7: First two POD velocity modes of the PIV and LES for axial and radial components.

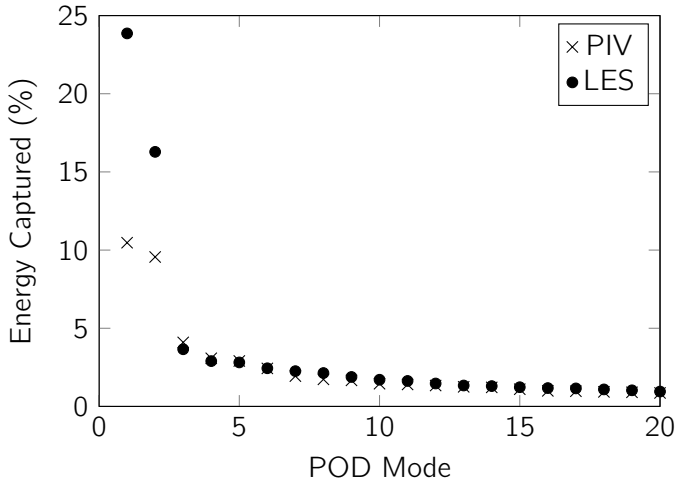

Figure 13.8: Energy content of the first 20 modes for experiment (PIV) and simulation (LES).

from. By projecting the second data set onto the eigenvectors of the original POD modes the procedure extracts the signal of $\widehat{Q}(\vec{x},t)$ which is correlated to the original POD modes (Duwig

et al., 2010; Duwig et al., 2009; Maurel et al., 2001). Thus, the extended modes Ψ reads as:

$$\Psi_i(\vec{x}) = \frac{1}{\hat{\lambda}_i N} \sum_t e_i(t)\, \widehat{Q}(\vec{x},t), \tag{13.5}$$

In the present study the three-dimensional velocity field was projected onto the eigenvectors of the original POD. The results of the extended POD are also depicted through an isosurface of the first and second axial mode distribution in Figure 13.9. Evidently, the reconstruction from the pressure criterion (opaque) identifies similar structures as the direct reconstruction from the modal analysis from an instantaneous time step (semitransparent). Due to the different choice of isosurface criterion the isosurfaces do not collapse. However, it is evident that both visualization techniques identify the same helical coherent structure rotating around the central axis and anchored at the center body. In the literature this coherent structure is usually denoted PVC.

In gas turbine combustors, the mode of fuel injection and mixing process largely influences the production of emissions, thermoacoustic instabilities, blowout or flashback. Freitag et al. (2006) conducted a Direct Numerical Simulation (DNS) for a similar burner (Tecflam burner) with a swirl number of $S_{th} = 0.64$ and a Reynolds number of $\mathrm{Re} = 5000$ for non-premixed

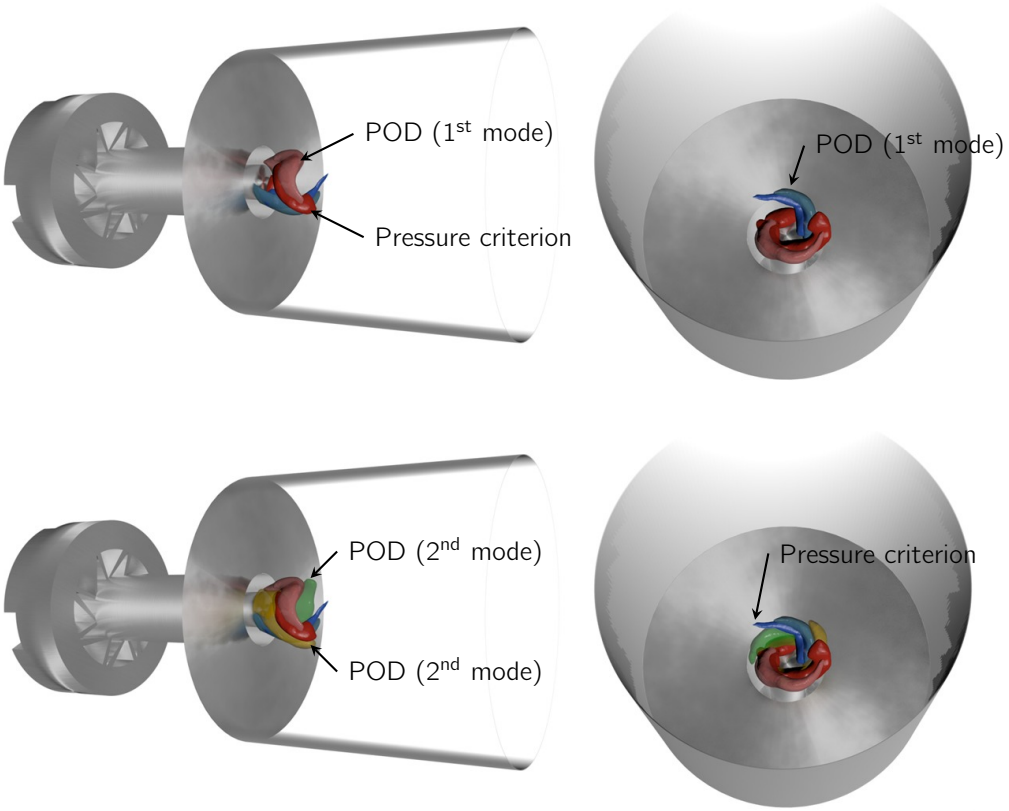

Figure 13.9: Visualization of the coherent structure.

and non-reacting conditions that the PVC enhances the fuel-air mixing significantly. Fröhlich et al. (2007) came to the same conclusion with performing an LES for a similar configuration. For a reacting case Stöhr et al. (2014) demonstrated experimentally that the PVC does not only cause an enhanced mixing of fuel and air, but also affects the mixing of the burned and unburned gases, which is also supported by the finding of Galley et al. (2011) and Stöhr et al. (2011). Furthermore, the PVC has an direct effect on the flame, by causing flame roll-up, flame stretch and local flame quenching (Stöhr et al., 2014). However, the influence of the PVC on the combustion process is still discussed and strongly depends on the investigated configuration. Thus, the influence of coherent structures on the combustion process has to be addressed individually. For the flame configurations presented in the next chapter no coherent structures were found.

> *In this chapter the near-field dynamics of an isothermal turbulent swirling jet in a generic swirl burner was numerically investigated and validated. The results were compared to experimental data obtained with PIV. Employing Large Eddy Simulations, the sensitivity was assessed regarding the grid resolution and the subgrid-scale modeling. Some minor discrepancies between the simulations and the experiments were found. However, the overall influence of the computational grid and the subgrid-scale models was found to be low. In general, the simulations showed a good agreement with the experimental data. The turbulent kinetic energy spectrum showed a dominant frequency which was identified as the motion of a coherent structure. In particular the coherent structure was determined as a helical instability triggered by a PVC was identified and represented by a pair of modes. In conclusion it was shown, that flow dynamics of a swirling flow are excellently captured qualitatively and quantitatively by applying LES with the Smagorinsky subgrid model. Thus, the turbulence modeling is found to be sufficient and gives confidence in simulating the reacting flow.*

13.2 Reacting Flow

In this section, the results of the sensitivity analysis regarding the grid resolution and the combustion closure are presented. Subsequently, the influence of steam content is assessed. Velocity profiles, flame shape and positions are compared to OH^* chemiluminescence recordings and PIV measurements. Finally, the results are summarized and conclusions are drawn. For the simulations the complete combined reaction scheme as is used, including Burke's reaction scheme, the OH^* chemiluminescence mechanism of Smith (Smith et al., 2002; Smith et al., 2005) and the San Diego $\mathrm{NO_x}$ subset is listed in Appendix A (p. 165).

13.2.1 Sensitivity Analysis

As previously stated, LES is only capable of resolving turbulent scales that are larger than the grid spacing. Thus, the level of uncertainty depends on the grid quality and so it is essential to verify grid convergence. Therefore, the sensitivity of the results to spatial resolution is presented in the first step. The sensitivity of the solution to the grid resolution and the combustion closure is investigated by comparing velocity, density gradients, and OH^* species concentration. Due to the high computational costs, it is difficult to consider various large grid variations. Therefore, only two simulations are conducted. The findings of the isothermal investigation

in the previous chapter section 13.1 limit the grid resolution to a minimum value in order to sufficiently resolve the flow induced fluctuations sufficiently. The calculated thermal thickness as presented in Table 12.3 restricts the mesh resolution further to resolve the flame front with at least three grid points as is necessary for the ILES model. The first computation is performed with a "coarse" baseline mesh. Based on the "coarse" mesh a second "finer" mesh is used, for which the spatial density of the mesh is doubled in the zone where the main reactions and steep gradients are expected. The resulting mesh characteristics are depicted in section 12.4. Figure 13.10 presents a comparison of the measured and simulated mean axial

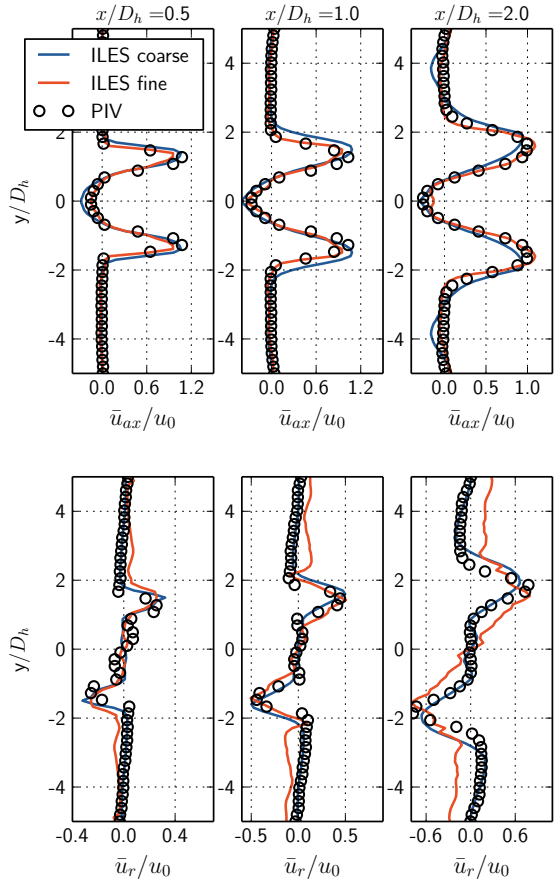

Figure 13.10: Mean axial and radial velocity profiles for different mesh sizes at different streamwise positions ($^x/_{D_h} = 0.5$; 1.0; 2.0) at ambient pressure ($\Omega = 0.0$, $\Phi = 0.5$, $T_u = 293\,\mathrm{K}$). Profiles are normalized by the burner exit velocity u_0.

and radial flow field at different axial positions. These locations are depicted in Figure 13.1 and the origin ($^x/_{D_h} = 0.0$) is located at the burner exit. The profiles are normalized by the burner exit velocity u_0. The computations are conducted at ambient pressure and temperature $T_u = 293\,\mathrm{K}$ with the ILES model at dry conditions ($\Omega = 0.0$) and an equivalence ratio of $\Phi = 0.5$, resulting in an adiabatic flame temperature of $T_{ad} = 1643\,\mathrm{K}$. The other operating conditions can be found in Table 12.3 (107). Near the burner exit an inner recirculation zone is established due to the vortex breakdown downstream of the sudden expansion. A shear layer is

formed between the inner recirculation and the surrounding swirling flow, where high gradients are present. The axial velocities are well in line with the measurements for the axial velocity. Near the burner exit, the negative axial velocity in the inner recirculation zone is slightly over predicted for the baseline case. Furthermore, at $^{x}/_{D_h} = 2.0$, the LES predicts the slope at the inner shear layer slightly different and reveals an external recirculation zone, which cannot be observed in the measurements. On the one hand, this could stem from higher measurement uncertainties near the walls, for example caused by reflections or seeding residuals. On the other hand, this could indicate a too short averaging time for the computations. The predicted radial velocities show for the fine case, a small deviation from the measurements. As is the case for the simulations, the radial velocity should become zero for the measurements at the walls. Again, the discrepancies with the experimental data can be attributed to reflections and adhesion of seeding particles near to the walls. Nevertheless, both simulations show a good agreement with the measurements. By applying a Sobel filter to the PIV images the flame

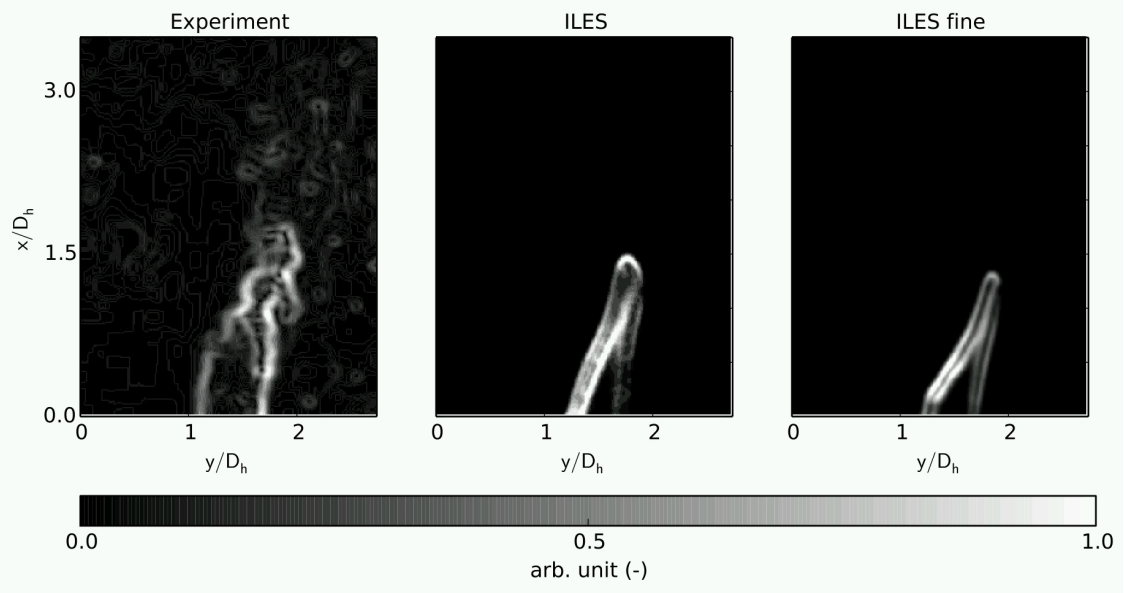

Figure 13.11: Visualization of the flame front. Processed PIV (left); Inverse temperature gradient of LES (middle and right).

front shape can be deduced from the step in the particle number density caused by the steep temperature increase in the reaction zone. Pfadler et al. (2007) as well as Tachibana et al. (2004) revealed that this method, yields nearly the same spatial position as the heat release measurements, the flame front wrinkling or the steepest slope in the OH^* distribution as is the case for planar OH Laser-Induced Fluorescence (LIF) measurements. In order to compare the simulations to the processed PIV recordings the inverse temperature gradient is used. Figure 13.11 shows the Sobel filtered PIV recordings and the according LES results. Apparently, the measurement exhibits small scales that are not predicted by the computations. Especially the wrinkling of the flame front is not predicted. However, the flame shape, position and angle are reproduced. It should be mentioned, that the small scales of the measurements are not necessarily directly linked with the density gradient, since the particles are subject to turbulence

and therefore, discrepancies cannot solely be attributed to the grid resolution. Nevertheless, the differences between the simulations are small. The flame is approximately represented

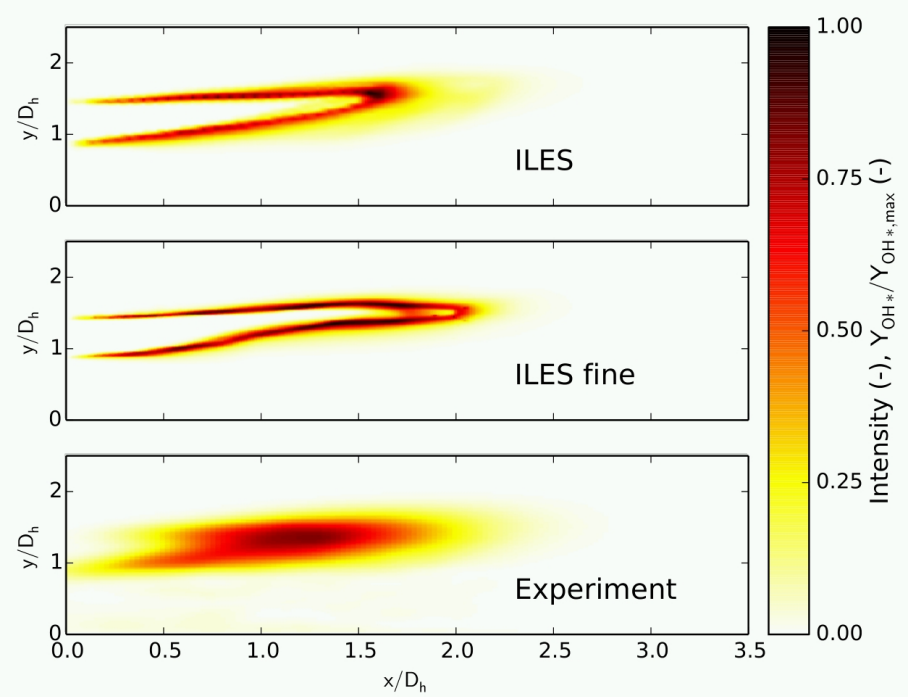

Figure 13.12: Comparison of the LES with OH^* chemiluminescence measurements ($\Omega = 0.0$, $\Phi = 0.5$, $T_u = 293\,K$). Top and middle: Slices of the normalized OH^* mass fractions (LES), Bottom: Processed Abel inversion of OH^* recordings (Exp.).

by the concentration of active OH radicals (Güthe et al., 2012). In order to compare the OH^* chemiluminescence measurements qualitatively with the computations, the recordings are transformed by an Abel inversion to give a view of the flame in a slice without losses induced by the integration through the line of sight. The algorithm is discussed in detail in Jaffe et al., 1991. Figure 13.12 shows the deconvoluted OH^* chemiluminescence recordings as well as streamwise slices of OH^* mass fraction of the LES. The LES predicts a non-reacting jet surrounded by a thin reaction layer with a steep gradient. The maximum OH^* concentration is located at the tip of the reaction layer, contrary to what is observed in the experiments. Compared to the computations the experiments show a shorter jet that leads to a more distributed main reaction zone with a weaker gradient. For the measurements as well as for the computations an area of low OH^* concentration is located downstream of the thin reaction layer, which is probably caused by convection. Due to the very small reaction layer thickness, the spatial resolution of the OH^* recordings is probably too low to resolve the gradients sufficiently. Nevertheless, the thin flame zone is in line with the previously presented findings, but could also be affected by higher mixing. Compared to the baseline case the simulation for the finer grid offers a thinner reaction layer. To finally address the question about the thickness and wrinkling of the flame front, more detailed flame front measurements (i.e., Planar Laser-Induced Fluorescence (PLIF) measurements) would be necessary, and are recommended for future investigations.

In conclusion, the flame shape and dimension is well represented by the computations. Due to the fact, that both grids showed similar results, the baseline mesh will be used for the following investigations. To assess the sensitivity of the solution on the combustion closure

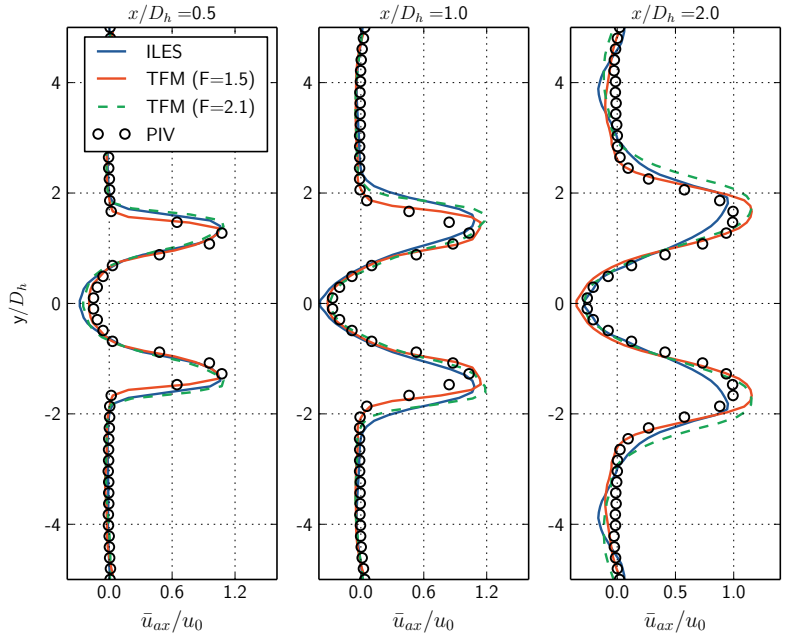

Figure 13.13: Mean axial and radial velocity profiles at different streamwise positions ($^x/_{D_h}$ = 0.5; 1.0; 2.0) normalized by the burner exit velocity u_0.

two additional simulations are conducted employing the Thickened Flame Model (TFM) with $F = 1.5$ and $F = 2.1$. Due to the fact that for a flame thickening factor of $F = 1$ the TFM is formally identical to the ILES closure, the results of the previously shown ILES model are shown for comparison. Figure 13.13 presents the mean axial velocity for the computations compared to the experimental data. The highest differences appear in the shear-layer and the inner recirculation zone. But as can be seen all computations are well in line with the experiments. The Sobel filtered PIV and the accordingly processed computations are given in Figure 13.14. With increasing F the flame gets slightly sharper and the flame tip moves closer to the combustor wall. By artificially thickening the flame, the flame seems to be more affected by the convection of the inner shear-layer and the flame extends further downstream. This behavior can also be observed in Figure 13.15 where OH^* chemiluminescence recordings as well as a streamwise slices of OH^* mass fraction of the simulations are shown. There the reaction zone is more distributed and extends further downstream. With decreasing F the flame gets closer to the measurements and agrees best for values of F close to unity, which is formally identical to the ILES formulation. In order to gain deeper insight into the combustion process incorporating the dilution of steam the ILES model with the baseline mesh is employed.

> *In this section the sensitivity regarding the spatial grid resolution and the combustion closure was assessed. The sensitivity of the solution was scrutinized by comparing velocity, density gradients and* OH^* *species concentration. Due to the high computational cost of*

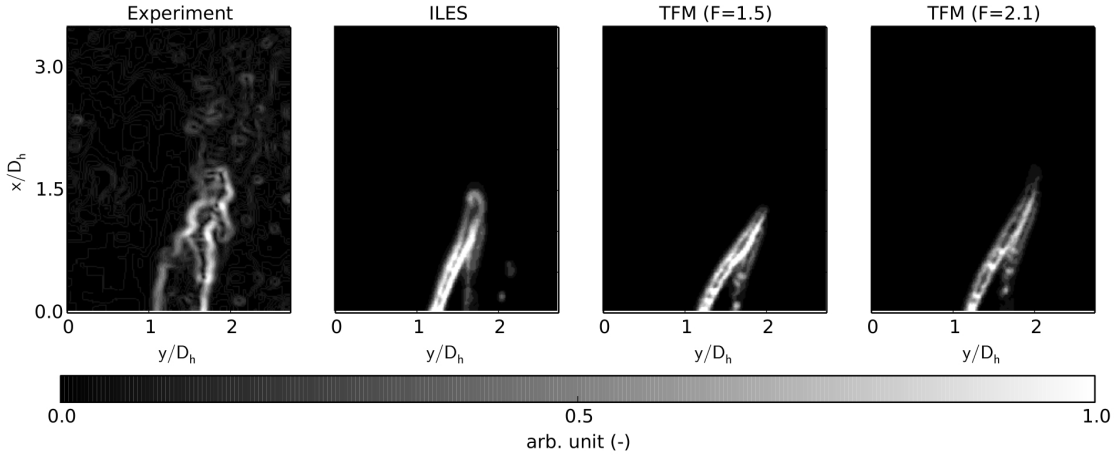

Figure 13.14: Visualization of the flame front. Processed PIV (left); Inverse temperature gradient of LES (middle to right).

LES two meshes were assessed, however the mesh resolution was based on the findings of the isothermal grid study. It turned out that the baseline mesh sufficiently resolves the velocity field in terms of axial and radial velocity components. Some differences in the comparison of the flame front in terms of flame thickness and wrinkling emerged. The reason for the differences could not be answered conclusively, because the flame front measurements lack of the required high spatial and temporal resolution. However, the flame shape and distribution is well in line with the measured mean flame recordings. Thus, the application of a higher resolved technique is recommended for future investigations. In addition, two combustion closures, were compared. It was found that the ILES and the TFM with a flame thickening factor close to unity were able to capture the velocity field and flame shape/position well compared to experimental data. For higher values of the flame thickening factor the flame front is stronger influenced by the velocity field. Thus, the reaction zone is further distributed and the flame angle is tilted closer to the combustion chamber walls. Thus, the investigations concerning the steam dilution are conducted with the ILES model on the baseline grid.

13.2.2 Influence of Steam

In order to investigate the influence of steam on hydrogen oxidation three simulations with different steam content Ω are conducted. The first case is carried out without steam, the second case with moderate steam content ($\Omega = 20\%$) and the last at ultra-wet conditions ($\Omega = 50\%$). For all cases the adiabatic flame temperature was kept approximately constant. The operating conditions for all three cases are listed in Table 12.3. Figure 13.16 depicts the mean axial velocity for all three cases. As described in the sensitivity analysis, an inner recirculation zone is confined by a shear-layer. For the wet cases, a flat velocity profile in the inner recirculation zone can be observed. One could argue that the higher inlet temperature for the steam diluted cases triggers the change of the velocity field. In addition to that Terhaar et al. (2014) revealed that on the one hand the flame shape corresponds to distinct type

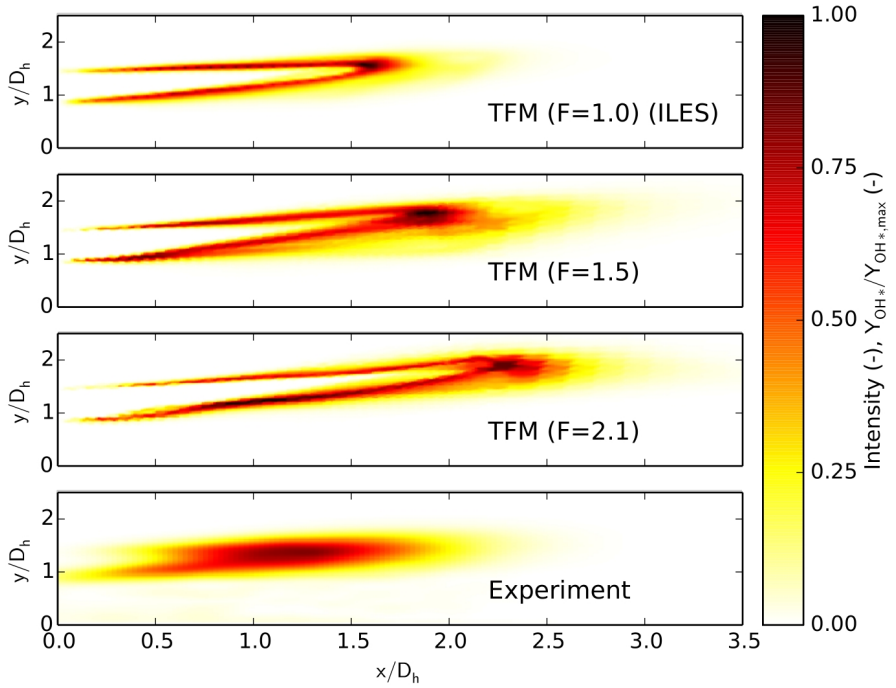

Figure 13.15: Comparison of the LES with OH^* chemiluminescence measurements ($\Omega = 0.0$, $\Phi = 0.5$, $T_u = 293\,\mathrm{K}$). Top to middle: Slices of the normalized OH* mass fractions (LES), Bottom: Processed Abel inversion of OH* recordings (Exp.).

of velocity field and on the other hand that the density distribution has a strong influence on the helical instabilities. Consequently, the change of the density field triggers the change of the velocity field and flame shape/position. Terhaar et al. (2014) investigated mainly methane flames, and reported that by adding steam the flame changes from a V-type to a detached or trumpet like flame. It was also found that the flow field of a dry hydrogen flame is comparable to a detached flame velocity field, however, the flame itself is very short, and resides in the inner and outer shear layer due to the high reactivity. Beside the change of the velocity profiles the overall predictions of the LES are well in line with the experimental data. Figure 13.17 gives an impression of the instantaneous velocity and temperature field distribution. On both fields the mean axial velocity is superimposed; negative velocities are indicated by dashed lines. For the dry case the emanating jet from the burner exit features a small opening angle. By adding steam the opening angle grows and the jet becomes more compact featuring steeper gradients. When the steam content is further increased to $\Omega = 50\%$ the opening angle decreases again. The temperature field distribution supports this observation. For the dry case the hottest gases are locked in the inner recirculation zone, indicating that the hot reaction products are transported and recirculated in the IRZ. Increasing the steam content to a moderate steam level $\Omega = 20\%$ shifts the high temperature gases further outside, and are thus, more affected by the the outer shear layer as indicated by the vortex shedding in the wake of the supposed flame. By further increasing the steam content to $\Omega = 50\%$ the main reaction zone is pushed even further to the combustor walls yielding a more uniform

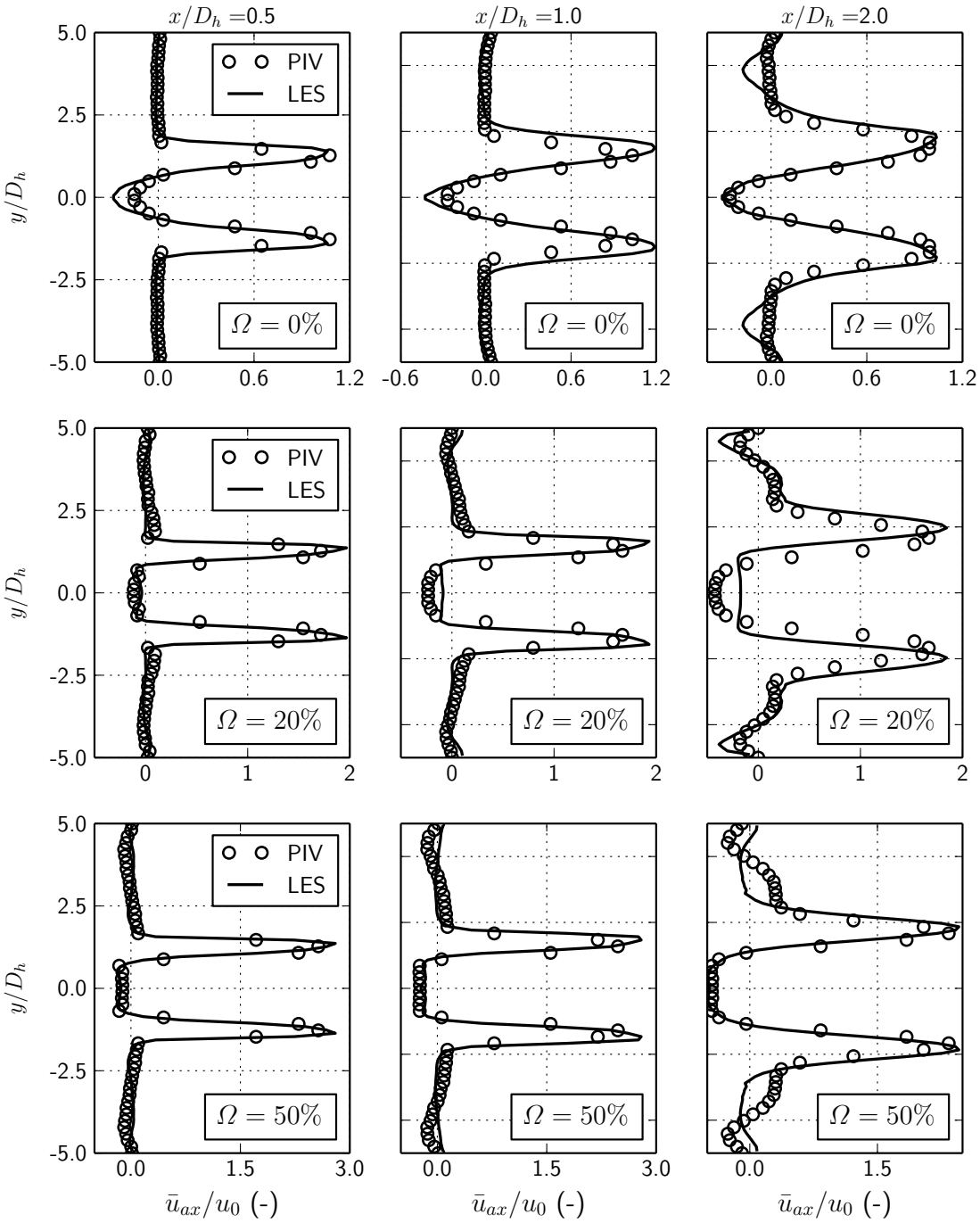

Figure 13.16: Mean axial velocity profiles at different streamwise positions ($^{x}/_{D_h} = 0.5$; 1.0; 2.0) for different steam levels normalized by the burner exit velocity u_0.

distribution of the temperature field with less steep gradients. Aside from OH^* also HO_2 and

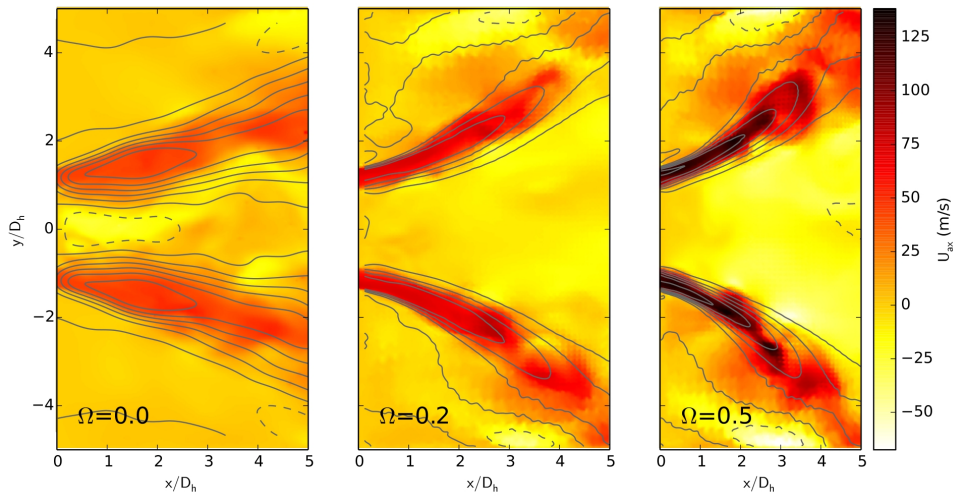

(a) Axial velocity field

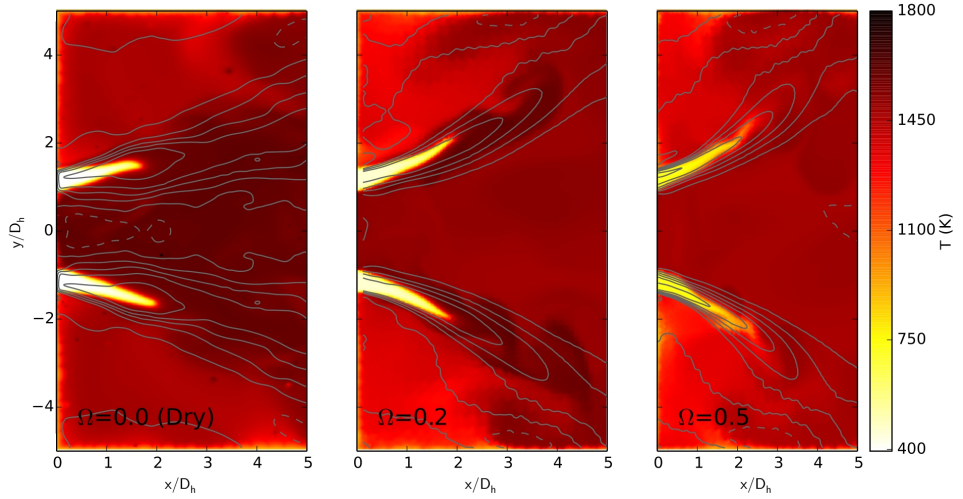

(b) Temperature field

Figure 13.17: Instantaneous axial velocity (top) and temperature (bottom) field for an arbitrary time step. The contours of the mean velocity field are superimposed.

H_2O_2 can serve as precursors to trace the heat release zone and the inner reaction layer. The instantaneous HO_2 and H_2O_2 species distribution (normalized mass fraction) for the three cases are depicted in Figure 13.18. For all three cases both precursors enwrap the cold emanating jet and feature a steep concentration gradient. By adding steam also the hydrogen content is increased to keep the flame temperature constant, and thus the maximum mass fraction of HO_2 also raises. A similar behavior is found for the H_2O_2 concentration, albeit a magnitude smaller in terms of concentration. In contrast to HO_2 it seems that by adding steam H_2O_2 is more affected by the flow and thus convected further downstream. This may be explained by the fact that HO_2 is part of the radical pool, highly reactive and through reaction $R15$

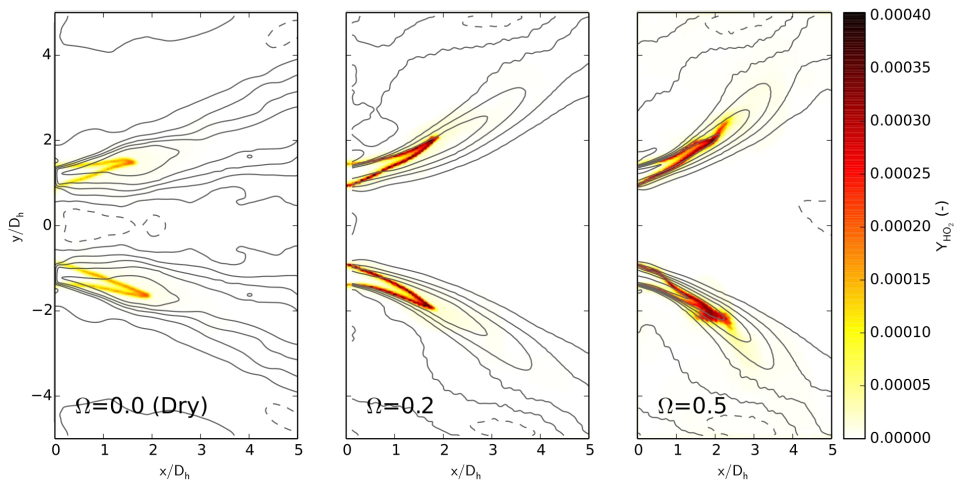

(a) HO_2

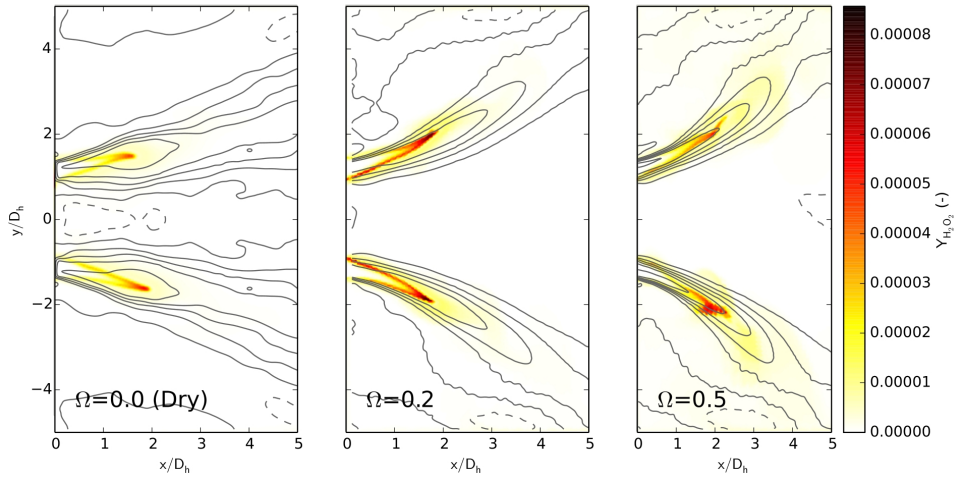

(b) H_2O_2

Figure 13.18: Instantaneous normalized mass fraction distribution of HO_2 (left) and H_2O_2 (right) for an arbitrary time step. The contours of the mean velocity field are superimposed.

($H + O_2(+M) \rightleftharpoons HO_2(+M)$, Table 5.1) the most sensitive reaction (see Chapter 5), whereas H_2O_2 is mainly involved in chain terminating reactions. Nevertheless, both species indicate the main heat release zone, showing that the flame angle grows with increasing steam content. Terhaar et al. (2014) found a coherent structure for a dry hydrogen flame. For the present case the inlet temperature, and hence the adiabatic flame temperature were almost 200 K smaller, and thus, no helical structure is found. Since the density gradient is the main driver for the flame shape and velocity field type the different inlet temperatures are the reason for the different behaviors. While finding coherent structures is not in the focus of the present study no further effort is done to investigate the onset of helical instabilities. In Figure 13.19(a) the Sobel detected flame front given. The experiments show, that with rising steam content

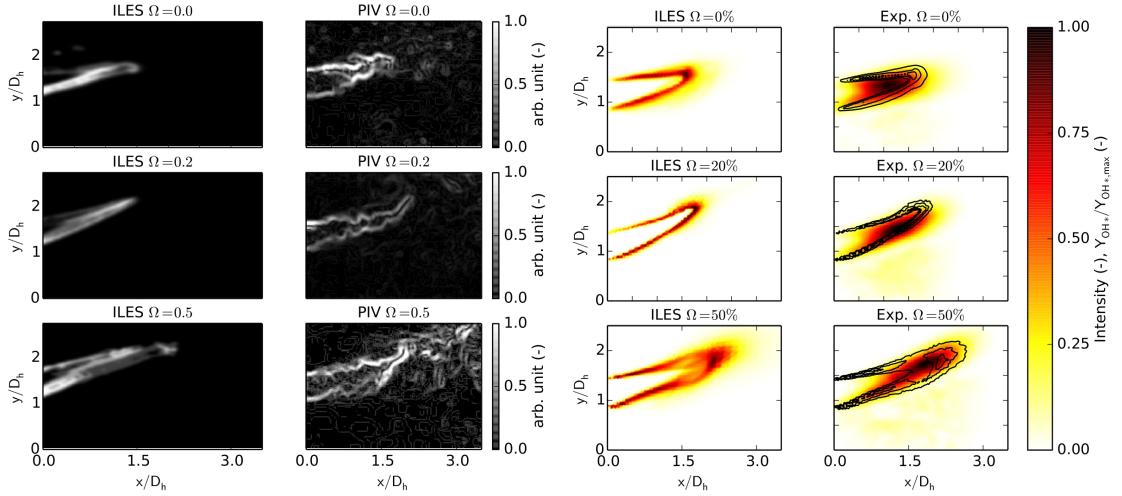

(a) Visualization of the flame front. Inverse temperature gradient of LES (left column); Processed PIV (right column).

(b) Comparison of the LES with OH^* chemiluminescence measurements. Left: Slices of the normalized OH^* mass fractions (LES), Right: Processed Abel inversion of OH^* recordings (Exp.). Contour lines of the OH^* concentration (mass fraction) of the LES are superimposed.

Figure 13.19: Flame characteristics for different steam contents.

the flame is more influenced by turbulent fluctuations and becomes more wrinkled. Moreover, the figure depicts, that the flame extends further downstream. The simulations reproduce the same trend. As seen before in the sensitivity analysis the wrinkling is not predicted. However, the length, angle and dimensions of the flame are well represented. A similar behavior is shown in Figure 13.19(b). There, the computations show a larger spatial distributed reaction zone, with less steep gradients, apparently the heat release spreads. This increase is well in line with the findings of the kinetic assessment, where it was shown that the thermal thickness spreads with the steam content. The prediction of the position of the maximum heat release is again in close agreement with the experiments. Moreover, the computations of the flame shape and distribution agree well with the measurements.

To get an impression of the three-dimensional flame dynamics an isovolume of the OH^* mass fraction is depicted for the ultra-wet case in Figure 13.20. The figure shows three perspectives and the flame is colored by the normalized axial velocity fluctuations. As is apparent in the bottom right view, the flame consists of a rapid cold jet surrounded by low velocity fluctuations. Further downstream the flow accelerates and the fluctuation level rises. The flame structure illustrates the swirling motion of the flow, and thus, of the flame itself. Even if the modeling approach presented in this study leads to reasonable results, some limitations are presented. As it is shown, the prediction of the reaction zone distribution differs slightly between the measurements and the computations. It is assumed that the spatial resolution of the applied OH^* chemiluminescence measurement technique is not sufficient enough to capture fine structures. Probably, this effect is further amplified by the Abel deconvoluted processing. Also Sobel filtered PIV images are an attractive way to detect the flame front, the small scales of the

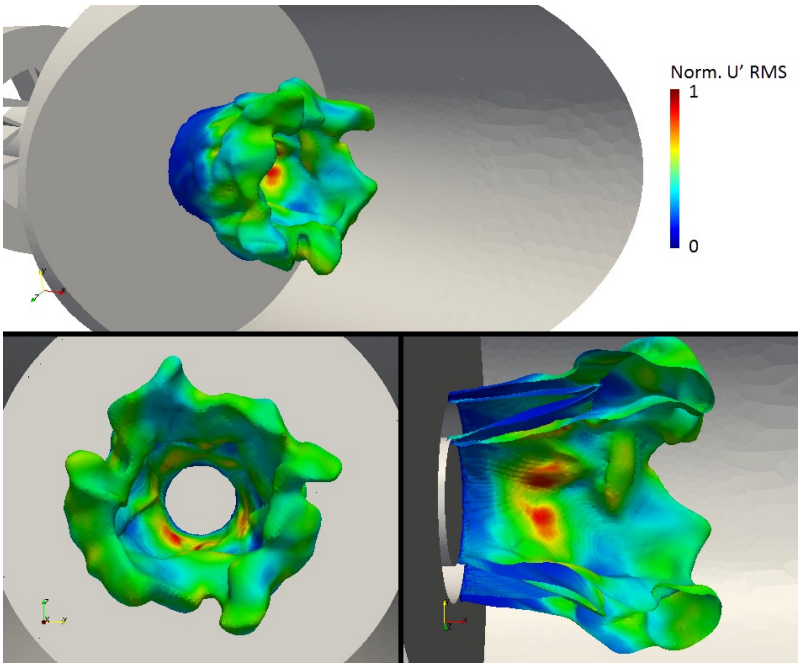

Figure 13.20: Visualization of the flame dynamics for the ultra-wet case ($\Omega = 0.5, \Phi = 0.75, T_{in} = 673\,\mathrm{K}$). The structure is represented by an isovolume of OH^* and colored by the normalized axial velocity fluctuations.

measurements are not necessarily directly linked with the density gradient, since the particles are subject to turbulence. To finally resolve the issue concerning the flame front thickness and wrinkling, more detailed flame front measurements (i.e., PLIF measurements) are necessary, and are recommended for future investigations. However, the velocity field predictions as well as the flame shape and dimension agree well with the experiments. The comparison shows that the detailed mechanism of Burke is suitable to predict steam diluted hydrogen flames under atmospheric gas turbine conditions in terms of inlet temperature. By adding steam to the combustion process, the flame becomes less compact and extends further downstream. Even with high steam content, the extension is small compared to methane flames, as observed by Krüger et al. (2014).

> *In this section the influence of steam on the combustion process was investigated. It was shown that by adding steam the heat release spreads the flame front thickens and the flame extends slightly further downstream. In order to compare the simulations with the measurements, averaged OH^* chemiluminescence images and PIV measurements serve as a reference. Also the PIV recordings were further processed by a Sobel filter as marker for the flame front. It was found that the velocity fields predicted by the computations were well in line with the measurements. In comparison with the OH^* chemiluminescence images the simulated flame shape and positions were in line with the experiments, however some small differences were observed. It is assumed that the spatial resolution of the recordings was not sufficiently high enough to account for the small scales. In addition, the flame*

> *front detection showed a flame wrinkling that was not observed in the computations that probably stems from a seeding-turbulence interaction that is not necessarily linked to the flame front. Nevertheless, the average flame shape and positions agreed well for both the dry and the wet case. As bottom line of the comparison showed that ILES is able to recover the flow field of steam diluted hydrogen flames by employing the extended mechanism of Burke.*

14

Summary of the Turbulent Flame Assessment

The second part of the present study evaluates turbulent hydrogen-air-steam flames in a generic model gas turbine burner and aims at two aspects. The first goal is to demonstrate by comparison with accompanying measurements that the simulation technique can reliably predict reactive flows. In order to gain confidence in the numerical schemes and modeling techniques isothermal LES simulations were conducted in a first step. To determine the influence of the spatial grid resolution and turbulence modeling a sensitivity study was performed. The isothermal flow field was discussed in detail and validated against experimentally obtained data. Subsequently the reacting flow field was assessed numerically and also validated against experimentally obtained data. As an oxidation mechanism the reaction scheme of Burke was used and extended by an OH^* subset as presented in the first part. Again, the sensitivity was determined regarding the mesh resolution and combustion closure by comparing velocity, density gradients and OH^* species concentration. The second goal is to gain further insight in the turbulent combustion process of steam diluted hydrogen flames. Therefore, the amount of steam was varied between a state without steam, a moderately dilution level of steam and a highly diluted case.

For the isothermal analysis some minor discrepancies between the simulations and the experiments were found. However, the overall influence of the computational grid and the subgrid-scales model on the final result was found to be low and the simulations were in general in line with the experimental data. The turbulent kinetic energy spectrum showed a dominant frequency which was identified as the motion of a coherent structure, a helical instability triggered by a PVC. In conclusion it was shown, that flow dynamics of the isothermal swirling flow are qualitatively and quantitatively captured by applying LES with the Smagorinsky subgrid model.

For the sensitivity assessment of the reactive computations it was found that the baseline mesh sufficiently resolves the flow field in terms of velocity components and turbulence levels. Some differences in the comparison of the flame front in terms of flame thickness and wrinkling emerged. The reason for the differences could not be answered conclusively, because the flame front measurements lack the required spatial and temporal resolution. However, the flame shape and distribution is well in line with the measured mean flame recordings. It is recommended to apply finer resolved measurement techniques in future investigations. The sensitivity analysis

concerning the combustion closures revealed that the Implicit Large Eddy Simulation (ILES) and the Thickened Flame Model (TFM) with a flame thickening factor close to unity were able to capture the velocity field and flame shape/position well, compared to experimental data. Evaluating higher values for the flame thickening factor resulted in a stronger impact of the flow field on the flame front, the reaction zone is further spatially distributed and the flame angle is tilted towards the combustion chamber walls. Due to this findings the ILES model and the baseline mesh were chosen to determine the influence of steam on the combustion process. It was shown that with the addition of steam, the heat release spreads, the flame front thickens, and the flame extends slightly further downstream. By comparing with the OH^* chemiluminescence images it was seen that the simulated flame shape and positions were in line with the experiments, however some small differences were observed. It is assumed that the spatial resolution of the recordings was not sufficient enough to account for the small scales. In addition, the flame front detection showed a flame wrinkling that was not observed in the computations, which are likely to stem from a seeding-turbulence interaction that is not necessarily linked to the flame front. Nevertheless, the average flame shape and positions agreed well for both the dry and the wet case. In conclusion the findings showed that the ILES model together with the extended reaction mechanism of Burke is able to predict the flow field and oxidation process of steam diluted hydrogen flames. Thus, the combustion closure is recommended as a design tool for diluted and pure hydrogen flames at gas turbine conditions.

Concluding Remarks

Following the limited availability of fossil fuels and growing environmental concerns, energy transition is beside energy storage and grid balancing one of the major challenges of the 21st century. Among the variety of alternative and renewable fuels, hydrogen is a promising candidate if produced from water and excess electricity or biomass. Therefore, hydrogen is likely to play an important role for future power generation. However, hydrogen combustion properties differ significantly from established fossil fuels. For instance, it is not possible to operate safely a traditional gas turbine on high hydrogen content fuels, due to the high risk of flashback. In particular it is challenging to retrofit conventional gas turbine applications to allow for an efficiently and clean usage of hydrogen or hydrogen-rich fuels. In fact, it calls for a new generation of combustion technologies based on deep understanding of new fuels and their combustion behavior.
This thesis addresses the possibility to burn hydrogen in heavy-duty gas turbine applications by adding steam directly into the combustion process. Such a Humid Gas Turbine (HGT) offers the attractive possibility of increasing the plant efficiency without the need of an additional steam turbine, as is the case for combined cycles. In addition to efficiency gains, the addition of steam into the combustion process reduces $\mathrm{NO_x}$ emissions. Moreover, a possible future gas turbine cycle is discussed that allows for the efficient combustion of hydrogen, energy storage and grid balancing. The main idea of the cycle is to employ renewable energies, to generate hydrogen and oxygen in the off-peak hours via electrolysis. The products are stored and burned in a gas turbine application in peak hours. This allows for energy storage and power generation at zero emissions. Therefore, this thesis aims on the investigation of premixed combustion of pure hydrogen, diluted with varying amounts of steam for gas turbine applications. As oxidizer both molecular oxygen and air are considered, and the effect of steam on the combustion process is addressed by using detailed chemistry.

In the first part of the thesis laminar premixed flames were scrutinized. In a first step an adequate reaction scheme for hydrogen oxidation at gas turbine conditions was identified, by comparing several candidates. Their performances was assessed based on one-dimensional freely propagating flame calculations and auto-ignition processes under dry and steam diluted conditions, where experimentally determined data was available. In comparison with the experimental data for hydrogen-air-steam flames, the reaction mechanisms of Kéromnès and Burke showed the best agreement, in particular at high steam concentrations. The thermal thickness is an important parameter for most combustion modeling approaches (e.g., Large Eddy Simulation (LES)) and was therefore evaluated for the different reaction models and

steam levels. Although a common tendency was apparent and the results were found to be reasonable, it is highly recommended to perform further measurements at gas turbine conditions for a better validation. The comparisons of model predictions and measurements regarding auto-ignition events revealed that the reaction schemes were well in line with the experiments, except for the low-temperature regime, where all models failed. In conclusion, the benchmarks clearly revealed that the mechanisms of Burke and Kéromnès are the best suited schemes for predicting combustion processes with steam dilution.

In the combustion test rig OH^* chemiluminescence images are recorded to assess the flame shape and location. In order to compare the LES simulations with according OH^* recordings from the experiments, a reaction subset is needed that allows for prediction of OH^* chemiluminescence. Therefore five promising candidates were selected, and compared to in the literature available shock tube measurements of highly diluted hydrogen-air flames. In conclusion, the benchmark of the different OH^* chemiluminescence subsets revealed that the updated subset of Smith (Smith et al., 2002; Smith et al., 2005) is the best suited scheme for predicting highly diluted hydrogen flames.

The influence of steam on the formation of OH^* was also assessed, even though there was no experimental data available for validation purposes. However, Petersen et al. (2012) conducted experiments with nitrogen dilution. Nitrogen and steam share similar thermal diffusivities, and thus, nitrogen was replaced with steam and an artificial inert steam. It was found that the results of the nitrogen and inert steam computations collapse, whereas the replacement with steam showed significant differences. Evidently, the presence of steam impairs the production of OH^* through third-body collisions over a wide range of temperatures.

Due to the fact that besides pure oxygen also air was evaluated as oxidizer, the formation of nitrogen oxides was briefly investigated. Nitrogen oxides are harmful to health and environment, and hence, the control and prediction of nitrogen oxides is of high importance. Therefore, four $\mathrm{NO_x}$ subsets were benchmarked and the subset from the University of California in San Diego (UCSD, 2014) showed the closest agreement to the experimental data of Skottene et al. (2007). To get an impression of the influence of steam on th emission formation a numerical experiment was conducted, revealing that steam significantly affects the formation of harmful emissions. However, accompanying measurements for model validation were not available.

Aside from the model validation, one purpose of this thesis is to examine the influence of steam addition on the combustion process, in particular on the laminar burning velocity, as well as on the auto-ignition event. By assessing laminar premixed flames and introducing an inert species with the same thermophysical properties as steam, it was shown that steam has a significant chemical effect that differs from ideal diluents. The one-dimensional hydrogen flame computations revealed that steam shifts the preheat zone towards higher temperatures.

By applying a sensitivity analysis in combination with the inspection of species concentration profiles, it was seen that the addition of steam mostly affects the third-body reaction ($H + O_2(+M) \rightleftharpoons HO_2(+M)$), leading to a shift of the preheat zone and thus, has a strong impact on the radical pool. Steam promotes the formation of $\mathrm{HO_2}$ and simultaneously decreases the concentration of H radicals, impairing the laminar burning velocity. In addition, by setting all third-body efficiencies of steam to zero an ideal diluent behavior was achieved emphasizing that the high third-body efficiency of water is the dominant chemical effect. The impact of steam on the preheat zone was also examined for self-ignition events. Computations of the auto-ignition

processes revealed that the ignition event primarily depends on the initial temperature rather than on the level of dilution. In contrast to that, dilution with steam showed a shift of the ignition event towards higher temperatures, and thus, prolongates the ignition time delay. This effect can also be related to steam affecting the radical pool, and hence, impairs the ignition process. In addition to the chemical effects impairing the reactivity, steam has a supplementary cooling effect on the adiabatic flame temperature due to the higher specific heat capacity. Thus, the flame temperature can be significantly reduced to apply hydrogen combustion at conventional gas turbine conditions.

The outcome of the first part of the thesis is a validated combined reaction scheme, including Burke's detailed hydrogen reaction scheme (Burke et al., 2012), the OH^* chemiluminescence mechanism of Smith (Smith et al., 2002; Smith et al., 2005) and the San Diego $\mathrm{NO_x}$ subset (UCSD, 2014), which was then further used for the investigation of turbulent flames. Furthermore, the first part revealed the need for further experimental data of hydrogen flames with high steam dilution to further validate the assembled mechanism at gas turbine conditions, especially at elevated pressures.

In the second part of the present study turbulent hydrogen-air-steam flames in a generic model gas turbine burner were evaluated, focusing at two aspects. The first purpose was to demonstrate by comparison with accompanying measurements that the simulation technique can reliably predict reacting flows. In a first step isothermal LES simulations were conducted, in order to gain confidence in the numerical schemes and modeling techniques. A sensitivity study was performed to determine the influence of the spatial grid resolution and turbulence modeling. The isothermal flow field was discussed in detail and validated against experimentally obtained data. It turned out that besides some minor discrepancies between the simulations and the experiments, the overall influence of the computational grid and the subgrid-scales model was found to be low and that the simulations were in general in line with the experimental data. The turbulent kinetic energy spectrum showed a dominant frequency which was identified as the motion of a coherent structure.

Subsequently, the reacting flow field was assessed numerically and validated against experimentally obtained data. Again, the sensitivity was determined regarding the mesh resolution and combustion closure by comparing velocity, density gradients and OH^* species concentration. For the sensitivity assessment of the reactive computations it was found that the baseline mesh sufficiently resolves the flow field in terms of velocity components and turbulence levels. Some differences in the comparison of the flame front in terms of flame thickness and wrinkling emerged. The reason for the differences could not be answered conclusively, because the flame front measurements lack of the required high spatial and temporal resolution. Nevertheless, the flame shape and distribution is well in line with the measured mean flame recordings. It is recommended to apply a finer resolved measurement technique in future investigations. The comparison between the combustion closures revealed that the Implicit Large Eddy Simulation (ILES) and the Thickened Flame Model (TFM) with a flame thickening factor close to unity, were able to capture the velocity field and flame shape/position well compared to experimental data. Evaluating higher values for the flame thickening factor resulted in a stronger impact of the flow field on the flame front, the reaction zone is further spatially distributed and the flame angle is tilted towards the combustion chamber walls.

The second purpose of the turbulent flame investigation was to gain further insight in the

turbulent combustion process of steam diluted hydrogen flames. Therefore, the amount of steam was varied between a state without steam, a moderately diluted level of steam and a highly diluted case. It was shown that the addition of steam, the heat release spreads, the flame front thickens and the flame extends slightly further downstream. In comparison with the OH^* chemiluminescence images the simulated flame shape and positions were in line with the experiments. In conclusion the findings showed that the ILES model together with the extended reaction mechanism of Burke is able to predict the flow field and oxidation process of steam diluted hydrogen flames. Thus, the combustion closure is recommended as a design tool for diluted and pure hydrogen flames at gas turbine conditions.

Within the scope of this thesis new insight into the combustion process of highly steam diluted hydrogen flames was given, showing that steam dilution is a promising alternative for an efficiently low- or zero-emission combustion. An additional outcome of this study is a accurate and validated set of tools and methods for a further design process of a hydrogen powered gas turbine cycle.

Bibliography

Alkishali, K., Bradley, D., and Hall, S. (1983). 'Turbulent combustion of near-limit hydrogen-air mixtures'. In: *Combustion and Flame* 54.1-3, pp. 61–70. DOI: 10.1016/0010-2180(83)90022-6. URL: http://linkinghub.elsevier.com/retrieve/pii/0010218083900226 (cit. on p. 12).

Anacelto, P. M., Fernandes, E. C., Heitor, M. V., and Shtork, S. I. (2003). 'Swirl flow structure and flame charateristics in a model model lean premixed combustor'. In: *Combustion Science and Technology* 175, pp. 1369–1388 (cit. on p. 79).

Bannister, R. L., Newby, R. A., and Yang, W. C. (1999). 'Final Report on the Development of a Hydrogen-Fueled Combustion Turbine Cycle for Power Generation'. In: *Journal of Engineering for Gas Turbines and Power* 121.1, p. 38. DOI: 10.1115/1.2816310. URL: http://gasturbinespower.asmedigitalcollection.asme.org/article.aspx?articleid=1420859 (cit. on p. 4).

Barber, J. (1791). *A Method of Rising Inflammable Air for the Purposes of Procuring Motion, and Facilitating Metallurgical Operations* (cit. on p. 3).

Baudoin, E., Yu, R., Nogenmur, K. J., Bai, X.-S., and Fureby, C. (2009). 'Comparison of LES Models Applied to a Bluff Body Stabilized Flame'. In: *47th AIAA Aerospace Sciences Meeting including The New Horizons Forum and Aerospace Exposition*. Reston, Virigina: American Institute of Aeronautics and Astronautics. DOI: 10.2514/6.2009-1178. URL: http://arc.aiaa.org/doi/abs/10.2514/6.2009-1178 (cit. on p. 97).

Becher, J. J. (1669). *Physica subterranea profundam subterraneorum genesin e principiis hucusque ignotis ostendens : opus sine pari, primum hactenus et princeps*. Lipsiae : Ex officina Weidmanniana (cit. on p. 51).

Beér, J. M. and Chigier, N. A. (1972). *Combustion Aerodynamics*. Krieger Publishing Company, pp. 1–264 (cit. on p. 86).

Beerer, D. J. and McDonell, V. G. (2008). 'Autoignition of Hydrogen and Air Inside a Continuous Flow Reactor With Application to Lean Premixed Combustion'. In: *Journal of Engineering for Gas Turbines and Power* 130. DOI: 10.1115/1.2939007. URL: http://link.aip.org/link/?GTP/130/051507/1 (cit. on p. 12).

Berglund, M. and Fureby, C. (2007). 'LES of supersonic combustion in a scramjet engine model'. In: *Proceedings of the Combustion Institute* 31.2, pp. 2497–2504. DOI: 10.1016/j.proci.2006.07.074. URL: http://linkinghub.elsevier.com/retrieve/pii/S1540748906000915 (cit. on p. 81).

Bhargava, A., Colket, M., Sowa, W., Casleton, K., and Maloney, D. (2000). 'An Experimental and Modeling Study of Humid Air Premixed Flames'. In: *Journal of Engineering for Gas Turbines and Power* 122, pp. 405–411 (cit. on p. 3).

Bianco, M., Camporeale, S. M., and Fortunato, B. (2001). 'CFD Simulation of Humid Air Premixed Flame Combustion Chamber for Evaporative Gas Turbine Cycles'. In: *Proceedings of ASME Turbo Expo 2001*. Vol. 2001-GT-00. Louisiana, pp. 1–12 (cit. on p. 81).

Bilger, R. W., Pope, S. B., Bray, K. N. C., and Driscoll, J. F. (2005). 'Paradigms in turbulent combustion research'. In: *Proceedings of the Combustion Institute* 30.1, pp. 21–42. DOI: 10.1016/j.proci.2004.08.273. URL: http://linkinghub.elsevier.com/retrieve/pii/S0082078404003297 (cit. on pp. 80, 96, 98).

Billant, P., Chomaz, J., and Huerre, P. (1998). 'Experimental study of vortex breakdown in swirling jets'. In: *Journal of Fluid Mechanics* 376, pp. 183–219. URL: http://journals.cambridge.org/production/action/cjoGetFulltext?fulltextid=14584 (cit. on p. 79).

Bouvet, N., Halter, F., Chauveau, C., and Yoon, Y. (2013). 'On the effective Lewis number formulations for lean hydrogen/hydrocarbon/air mixtures'. In: *International Journal of Hydrogen Energy* 38.14, pp. 5949–5960. DOI: 10.1016/j.ijhydene.2013.02.098. URL: http://linkinghub.elsevier.com/retrieve/pii/S0360319913005314 (cit. on p. 59).

Bray, K. N. C. (1996). 'The challenge of turbulent combustion'. In: *Symposium (International) on Combustion* 26.1, pp. 1–26. DOI: 10.1016/S0082-0784(96)80195-0. URL: http://linkinghub.elsevier.com/retrieve/pii/S0082078496801950 (cit. on pp. 80, 96).

Burgess, D. R. (2014). 'Thermochemical Data'. In: *NIST Chemistry WebBook, NIST Standard Reference Database Number 69*. Ed. by Linstrom, P. J. and Mallard, W. G. Gaithersburg MD: National Institute of Standards and Technology. DOI: (retrived17.10.2014). URL: http://webbook.nist.gov (cit. on p. 34).

Burke, M. P., Chaos, M., Ju, Y., Dryer, F. L., and Klippenstein, S. J. (2011a). 'Comprehensive H2/O2 Kinetic Model for High-Pressure Combustion'. In: *International Journal of Chemical Kinetics* (in press), pp. 1–135 (cit. on p. 165).

Burke, M. P., Dryer, F. L., and Ju, Y. (2011b). 'Assessment of kinetic modeling for lean H2/CH4/O2/diluent flames at high pressures'. In: *Proceedings of the Combustion Institute* 33.1, pp. 905–912. DOI: 10.1016/j.proci.2010.05.021. URL: http://linkinghub.elsevier.com/retrieve/pii/S1540748910000623 (cit. on p. 26).

Burke, M. P., Chaos, M., Ju, Y., Dryer, F. L., and Klippenstein, S. J. (2012). 'Comprehensive H2/O2 kinetic model for high-pressure combustion'. In: *International Journal of Chemical Kinetics* 44.7, pp. 444–474. DOI: 10.1002/kin.20603. URL: http://onlinelibrary.wiley.com/doi/10.1002/kin.20603/full%20http://doi.wiley.com/10.1002/kin.20603 (cit. on pp. 23, 34–37, 39–42, 46, 48, 49, 61, 63, 67, 70, 71, 135).

Butler, T. D. and O'Rourke, P. J. (1977). 'A Numerical Method for Two Dimensional Unsteady Reacting Flows'. In: *Symposium (International) on Combustion* 16.1, pp. 1503–1515. DOI: http://dx.doi.org/10.1016/S0082-0784(77)80432-3. URL: http://www.sciencedirect.com/science/article/pii/S0082078477804323 (cit. on p. 101).

Cala, C. E., Fernandes, E. C., Heitor, M. V., and Shtork, S. I. (2006). 'Coherent structures in unsteady swirling jet flow'. In: *Experiments in Fluids* 40, pp. 267–276 (cit. on p. 79).

Cambon, C., Jacquin, L., and Lubrano, J. L. (1992). 'Toward a new Reynolds stress model for rotating turbulent flows'. In: *Physics of Fluids A: Fluid Dynamics* 4.4, p. 812. DOI: 10.1063/1.858298. URL: http://link.aip.org/link/PFADEB/v4/i4/p812/s1%5C&Agg=doi (cit. on p. 80).

Canepa, E., Di Martino, P., Formosa, P., Ubaldi, M., and Zuino, P. (2006). 'Unsteady Aerodynamics of an Aeroengine Double Swirler Lean Premixing Prevaporizing Burner'. In: *Journal of Engineering for Gas Turbines and Power* 128.4, pp. 755–764 (cit. on p. 79).

Carlsson, H., Yu, R., and Bai, X.-S. (2014). 'Direct Numerical Simulation of Lean Premixed CH4/Air and H2/Air Flames at High Karlovitz Numbers'. In: *International Journal of Hydrogen Energy* 39.35, pp. 20216–20232. DOI: 10.1016/j.ijhydene.2014.09.173 (cit. on p. 83).

Castiñeira, D. and Edgar, T. F. (2006). 'CFD for Simulation of Steam-Assisted and Air-Assisted Flare Combustion Systems'. In: *Energy & Fuels* 20.3, pp. 1044–1056. DOI: 10.1021/ef050332v. URL: http://pubs.acs.org/doi/abs/10.1021/ef050332v (cit. on p. 81).

Cavaliere, A. and Joannon, M. de (2004). 'Mild Combustion'. In: *Progress in Energy and Combustion Science* 30.4, pp. 329–366. DOI: 10.1016/j.pecs.2004.02.003. URL: http://linkinghub.elsevier.com/retrieve/pii/S0360128504000127 (cit. on p. 83).

Chapman, I. (2014). 'The end of Peak Oil? Why this topic is still relevant despite recent denials'. In: *Energy Policy* 64, pp. 93–101. DOI: 10.1016/j.enpol.2013.05.010. URL: http://linkinghub.elsevier.com/retrieve/pii/S030142151300342X (cit. on p. 1).

Christo, F. and Dally, B. (2005). 'Modeling turbulent reacting jets issuing into a hot and diluted coflow'. In: *Combustion and Flame* 142.1-2, pp. 117–129. DOI: 10.1016/j.combustflame.2005.03.002. URL: http://linkinghub.elsevier.com/retrieve/pii/S001021800500074X (cit. on p. 83).

Cicconardi, S. P., Perna, A., and Spazzafumo, G. (2004). 'Steam power-plants fed by high pressure electrolytic hydrogen'. In: *International Journal of Hydrogen Energy* 29.5, pp. 547–551. DOI: 10.1016/S0360-3199(03)00085-5. URL: http://linkinghub.elsevier.com/retrieve/pii/S0360319903000855 (cit. on p. 4).

Clark, T. P. (1958). *Studies of OH, CO, CH, and C2 radiation from laminar and turbulent propane-air and ethylene-air flames*. English. Washington: National Advisory Committee for Aeronautics (cit. on p. 59).

Cohen, A. and Larsen, J. (1967). *Explosive mechanism of the H2-O2 reaction near the second ignition limit*. Tech. rep. U.S. Army Ballistic Research Laboratory, pp. 1–35 (cit. on p. 12).

Colin, O., Ducros, F., Veynante, D., and Poinsot, T. (2000). 'A thickened flame model for large eddy simulations of turbulent premixed combustion'. In: *Physics of Fluids* 12.7, p. 1843. DOI: 10.1063/1.870436. URL: http://link.aip.org/link/PHFLE6/v12/i7/p1843/s1%5C&Agg=doi (cit. on p. 101).

Damköhler, G. (1940). 'Der Einfluss der Turbulenz auf die Flammengeschwindigkeit in Gasgemischen'. In: *Zeitschrift für Elektrochemie und angewandte physikalische Chemie* 46.11, pp. 601–652. DOI: 10.1002/bbpc.19400461102 (cit. on pp. 75, 76).

Das, A. K., Kumar, K., and Sung, C.-J. (2011). 'Laminar flame speeds of moist syngas mixtures'. In: *Combustion and Flame* 158.2, pp. 345–353. DOI: 10.1016/j.combustflame.2010.

09.004. URL: http://linkinghub.elsevier.com/retrieve/pii/S0010218010002476 (cit. on pp. 10, 13).

Das, A. K., Sung, C.-J., Zhang, Y., and Mittal, G. (2012). 'Ignition delay study of moist hydrogen/oxidizer mixtures using a rapid compression machine'. In: *International Journal of Hydrogen Energy* 37.8, pp. 6901–6911. DOI: 10.1016/j.ijhydene.2012.01.111. URL: http://linkinghub.elsevier.com/retrieve/pii/S0360319912002078 (cit. on pp. 11, 13).

David, W. T. and Mann, J. (1942). 'Influence of Water Vapour on Flame Gas Temperatures'. In: *Nature* 150.3809, pp. 521–522. DOI: 10.1038/150521b0. URL: http://www.nature.com/doifinder/10.1038/150521b0 (cit. on pp. 12, 33).

De Leo, M., Saveliev, A., Kennedy, L., and Zelepouga, S. (2007). 'OH and CH luminescence in opposed flow methane oxy-flames'. In: *Combustion and Flame* 149.4, pp. 435–447. DOI: 10.1016/j.combustflame.2007.01.008. URL: http://linkinghub.elsevier.com/retrieve/pii/S0010218007000600 (cit. on p. 52).

Dixon-Lewis, G. and Williams, A. (1964). 'The rate of heat release in some slow burning hydrogen-oxygen flames'. In: *Combustion and Flame* 8.4, pp. 249–255. DOI: 10.1016/0010-2180(64)90078-1. URL: http://linkinghub.elsevier.com/retrieve/pii/0010218064900781 (cit. on pp. 12, 13).

Dodoulas, I. A. and Navarro-Martinez, S. (2013). 'Large Eddy Simulation of Premixed Turbulent Flames Using the Probability Density Function Approach'. In: *Flow, Turbulence and Combustion* 90.3, pp. 645–678. DOI: 10.1007/s10494-013-9446-z. URL: http://link.springer.com/10.1007/s10494-013-9446-z (cit. on p. 99).

Donohoe, N., Heufer, K. a., Aul, C. J., Petersen, E. L., Bourque, G., Gordon, R., and Curran, H. J. (2014). 'Influence of steam dilution on the ignition of hydrogen, syngas and natural gas blends at elevated pressures'. In: *Combustion and Flame*. DOI: 10.1016/j.combustflame.2014.10.005. URL: http://linkinghub.elsevier.com/retrieve/pii/S0010218014003149 (cit. on pp. 13, 29–31).

Doom, J., Hou, Y., and Mahesh, K. (2007). 'A numerical method for DNS/LES of turbulent reacting flows'. In: *Journal of Computational Physics* 226.1, pp. 1136–1151. DOI: 10.1016/j.jcp.2007.05.037. URL: http://linkinghub.elsevier.com/retrieve/pii/S0021999107002252 (cit. on p. 80).

Doom, J. and Mahesh, K. (2009). 'Direct numerical simulation of auto-ignition of a hydrogen vortex ring reacting with hot air'. In: *Combustion and Flame* 156.4, pp. 813–825. DOI: 10.1016/j.combustflame.2009.01.010. URL: http://linkinghub.elsevier.com/retrieve/pii/S0010218009000169 (cit. on p. 82).

Dowdy, D. (1991). 'The use of expanding spherical flames to determine burning velocities and stretch effects in hydrogen/air mixtures'. In: *Symposium (International) on Combustion* 23.1, pp. 325–332. DOI: 10.1016/S0082-0784(06)80275-4. URL: http://linkinghub.elsevier.com/retrieve/pii/S0082078406802754 (cit. on pp. 12, 24).

Drake, M. C. and Blint, R. J. (1989). 'Thermal NOx in stretched laminar opposed-flow diffusion flames with CO/H2/N2 fuel'. In: *Combustion and Flame* 76.2, pp. 151–167. DOI: 10.1016/0010-2180(89)90064-3. URL: http://linkinghub.elsevier.com/retrieve/pii/0010218089900643 (cit. on p. 82).

Dubief, Y. and Delcayre, F. (2000). 'On coherent-vortex identification in turbulence'. In: *Journal of Turbulence* 1.11 (cit. on p. 114).

Duwig, C. (2011). 'Large Eddy Simulation of flame stabilisation dynamics and vortex control in a lifted H2/N2 jet flame'. In: *Combustion Theory and Modelling* 15.3, pp. 325–346. DOI: 10.1080/13647830.2010.539705. URL: http://www.tandfonline.com/doi/abs/10.1080/13647830.2010.539705 (cit. on p. 81).

Duwig, C., Ducruix, S., and Veynante, D. (2012). 'Studying the Stabilization Dynamics of Swirling Partially Premixed Flames by Proper Orthogonal Decomposition'. In: *Journal of Engineering for Gas Turbines and Power* 134.10, p. 101501. DOI: 10.1115/1.4007013. URL: http://link.aip.org/link/JETPEZ/v134/i10/p101501/s1%5C&Agg=doi (cit. on p. 81).

Duwig, C. and Dunn, M. J. (2013). 'Large Eddy Simulation of a premixed jet flame stabilized by a vitiated co-flow: Evaluation of auto-ignition tabulated chemistry'. In: *Combustion and Flame* 160.12, pp. 2879–2895. DOI: 10.1016/j.combustflame.2013.06.011. URL: http://linkinghub.elsevier.com/retrieve/pii/S0010218013002368 (cit. on p. 98).

Duwig, C. and Fuchs, L. (2007a). 'Large eddy simulation of vortex breakdown/flame interaction'. In: *Physics of Fluids* 19.7, pp. 1–20. DOI: 10.1063/1.2749812. URL: http://link.aip.org/link/?PHF/19/075103/1%20http://link.aip.org/link/PHFLE6/v19/i7/p075103/s1%5C&Agg=doi (cit. on pp. 80, 81).

– (2005). 'Study of Flame Stabilization in a Swirling Combustor Using a New Flamelet Formulation'. In: *Combustion Science and Technology* 177, p. 1485 (cit. on p. 97).

Duwig, C., Fuchs, L., Griebel, P., Siewert, P., and Boschek, E. (2007b). 'Study of a Confined Turbulent Jet: Influence of Combustion and Pressure'. In: *AIAA Journal* 45.3, pp. 624–639. DOI: 10.2514/1.26352. URL: http://doi.aiaa.org/10.2514/1.26352 (cit. on pp. 97, 113).

Duwig, C. and Gutmark, E. (2008a). 'Large scale rotating motions in a multiple jets combustor'. In: *Physics of Fluids* 20.4, p. 41705. DOI: 10.1063/1.2904992. URL: http://link.aip.org/link/?PHF/20/041705/1 (cit. on p. 113).

Duwig, C. and Iudiciani, P. (2010). 'Extended Proper Orthogonal Decomposition Analysis of Flame/Acoustic Interaction.' In: *Flow, Turbulence and Combustion* 84.1, pp. 25–47 (cit. on pp. 112, 115).

– (2009). 'Extended Proper Orthogonal Decomposition for Analysis of Unsteady Flames'. In: *Flow, Turbulence and Combustion* 84.1, pp. 25–47. DOI: 10.1007/s10494-009-9210-6. URL: http://link.springer.com/10.1007/s10494-009-9210-6 (cit. on p. 116).

Duwig, C., Nogenmyr, K.-J., Chan, C., and Dunn, M. J. (2011). 'Large Eddy Simulations of a piloted lean premix jet flame using finite-rate chemistry'. In: *Combustion Theory and Modelling* 15.4, pp. 537–568. DOI: 10.1080/13647830.2010.548531. URL: http://www.tandfonline.com/doi/abs/10.1080/13647830.2010.548531 (cit. on pp. 99, 101).

Duwig, C., Stankowic, D., Fuchs, L., Li, G., and Gutmark, E. (2008b). 'Experimental and Numerical Study of Flameless Combustion in a Model Gas Turbine Combustor'. In: *Combustion Science and Technology* 180, pp. 279–295. DOI: 10.1080/00102200701739164 (cit. on pp. 97, 99, 100).

Eastman, E. D. (1928). 'Theory of the Soret Effect'. In: *Journal of the American Chemical Society* 50.2, pp. 283–291. DOI: 10.1021/ja01389a007. URL: http://pubs.acs.org/doi/abs/10.1021/ja01389a007 (cit. on p. 17).

Echekki, T. and Mastorakos, E. (2011). 'Turbulent Combustion Modeling'. In: Fluid Mechanics and Its Applications 95. Ed. by Echekki, T. and Mastorakos, E., pp. 19–40. DOI: 10.1007/978-94-007-0412-1. URL: http://link.springer.com/10.1007/978-94-007-0412-1 (cit. on pp. 96, 97).

Eckbreth, A. C. (1996). *Laser diagnostics for combustion temperature and species*. 2nd ed. Informa Healthcare, p. 596 (cit. on p. 80).

Edmondson, H. and Heap, M. (1971). 'The burning velocity of hydrogen-air flames'. In: *Combustion and flame* 16.2, pp. 161–165. URL: http://www.sciencedirect.com/science/article/pii/S0010218071800810 (cit. on pp. 12, 25, 26).

Escudier, M. P. and Keller, J. J. (1985). 'Recirculation in Swirling Flow: A Manifestation of Vortex Breakdown'. In: *AIAA Journal* 23.1, pp. 111–116 (cit. on p. 79).

Favre, A. (1983). 'Turbulence: Space-time statistical properties and behavior in supersonic flows'. In: *Physics of Fluids* 26.10, p. 2851. DOI: 10.1063/1.864049. URL: http://scitation.aip.org/content/aip/journal/pof1/26/10/10.1063/1.864049 (cit. on p. 94).

Ferziger, J. H. and Perić, M. (2001). *Computational Methods for Fluid Dynamics*. Springer (cit. on p. 93).

Finesso, R. and Spessa, E. (2014). 'Ignition delay prediction of multiple injections in diesel engines'. In: *Fuel* 119, pp. 170–190. DOI: 10.1016/j.fuel.2013.11.040. URL: http://linkinghub.elsevier.com/retrieve/pii/S0016236113011113 (cit. on p. 11).

Frassoldati, A., Faravelli, T., and Ranzi, E. (2007). 'The ignition, combustion and flame structure of carbon monoxide/hydrogen mixtures. Note 1: Detailed kinetic modeling of syngas combustion also in presence of nitrogen compounds'. In: *International Journal of Hydrogen Energy* 32.15, pp. 3471–3485. DOI: 10.1016/j.ijhydene.2007.01.011. URL: http://linkinghub.elsevier.com/retrieve/pii/S0360319907000432 (cit. on pp. 24, 63, 83).

Frassoldati, A., Sharma, P., Cuoci, A., Faravelli, T., and Ranzi, E. (2010). 'Kinetic and fluid dynamics modeling of methane/hydrogen jet flames in diluted coflow'. In: *Applied Thermal Engineering* 30.4, pp. 376–383. DOI: 10.1016/j.applthermaleng.2009.10.001. URL: http://linkinghub.elsevier.com/retrieve/pii/S1359431109002920 (cit. on p. 83).

Freitag, M. and Janicka, J. (2007). 'Investigation of a strongly swirled unconfined premixed flame using LES'. In: *Proceedings of the Combustion Institute* 31.1, pp. 1477–1485. DOI: 10.1016/j.proci.2006.07.225. URL: http://linkinghub.elsevier.com/retrieve/pii/S1540748906002343 (cit. on p. 81).

Freitag, M., Klein, M., Gregor, M., Geyer, D., Schneider, C., Dreizler, A., and Janicka, J. (2006). 'Mixing analysis of a swirling recirculating flow using DNS and experimental data'. In: *International Journal of Heat and Fluid Flow* 27.4, pp. 636–643. DOI: 10.1016/j.ijheatfluidflow.2006.02.020. URL: http://linkinghub.elsevier.com/retrieve/pii/S0142727X06000348 (cit. on pp. 80, 116).

Frenklach, M. (1984). 'Dynamics models in chemical kinetics'. In: *Combustion Chemistry*. Chap. Dynamics m, pp. 438–453 (cit. on p. 43).

Fröhlich, J., García-Villalba, M., and Rodi, W. (2007). 'Scalar Mixing and Large-Scale Coherent Structures in a Turbulent Swirling Jet'. In: *Flow, Turbulence and Combustion* 80.1, pp. 47–59. DOI: 10.1007/s10494-007-9121-3. URL: http://link.springer.com/10.1007/s10494-007-9121-3 (cit. on p. 117).

Fudihara, T. J., Goldstein Jr., L., and Mori, M. (2003). 'The Three-dimensional Numerical Aerodynamics of a Movable Block Burner'. In: *Brazilian Journal of Chemical Engineering* 20.04, pp. 391–401 (cit. on pp. 80, 86).

Fureby, C. (2005). 'A fractal flame-wrinkling large eddy simulation model for premixed turbulent combustion'. In: *Proceedings of the Combustion Institute* 30.1, pp. 593–601. DOI: 10.1016/j.proci.2004.08.068. URL: http://linkinghub.elsevier.com/retrieve/pii/S0082078404001316 (cit. on p. 101).

– (2007). 'Comparison of Flamelet and Finite Rate Chemistry LES for Premixed Turbulent Combustion'. In: *AIAA paper* 1413 (cit. on pp. 97–100).

– (1999). 'Monotonically Integrated Large Eddy Simulation of Free Shear Flows Introduction'. In: 37.5 (cit. on p. 99).

Gabriel, S., Baschwitz, A., Mathonnière, G., Fizaine, F., and Eleouet, T. (2013). 'Building future nuclear power fleets: The available uranium resources constraint'. In: *Resources Policy* 38.4, pp. 458–469. DOI: 10.1016/j.resourpol.2013.06.008. URL: http://linkinghub.elsevier.com/retrieve/pii/S0301420713000494 (cit. on p. 1).

Galley, D., Ducruix, S., Lacas, F., and Veynante, D. (2011). 'Mixing and stabilization study of a partially premixed swirling flame using laser induced fluorescence'. In: *Combustion and Flame* 158.1, pp. 155–171. DOI: 10.1016/j.combustflame.2010.08.004. URL: http://linkinghub.elsevier.com/retrieve/pii/S0010218010002300 (cit. on p. 117).

Gambini, M., Guizzi, G. L., and Vellini, M. (2005). 'H2/O2 Cycles: Thermodynamic Potentialities and Limits'. In: *Journal of Engineering for Gas Turbines and Power* 127.3, p. 553. DOI: 10.1115/1.1924401. URL: http://link.aip.org/link/JETPEZ/v127/i3/p553/s1%5C&Agg=doi (cit. on p. 4).

García-Armingol, T. and Ballester, J. (2014). 'Flame chemiluminescence in premixed combustion of hydrogen-enriched fuels'. In: *International Journal of Hydrogen Energy* 39.21, pp. 11299–11307. DOI: 10.1016/j.ijhydene.2014.05.109. URL: http://linkinghub.elsevier.com/retrieve/pii/S0360319914014918 (cit. on pp. 53, 54).

García-Villalba, M., Fröhlich, J., and Rodi, W. (2006). 'Identification and analysis of coherent structures in the near field of a turbulent unconfined annular swirling jet using large eddy simulation'. In: *Physics of Fluids* 18, pp. 1–17 (cit. on pp. 80, 111, 114).

Gauthier, B., Davidson, D. F., and Hanson, R. (2004). 'Shock tube determination of ignition delay times in full-blend and surrogate fuel mixtures'. In: *Combustion and Flame* 139.4, pp. 300–311. DOI: 10.1016/j.combustflame.2004.08.015. URL: http://linkinghub.elsevier.com/retrieve/pii/S0010218004001890 (cit. on p. 11).

Gaydon, A. G. (1974). *The Spectroscopy of Flames*. 2nd ed. Edinburgh: Chapman and Hall Ltd, p. 412 (cit. on pp. 51, 54).

Georgiadis, N. J., Rizzetta, D. P., and Fureby, C. (2009). 'Large-Eddy Simulation : Current Capabilities , Recommended Practices , and Future Research'. In: *47th AIAA Aerospace Sciences Meeting* AIAA 2009-948, pp. 1–20 (cit. on p. 102).

Giacomazzi, E. and Battaglia, V. (2004). 'The coupling of turbulence and chemistry in a premixed bluff-body flame as studied by LES'. In: *Combustion and Flame* 134-4, pp. 320–335 (cit. on p. 97).

Gicquel, L., Staffelbach, G., and Poinsot, T. (2012). 'Large Eddy Simulations of gaseous flames in gas turbine combustion chambers'. In: *Progress in Energy and Combustion Science* 38.6, pp. 782–817. DOI: 10.1016/j.pecs.2012.04.004. URL: http://linkinghub.elsevier.com/retrieve/pii/S0360128512000366 (cit. on pp. 80, 81).

Glarborg, P., Dam-Johansen, K., Miller, J. A., Kee, R. J., and Coltrin, M. E. (1994). 'Modeling the thermal DENOx process in flow reactors. Surface effects and Nitrous Oxide formation'. In: *International Journal of Chemical Kinetics* 26.4, pp. 421–436. DOI: 10.1002/kin.550260405. URL: http://doi.wiley.com/10.1002/kin.550260405 (cit. on p. 63).

Gobbato, P., Masi, M., Toffolo, A., and Lazzaretto, A. (2011). 'Numerical simulation of a hydrogen fuelled gas turbine combustor'. In: *International Journal of Hydrogen Energy* 36.13, pp. 7993–8002. DOI: 10.1016/j.ijhydene.2011.01.045. URL: http://linkinghub.elsevier.com/retrieve/pii/S0360319911000875 (cit. on p. 83).

Göckeler, K., Göke, S., Schimek, S., and Paschereit, C. O. (2010). 'Enhanced Recirculation in the Cold Flow Field of a Swirl-stabilized Burner for Ultra Wet Combustion'. In: *Int. Conf. on Jets, Wakes and Separated Flows* (cit. on p. 89).

Göckeler, K., Krüger, O., and Paschereit, C. O. (2014). 'Laminar burning velocities and emissions of hydrogen-methane-air-steam mixtures'. In: *Journal of Engineering for Gas Turbines and Power*. DOI: 10.1115/1.4028460. URL: http://gasturbinespower.asmedigitalcollection.asme.org/article.aspx?doi=10.1115/1.4028460 (cit. on p. 10).

Göke, S. (2012). 'Ultra Wet Combustion An Experimental and Numerical Study'. PhD thesis. Technische Universität Berlin, pp. 1–170 (cit. on pp. 46, 63, 67).

Göke, S., Füri, M., Bourque, G., Bobusch, B. C., Göckeler, K., Krüger, O., Schimek, S., Terhaar, S., and Paschereit, C. O. (2013). 'Influence of steam dilution on the combustion of natural gas and hydrogen in premixed and rich-quench-lean combustors'. In: *Fuel Processing Technology* 107, pp. 14–22. DOI: 10.1016/j.fuproc.2012.06.019. URL: http://linkinghub.elsevier.com/retrieve/pii/S0378382012002408 (cit. on p. 3).

Göke, S., Terhaar, S., Schimek, S., Göckeler, K., and Paschereit, C. O. (2011). 'Combustion of Natural Gas, Hydrogen And Bio-Fuels at Ultra-Wet Conditions'. In: *Proceedings of ASME Turbo Expo 2011* GT2011-456 (cit. on p. 86).

Goldin, G. M. (2005). 'Evaluation of LES subgrid reaction models in a lifted flame'. In: *43rd AIAA Aerospace Sciences Meeting and Exhibit, Reno*, p. 555 (cit. on p. 100).

Goodwin, D. G. (1994). 'An Open-Source, Extensible Software Suite for CVD Process Simulation'. In: *Egyptian Computer Science Journal* 98.40, p. 10147 (cit. on p. 15).

– (2004). 'One-Dimensional Flames'. In: *30th Symposium on Combustion*. Chicago: The National Energy Technology Laboratory, pp. 1–40. URL: http://www.et.byu.edu/~Tom/classes/641/Cantera/Workshop/flames.pdf (cit. on pp. 19, 20).

Gouldin, F. C., Depsky, J. S., and Lee, S.-L. (1985). 'Velocity field characteristics of a swirling flow combustor'. In: *AIAA Journal* 23.1, pp. 95–102. DOI: 10.2514/3.8876. URL: http://arc.aiaa.org/doi/abs/10.2514/3.8876 (cit. on p. 79).

Grcar, J. F., Bell, J. B., and Day, M. S. (2009). 'The Soret effect in naturally propagating, premixed, lean, hydrogen–air flames'. In: *Proceedings of the Combustion Institute* 32.1, pp. 1173–1180. DOI: 10.1016/j.proci.2008.06.075. URL: http://linkinghub.elsevier.com/retrieve/pii/S154074890800148X (cit. on p. 17).

Grinstein, F. and Kailasanath, K. (1994). 'Three Dimensional Numerical Simulations of Unsteady Reactive Square Jets'. In: *Combustion and Flame* 100, pp. 2–10 (cit. on p. 100).

Gui, N., Fan, J., Cen, K., and Chen, S. (2010). 'A direct numerical simulation study of coherent oscillation effects of swirling flows'. In: *Fuel* 89.12, pp. 3926–3933. DOI: 10.1016/j.fuel.2010.06.037. URL: http://linkinghub.elsevier.com/retrieve/pii/S0016236110003194 (cit. on p. 80).

Guo, P., Zang, S., and Ge, B. (2008). 'LES and Experimental Study of Flow Features in Humid-Air Combustion Chamber with Non-Premixed Circular-Disc Stabilized Flames'. In: *Proceedings of ASME Turbo Expo 2008* GT2008-50940, pp. 1–10 (cit. on p. 82).

Gupta, A., Beér, J. M., and Swithenbank, J. (1977). 'Concentric multi-annular swirl burner: Stability limits and emission characteristics'. In: *Symposium (International) on Combustion* 16.1, pp. 79–91. DOI: 10.1016/S0082-0784(77)80315-9. URL: http://linkinghub.elsevier.com/retrieve/pii/S0082078477803159 (cit. on p. 79).

Güthe, F., Guyot, D., Singla, G., Noiray, N., and Schuermans, B. (2012). 'Chemiluminescence as diagnostic tool in the development of gas turbines'. In: *Applied Physics B* 107.3, pp. 619–636. DOI: 10.1007/s00340-012-4984-y. URL: http://link.springer.com/10.1007/s00340-012-4984-y (cit. on p. 120).

Gutman, D. (1969). 'Erratum: Shock-Tube Study of OH Chemiluminescence in the Hydrogen–Oxygen Reaction'. In: *The Journal of Chemical Physics* 50.1, p. 572. DOI: 10.1063/1.1670865. URL: http://scitation.aip.org/content/aip/journal/jcp/50/1/10.1063/1.1670865 (cit. on p. 11).

Haber, L. C. and Vandsburger, U. (2003). 'A global reaction model for OH* chemiluminescence applied to a laminar flat-flame burner'. In: *Combustion Science and Technology* 175.10, pp. 1859–1891. DOI: 10.1080/713713115. URL: http://www.tandfonline.com/doi/abs/10.1080/713713115 (cit. on pp. 52, 53).

Hadjipaschalis, I., Poullikkas, A., and Efthimiou, V. (2009). 'Overview of current and future energy storage technologies for electric power applications'. In: *Renewable and Sustainable Energy Reviews* 13.6-7, pp. 1513–1522. DOI: 10.1016/j.rser.2008.09.028. URL: http://linkinghub.elsevier.com/retrieve/pii/S1364032108001664 (cit. on p. 2).

Hall, J. M. and Petersen, E. L. (2006a). 'An optimized kinetics model for OH chemiluminescence at high temperatures and atmospheric pressures'. In: *International Journal of Chemical Kinetics* 38.12, pp. 714–724. DOI: 10.1002/kin.20196. URL: http://doi.wiley.com/10.1002/kin.20196 (cit. on p. 54).

– (2006b). 'An optimized kinetics model for OH chemiluminescence at high temperatures and atmospheric pressures'. In: *International Journal of Chemical Kinetics* 38.12, pp. 714–724. DOI: 10.1002/kin.20196. URL: http://doi.wiley.com/10.1002/kin.20196 (cit. on pp. 56, 57).

Hardalupas, Y. and Orain, M. (2004). 'Local measurements of the time-dependent heat release rate and equivalence ratio using chemiluminescent emission from a flame'. In: *Combustion and Flame* 139.3, pp. 188–207. DOI: 10.1016/j.combustflame.2004.08.003. URL: http://linkinghub.elsevier.com/retrieve/pii/S001021800400152X (cit. on p. 53).

Heimel, S. (1957). *Effect of Initial Mixture Temperature on Burning Velocity of Hydrogen-Air Mixtures with Preheating and Simulated Preburning*. Tech. rep. Cleveland: NACA, pp. 1–24. URL: http://naca.central.cranfield.ac.uk/reports/1958/naca-tn-4156.pdf (cit. on p. 12).

Hiddemann, M., Hummel, F., Schmidli, J., and Argüelles Tunon, P. (2011). 'The Next Generation Alstom GT26 - The Pioneer in Operational Flexibility'. In: *Power-Gen Europe*. Milan, pp. 1–16 (cit. on p. 11).

Hu, G.-H., Sun, D.-J., and Yin, X.-Y. (2001). 'A numerical study of dynamics of a temporally evolving swirling jet'. In: *Physics of Fluids* 13.4, p. 951. DOI: 10.1063/1.1350876. URL: http://scitation.aip.org/content/aip/journal/pof2/13/4/10.1063/1.1350876 (cit. on p. 80).

Huang, Y. and Yang, V. (2009). 'Dynamics and stability of lean-premixed swirl-stabilized combustion'. In: *Progress in Energy and Combustion Science* 35.4, pp. 293–364. DOI: 10.1016/j.pecs.2009.01.002. URL: http://linkinghub.elsevier.com/retrieve/pii/S0360128509000094 (cit. on pp. 79, 81).

Huang, Y., Sung, H.-G., Hsieh, S.-Y., and Yang, V. (2003). 'Large-Eddy Simulation of Combustion Dynamics of Lean-Premixed Swirl-Stabilized Combustor'. In: *Journal of Propulsion and Power* 19.5, pp. 782–794. DOI: 10.2514/2.6194. URL: http://arc.aiaa.org/doi/abs/10.2514/2.6194 (cit. on p. 81).

Hubbert, M. K. (1971). 'Energy Resources of the Earth'. In: *Scientific American Book* 224.3, pp. 60–70 (cit. on p. 1).

Ibrahim, H., Ilinca, a., and Perron, J. (2008). 'Energy storage systems—Characteristics and comparisons'. In: *Renewable and Sustainable Energy Reviews* 12.5, pp. 1221–1250. DOI: 10.1016/j.rser.2007.01.023. URL: http://linkinghub.elsevier.com/retrieve/pii/S1364032107000238 (cit. on p. 2).

Iijima, T. and Takeno, T. (1986). 'Effects of temperature and pressure on burning velocity'. In: *Combustion and Flame* 65.1, pp. 35–43. DOI: 10.1016/0010-2180(86)90070-2. URL: http://linkinghub.elsevier.com/retrieve/pii/0010218086900702 (cit. on pp. 12, 24).

Issa, R. I. (1986). 'Solution of the implicitly discretized fluid flow equations by operator-splitting'. In: *Journal of Computational Physics* 62, pp. 40–65 (cit. on pp. 102, 106).

Jaffe, S. M., Larjo, J., and Henberg, R. (1991). 'Abel Inversion Using the Fast Fourier Transform'. In: *10th International Symposium on Plasma Chemistry* (cit. on pp. 89, 120).

James, S., Zhu, J., and Anand, M. S. (2006). 'Large-Eddy Simulations as a Design Tool'. In: *AIAA Journal* 44.4, pp. 674–686 (cit. on pp. 80, 81).

Janicka, J., Sadiki, A., Schäfer, M., and Heeger, C., eds. (2013). *Flow and Combustion in Advanced Gas Turbine Combustors*. Vol. 1581. Fluid Mechanics and Its Applications. Dordrecht: Springer Netherlands. DOI: 10.1007/978-94-007-5320-4. URL: http://link.springer.com/10.1007/978-94-007-5320-4 (cit. on p. 80).

Janssen, H., Emonts, B., Groehn, H.-G., Mai, H., Reichel, R., and Stolten, D. (2001). 'High pressure electrolysis : the key technology for efficient H2 production'. In: *4th Hydrogen Power - Theoretical and Engineering Solutions International Symposium*. Stralsund, pp. 172–177 (cit. on p. 4).

Jasak, H. (1996). 'Error Analysis and Estimation for the Finite Volume Method with Applications to Fluid Flows'. PhD thesis. Imperial College, pp. 1–394. URL: http://powerlab.fsb.hr/ped/kturbo/OpenFOAM/docs/HrvojeJasakPhD.pdf (cit. on p. 106).

Jehong, J. and Hussain, F. (1995). 'On the identification of a vortex'. In: *Journal of Fluid Mechanics* 285.69 (cit. on p. 114).

Jiang, X. and Luo, K. (2001). 'Direct Numerical Simulation of Transitional Noncircular Buoyant Reactive Jets'. In: *Theoretical and Computational Fluid Dynamics* 15.3, pp. 183–198. DOI: 10.1007/PL00013288. URL: http://link.springer.com/10.1007/PL00013288 (cit. on p. 80).

Jonsson, M. and Yan, J. (2005). 'Humidified gas turbine - a review of proposed and implemented cycles'. In: *Energy* 30, pp. 1013–1078. DOI: doi:10.1016/j.energy.2004.08.005. URL: http://www.sciencedirect.com/science/article/B6V2S-4DDTKWM-1/1/df468165e46c2765c423f1563b5d135f (cit. on p. 3).

Juste, G. (2006). 'Hydrogen injection as additional fuel in gas turbine combustor. Evaluation of effects'. In: *International Journal of Hydrogen Energy* 31.14, pp. 2112–2121. DOI: 10.1016/j.ijhydene.2006.02.006. URL: http://linkinghub.elsevier.com/retrieve/pii/S036031990600067X (cit. on p. 4).

Kathrotia, T., Fikri, M., Bozkurt, M., Hartmann, M., Riedel, U., and Schulz, C. (2010). 'Study of the H+O+M reaction forming OH*: Kinetics of OH* chemiluminescence in hydrogen combustion systems'. In: *Combustion and Flame* 157.7, pp. 1261–1273. DOI: 10.1016/j.combustflame.2010.04.003. URL: http://linkinghub.elsevier.com/retrieve/pii/S0010218010001070 (cit. on p. 54).

Kato, S. and Nomura, N. (1997). 'Hydrogen gas-turbine characteristics and hydrogen energy system schemes'. In: *Energy Conversion and Management* 38.10-13, pp. 1319–1326. DOI: 10.1016/S0196-8904(96)00161-6. URL: http://linkinghub.elsevier.com/retrieve/pii/S0196890496001616 (cit. on pp. 4, 5).

Kazakov, A. and Frenklach, M. (1994). *Reduced Reaction Sets based on GRI-Mech 1.2*. URL: http://www.me.berkeley.edu/drm/ (cit. on p. 82).

Kee, R. J., Coltrin, M. E., and Glarborg, P. (2003). *Chemically Reacting Flow*. Hoboken, NJ, USA: John Wiley & Sons, Inc. DOI: 10.1002/0471461296. URL: http://doi.wiley.com/10.1002/0471461296 (cit. on pp. 11, 19).

Kéromnès, A., Metcalfe, W. K., Heufer, K. a., Donohoe, N., Das, A. K., Sung, C.-J., Herzler, J., Naumann, C., Griebel, P., Mathieu, O., Krejci, M. C., Petersen, E. L., Pitz, W. J., and Curran, H. J. (2013). 'An experimental and detailed chemical kinetic modeling study of hydrogen and syngas mixture oxidation at elevated pressures'. In: *Combustion and Flame* 160, pp. 995–1011. DOI: 10.1016/j.combustflame.2013.01.001. URL: http://linkinghub.elsevier.com/retrieve/pii/S0010218013000023 (cit. on pp. 23, 34, 35, 46, 54).

Kerstein, A. R. (1988). 'A Linear- Eddy Model of Turbulent Scalar Transport and Mixing'. In: *Combustion Science and Technology* 60.4-6, pp. 391–421. DOI: 10.1080/00102208808923995 (cit. on p. 97).

Knowlton, R. (1984). 'An investigation of the safety aspects in the use of hydrogen as a ground transportation fuel'. In: *International Journal of Hydrogen Energy* 9.1-2, pp. 129–136. DOI: 10.1016/0360-3199(84)90041-7. URL: http://linkinghub.elsevier.com/retrieve/pii/0360319984900417 (cit. on p. 12).

Konnov, A. A., Colson, G., and De Ruyck, J. (2001). 'NO formation rates for hydrogen combustion in stirred reactors'. In: *Fuel* 80.1, pp. 49–65. DOI: 10.1016/S0016-2361(00)00060-0. URL: http://linkinghub.elsevier.com/retrieve/pii/S0016236100000600 (cit. on p. 66).

Koroll, G. W., Kumar, R. K., and Bowles, E. M. (1993). 'Burning velocities of hydrogen-air mixtures'. In: *Combustion and Flame* 94.3, pp. 330–340. DOI: 10.1016/0010-2180(93)90078-H. URL: http://linkinghub.elsevier.com/retrieve/pii/001021809390078H (cit. on pp. 13, 24, 25, 31).

Koroll, G. W. and Mulpuru, S. R. (1988). 'The effect of dilution with steam on the burning velocity and structure of premixed hydrogen flames'. In: *Symposium (International) on Combustion* 21.1, pp. 1811–1819. DOI: 10.1016/S0082-0784(88)80415-6. URL: http://linkinghub.elsevier.com/retrieve/pii/S0082078488804156 (cit. on pp. 10, 13, 25, 28, 33–35).

Kostas, J., Soria, J., and Chong, M. S. (2005). 'A comparison between snapshot POD analysis of PIV velocity and vorticity data'. In: *Experiments in Fluids* 38.2, pp. 146–160. URL: http://dx.doi.org/10.1007/s00348-004-0873-4 (cit. on p. 113).

Koutmos, P. and McGuirk, J. J. (1990). 'Isothermal Modeling of Gas Turbine Combustors: Computational Study'. In: *Journal of Propulsion* 7.6, pp. 1064–1071 (cit. on p. 80).

Krüger, O., Duwig, C., Göckeler, K., Terhaar, S., Strangfeld, C., Paschereit, C. O., and Fuchs, L. (2011a). 'Identification of Coherent Structures in a Turbulent Generic Swirl Burner using Large Eddy Simulations'. In: *20th AIAA Computational Fluid Dynamics Conference* AIAA 2011-3549, pp. 1–14 (cit. on p. 102).

Krüger, O., Duwig, C., Göke, S., Göckeler, K., Terhaar, S., Paschereit, C. O., and Fuchs, L. (2011b). 'Numerical Investigations of a Swirl-stabilized Premixed Flame at Ultra-Wet Conditions'. In: *Proceedings of ASME Turbo Expo 2011* GT2011-45866, pp. 1–12 (cit. on pp. 100, 105).

Krüger, O., Duwig, C., Göke, S., Paschereit, C. O., and Fuchs, L. (2011c). 'Large Eddy Simulation of Ultra-Wet Premixed Flames for Gas Turbine Applications'. In: *Proceedings of the European Combustion Meeting 2011*, pp. 1–6 (cit. on p. 105).

Krüger, O., Duwig, C., Terhaar, S., and Paschereit, C. O. (2014). 'Large eddy simulations of methane oxidation at ultra-wet conditions in a model gas turbine combustor applying detailed chemistry'. In: *Journal of Fluid Science and Technology* 9.3, pp. 1–12. DOI: 10.1299/jfst.2014jfst00. URL: https://www.jstage.jst.go.jp/article/jfst/9/3/9%5C_2014jfst0040/%5C_pdf (cit. on p. 128).

Krüger, O., Terhaar, S., Paschereit, C. O., and Duwig, C. (2013). 'Large Eddy Simulations of Hydrogen Oxidation at Ultra-Wet Conditions in a Model Gas Turbine Combustor Applying Detailed Chemistry'. In: *Journal of Engineering for Gas Turbines and Power* 135.2, pp. 021501–

0215010. DOI: 10.1115/1.4007718. URL: http://link.aip.org/link/JETPEZ/v135/i2/p021501/s1%5C&Agg=doi (cit. on pp. 25, 31, 100).

Kuehl, D. K. (1962). 'Effects of water on burning velocity of hydrogen-air flames'. In: *American Rocket Society Journal* 32, pp. 1724–1726 (cit. on pp. 12, 33).

Kuznetsov, M., Redlinger, R., Breitung, W., Grune, J., Friedrich, A., and Ichikawa, N. (2011). 'Laminar burning velocities of hydrogen-oxygen-steam mixtures at elevated temperatures and pressures'. In: *Proceedings of the Combustion Institute* 33.1, pp. 895–903. DOI: 10.1016/j.proci.2010.06.050. URL: http://linkinghub.elsevier.com/retrieve/pii/S1540748910000763 (cit. on pp. 10, 26, 28, 34, 35, 45, 46).

Kwon, O. C. and Faeth, G. M. (2001). 'Flame/stretch interactions of premixed hydrogen-fueled flames: measurements and predictions'. In: *Combustion and Flame* 124.4, pp. 590–610. DOI: 10.1016/S0010-2180(00)00229-7. URL: http://linkinghub.elsevier.com/retrieve/pii/S0010218000002297 (cit. on p. 13).

Lamoureux, N., Djebaili-Chaumeix, N., and Paillard, C. E. (2002). 'Laminarflame velocity determination for H2-air-steam mixtures using the spherical bomb method'. In: *Journal de Physique IV* 12.7, pp. 445–452 (cit. on pp. 13, 25, 26, 31).

Law, C. K. (2006). *Combustion Physics*. Cambridge: Cambridge University Press. DOI: 10.1017/CBO9780511754517 (cit. on p. 9).

Le Cong, T. and Dagaut, P. (2009). 'Oxidation of H2/CO2 mixtures and effect of hydrogen initial concentration on the combustion of CH4 and CH4/CO2 mixtures: Experiments and modeling'. In: *Proceedings of the Combustion Institute* 32.1, pp. 427–435. DOI: 10.1016/j.proci.2008.05.079. URL: http://linkinghub.elsevier.com/retrieve/pii/S1540748908003490 (cit. on pp. 29, 31, 43).

Le Cong, T. and Dagaut, P. (2008). 'Effect of Water Vapor on the Kinetics of Combustion of Hydrogen and Natural Gas: Experimental and Detailed Modeling Study'. In: *Proceedings of ASME Turbo Expo 2008* GT2008-50272, pp. 1–10 (cit. on pp. 13, 24).

Lee, H., Jiang, L., and Mohamad, a.a. (2014). 'A review on the laminar flame speed and ignition delay time of Syngas mixtures'. In: *International Journal of Hydrogen Energy* 39.2, pp. 1105–1121. DOI: 10.1016/j.ijhydene.2013.10.068. URL: http://linkinghub.elsevier.com/retrieve/pii/S036031991302541X (cit. on pp. 11, 12).

Legier, J. P., Poinsot, T., and Veynante, D. (2000). 'Dynamically thickened flame LES model for premixed and non-premixed turbulent combustion'. In: *Proc. of the summer program*, pp. 157–168. URL: http://ctr.stanford.edu/Summer00/poinsot.pdf (cit. on pp. 101, 102).

Lei, Y., Cui, Y., Xu, G., Nie, C., and Huang, W. (2007). 'The Effects of Fuel Dilution With Steam on Gas Turbine Combustor Performance'. In: *Volume 2: Turbo Expo 2007*, pp. 525–530. DOI: 10.1115/GT2007-27681. URL: http://proceedings.asmedigitalcollection.asme.org/proceeding.aspx?articleid=1601788 (cit. on p. 82).

Leibovich, S. (1984). 'Vortex stability and breakdown: Survey and extension'. In: *AIAA Journal* 22.1192 (cit. on p. 78).

Leuckel, W. (1967). 'Swirl intensities, swirl types and energy losses of different swirl generating devices'. In: *IFRF Doc. No. G* 2, pp. 1–54. URL: http://scholar.google.com/scholar?hl=en%5C&btnG=Search%5C&q=intitle:Swirl+intensities,+swirl+types+and+energy+losses+of+different+swirl+generating+devices%5C#0 (cit. on p. 79).

Levy, A. (1963). 'Effects of Water on Hydrogen Flames'. In: *AIAA Journal* 1.5, pp. 1239–1239. DOI: 10.2514/3.54904. URL: http://doi.aiaa.org/10.2514/3.54904 (cit. on pp. 13, 33).

Li, J., Zhao, Z., Kazakov, A., and Dryer, F. L. (2004a). 'An updated comprehensive kinetic model of hydrogen combustion'. In: *International Journal of Chemical Kinetics* 36.10, pp. 566–575. DOI: 10.1002/kin.20026. URL: http://doi.wiley.com/10.1002/kin.20026 (cit. on p. 23).

Li, J., Zhao, Z., Kazakov, A., and Dryer, F. L. (2004b). 'An updated comprehensive kinetic model of hydrogen combustion'. In: *International Journal of Chemical Kinetics* 36.10, pp. 566–575. DOI: 10.1002/kin.20026. URL: http://doi.wiley.com/10.1002/kin.20026 (cit. on pp. 23, 24, 37, 63, 83).

Lilley, D. G. (1977). 'Swirl Flows in Combustion: A Review'. In: *AIAA Journal* 15.8, pp. 1063–1078. DOI: 10.2514/3.60756. URL: http://arc.aiaa.org/doi/abs/10.2514/3.60756 (cit. on p. 79).

Liu, D. and MacFarlane, R. (1983). 'Laminar burning velocities of hydrogen-air and hydrogen-air-steam flames'. In: *Combustion and Flame* 49.1-3, pp. 59–71. URL: http://www.sciencedirect.com/science/article/pii/0010218083901517 (cit. on pp. 13, 25, 31, 33).

Lu, P. and Semi, V. (2003). 'A new second-moment closure approach for turbulent swirling confined flows'. In: *International Journal for Numerical Methods in Fluids* 150.September 2001, pp. 133–150 (cit. on p. 80).

Lucca-Negro, O. and O'Doherty, T. (2001). 'Vortex breakdown: A review'. In: *Progress in Energy and Combustion Science* 27, pp. 431–481 (cit. on p. 79).

Lumley, J. L. (1967). 'Atmospheric turbulence and radio wave propagation'. In: *Nauka*, pp. 116–178 (cit. on p. 112).

Maggio, G. and Cacciola, G. (2012). 'When will oil, natural gas, and coal peak?' In: *Fuel* 98.2012, pp. 111–123. DOI: 10.1016/j.fuel.2012.03.021. URL: http://linkinghub.elsevier.com/retrieve/pii/S001623611200230X (cit. on p. 1).

Mallard, E. and Le Chatelier, H. L. (1883). 'Thermal Model for Flame Propagation'. In: *Annals of Mines* 4, p. 379 (cit. on p. 9).

Malyshenko, S. P., Gryaznov, A. N., and Filatov, N. I. . (2004). 'High-pressure H2/O2-steam generators and their possible applications'. In: *International Journal of Hydrogen Energy* 29.6, pp. 589–596. DOI: 10.1016/j.ijhydene.2003.08.004. URL: http://linkinghub.elsevier.com/retrieve/pii/S0360319903002271 (cit. on p. 4).

Mancaruso, E. and Vaglieco, B. M. (2011). 'Spectroscopic measurements of premixed combustion in diesel engine'. In: *Fuel* 90.2, pp. 511–520. DOI: 10.1016/j.fuel.2010.09.052. URL: http://linkinghub.elsevier.com/retrieve/pii/S0016236110005247 (cit. on p. 51).

Marshall, B. W. (1986). *Hydrogen : Air : Steam Flammability Limits and Combustion Characteristics in the FITS Vessel*. Tech. rep. December. Livermore: Sandia National Laboratories, pp. 1–151 (cit. on p. 12).

Maurel, S., Borée, J., and Lumley, J. L. (2001). 'Extended Proper Orthogonal Decomposition : Application to Jet/Vortex Interaction'. In: *Flow, Turbulence and Combustion* 67.2, pp. 125–

136. DOI: 10.1023/A:1014050204350. URL: http://dx.doi.org/10.1023/A:1014050204350 (cit. on p. 116).

McMurtry, P. A., Jou, W.-H., Riley, J., and Metcalfe, R. W. (1986). 'Direct numerical simulations of a reacting mixing layer with chemical heat release'. In: *AIAA Journal* 24.6, pp. 962–970. DOI: 10.2514/3.9371. URL: http://arc.aiaa.org/doi/abs/10.2514/3.9371 (cit. on p. 80).

Midgley, K., Spencer, A., and McGuirk, J. J. (2005). 'Unsteady Flow Structures in Radial Swirler Fed Fuel Injectors'. In: *Journal of Engineering for Gas Turbines and Power* 127.4, pp. 755–764 (cit. on p. 79).

Moeck, J. P., Bourgouin, J.-F., Durox, D., Schuller, T., and Candel, S. (2013). 'Tomographic reconstruction of heat release rate perturbations induced by helical modes in turbulent swirl flames'. In: *Experiments in Fluids* 54.4, p. 1498. DOI: 10.1007/s00348-013-1498-2. URL: http://link.springer.com/10.1007/s00348-013-1498-2 (cit. on p. 80).

Montgomery, C., Kosály, G., and Riley, J. (1993). 'Direct numerical simulation of turbulent reacting flow using a reduced hydrogen-oxygen mechanism'. In: *Combustion and Flame* 95.3, pp. 247–260. DOI: 10.1016/0010-2180(93)90130-U. URL: http://linkinghub.elsevier.com/retrieve/pii/001021809390130U (cit. on p. 80).

Najm, H. N., Paul, P. H., Mueller, C. J., and Wyckoff, P. S. (1998). 'On the Adequacy of Certain Experimental Observables as Measurements of Flame Burning Rate'. In: *Combustion and Flame* 113.3, pp. 312–332. DOI: 10.1016/S0010-2180(97)00209-5. URL: http://linkinghub.elsevier.com/retrieve/pii/S0010218097002095 (cit. on p. 59).

Nikolaou, Z. M., Chen, J.-Y., and Swaminathan, N. (2013). 'A 5-step reduced mechanism for combustion of CO/H2/H2O/CH4/CO2 mixtures with low hydrogen/methane and high H2O content'. In: *Combustion and Flame* 160.1, pp. 56–75. DOI: 10.1016/j.combustflame.2012.09.010. URL: http://linkinghub.elsevier.com/retrieve/pii/S0010218012002714 (cit. on p. 24).

Nori, V. and Seitzman, J. (2009). 'CH chemiluminescence modeling for combustion diagnostics'. In: *Proceedings of the Combustion Institute* 32.1, pp. 895–903. DOI: 10.1016/j.proci.2008.05.050. URL: http://www.sciencedirect.com/science/article/pii/S1540748908001089%20http://linkinghub.elsevier.com/retrieve/pii/S1540748908001089 (cit. on pp. 53, 57).

Ó Conaire, M., Curran, H. J., Simmie, J. M., Pitz, W. J., and Westbrook, C. K. (2004). 'A comprehensive modeling study of hydrogen oxidation'. In: *International Journal of Chemical Kinetics* 36.11, pp. 603–622. DOI: 10.1002/kin.20036. URL: http://doi.wiley.com/10.1002/kin.20036 (cit. on pp. 12, 23, 25).

Oberleithner, K., Sieber, M., Nayeri, C. N., and Paschereit, C. O. (2011). 'On the control of global modes in swirling jet experiments'. In: *Journal of Physics: Conference Series* 318.3, p. 032050. DOI: 10.1088/1742-6596/318/3/032050. URL: http://stacks.iop.org/1742-6596/318/i=3/a=032050?key=crossref.8f07b586ad5ad99b9600f80216df2d7b (cit. on p. 113).

Olm, C., Zsély, I. G., Pálvölgyi, R., Varga, T., Nagy, T., Curran, H. J., and Turányi, T. (2014). 'Comparison of the performance of several recent hydrogen combustion mechanisms'. In: *Combustion and Flame* 161.9, pp. 2219–2234. DOI: 10.1016/j.combustflame.2014.03.

006. URL: http://linkinghub.elsevier.com/retrieve/pii/S0010218014000868 (cit. on pp. 23, 30, 31, 69).

Oran, E., Young, T., Boris, J., and Cohen, A. (1982). 'Weak and strong ignition. I. Numerical simulations of shock tube experiments'. In: *Combustion and Flame* 48, pp. 135–148. DOI: 10.1016/0010-2180(82)90123-7. URL: http://linkinghub.elsevier.com/retrieve/pii/0010218082901237 (cit. on p. 12).

Panoutsos, C., Hardalupas, Y., and Taylor, A. (2009). 'Numerical evaluation of equivalence ratio measurement using OH* and CH* chemiluminescence in premixed and non-premixed methane–air flames'. In: *Combustion and Flame* 156.2, pp. 273–291. DOI: 10.1016/j.combustflame.2008.11.008. URL: http://linkinghub.elsevier.com/retrieve/pii/S0010218008003623 (cit. on pp. 53, 54).

Paschereit, C. O., Gutmark, E., and Weisenstein, W. (1999). 'Coherent Structures in Swirling Flows and their Role in Acoustic Combustion Control'. In: *Physics of Fluids* 11.9 (cit. on p. 79).

Perret, L., Delville, J., Manceau, R., and Bonnet, J. P. (2008). 'Turbulent inflow conditions for large-eddy simulation based on low-order empirical model'. In: *Physics of Fluids* 20.7, p. 75107. DOI: 10.1063/1.2957019. URL: http://link.aip.org/link/?PHF/20/075107/1 (cit. on p. 113).

Peters, N. (1984). 'Laminar diffusion flamelet models in non-premixed turbulent combustion'. In: *Progress in Energy and Combustion Science* 10, pp. 319–339. DOI: doi:10.1016/0360-1285(84)90114-X. URL: http://www.sciencedirect.com/science/article/B6V3W-497BC3D-4C/1/2bef68fdbd1f884b895c3a1fa3da41a8 (cit. on p. 97).

Petersen, E., Kalitan, D., and Rickard, M. (2003). 'Calibration and Chemical Kinetics Modeling of an OH Chemiluminesence Diagnostic'. In: *39th AIAA/ASME/SAE/ASEE Joint Propulsion Conference and Exhibit*. July. Reston, Virigina: American Institute of Aeronautics and Astronautics, pp. 2–9. DOI: 10.2514/6.2003-4493. URL: http://arc.aiaa.org/doi/abs/10.2514/6.2003-4493 (cit. on pp. 55, 56).

Petersen, E., Kopp, M., Donato, N., and Güthe, F. (2012). 'Assessment of Current Chemiluminescence Kinetics Models at Engine Conditions'. In: *Journal of Engineering for Gas Turbines and Power* 134.5, p. 051501. DOI: 10.1115/1.4004735. URL: http://gasturbinespower.asmedigitalcollection.asme.org/article.aspx?articleid=1429887 (cit. on pp. 57, 58, 61, 70, 134).

Pfadler, S., Beyrau, F., and Leipertz, A. (2007). 'Flame front detection and characterization using conditioned particle image velocimetry (CPIV)'. In: *Optics Express* 81.1-2, pp. 205–219. DOI: 10.1007/s10494-007-9102-6. URL: http://www.springerlink.com/index/10.1007/s10494-007-9102-6 (cit. on p. 119).

Pierce, C. and Moin, P. (1998). 'Large eddy simulation of a confined coaxial jet with swirl and heat release'. In: *29th AIAA, Fluid Dynamics Conference*. Reston, Virigina: American Institute of Aeronautics and Astronautics. DOI: 10.2514/6.1998-2892. URL: http://arc.aiaa.org/doi/abs/10.2514/6.1998-2892 (cit. on p. 80).

Pilch, M. M. (1996). 'Hydrogen combustion during direct containment heating events'. In: *Nuclear Engineering and Design* 164.1-3, pp. 117–136. DOI: 10.1016/0029-5493(96)01228-9. URL: http://linkinghub.elsevier.com/retrieve/pii/0029549396012289 (cit. on p. 12).

Pitsch, H. (2002). 'Improved pollutant predictions in large-eddy simulations of turbulent non-premixed combustion by considering scalar dissipation rate fluctuations'. In: *Proceedings of the Combustion Institute* 29.2, pp. 1971–1978. DOI: 10.1016/S1540-7489(02)80240-1. URL: http://linkinghub.elsevier.com/retrieve/pii/S1540748902802401 (cit. on p. 97).

– (2006). 'Large-Eddy Simulation of Turbulent Combustion'. In: *Annual Review of Fluid Mechanics* 38.1, pp. 453–482. DOI: 10.1146/annurev.fluid.38.050304.092133. URL: http://www.annualreviews.org/doi/abs/10.1146/annurev.fluid.38.050304.092133 (cit. on pp. 80, 96).

Pitsch, H. and Lageneste, L. de (2003). 'Large-Eddy Simulation of Premixed Turbulent Combustion Using a Level-Set Approach'. In: *Proceedings of the Combustion Institute* 29, pp. 2001–2008 (cit. on p. 97).

Poinsot, T. and Veynante, D. (2005). *Theoretical and Numerical Combustion*. 2nd. R T Edwards Inc, pp. 1–522 (cit. on pp. 26, 36, 76–78, 93, 94, 97, 101).

Pope, S. B. (2013). 'Small scales, many species and the manifold challenges of turbulent combustion'. In: *Proceedings of the Combustion Institute* 34.1, pp. 1–31. DOI: 10.1016/j.proci.2012.09.009. URL: http://linkinghub.elsevier.com/retrieve/pii/S1540748912003963 (cit. on pp. 79, 80, 96, 97).

Raman, S. and Pitsch, H. (2007). 'A consistent LES/filtered-density function formulation for the simulation of turbulent flames with detailed chemistry'. In: *Proceedings of the Combustion Institute* 31, pp. 1711–1719 (cit. on p. 97).

Ranga Dinesh, K., Jenkins, K., Kirkpatrick, M., and Malalasekera, W. (2010). 'Modelling of instabilities in turbulent swirling flames'. In: *Fuel* 89.1, pp. 10–18. DOI: 10.1016/j.fuel.2009.06.024. URL: http://linkinghub.elsevier.com/retrieve/pii/S001623610900307X (cit. on p. 81).

Ranga Dinesh, K. and Kirkpatrick, M. (2009). 'Study of jet precession, recirculation and vortex breakdown in turbulent swirling jets using LES'. In: *Computers & Fluids* 38.6, pp. 1232–1242. DOI: 10.1016/j.compfluid.2008.11.015. URL: http://linkinghub.elsevier.com/retrieve/pii/S0045793008002314 (cit. on p. 80).

Reinke, M., Mantzaras, J., Schaeren, R., Bombach, R., Inauen, A., and Schenker, S. (2005). 'Homogeneous ignition of CH4/air and H2O and CO2-diluted CH4/O2 mixtures over Pt; an experimental and numerical investigation at pressures up to 16bar'. In: *Proceedings of the Combustion Institute* 30.2, pp. 2519–2527. DOI: 10.1016/j.proci.2004.08.054. URL: http://linkinghub.elsevier.com/retrieve/pii/S0082078404001080 (cit. on p. 12).

Rhode, D., Lilley, D., and McLaughlin, D. (1983). 'Mean Flowfields in Axisymmetric Geometries with Swirl Combustor'. In: *AIAA Journal* 21.4, pp. 593–600. DOI: 10.2514/3.60127. URL: http://arc.aiaa.org/doi/abs/10.2514/3.60127 (cit. on p. 79).

Riahi, A. (1990). 'Computer simulation of turbulent swirling flows'. In: *International Journal for Numerical Methods in Engineering* 29, pp. 533–557 (cit. on p. 80).

Sagaut, P., Comte, P., and Ducros, F. (2000). 'Filtered subgrid-scale models'. In: *Physics of Fluids* 12.1, p. 233. DOI: 10.1063/1.870297. URL: http://scitation.aip.org/content/aip/journal/pof2/12/1/10.1063/1.870297 (cit. on pp. 95, 96, 102).

Sankaran, V. and Menon, S. (2000). 'Structure of premixed turbulent flames in the thin-reaction-zones regime'. In: *Proceedings of the Combustion Institute* 28.1, pp. 203–209. DOI: 10.1016/S0082-0784(00)80212-X. URL: http://linkinghub.elsevier.com/retrieve/pii/S008207840080212X (cit. on p. 97).

Santner, J. S., Dryer, F. L., and Ju, Y. (2011). 'Effect of Water Content on Syngas Combustion at Elevated Pressure'. In: *American Institute of Aeronautics and Astronautics*, pp. 1–6 (cit. on pp. 13, 43).

Schmitt, P., Poinsot, T., Schuermans, B., and Geigle, K. P. (2007). 'Large-eddy simulation and experimental study of heat transfer, nitric oxide emissions and combustion instability in a swirled turbulent high-pressure burner'. In: *Journal of Fluid Mechanics* 570, p. 17. DOI: 10.1017/S0022112006003156. URL: http://www.journals.cambridge.org/abstract%5C_S0022112006003156 (cit. on p. 81).

Scholte, T. G. and Vaags, P. B. (1959). 'The burning velocity of hydrogen-air mixtures and mixtures of some hydrocarbons with air'. In: *Combustion and Flame* 3, pp. 495–501. DOI: 10.1016/0010-2180(59)90055-0. URL: http://linkinghub.elsevier.com/retrieve/pii/0010218059900550 (cit. on p. 12).

Schönborn, A., Sayad, P., Konnov, A. a., and Klingmann, J. (2014). 'OH*-chemiluminescence during autoignition of hydrogen with air in a pressurised turbulent flow reactor'. In: *International Journal of Hydrogen Energy* 39.23, pp. 12166–12181. DOI: 10.1016/j.ijhydene.2014.05.157. URL: http://linkinghub.elsevier.com/retrieve/pii/S0360319914015699 (cit. on p. 53).

Selle, L., Lartigue, G., Poinsot, T., Koch, R., Schildemacher, K.-U., Krebs, W., Prade, B., Kaufmann, P., and Veynante, D. (2004). 'Compressible large eddy simulation of turbulent combustion in complex geometry on unstructured meshes'. In: *Combustion and Flame* 137, pp. 489–505 (cit. on p. 101).

Sen, B. A. and Menon, S. (2010). 'Linear eddy mixing based tabulation and artificial neural networks for large eddy simulations of turbulent flames'. In: *Combustion and Flame* 157, pp. 62–74 (cit. on p. 97).

Sengissen, A. X., Van Kampen, J. F., Huls, R. A., Stoffels, G. G. M., Kok, J. B. W., and Poinsot, T. J. (2007). 'LES and experimental studies of cold and reacting flow in a swirled partially premixed burner with and without fuel modulation'. In: *Combustion and Flame* 150.1-2, pp. 40–53. DOI: 10.1016/j.combustflame.2007.02.009. URL: http://linkinghub.elsevier.com/retrieve/pii/S0010218007000843 (cit. on p. 81).

Senior, D. (1961). 'Burning velocities of hydrogen-air and hydrogen-oxygen mixtures'. In: *Combustion and Flame* 5, pp. 7–10. DOI: 10.1016/0010-2180(61)90067-0. URL: http://linkinghub.elsevier.com/retrieve/pii/0010218061900670 (cit. on p. 12).

Sherman, M. (1984). 'Hydrogen combustion in nuclear plant accidents and associated containment loads'. In: *Nuclear Engineering and Design* 82.1, pp. 13–24. DOI: 10.1016/0029-5493(84)90263-2. URL: http://linkinghub.elsevier.com/retrieve/pii/0029549384902632 (cit. on p. 12).

Shih, T.-H., Zhu, J., Liou, W. W., Chen, K.-H., Liu, N.-S., and Lumley, J. L. (1997). *Modeling of Turbulent Swirling Flows*. Tech. rep. Cleveland: Institute for Computational Mechanics in Propulsion, Center for Modeling of turbulence, and Transition, pp. 1–51 (cit. on p. 80).

Singh, D., Nishiie, T., Tanvir, S., and Qiao, L. (2012). 'An experimental and kinetic study of syngas/air combustion at elevated temperatures and the effect of water addition'. In: *Fuel* 94, pp. 448–456. DOI: 10.1016/j.fuel.2011.11.058. URL: http://linkinghub.elsevier.com/retrieve/pii/S0016236111007538 (cit. on p. 43).

Sirovich, L. (1987). 'Turbulence and the Dynamics of Coherent Structures. Part 1: Coherent Structures'. In: *Quarterly of Applied Mathematics* 45, pp. 561–571 (cit. on p. 113).

Skottene, M. and Rian, K. E. (2007). 'A study of NOx formation in hydrogen flames'. In: *International Journal of Hydrogen Energy* 32.15, pp. 3572–3585. DOI: 10.1016/j.ijhydene.2007.02.038. URL: http://linkinghub.elsevier.com/retrieve/pii/S0360319907001334 (cit. on pp. 63–67, 71, 134).

Sloan, D. G., Smith, P. J., and Smoot, L. D. (1986). 'Modeling of Swirl in Turbulent Flow Systems'. In: *Progress in Energy and Combustion Science* 12, pp. 163–250 (cit. on p. 80).

Smagorinsky, J. (1963). 'General circulation experiments with the primitive equations, I. the basic experiment'. In: *Monthly Weather Review* 91.3, pp. 99–164 (cit. on pp. 95, 96).

Smith, G. P., Golden, D. M., Frenklach, M., Moriarty, N. W., Eiteneer, B., Goldenberg, M., Bowman, C. T., Hanson, R. K., Song, S., Gardiner, W. C. J., Lissianski, V. V., and Qin, Z. (2000). *GRI 3.0*. http://www.me.berkeley.edu/gri_mech/. URL: http://www.me.berkeley.edu/gri%5C_mech/ (cit. on pp. 24, 64, 165).

Smith, G. P., Luque, J., Park, C., Jeffries, J. B., and Crosley, D. R. (2002). 'Low pressure flame determinations of rate constants for OH(A) and CH(A) chemiluminescence'. In: *Combustion and Flame* 131.1-2, pp. 59–69. DOI: 10.1016/S0010-2180(02)00399-1. URL: http://linkinghub.elsevier.com/retrieve/pii/S0010218002003991 (cit. on pp. 54, 59, 61, 67, 70, 71, 117, 134, 135, 165).

Smith, G. P., Park, C., and Luque, J. (2005). 'A note on chemiluminescence in low-pressure hydrogen and methane-nitrous oxide flames'. In: *Combustion and Flame* 140.4, pp. 385–389. DOI: 10.1016/j.combustflame.2004.11.011. URL: http://linkinghub.elsevier.com/retrieve/pii/S0010218004002469 (cit. on pp. 53, 54, 59, 61, 67, 70, 71, 112, 117, 134, 135, 165).

Sohn, C. H., Aum, Y. G., Chung, S. H., Hong, S. W., and Kim, H. D. (1999). 'A Burning Velocity Correlation for Premixed Hydrogen / Air / Steam Flames'. In: *The Korean Society of Mechanical Engineers International Journal* 13.3, pp. 294–303 (cit. on p. 13).

Spalding, D. B. (1971). 'Mixing and chemical reaction in steady confined turbulent flames'. In: *Symposium (International) on Combustion* 13.1, pp. 649–657. DOI: 10.1016/S0082-0784(71)80067-X (cit. on p. 97).

Srivastava, D. K., Dharamshi, K., and Agarwal, A. K. (2011). 'Flame kernel characterization of laser ignition of natural gas–air mixture in a constant volume combustion chamber'. In: *Optics and Lasers in Engineering* 49.9-10, pp. 1201–1209. DOI: 10.1016/j.optlaseng.2011.04.015. URL: http://linkinghub.elsevier.com/retrieve/pii/S0143816611001266 (cit. on p. 12).

Stathopoulos, P. and Paschereit, C. O. (2014). 'Retrofitting micro gas turbines for wet operation . An alternative way to introduce operational flexibility in CHP plants'. In: *Applied Energy Journal* accepted, pp. 1–24 (cit. on p. 4).

Sternfeld, H. and Heinrich, P. (1989). 'A demonstration plant for the hydrogen/oxygen spinning reserve'. In: *International Journal of Hydrogen Energy* 14.10, pp. 703–716. DOI: 10.1016/

0360-3199(89)90087-6. URL: http://linkinghub.elsevier.com/retrieve/pii/0360319989900876 (cit. on p. 4).

Sternfeld, H., Wojkowsky, H., and Schnurnberger, W. (1982). 'Wirkungsgrade und Kosten bei der Spitzenstromerzeugung aus Wasserstoff'. In: *Brennstoff, Wärme, Kraft* 8.9, pp. 401–403 (cit. on p. 3).

Stöhr, M., Arndt, C., and Meier, W. (2014). 'Transient effects of fuel–air mixing in a partially-premixed turbulent swirl flame'. In: *Proceedings of the Combustion Institute*. DOI: 10.1016/j.proci.2014.06.095. URL: http://linkinghub.elsevier.com/retrieve/pii/S1540748914002533 (cit. on p. 117).

Stöhr, M., Sadanandan, R., and Meier, W. (2011). 'Phase-resolved characterization of vortex–flame interaction in a turbulent swirl flame'. In: *Experiments in Fluids* 51.4, pp. 1153–1167. DOI: 10.1007/s00348-011-1134-y. URL: http://link.springer.com/10.1007/s00348-011-1134-y (cit. on p. 117).

Ströhle, J. and Myhrvold, T. (2007). 'An evaluation of detailed reaction mechanisms for hydrogen combustion under gas turbine conditions'. In: *International Journal of Hydrogen Energy* 32.1, pp. 125–135. DOI: 10.1016/j.ijhydene.2006.04.005. URL: http://linkinghub.elsevier.com/retrieve/pii/S0360319906001716 (cit. on p. 23).

Sweby, P. K., Journal, S., and Oct, N. (1984). 'High Resolution Schemes Using Flux Limiters for Hyperbolic Conservation Laws'. In: *SIAM Journal on Numerical Analysis* 21.5, pp. 995–1011 (cit. on p. 106).

Syred, N. (2006). 'A review of oscillation mechanisms and the role of the precessing vortex core (PVC) in swirl combustion systems'. In: *Progress in Energy and Combustion Science* 32.2, pp. 93–161. DOI: 10.1016/j.pecs.2005.10.002. URL: http://linkinghub.elsevier.com/retrieve/pii/S0360128505000353 (cit. on p. 79).

Syred, N. and Beér, J. M. (1974). 'Combustion in swirling flows: A review'. In: *Combustion and Flame* 23.2, pp. 143–201. DOI: 10.1016/0010-2180(74)90057-1. URL: http://linkinghub.elsevier.com/retrieve/pii/0010218074900571 (cit. on p. 79).

Szabó, T., Yáñez, J., Kotchourko, a., Kuznetsov, M., and Jordan, T. (2012). 'Parameterization of Laminar Burning Velocity Dependence on Pressure and Temperature in Hydrogen/Air/Steam Mixtures'. In: *Combustion Science and Technology* 184.10-11, pp. 1427–1444. DOI: 10.1080/00102202.2012.690253. URL: http://www.tandfonline.com/doi/abs/10.1080/00102202.2012.690253 (cit. on p. 13).

Tachibana, S., Zimmer, L., and Kazuo, S. (2004). 'Flame front detection and dynamics using PIV in a turbulent premixed flame'. In: *12th International Symposium on Applications of Laser Techniques to Fluid Mechanics*. URL: http://in3.dem.ist.utl.pt/lxlaser2004/pdf/paper%5C_04%5C_4.pdf (cit. on p. 119).

Takahashi, F., Mizomoto, M., and Ikai, S. (1983). 'Laminar Burning Velocities of Hydrogen/Oxygen/Inert Gas Mixtures'. In: *Alternative Energy Sources III* 5, pp. 447–457 (cit. on pp. 12, 24).

Tamura, M., Berg, P. A., Harrington, J. E., Luque, J., Jeffries, J. B., Smith, G. P., and Crosley, D. R. (1998). 'Collisional Quenching of CH(A), OH(A), and NO(A) in Low Pressure Hydrocarbon Flames'. In: *Combustion and Flame* 114.3-4, pp. 502–514. DOI: 10.1016/S0010-2180(97)00324-6. URL: http://linkinghub.elsevier.com/retrieve/pii/S0010218097003246 (cit. on pp. 54, 61).

Terhaar, S., Bobusch, B. C., and Paschereit, C. O. (2012). 'Effects of Outlet Boundary Conditions on the Reacting Flow Field in a Swirl-Stabilized Burner at Dry and Humid Conditions'. In: *Journal of Engineering for Gas Turbines and Power* 134.11, p. 111501. DOI: 10.1115/1.4007165. URL: http://gasturbinespower.asmedigitalcollection.asme.org/article.aspx?articleid=1477137 (cit. on p. 104).

Terhaar, S., Göckeler, K., Schimek, S., Göke, S., and Paschereit, C. O. (2011). 'Non-Reacting and Reacting Flow in a Swirl-Stabilized Burner for Ultra-Wet Combustion'. In: *41st AIAA Fluid Dynamics Conference and Exhibit, 27-30 June 2011, Honolulu, Hawaii*. AIAA 2011-3584 (cit. on p. 89).

Terhaar, S., Krüger, O., and Paschereit, C. O. (2014). 'Flow Field and Flame Dynamics of Swirling Methane and Hydrogen Flames at Dry and Steam Diluted Conditions'. In: *Journal of Engineering for Gas Turbines and Power* 137.4, p. 041503. DOI: 10.1115/1.4028392. URL: http://gasturbinespower.asmedigitalcollection.asme.org/article.aspx?doi=10.1115/1.4028392 (cit. on pp. 122, 123, 126).

Tropea, C., Yarin, A. L., and Foss, J. F. (2007). *Springer Handbook of Experimental Fluid Mechanics*. Ed. by Tropea, C., Yarin, A. L., and Foss, J. F. Berlin, Heidelberg: Springer Berlin Heidelberg. DOI: 10.1007/978-3-540-30299-5. URL: http://link.springer.com/10.1007/978-3-540-30299-5 (cit. on p. 80).

Tse, S. D., Zhu, D. L., and Law, C. K. (2000). 'Morphology and burning rates of expanding spherical flames in H2/O2/inert mixtures up to 60 atmospheres'. In: *Proceedings of the Combustion Institute* 28.2, pp. 1793–1800. DOI: 10.1016/S0082-0784(00)80581-0. URL: http://linkinghub.elsevier.com/retrieve/pii/S0082078400805810 (cit. on pp. 10, 12, 24).

Turányi, T. (1997). 'Applications of sensitivity analysis to combustion chemistry'. In: *Reliability Engineering and System Safety* 57, pp. 41–48 (cit. on p. 43).

Turner, J. A. (2004). 'Sustainable hydrogen production.' In: *Science (New York, N.Y.)* 305.5686, pp. 972–4. DOI: 10.1126/science.1103197. URL: http://www.ncbi.nlm.nih.gov/pubmed/15310892 (cit. on p. 4).

UCSD (2014). *Chemical-Kinetic Mechanisms for Combustion Applications*. URL: http://combustion.ucsd.edu (cit. on pp. 63, 67, 71, 134, 135, 165).

Veynante, D. (2002). 'Turbulent combustion modeling'. In: *Progress in Energy and Combustion Science* 28.3, pp. 193–266. DOI: 10.1016/S0360-1285(01)00017-X. URL: http://linkinghub.elsevier.com/retrieve/pii/S036012850100017X (cit. on pp. 80, 96).

Wang, B., Olivier, H., and Grönig, H. (2003). 'Ignition of shock-heated H2-air-steam mixtures'. In: *Combustion and Flame* 133.1-2, pp. 93–106. DOI: 10.1016/S0010-2180(02)00552-7. URL: http://linkinghub.elsevier.com/retrieve/pii/S0010218002005527 (cit. on pp. 13, 22, 29, 31, 47).

Wang, H., Luo, K., Lu, S., and Fan, J. (2011). 'Direct numerical simulation and analysis of a hydrogen/air swirling premixed flame in a micro combustor'. In: *International Journal of Hydrogen Energy* 36.21, pp. 13838–13849. DOI: 10.1016/j.ijhydene.2011.07.136. URL: http://dx.doi.org/10.1016/j.ijhydene.2011.07.136 (cit. on p. 82).

Wang, Y., Xu, G., Nie, C., Xiao, Y., Huang, W., Zhang, Z., and Cui, Y. (2005). 'Influence Of Humid Air On Gaseous Combustion Of Gas Turbines'. In: *ASME Turbo Expo 2005, ASME Paper 2006-GT-68946* (cit. on p. 80).

Warnatz, J., Maas, U., and Dibble, R. W. (2001). *Combustion*. Berlin, Heidelberg: Springer Berlin Heidelberg. DOI: 10.1007/978-3-662-04508-4. URL: http://link.springer.com/10.1007/978-3-662-04508-4 (cit. on p. 10).

Weller, H. G., Tabora, G., and Jasak, H. (1998). 'A tensorial approach to computational continuum mechanics using object-oriented techniques'. In: *Computers in Physics* 12.6, pp. 620–631 (cit. on p. 93).

Wilkening, H. and Baraldi, D. (2007). 'CFD modelling of accidental hydrogen release from pipelines'. In: *International Journal of Hydrogen Energy* 32.13, pp. 2206–2215. DOI: 10.1016/j.ijhydene.2007.04.022. URL: http://linkinghub.elsevier.com/retrieve/pii/S0360319907002133 (cit. on p. 12).

Wu, C. and Law, C. (1985). 'On the determination of laminar flame speeds from stretched flames'. In: *Symposium (International) on Combustion* 20.1, pp. 1941–1949. DOI: 10.1016/S0082-0784(85)80693-7. URL: http://linkinghub.elsevier.com/retrieve/pii/S0082078485806937 (cit. on pp. 10, 12, 24).

Yang, F., Law, C., Sung, C., and Zhang, H. (2010). 'A mechanistic study of Soret diffusion in hydrogen–air flames'. In: *Combustion and Flame* 157.1, pp. 192–200. DOI: 10.1016/j.combustflame.2009.09.018. URL: http://linkinghub.elsevier.com/retrieve/pii/S0010218009002764 (cit. on p. 17).

Yang, W.-C. (2006). 'Hydrogen-Fueled Power Systems'. In: *The Gas Turbine Handbook*. Ed. by Dennis, R. Vol. 15261. 724. Morgantown: U.S. Department of Energy. Chap. 1.3.1.3, pp. 107–115. URL: http://www.netl.doe.gov/research/coal/energy-systems/turbines/reference-shelf/handbook (cit. on p. 4).

Yeh, Y. and Cummins, H. Z. (1964). 'Localized Fluid FLow Measurements with an He-Ne Laser Spectrometer'. In: *Applied Physics Letters* 4.10, p. 176. DOI: 10.1063/1.1753925. URL: http://scitation.aip.org/content/aip/journal/apl/4/10/10.1063/1.1753925 (cit. on p. 79).

Zeldovich, J. (1946). 'The Oxidation of Nitrogen Combustion and Explosions'. In: *Acta Physicochimca* 21.4, pp. 577–628 (cit. on p. 65).

Zemtsop, C. P., Stöllinger, M. K., Heinz, S., and Stanescu, D. (2009). 'Large-Eddy Simulation of Swirling Turbulent Jet Flows in Absence of Vortex Breakdown'. In: *AIAA Journal* 47.12, pp. 3011–3021. DOI: 10.2514/1.43813. URL: http://arc.aiaa.org/doi/abs/10.2514/1.43813 (cit. on p. 80).

List of Figures

List of Tables

APPENDIX A

Reaction Mechanism

The reaction scheme as used for Large Eddy Simulations is presented in Table A.1. The reaction scheme is based on the reaction scheme of Burke et al. (2011a) and extended by the OH^* chemiluminescence subset of Smith (Smith et al., 2002; Smith et al., 2005) and the nitrogen subset (2004-12-09 (2)) of the *University of California at San Diego* (UCSD, 2014). For the molecular transport the data of the GRI 3.0 was used Smith et al., 2000.

Table A.1: Reaction mechanism for highly steam diluted hydrogen combustion.

#	**Equation**	A (**cm^3,mol,s**)	n $(-)$	E_a ($^{\text{kJ}}/_{\text{mol}}$)	**Comment**
$H_2 - O_2$ Chain Reactions					
$R1$	$H + O_2 \rightleftharpoons O + OH$	$1.04 \cdot 10^{14}$	0.0	$1.5286 \cdot 10^{4}$	
$R2$	$O + H_2 \rightleftharpoons H + OH$	$3.818 \cdot 10^{12}$	0.0	$7.948 \cdot 10^{3}$	Duplicate
$R3$	$O + H_2 \rightleftharpoons H + OH$	$8.792 \cdot 10^{14}$	0.0	$1.917 \cdot 10^{4}$	Duplicate
$R4$	$H_2 + OH \rightleftharpoons H_2O + H$	$0.216 \cdot 10^{9}$	1.51	$0.343 \cdot 10^{4}$	
$R5$	$OH + OH \rightleftharpoons O + H_2O$	$3.34 \cdot 10^{4}$	2.42	$-1.93 \cdot 10^{3}$	
$H_2 - O_2$ Dissociation Reactions					
$R6$	$H_2(+M) \rightleftharpoons H + H(+M)$	$4.577 \cdot 10^{19}$	-1.40	$1.0438 \cdot 10^{5}$	
	$H_2 : 2.5, H_2O : 12, CO : 1.9, CO_2 : 3.8, AR : 0, HE : 0$				
$R7$	$H_2 + AR \rightleftharpoons H + H + AR$	$5.840 \cdot 10^{18}$	-1.10	$1.0438 \cdot 10^{5}$	
$R8$	$H_2 + HE \rightleftharpoons H + H + HE$	$5.840 \cdot 10^{18}$	-1.10	$1.0438 \cdot 10^{5}$	
$R9$	$O + O(+M) \rightleftharpoons O_2(+M)$	$6.165 \cdot 10^{15}$	-0.50	0	
	$H_2 : 2.5, H_2O : 12, CO : 1.9, CO_2 : 3.8, AR : 0, HE : 0$				
$R10$	$O + O + AR \rightleftharpoons O_2 + AR$	$1.886 \cdot 10^{13}$	0.0	$-1.788 \cdot 10^{3}$	

continued on next page ...

#	Equation	A (cm^3,mol,s)	n $(-)$	E_a ($^{kJ}/_{mol}$)	Comment
$R11$	$O + O + HE \rightleftharpoons O_2 + HE$	$1.886 \cdot 10^{13}$	0.0	$-1.788 \cdot 10^{3}$	
$R12$	$O + H(+M) \rightleftharpoons OH(+M)$	$4.714 \cdot 10^{18}$	-1.00	0	
	$H_2 : 2.5, H_2O : 12, CO : 1.9, CO_2 : 3.8, AR : 0.75, HE : 0.75$				
$R13$	$H_2O(+M) \rightleftharpoons H + OH(+M)$	$6.064 \cdot 10^{27}$	-3.322	$1.2079 \cdot 10^{5}$	
	$H_2 : 3.0, H_2O : 0, O_2 : 1.5, N_2 : 2.0, CO : 1.9, CO_2 : 3.8$				
$R14$	$H_2O + H_2O \rightleftharpoons H + OH + H_2O$	$1.006 \cdot 10^{26}$	-2.44	$1.2018 \cdot 10^{5}$	
Formation and consumption of $\mathbf{HO_2}$					
$R15$	$H + O_2(+M) \rightleftharpoons HO_2(+M)$	$4.65084 \cdot 10^{12}$	0.44	0	
	Low	$6.366 \cdot 10^{20}$	-1.72	$5.248 \cdot 10^{2}$	
	$Troe$	0.5	$1 \cdot 10^{-30}$	$1 \cdot 10^{30}$	
	$H_2 : 2.0, H_2O : 14, O_2 : 0.78, AR : 0.67, HE : 0.8, CO : 1.9, CO_2 : 3.8$				
$R16$	$HO_2 + H \rightleftharpoons H_2 + O_2$	$2.750 \cdot 10^{6}$	2.09	$-1.451 \cdot 10^{3}$	
$R17$	$HO_2 + H \rightleftharpoons OH + OH$	$7.079 \cdot 10^{13}$	0.0	$2.950 \cdot 10^{2}$	
$R18$	$HO_2 + O \rightleftharpoons O_2 + OH$	$2.850 \cdot 10^{10}$	1.0	$-7.2393 \cdot 10^{2}$	
$R19$	$HO_2 + OH \rightleftharpoons H_2O + O_2$	$2.890 \cdot 10^{13}$	0.0	$-4.970 \cdot 10^{2}$	
Formation and consumption of $\mathbf{H_2O_2}$					
$R20$	$HO_2 + HO_2 \rightleftharpoons H_2O_2 + O_2$	$4.200 \cdot 10^{14}$	0.0	$1.1982 \cdot 10^{4}$	Duplicate
$R21$	$HO_2 + HO_2 \rightleftharpoons H_2O_2 + O_2$	$1.300 \cdot 10^{11}$	0.0	$-1.6293 \cdot 10^{3}$	Duplicate
$R22$	$H_2O_2(+M) \rightleftharpoons OH + OH(+M)$	$2.00 \cdot 10^{12}$	0.9	$4.8749 \cdot 10^{4}$	
	Low	$2.49 \cdot 10^{24}$	-2.30	$4.8749 \cdot 10^{4}$	
	$Troe$	0.43	$1 \cdot 10^{-30}$	$1 \cdot 10^{30}$	
	$H2 : 3.7, H_2O2 : 7.7, H_2O : 7.5, O_2 : 1.2, HE : 0.65, N2 : 1.5, CO : 2.8, CO_2 : 1.6$				
$R23$	$H_2O_2 + H \rightleftharpoons H_2O + OH$	$2.410 \cdot 10^{13}$	0.0	$3.970 \cdot 10^{3}$	
$R24$	$H_2O_2 + H \rightleftharpoons HO_2 + H_2$	$4.820 \cdot 10^{13}$	0.0	$7.950 \cdot 10^{3}$	
$R25$	$H_2O_2 + O \rightleftharpoons OH + HO_2$	$9.550 \cdot 10^{6}$	2.0	$3.970 \cdot 10^{3}$	
$R26$	$H_2O_2 + OH \rightleftharpoons HO_2 + H_2O$	$1.740 \cdot 10^{12}$	0.0	$3.180 \cdot 10^{2}$	Duplicate
$R27$	$H_2O_2 + OH \rightleftharpoons HO_2 + H_2O$	$1.740 \cdot 10^{12}$	0.0	$3.180 \cdot 10^{2}$	Duplicate
$\mathbf{OH^*}$ subset by Smith (2002)					
$R28$	$H + O(+M) \rightleftharpoons OH^*(+M)$	$5.450 \cdot 10^{12}$	0.0	0	

continued on next page ...

#	Equation	A (cm^3,mol,s)	n $(-)$	E_a (kJ/mol)	Comment
	$H2 : 2.5, H_2O2 : 12.0$				
$R29$	$OH + OH + H \rightarrow OH^* + H2O$	$1.450 \cdot 10^{15}$	0.0	0	
$R30$	$OH^* \rightarrow OH + h\nu$	$1.45 \cdot 10^{+6}$	0.0	0	
$R31$	$OH^* + N_2 \rightarrow OH + N_2$	$1.08 \cdot 10^{11}$	0.5	-1238	
$R32$	$OH^* + H_2O \rightarrow OH + H_2O$	$5.92 \cdot 10^{12}$	0.5	-861	
$R33$	$OH^* + H_2 \rightarrow OH + H_2$	$2.95 \cdot 10^{12}$	0.5	-444	
$R34$	$OH^* + CO_2 \rightarrow OH + CO_2$	$2.75 \cdot 10^{12}$	0.5	-968	
$R35$	$OH^* + CO \rightarrow OH + CO$	$3.23 \cdot 10^{12}$	0.5	-787	
Nitrogen subset by San Diego (2002)					
$R36$	$O + N_2 \rightleftharpoons NO + N$	$1.470 \cdot 10^{13}$	0.300	75286.81	
$R37$	$N + O_2 \rightleftharpoons NO + O$	$6.400 \cdot 10^{9}$	1.000	6285.85	
$R38$	$N + OH \rightleftharpoons NO + H$	$3.800 \cdot 10^{13}$	0.000	0.00	
$R39$	$NH + H \rightleftharpoons N + H_2$	$1.000 \cdot 10^{13}$	0.000	0.00	
$R40$	$NH + O \rightleftharpoons NO + H$	$9.200 \cdot 10^{13}$	0.000	0.00	
$R41$	$NH + OH \rightleftharpoons HNO + H$	$4.000 \cdot 10^{13}$	0.000	0.00	
$R42$	$NH + OH \rightleftharpoons N + H_2O$	$5.000 \cdot 10^{11}$	0.500	2000.48	
$R43$	$NH + O_2 \rightleftharpoons HNO + O$	$4.600 \cdot 10^{5}$	2.000	6500.96	
$R44$	$NH + NO \rightleftharpoons N_2O + H$	$3.200 \cdot 10^{14}$	-0.450	0.00	
$R45$	$NH + NO \rightleftharpoons N_2 + OH$	$2.200 \cdot 10^{13}$	-0.230	0.00	
$R46$	$NH_2 + H \rightleftharpoons NH + H_2$	$4.000 \cdot 10^{13}$	0.000	3652.01	
$R47$	$NH_2 + O \rightleftharpoons HNO + H$	$9.900 \cdot 10^{14}$	-0.500	0.00	
$R48$	$NH_2 + OH \rightleftharpoons NH + H_2O$	$4.000 \cdot 10^{6}$	2.000	1001.43	
$R49$	$NH_2 + NO \rightleftharpoons N_2 + H_2O$	$2.000 \cdot 10^{20}$	-2.600	924.95	
$R50$	$NH_2 + NO \rightleftharpoons N_2H + OH$	$9.300 \cdot 10^{11}$	0.000	0.00	
$R51$	$NH_3 + M \rightleftharpoons NH_2 + H + M$	$2.200 \cdot 10^{16}$	0.000	93451.24	
$R52$	$NH_3 + H \rightleftharpoons NH_2 + H_2$	$6.400 \cdot 10^{5}$	2.390	10181.64	
$R53$	$NH_3 + O \rightleftharpoons NH_2 + OH$	$9.400 \cdot 10^{6}$	1.940	6465.11	
$R54$	$NH_3 + OH \rightleftharpoons NH_2 + H_2O$	$2.040 \cdot 10^{6}$	2.040	566.44	
$R55$	$N_2H \rightleftharpoons N_2 + H$	$1.000 \cdot 10^{8}$	0.000	0.00	

continued on next page . . .

#	Equation	A (cm^3,mol,s)	n $(-)$	E_a (kJ/mol)	Comment
$R56$	$N_2H + H \rightleftharpoons N_2 + H_2$	$1.000 \cdot 10^{14}$	0.000	0.00	
$R57$	$N_2H + O \rightleftharpoons N_2O + H$	$1.000 \cdot 10^{14}$	0.000	0.00	
$R58$	$N_2H + OH \rightleftharpoons N_2 + H_2O$	$5.000 \cdot 10^{13}$	0.000	0.00	
$R59$	$HNO + M \rightleftharpoons H + NO + M$	$1.500 \cdot 10^{16}$	0.000	48757.17	
	$H_2 : 2.0, H_2O : 10.0, O_2 : 2.0, N_2 : 2.0$				
$R60$	$HNO + H \rightleftharpoons NO + H_2$	$4.400 \cdot 10^{11}$	0.720	650.10	
$R61$	$HNO + OH \rightleftharpoons NO + H_2O$	$3.600 \cdot 10^{13}$	0.000	0.00	
$R62$	$N_2O(+M) \rightleftharpoons N_2 + O(+M)$	$8.000 \cdot 10^{11}$	0.000	62619.50	
	Low	$2.000 \cdot 10^{14}$	0.0	56644.36	
$R63$	$N_2O + H \rightleftharpoons N_2 + OH$	$2.230 \cdot 10^{14}$	0.000	16754.30	
$R64$	$N_2O + O \rightleftharpoons 2NO$	$2.900 \cdot 10^{13}$	0.000	23159.66	
$R65$	$N_2O + OH \rightleftharpoons N_2 + HO2$	$2.000 \cdot 10^{12}$	0.000	10000.00	
$R66$	$NO_2 + M \rightleftharpoons NO + O + M$	$1.000 \cdot 10^{16}$	0.000	65965.58	
$R67$	$NO + HO_2 \rightleftharpoons NO_2 + OH$	$2.100 \cdot 10^{12}$	0.000	−480.40	
$R68$	$NO_2 + H \rightleftharpoons NO + OH$	$3.500 \cdot 10^{14}$	0.000	1500.96	
$R69$	$NO_2 + O \rightleftharpoons NO + O_2$	$1.000 \cdot 10^{13}$	0.000	599.90	

Table A.2: Thermophysical data for the reaction mechanism for highly steam diluted hydrogen combustion.

					#
H	120186H 1 G	0300.00	5000.00	1000.00	1
$0.02500000 \cdot 10^2$	0.00000000	0.00000000	0.00000000	0.00000000	2
$0.02547163 \cdot 10^6$	$-0.04601176 \cdot 10^1$	$0.02500000 \cdot 10^2$	0.00000000	0.00000000	3
0.00000000	0.00000000	$0.02547163 \cdot 10^6$	$-0.04601176 \cdot 10^1$		4
H_2	121286H 2 G	0300.00	5000.00	1000.00	1
$0.02991423 \cdot 10^2$	$0.07000644 \cdot 10^{-2}$	$-0.05633829 \cdot 10^{-6}$	$-0.09231578 \cdot 10^{-10}$	$0.01582752 \cdot 10^{-13}$	2
$-0.08350340 \cdot 10^4$	$-0.01355110 \cdot 10^2$	$0.03298124 \cdot 10^2$	$0.08249442 \cdot 10^{-2}$	$-0.08143015 \cdot 10^{-5}$	3
$-0.09475434 \cdot 10^{-9}$	$0.04134872 \cdot 10^{-11}$	$-0.01012521 \cdot 10^5$	$-0.03294094 \cdot 10^2$		4
O	120186O 1 G	0300.00	5000.00	1000.00	1

continued on next page . . .

					#
$0.02542060 \cdot 10^{2}$	$-0.02755062 \cdot 10^{-3}$	$-0.03102803 \cdot 10^{-7}$	$0.04551067 \cdot 10^{-10}$	$-0.04368052 \cdot 10^{-14}$	2
$0.02923080 \cdot 10^{6}$	$0.04920308 \cdot 10^{2}$	$0.02946429 \cdot 10^{2}$	$-0.01638166 \cdot 10^{-1}$	$0.02421032 \cdot 10^{-4}$	3
$-0.01602843 \cdot 10^{-7}$	$0.03890696 \cdot 10^{-11}$	$0.02914764 \cdot 10^{6}$	$0.02963995 \cdot 10^{2}$		4
OH	S 9/01O 1H 1 0 G	200.000	6000.000	1000.	1
2.86472886	$1.05650448 \cdot 10^{-3}$	$-2.59082758 \cdot 10^{-7}$	$3.05218674 \cdot 10^{-11}$	$-1.33195876 \cdot 10^{-15}$	2
$3.68362875 \cdot 10^{3}$	5.70164073	4.12530561	$-3.22544939 \cdot 10^{-3}$	$6.52764691 \cdot 10^{-6}$	3
$-5.79853643 \cdot 10^{-9}$	$2.06237379 \cdot 10^{-12}$	$3.34630913 \cdot 10^{3}$	$-6.90432960 \cdot 10^{-1}$	$4.51532273 \cdot 10^{3}$	4
OHA	S /01O H 1 0 0G	200.000	6000.000	1000.	1
2.86472886	$1.05650448 \cdot 10^{-3}$	$-2.59082758 \cdot 10^{-7}$	$3.05218674 \cdot 10^{-11}$	$-1.33195876 \cdot 10^{-15}$	2
$3.68362875 \cdot 10^{3}$	5.70164073	4.12530561	$-3.22544939 \cdot 10^{-3}$	$6.52764691 \cdot 10^{-6}$	3
$-5.79853643 \cdot 10^{-9}$	$2.06237379 \cdot 10^{-12}$	$3.34630913 \cdot 10^{3}$	$-6.90432960 \cdot 10^{-1}$	$4.51532273 \cdot 10^{3}$	4
$\mathbf{H_2O}$	20387H 2O 1 G	0300.00	5000.00	1000.00	1
$0.02672146 \cdot 10^{2}$	$0.03056293 \cdot 10^{-1}$	$-0.08730260 \cdot 10^{-5}$	$0.01200996 \cdot 10^{-8}$	$-0.06391618 \cdot 10^{-13}$	2
$-0.02989921 \cdot 10^{6}$	$0.06862817 \cdot 10^{2}$	$0.03386842 \cdot 10^{2}$	$0.03474982 \cdot 10^{-1}$	$-0.06354696 \cdot 10^{-4}$	3
$0.06968581 \cdot 10^{-7}$	$-0.02506588 \cdot 10^{-10}$	$-0.03020811 \cdot 10^{6}$	$0.02590233 \cdot 10^{2}$		4
$\mathbf{vH_2O}$	20387H 2O 1 G	0300.00	5000.00	1000.00	1
$0.02672146 \cdot 10^{2}$	$0.03056293 \cdot 10^{-1}$	$-0.08730260 \cdot 10^{-5}$	$0.01200996 \cdot 10^{-8}$	$-0.06391618 \cdot 10^{-13}$	2
$-0.02989921 \cdot 10^{6}$	$0.06862817 \cdot 10^{2}$	$0.03386842 \cdot 10^{2}$	$0.03474982 \cdot 10^{-1}$	$-0.06354696 \cdot 10^{-4}$	3
$0.06968581 \cdot 10^{-7}$	$-0.02506588 \cdot 10^{-10}$	$-0.03020811 \cdot 10^{6}$	$0.02590233 \cdot 10^{2}$		4
$\mathbf{O_2}$	121386O 2 G	0300.00	5000.00	1000.00	1
$0.03697578 \cdot 10^{2}$	$0.06135197 \cdot 10^{-2}$	$-0.01258842 \cdot 10^{-5}$	$0.01775281 \cdot 10^{-9}$	$-0.01136435 \cdot 10^{-13}$	2
$-0.01233930 \cdot 10^{5}$	$0.03189166 \cdot 10^{2}$	$0.03212936 \cdot 10^{2}$	$0.01127486 \cdot 10^{-1}$	$-0.05756150 \cdot 10^{-5}$	3
$0.01313877 \cdot 10^{-7}$	$-0.08768554 \cdot 10^{-11}$	$-0.01005249 \cdot 10^{5}$	$0.06034738 \cdot 10^{2}$		4
$\mathbf{HO_2}$	L 5/89H 1O 2 00 00G	200.000	3500.000	1000.000	1
4.01721090	$2.23982013 \cdot 10^{-3}$	$-6.33658150 \cdot 10^{-7}$	$1.14246370 \cdot 10^{-10}$	$-1.07908535 \cdot 10^{-14}$	2

continued on next page . . .

					#
$1.11856713 \cdot 10^{2}$	3.78510215	4.30179801	$-4.74912051 \cdot 10^{-3}$	$2.11582891 \cdot 10^{-5}$	3
$-2.42763894 \cdot 10^{-8}$	$9.29225124 \cdot 10^{-12}$	$2.94808040 \cdot 10^{2}$	3.71666245	$1.00021620 \cdot 10^{4}$	4
H_2O_2	120186H 2O 2 G	0300.00	5000.00	1000.00	1
$0.04573167 \cdot 10^{2}$	$0.04336136 \cdot 10^{-1}$	$-0.01474689 \cdot 10^{-4}$	$0.02348904 \cdot 10^{-8}$	$-0.01431654 \cdot 10^{-12}$	2
$-0.01800696 \cdot 10^{6}$	$0.05011370 \cdot 10^{1}$	$0.03388754 \cdot 10^{2}$	$0.06569226 \cdot 10^{-1}$	$-0.01485013 \cdot 10^{-5}$	3
$-0.04625806 \cdot 10^{-7}$	$0.02471515 \cdot 10^{-10}$	$-0.01766315 \cdot 10^{6}$	$0.06785363 \cdot 10^{2}$		4
N_2	121286N 2 G	0300.00	5000.00	1000.00	1
$0.02926640 \cdot 10^{2}$	$0.01487977 \cdot 10^{-1}$	$-0.05684761 \cdot 10^{-5}$	$0.01009704 \cdot 10^{-8}$	$-0.06753351 \cdot 10^{-13}$	2
$-0.09227977 \cdot 10^{4}$	$0.05980528 \cdot 10^{2}$	$0.03298677 \cdot 10^{2}$	$0.01408240 \cdot 10^{-1}$	$-0.03963222 \cdot 10^{-4}$	3
$0.05641515 \cdot 10^{-7}$	$-0.02444855 \cdot 10^{-10}$	$-0.01020900 \cdot 10^{5}$	$0.03950372 \cdot 10^{2}$		4
AR	120186AR 1 G	0300.00	5000.00	1000.00	1
$0.02500000 \cdot 10^{2}$	0.00000000	0.00000000	0.00000000	0.00000000	2
$-0.07453750 \cdot 10^{4}$	$0.04366001 \cdot 10^{2}$	$0.02500000 \cdot 10^{2}$	0.00000000	0.00000000	3
0.00000000	0.00000000	$-0.07453750 \cdot 10^{4}$	$0.04366001 \cdot 10^{2}$		4
HE	120186HE 1 G	0300.00	5000.00	1000.00	1
$0.02500000 \cdot 10^{2}$	0.00000000	0.00000000	0.00000000	0.00000000	2
$-0.07453750 \cdot 10^{4}$	$0.09153489 \cdot 10^{1}$	$0.02500000 \cdot 10^{2}$	0.00000000	0.00000000	3
0.00000000	0.00000000	$-0.07453750 \cdot 10^{4}$	$0.09153488 \cdot 10^{1}$		4
CO	121286C 1O 1 G	0300.00	5000.00	1000.00	1
$0.03025078 \cdot 10^{2}$	$0.01442689 \cdot 10^{-1}$	$-0.05630828 \cdot 10^{-5}$	$0.01018581 \cdot 10^{-8}$	$-0.06910952 \cdot 10^{-13}$	2
$-0.01426835 \cdot 10^{6}$	$0.06108218 \cdot 10^{2}$	$0.03262452 \cdot 10^{2}$	$0.01511941 \cdot 10^{-1}$	$-0.03881755 \cdot 10^{-4}$	3
$0.05581944 \cdot 10^{-7}$	$-0.02474951 \cdot 10^{-10}$	$-0.01431054 \cdot 10^{6}$	$0.04848897 \cdot 10^{2}$		4
CO_2	121286C 1O 2 G	0300.00	5000.00	1000.00	1
$0.04453623 \cdot 10^{2}$	$0.03140169 \cdot 10^{-1}$	$-0.01278411 \cdot 10^{-4}$	$0.02393997 \cdot 10^{-8}$	$-0.01669033 \cdot 10^{-12}$	2
$-0.04896696 \cdot 10^{6}$	$-0.09553959 \cdot 10^{1}$	$0.02275725 \cdot 10^{2}$	$0.09922072 \cdot 10^{-1}$	$-0.01040911 \cdot 10^{-3}$	3
$0.06866687 \cdot 10^{-7}$	$-0.02117280 \cdot 10^{-10}$	$-0.04837314 \cdot 10^{6}$	$0.01018849 \cdot 10^{3}$		4
NO	RUS 78N 1O 1 G	200.000	6000.000	1000.000	1

continued on next page . . .

					#
$0.32606056 \cdot 10^{1}$	$0.11911043 \cdot 10^{-2}$	$-0.42917048 \cdot 10^{-6}$	$0.69457669 \cdot 10^{-10}$	$-0.40336099 \cdot 10^{-14}$	2
$0.99209746 \cdot 10^{4}$	$0.63693027 \cdot 10^{1}$	$0.42184763 \cdot 10^{1}$	$-0.46389760 \cdot 10^{-2}$	$0.11041022 \cdot 10^{-4}$	3
$-0.93361354 \cdot 10^{-8}$	$0.28035770 \cdot 10^{-11}$	$0.98446230 \cdot 10^{+4}$	$0.22808464 \cdot 10^{1}$		4
NO_2	L 7/88N 1O 2 G	200.000	6000.000	1000.000	1
$0.48847542 \cdot 10^{1}$	$0.21723956 \cdot 10^{-2}$	$-0.82806906 \cdot 10^{-6}$	$0.15747510 \cdot 10^{-9}$	$-0.10510895 \cdot 10^{-13}$	2
$0.23164983 \cdot 10^{4}$	-0.11741695	$0.39440312 \cdot 10^{1}$	$-0.15854290 \cdot 10^{-2}$	$0.16657812 \cdot 10^{-4}$	3
$-0.20475426 \cdot 10^{-7}$	$0.78350564 \cdot 10^{-11}$	$0.28966179 \cdot 10^{4}$	$0.63119917 \cdot 10^{1}$		4
NH	And94 N 1H 1 G	200.000	6000.000	1000.000	1
$0.27836928 \cdot 10^{1}$	$0.13298430 \cdot 10^{-2}$	$-0.42478047 \cdot 10^{-6}$	$0.78348501 \cdot 10^{-10}$	$-0.55044470 \cdot 10^{-14}$	2
$0.42120848 \cdot 10^{5}$	$0.57407799 \cdot 10^{1}$	$0.34929085 \cdot 10^{1}$	$0.31179198 \cdot 10^{-3}$	$-0.14890484 \cdot 10^{-5}$	3
$0.24816442 \cdot 10^{-8}$	$-0.10356967 \cdot 10^{-11}$	$0.41880629 \cdot 10^{5}$	$0.18483278 \cdot 10^{1}$		4
NH2	And89 N 1H 2 G	200.000	6000.000	1000.000	1
$0.28347421 \cdot 10^{1}$	$0.32073082 \cdot 10^{-2}$	$-0.93390804 \cdot 10^{-6}$	$0.13702953 \cdot 10^{-9}$	$-0.79206144 \cdot 10^{-14}$	2
$0.22171957 \cdot 10^{5}$	$0.65204163 \cdot 10^{1}$	$0.42040029 \cdot 10^{1}$	$-0.21061385 \cdot 10^{-2}$	$0.71068348 \cdot 10^{-5}$	3
$-0.56115197 \cdot 10^{-8}$	$0.16440717 \cdot 10^{-11}$	$0.21885910 \cdot 10^{5}$	-0.14184248		4
HNO	And93 H 1N 1O 1 G	200.000	6000.000	1000.000	1
$0.29792509 \cdot 10^{1}$	$0.34944059 \cdot 10^{-2}$	$-0.78549778 \cdot 10^{-6}$	$0.57479594 \cdot 10^{-10}$	$-0.19335916E \cdot 15$	2
$0.11750582 \cdot 10^{5}$	$0.86063728 \cdot 10^{1}$	$0.45334916 \cdot 10^{1}$	$-0.56696171 \cdot 10^{-2}$	$0.18473207 \cdot 10^{-4}$	3
$-0.17137094 \cdot 10^{-7}$	$0.55454573 \cdot 10^{-11}$	$0.11548297 \cdot 10^{5}$	$0.17498417 \cdot 10^{1}$		4
N2O	L 7/88N 2O 1 G	200.000	6000.000	1000.000	1
$0.48230729 \cdot 10^{1}$	$0.26270251 \cdot 10^{-2}$	$-0.95850874 \cdot 10^{-6}$	$0.16000712 \cdot 10^{-9}$	$-0.97752303 \cdot 10^{-14}$	2
$0.80734048 \cdot 10^{4}$	$-0.22017207 \cdot 10^{1}$	$0.22571502 \cdot 10^{1}$	$0.11304728 \cdot 10^{-1}$	$-0.13671319 \cdot 10^{-4}$	3
$0.96819806 \cdot 10^{-8}$	$-0.29307182 \cdot 10^{-11}$	$0.87417744 \cdot 10^{4}$	$0.10757992 \cdot 10^{2}$		4
NH3	J 6/77N 1H 3 G	200.000	6000.000	1000.000	1
$0.26344521 \cdot 10^{1}$	$0.56662560 \cdot 10^{-2}$	$-0.17278676 \cdot 10^{-5}$	$0.23867161 \cdot 10^{-9}$	$-0.12578786 \cdot 10^{-13}$	2
$-0.65446958 \cdot 10^{4}$	$0.65662928 \cdot 10^{1}$	$0.42860274 \cdot 10^{1}$	$-0.46605230 \cdot 10^{-2}$	$0.21718513 \cdot 10^{-4}$	3

continued on next page . . .

				#
$-0.22808887 \cdot 10^{-7}$	$0.82638046 \cdot 10^{-11}$	$-0.67417285 \cdot 10^{4}$	-0.62537277	4

Acknowledgments

Foremost, I would like to express my gratitude to my supervisor, Professor Christian Oliver Paschereit, for giving me the opportunity to write this PhD thesis, and for the patient guidance, encouragement, and his professional advise he has provided throughout my time as his student. In particular, the given scientific freedom together with undisputed trust were the driving force for this thesis.

I would like to thank Professor Laszlo Fuchs, for enabling a very fruitful scientific stay at his research group at Lund University and the insightful and detailed discussions about swirling flows. Furthermore, I would like to thank him for introducing me to Professor Christophe Duwig.

My deepest appreciation goes to Professor Christophe Duwig. His patience, encouragement, and immense knowledge were key motivations throughout my PhD. Christophe has been a mentor and friend to me, which made him a guiding beacon for my academic and personal development through the last five years of PhD research. I am deeply thankful for his selfless dedication and I cannot think of a better mentor to have.

In addition, I would like to thank the "wet combustion" group for the discussions, ideas, the experimental assessments and the all-embracing perspective on the steam diluted combustion process. It was pleasure working with you.

I would also like to express my special gratitude to all other colleagues, the scientific personal, the secretaries, the workshop, the IT (Angela Pätzold, Martin Franke, and Nico Seiffert), and the students for the support, the helpfulness, and the pleasant working atmosphere.

Special thanks also to Katharina Göckeler, for the scientific input, the support, the encouragement and being a perfect travel companion.

I owe my deepest gratitude to the members of the CONFET, Bernhard Bobusch, Bernhard Ćosić, and Steffen Terhaar, for being the best friends, office partners, and colleagues one could think of. You did not only provided support and fruitful discussions, you also showed that it is possible to win an apparently lost match.

Last but not least I thank my friends and family, for the encouraging support. My deepest heartfelt thanks go to my mother Evelin Gutmann, for just everything.